ISSN: 2687 - 4539

CHAOS

THEORY AND APPLICATIONS

IN APPLIED SCIENCES AND ENGINEERING

VOLUME 6, ISSUE 3, JULY 2024

AN INTERDISCIPLINARY JOURNAL OF NONLINEAR SCIENCE

ISSN: 2687-4539

Chaos Theory and Applications (CHTA)
Volume: 6 – Issue No: 3 (July 2024)
https://dergipark.org.tr/en/pub/chaos/issue/86422

Editorial Board Members

ISSN: 2687-4539

Chaos Theory and Applications (CHTA)
Volume: 6 – Issue No: 3 (July 2024)
https://dergipark.org.tr/en/pub/chaos/issue/86422

Contents:

CHAOS
Theory and Applications
in Applied Sciences and Engineering

e-ISSN: 2687-4539
RESEARCH ARTICLE
Vol.6 / No.3 / 2024 / pp.159-169
https://doi.org/10.51537/chaos.1448912

Birth of Catastrophe and Strange Attractors through Generalized Hopf Bifurcations in Covid-19 Transmission Mathematical Model

Ario Wiraya [*,1], **Yudi Ari Adi** [α,2], **Laila Fitriana** [*,3], **Triyanto** [*,4], **Yuvita Andriani Kusumadewi** [*,5], **Azimatus Nur Safitri** [*,6] **and Aulia Nurmalitasari** [*,7]

*Universitas Sebelas Maret, Surakarta (UNS), 57126, Indonesia, αUniversitas Ahmad Dahlan, Yogyakarta, 55166, Indonesia.

ABSTRACT Coronavirus can be transmitted through the things that people carry or the things where it sticks to after being spread by the sufferer. Instead, various preventive measures have been carried out. We create a new mathematical model that represents Coronavirus that exists in non-living objects, susceptible, and infected subpopulations interaction by considering the Coronavirus transmission through non-living objects caused by susceptible and infected subpopulations along with its prevention to characterize the dynamics of Coronavirus transmission in the population under those conditions. One disease-free and two infection equilibrium points along with their local stability and coexistence are identified. Global stability of the disease-free equilibria and basic reproduction number are also investigated. Changes in susceptible-Coronavirus interaction rate generate Fold and Hopf bifurcations which represent the emergence of a cycle and the collision of two infection equilibrium points respectively. Catastrophe generated by the collision between an attractor and a repeller is found around a Generalized Hopf bifurcation point by changing susceptible-Coronavirus interaction rate and increasing rate of Coronavirus originating from infected subpopulation. It represents a momentary unpredictable dynamics as the effect of Coronavirus addition and infection. Non-chaotic strange attractors that represent complex but still predictable dynamics are also triggered by Generalized Hopf bifurcation when the susceptible-Coronavirus interaction rate and one of the following parameters, i.e. increasing rate of Coronavirus originating from infected subpopulation or infected subpopulation recovery rate vary.

KEYWORDS
Covid-19
Catastrophe
Generalized hopf
Strange attractor

INTRODUCTION

Covid-19 case was reported on the 31st of December 2019 in China (He *et al.* 2020; Zu *et al.* 2020). Covid-19 is a dangerous disease caused by Coronavirus (Pedersen and Ho 2020). Globally, as of April 23, 2023, there have been 764 million Covid-19 incidences which consist of 6 million death cases (WHO 2020). The most common form of Covid-19 transmission is direct contact transmission. The transmission occurs when interactions between an infected person and a susceptible person such as physical contact and contagion through air droplets exist. Things or non-living media exposed to the virus are also included as media of Covid-19 transmission (Ramesh *et al.* 2020).

There are several experiments have been carried out to analyze the lifecycle of Coronavirus as follows (van Doremalen *et al.* 2020). In aerosols, Coronavirus can survive for 3 hours. Coronavirus can not survive on copper after 4 hours. No viable Coronavirus was found on carton after 24 hours. On plastic and stainless steel, Coronavirus can survive better until 72 hours. Coronavirus can survive on different surfaces of various materials, such as paper, glass, PVC, metal, ceramic, and teflon until 5 days (Carraturo *et al.*

Manuscript received: 9 March 2024,
Revised: 25 May 2024,
Accepted: 10 June 2024.

[1]ariowiraya@staff.uns.ac.id (**Corresponding author**)
[2]yudi.adi@math.uad.ac.id
[3]lailafitrianafkip@staff.uns.ac.id
[4]triyanto.math@staff.uns.ac.id
[5]yuvitaandriani@student.uns.ac.id
[6]azimatusnur@student.uns.ac.id
[7]aulianurmalitasari16@student.uns.ac.id

2020). It provides critical information about the stability of Covid-19 and it is still possible for the virus to infect people after touching contaminated non-living media.

Asymptomatic and presymptomatic conditions also become an important factor in the Covid-19 spread. These silent carrier factors cause a dangerous impendence to Covid-19 treatment efforts for the precaution and countermeasures of Covid-19 since it is not detected (Obi and Odoh 2021). Even though the pandemic has been overcome in several countries, specific therapeutics and vaccines have not yet been found, while continuous spread by silent carrier factors could cause the incidence of these cases to increase again. Transmission of the silent carriers could be minimized by using face masks, maintaining social distancing, hand washing and sanitizing regularly, and avoiding crowds of people (Vermund and Pitzer 2021; for Disease Prevention and Control 2020; Gandhi *et al.* 2020). These imply that the transmission of Covid-19 also considers susceptible subpopulations and Coronavirus eradication efforts.

Mathematical modeling is an important tool to characterize and predict dynamics occurring in a system. Some researchers used it in many applications as follows. In the field of Biology, analysis of the predator-prey mathematical model reveals the extinction of prey or predator in a population (Mondal *et al.* 2024), the potential for environmental or human disturbance effects (Sk *et al.* 2023), the effects of species memory on the system (Thirthar *et al.* 2023), and the effects of additional food for the predator (Thirthar 2023). In the other fields, i.e. Economics and Environment, mathematical modeling is used to determine a strategy of inventory management in order to reduce global warming and carbon emission (Pakhira *et al.* 2024).

Until now, many researchers have constructed numerous models for Covid-19 by using the concepts of differential equations systems, such as the SIR mathematical model to characterize Covid-19 transmission. A mathematical model of Coronavirus infection in a population has been constructed (AlQadi and Bani-Yaghoub 2022). The research studies the interaction between susceptible, infected, and recovery subpopulations, but it has not considered the infection from Coronavirus that exists on non-living objects and its prevention. Another research is also conducted (Din and Algehyne 2021). They develop a mathematical model of Coronavirus transmission by considering the prevention of Coronavirus transmission. However, it still has not considered the infection from Coronavirus that exists on non-living objects. Other research has also been conducted by (Yang and Wang 2020) that reveals the effect of exposed and Coronavirus subpopulation addition to the system. The research has considered the infection from Coronavirus that exists on non-living objects. Meanwhile, it has not considered susceptible subpopulation as one of the Coronavirus carriers. It also has not considered the prevention of the infection from Coronavirus that exists on non-living objects.

Based on the previous studies that have not considered these three following factors together, i.e. the infection from Coronavirus that exists on non-living objects, susceptible subpopulation as one of the Coronavirus carriers, and the prevention of the infection from Coronavirus that exists on non-living objects, we create and analyze a new mathematical model, i.e. nonlinear ordinary differential equations system by considering those three factors to characterize the dynamics under those conditions so that the conditions of some important phenomena that should be reached or avoided can be revealed and become a medical recommendation to overcome Covid-19 in the population.

This research is conducted by explaining the motivation, state of the art, and novelty of this article in the introduction, constructing the mathematical model, analyzing the positivity, and boundedness of the model solution, equilibrium points, basic reproduction number, coexistence and local stability of the equilibrium points, and the bifurcations which consist of some phenomena such as strange attractors and catastrophe dynamics. Characterization of Covid-19 transmission shown by the phenomena becomes the indicator to predict the dynamics in the population as the parameters vary.

MATHEMATICAL MODEL

Development of the mathematical model is started by identifying the subpopulations that interact with each other in the population along with the assumption to limit the scope of this research. Based on the conditions which have been explained, there are three subpopulations which interact with each other in the population, i.e. Coronavirus that exists in non-living objects, susceptible, and infected subpopulations. In this research, we assume that the eradication of Coronavirus that exists in non-living objects is ignored and an increase in the number of Coronavirus that exists in non-living objects due to infected subpopulation has the same value as the number of infectious units of the Coronavirus enumerated by a plaque assay (Sender *et al.* 2021).

After identifying the subpopulations that interact with each other in the population along with the assumption, we define the subpopulations as the variables in the mathematical model. Definition of the variables are written in the Table 1. V, S, and I denote subpopulations and t denotes time so that they are non-negative.

Table 1 Variables in the Model

Variable	Definition	Initial Value	Unit
V	Coronavirus subpopulation attached to non-living media	Estimation	virion
S	Susceptible subpopulation	Estimation	person
I	Infected subpopulation	Estimation	person
t	Time	Estimation	day

Every subpopulation in the population which is defined as the variable in the mathematical model interacts with each other. The level of each interaction is defined as the parameters in the mathematical model. Definition of the parameters are written in the Table 2. The initial value for several parameters were set in accordance with the previous research, while the initial values for several other parameters were assumed because the data had not been found either from primary sources, or from the previous research. All of the parameters have a positive value. We define d as the difference between infection of Coronavirus that exists in non-living objects and the prevention rate of the infection from Coronavirus that exists on non-living objects, i.e. $d = p - q$. The parameter d is possible to be negative if the infection of Coronavirus that exists in

Table 2 Parameters in the Model

Parameter	Definition	Value	Unit	Reference
a	Coronavirus increasing rate from infected subpopulation	100	virion per day	(Sender *et al.* 2021)
b	Coronavirus death rate	1	virion per day	(Yang and Wang 2020)
c	Susceptible subpopulation natural birth rate	10.7	person per day	(Din and Algehyne 2021)
p	Infection of Coronavirus that exists in non-living objects rate	1	virion per day	Assumption
q	Prevention rate of Coronavirus that exists in non-living infection	0.5	virion per day	Assumption
m	Coronavirus increasing rate from suspected subpopulation	0.5	virion per day	Assumption
e	Susceptible subpopulation natural death rate	0.0062	per day	Assumption
f	Infected subpopulation recovery rate	1	per day	(AlQadi and Bani-Yaghoub 2022)
g	Susceptible-infected interaction rate	0.0707	per day	(Din and Algehyne 2021)
h	Infected subpopulation death rate due to Coronavirus infection	0.02	person per day	(Din and Algehyne 2021)

non-living objects rate (p) is less than its prevention rate (q).

According to the model variables and parameters that have been written, we illustrate the interaction between the variables with the parameters as the rate in Figure 1.
According to the transfer diagram in Figure 1, we create a system of nonlinear ordinary differential equations as a mathematical model that represents the interaction, i.e.

$$\frac{dV}{dt} = aI - bV + mS \tag{1}$$

$$\frac{dS}{dt} = c - dSV - eS + fI - gSI \tag{2}$$

$$\frac{dI}{dt} = dSV + gSI - fI - hI \tag{3}$$

Equation (1) represents the rate of change of the virus population with respect to time which is denoted by aI as the coronavirus addition from infected subpopulation, because they sneeze, or the other reason, bV as coronavirus death, and mS as the coronavirus addition from suspected subpopulation because they carried.

Equation (2) represents the rate of change in the susceptible population with respect to time. The first term is the increase of susceptible population caused by the susceptible population's natural birth by c. The second term is the reduction of the susceptible population due to its interaction with the virus, in which d denotes the interaction rate. The third term is the reduction of susceptible population caused by the susceptible population's natural

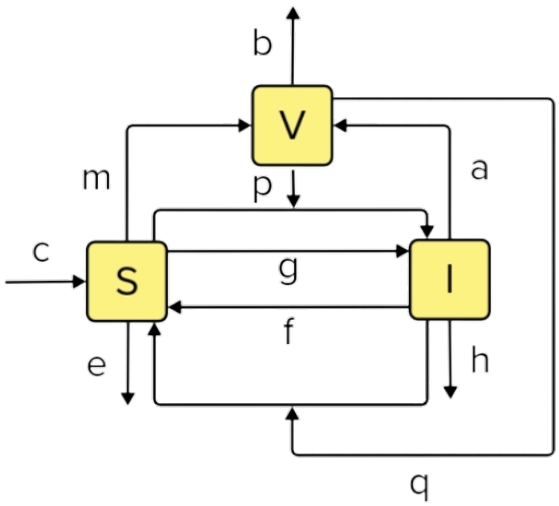

Figure 1 Transfer diagram of the interaction between Coronavirus, susceptible, and infected subpopulations.

death with e as its rate. The fourth term is the increase of susceptible population caused by the infected population recovery where f represents the rate. The fifth term is reducing the susceptible population due to its interaction with the infected population with g as its rate.

Equation (3) represents the rate of change in the infected population with respect to time. The first term is the increase in the infected population due to the interaction between the susceptible population and the virus where d denotes the interaction rate. The second term is the increase in the infected population caused by its interaction with the susceptible population by g. The third term is the reduction of the infected population caused by the infected population recovery, where f represents the rate. The fourth term is the reduction of the infected population caused by the infected population death due to Coronavirus with h as its rate.

POSITIVITY AND BOUNDEDNESS OF SOLUTION

Solution of the model must be positive in order to get the biological interpretation (Wiraya *et al.* 2022). The following theorem guarantees the positivity of the solution.

Theorem 1. The solution set $\{V, S, I\}$ of the model with non-negative initial condition $V(0) = V_0$, $S(0) = S_0$, and $I(0) = I_0$ remain non-negative for all time $t > 0$.

Proof. For the non-negative initial condition $V(0) = V_0$, $S(0) = S_0$, and $I(0) = I_0$, it is clear from the Equation (1) that $\frac{dV}{dt} + bV(t) \geq 0$, so that $\frac{d}{dt}\left[V(t)e^{bt}\right] \geq 0$. By integrating the last inequality, we obtain $V(t) \geq V(0)e^{-bt} > 0$ for all $t > 0$. Further, from Equation (2), we get $\frac{dS}{dt} + [dV(t) + e + gI(t)]S(t) \geq 0$, so that $S(t) \geq S(0)e^{-(et+d\int_0^t V(\tau)d\tau + g\int_0^t I(\tau)d\tau)} > 0$ for all $t > 0$. Similarly, it can be shown that $I(t) > 0$ for all $t > 0$.

Besides the positivity, the solution of the model must also be bounded, so that it has a biological meaning (Wiraya *et al.* 2022). Boundedness of the solution is guaranteed by the following theorem.

Theorem 2. Every solution of the model initiated in $\mathbb{R}^3_+$ is bounded.

Proof. By subtracting Equation (2) and Equation (3), we have $\frac{d}{dt}[S(t) + I(t)] = c - eS - hI \leq c - p[S(t) + I(t)]$, where $p = \min\{e, h\}$. Therefore $S(t) + I(t) \leq \frac{c}{p} + \left[S(0) + I(0) - \frac{c}{p}\right]e^{-pt}$. Hence, $S(t) + I(t) \to \frac{c}{p}$ as $t \to \infty$. Thus, $S(t)$ and $I(t)$ are bounded. Furthermore, from Equation (1), we get $\frac{dV}{dt} = aI - bV + mS \leq aI + mS \leq q[S(t) + I(t)]$, where $q = \max\{a, m\}$. Hence, $V(t)$ is bounded since $S(t)$ and $I(t)$ are bounded. Therefore, $V(t)$, $S(t)$, and $I(t)$ are bounded in $\mathbb{R}^3_+$.

EQUILIBRIUM POINTS

The equilibrium point represents a steady state condition of each subpopulation number over time. Consider $a_2 = gb^2eh$, $a_1 = (dbh - (f + h))(ae - mh) - gcb(ae + mh)$, $a_0 = gac^2m - ((f + h)mc + dac)(ae - mh)$. The equilibrium point of the model is explained in the following theorem.

Theorem 3. Equilibrium points of the system are

$$E_1 = \left(V_1^*, \frac{ac - bhV_1^*}{ae - mh}, \frac{ebV_1^* - mc}{ae - mh}\right)$$

and

$$E_2 = \left(V_2^*, \frac{ac - bhV_2^*}{ae - mh}, \frac{ebV_2^* - mc}{ae - mh}\right),$$

where

$$V_1^* = \frac{-a_1 + \sqrt{a_1^2 - 4a_2a_0}}{2a_2}$$

and

$$V_2^* = \frac{-a_1 - \sqrt{a_1^2 - 4a_2a_0}}{2a_2}$$

If $V_1^* = V_2^* = \frac{mc}{eb}$, then there is one disease-free equilibria, i.e. $E_1 = E_2 = E_0 = (\frac{mc}{eb}, \frac{c}{e}, 0)$. On the other condition, the system has two infection equilibrium points, i.e. E_1 and E_2.

Proof. The equilibrium points E^* are solutions of the model when Equation (1) = Equation (2) = Equation (3) = 0 (Wiggins 2003; Wiraya and Adi-Kusumo 2023), i.e.

$$aI - bV + mS = 0 \tag{4}$$

$$c - dSV - eS + fI - gSI = 0 \tag{5}$$

$$dSV + gSI - fI - hI = 0 \tag{6}$$

By adding Equation (5) and Equation (6), we found $c - eS - hI = 0$ which is equivalent to $I^* = \frac{c - eS}{h}$. By substituting I^** to Equation (4), we obtain $S^* = \frac{ac - bhV^*}{ae - mh}$. By substituting S^* to I^**, we found $I^* = \frac{ebV^* - mc}{ae - mh}$. By substituting S^* and I^* to Equation (6), we obtain a quadratic equation

$$a_2V^2 + a_1V + a_0 = 0. \tag{7}$$

Thus, we found that V_i^* for $i = 1, 2$ are the solutions of the quadratic equation, i.e. $V_1^* = \frac{-a_1 + \sqrt{a_1^2 - 4a_2a_0}}{2a_2}$ and $V_2^* = \frac{-a_1 - \sqrt{a_1^2 - 4a_2a_0}}{2a_2}$. Hence, $S_i^* = \frac{ac - bhV_i^*}{ae - mh}$ and $I_i^* = \frac{ebV_i^* - mc}{ae - mh}$, for $i = 1, 2$. Therefore, the equilibrium points are

$$E_1 = \left(V_1^*, \frac{ac - bhV_1^*}{ae - mh}, \frac{ebV_1^* - mc}{ae - mh}\right)$$

and

$$E_2 = \left(V_2^*, \frac{ac - bhV_2^*}{ae - mh}, \frac{ebV_2^* - mc}{ae - mh}\right).$$

Consider $V_1^* = V_2^* = \frac{mc}{eb}$, then we get $\frac{ebV_1^* - mc}{ae - mh} = \frac{ebV_2^* - mc}{ae - mh} = 0$ and $\frac{ac - bhV_1*}{ae - mh} = \frac{ac - bhV_1*}{ae - mh} = \frac{c}{e}$. Hence, we obtain $E_1 = E_2 = E_0 = (\frac{mc}{eb}, \frac{c}{e}, 0)$. It is a disease-free equilibria, because the infected subpopulation does not exist. Other than that condition, there are two infection equilibrium points, i.e. E_1 and E_2 since the infected subpopulation exists.

COEXISTENCE OF EQUILIBRIUM POINTS

The solution of the model must be real and positive in order to satisfy the existence of the equilibrium points. We see that $a_2 > 0$. We get different solutions depending on the signs of a_1 and a_0 that summarized in the following theorem.

Theorem 4. Consider one of the following conditions is fullfiled: i. $ae > mh$ and $\frac{mc}{eb} \leq V^* \leq \frac{ac}{bh}$; ii. $ae < mh$ and $\frac{ac}{bh} \leq V^* \leq \frac{mc}{eb}$. The System : a) has a unique equilibria if $a_0 < 0$; b) has two equilibrium if $a_0 > 0$ and $a_1 < 0$; c) has no equilibria if $a_0 > 0$ and $a_1 > 0$.

Proof. Consider the condition i or ii is fulfilled. Thus, S^* and I^* are non-negative. a) Consider $a_0 < 0$. We found that Equation (7) will have one positive and one negative value of V^*. Hence, the model has a unique equilibria. ii. Consider $a_0 > 0$ and $a_1 < 0$. Thus, Equation (7) will have two positive values of V^*. Hence, the model has two equilibrium points. iii. Consider $a_0 > 0$ and $a_1 > 0$. Hence, Equation (7) will have two negative values of V^*. Therefore, the model has no equilibria.

BASIC REPRODUCTION NUMBER

Transmission of a disease is determined by basic reproduction number. In this case, it becomes a parameter used to measure the potential of Coronavirus infection in a population.

Theorem 5. Basic reproduction number of the system is $R_0 = \frac{1}{2}(U + \sqrt{U^2 - 4W})$, where $U = \frac{c(bg-aq)}{be(f+h)}$ and $W = -\frac{ap}{b}$.

Proof. R_0 is calculated by using the Next Generation Matrix method (Castillo-Garsow and Castillo-Chavez 2020). R_0 is influenced by Equation (1) and Equation (3) because the Coronavirus infection originate from those equations. The positive and negative terms in those equations are grouped so that the following matrices are obtained.

$$\mu = \begin{pmatrix} aI + mS \\ pSV + gSI \end{pmatrix}, \psi = \begin{pmatrix} bV \\ qSV + fI + hI \end{pmatrix}.$$

Jacobian matrix of μ and ψ evaluated on E_0 are written as follows.

$$F = \begin{pmatrix} 0 & a \\ \frac{pc}{e} & \frac{gc}{e} \end{pmatrix}, G = \begin{pmatrix} b & 0 \\ \frac{qc}{e} & f+h \end{pmatrix}.$$

Hence, $G^{-1} = \begin{pmatrix} \frac{1}{b} & 0 \\ -\frac{qc}{be(f+h)} & \frac{1}{f+h} \end{pmatrix}$.

The Next Generation Matrix is

$$M = FG^{-1} = \begin{pmatrix} -\frac{aqc}{be(f+h)} & \frac{a}{f+h} \\ \frac{pce(f+h)-gqc^2}{be^2(f+h)} & \frac{gc}{e(f+h)} \end{pmatrix}.$$

The characteristic equation of M is

$$\lambda^2 + U\lambda + W = 0, \tag{8}$$

where λ is the eigen value of M, $U = \frac{c(bg-aq)}{be(f+h)}$, and $W = -\frac{ap}{b}$. Therefore, the eigenvalue of M are

$$\lambda_{1.2} = \frac{1}{2}(U \pm \sqrt{U^2 - 4W}).$$

Since the basic reproduction number is the largest eigenvalue (spectral radius) of M, we found that $R_0 = \frac{1}{2}(U + \sqrt{U^2 - 4W})$.

LOCAL STABILITY ANALYSIS

Local stability of the equilibrium points represents the convergence of the number of Coronavirus, susceptible, and infected subpopulations when the initial conditions of them are around the equilibrium points. We predict the dynamic of each subpopulation starting around the equilibrium points by analyzing the local stability using Routh-Hurwitz criteria (Perko 2001).

Consider $A = gI_i^* + dV_i^* + b + e + f + h$, $B = g^2S_i^* + dgS_i^*V_i^* + (bg + fg + gh)I_i^* + dmS_i^* + (b+h)dV_i^* + be + bf + bh + ef + eh - adS_i^* - fgS_i^*$, and $C = (adg + bg^2 + dgm)S_i^* + bdgS_i^*V_i^* + bg(f+h)I_i^* + dhmS_i^* + bdhV_i^* + be(f+h) - adgS_i^*I_i^* - adeS_i^* - bgfS_i^*$ for $i = 1, 2$. Local stability of the equilibrium points E^* is stated in the following theorem.

Theorem 6. The equilibrium points E_i^* for $i = 1, 2$ are locally asymptotically stable if $A > 0$, $C > 0$, and $AB - C > 0$.

Proof. To determine the local stability of equilibrium points E_i^* for $i = 1, 2$, we compute the Jacobian matrix given by

$$J_{E_i^*} = \begin{pmatrix} -b & m & a \\ -dS_i^* & -dV_i^* - e - gI_i^* & f - gS_i^* \\ dS_i^* & dV_i^* + gS_i^* & -(f+h) \end{pmatrix}.$$

Consider λ is the eigenvalue of $J_{E_i^*}$. The characteristic equation of $J_{E_i^*}$ is

$$\lambda^3 + A\lambda^2 + B\lambda + C = 0. \tag{9}$$

Based on the characteristic equation, we found that the equilibrium points E_i^* is locally asymptotically stable if $A > 0$, $C > 0$, and $AB - C > 0$ by using Routh-Hurwitz criteria.

We especially investigate the conditions that make the population free from Covid-19 which closely related to the disease-free equilibria stability condition. Local stability conditions of the disease-free equilibria are limited to the initial conditions of the subpopulations which are around the disease-free equilibria. Global stability conditions of the disease-free equilibria represent the criteria that should be fulfilled in order to make the population free from Covid-19 for any initial condition of the subpopulations.

GLOBAL STABILITY ANALYSIS

Global stability of the equilibrium points illustrates the convergence situation of the number of Coronavirus, susceptible, and infected subpopulations for any initial conditions of them. We especially analyze the global stabilty of $E_0 = \left(\frac{mc}{eb}, \frac{c}{e}, 0\right)$, i.e. the disease-free equilibria to obtain the conditions that make the population free from Covid-19 for any initial condition of the subpopulations. We analyze the dynamic of each subpopulation which can be started around or far from E_0 by using Lyapunov function (LaSalle and Lefschetz 1961). Global stability of the equilibrium points E_0 is stated in the following theorem.

Theorem 7. The disease-free equilibria E_0 is globally asymtotically stable if $p \le q$, $g \le e$, and $c \le f + h$.

Proof. We choose a function as follows.

$$L = Ie^{(S+I)}.$$

Hence, L and its first derivative is a continuous function on $\mathbb{R}^3_+$. For every $E = (V, S, I) \in \mathbb{R}^3_+$ and $E \neq E_0$, we obtain $L(E) > 0$. If $E = E_0$, then $L(E_0) = 0$. By using Equation (1), (2), and (3), the first derivative of L with respect to t is stated as follows.

$$\begin{aligned} \frac{dL}{dt} &= \frac{dI}{dt}e^{(S+I)} + Ie^{(S+I)}\left(\frac{dS}{dt} + \frac{dI}{dt}\right) \\ &= e^{(S+I)}\left[dSV + (g-e)SI - (f+h-c)I - hI^2\right], \end{aligned}$$

where $d = p - q$ by definition. Thus, $\frac{dL}{dt} \le 0$ if $p \le q$, $g \le e$, and $c \le f + h$.

BIFURCATION ANALYSIS

We vary some parameters of the model, i.e. susceptible-Coronavirus interaction rate (d), susceptible-infected interaction rate (g), infected subpopulation recovery rate (f), and Coronavirus increasing rate from infected subpopulation (a) and investigate its effect on the change of the number of equilibria and its stability to characterize the dynamics of Covid-19 transmission (Kuznetsov 1998).

Codimension-one Bifurcation

Fold and Hopf bifurcations occur when we make a E_2 as susceptible-Coronavirus interaction rate (d) decreases. The existence of Fold and Hopf bifurcations is presented analytically.

The existence of the Fold Bifurcation is written in the following theorem.

Theorem 8. Fold bifurcation occurs if $d = \frac{bg[(f-g)S_1^*-(f+h)I_1^*-(f+h)}{[a(g-e)+m(g+h)]S_1^*+(bV_1^*-aI_1^*)gS_1^*+bhV_1^*}$.

Proof. According to the theory in (Bosi and Desmarchelier 2019) and the characteristic Equation (9), we found that a Fold bifurcation occurs if $-C = 0$. It is equivalent with $d = \frac{bg[(f-g)S_1^*-(f+h)I_1^*-(f+h)}{[a(g-e)+m(g+h)]S_1^*+(bV_1^*-aI_1^*)gS_1^*+bhV_1^*}$.

The existence of the Non-neutral Hopf bifurcation is stated in the following theorem.

Theorem 9. Non-neutral Hopf bifurcation occurs if the value of d satisfies the quadratic equation $Pd^2 + Qd + R = 0$ where $P = (a-m)S_1^*V_1^* - (b+h)V_1^{*^2} - gS_1^*V_1^{*^2}$, $Q = (ag+gm-bm+ab-em-fm+fa+ah)S_1^* - (g^2+eg)S_1^*V_1^* - (2bf+ef+b^2+2bh+fh+h^2)V_1^* - mgS_1^*I_1^* - g^2S_1^*V_1^*I_1^* - (2bg+fg+2gh)V_1^*I_1^*$, and $R = (eg^2-efg+fg^2-f^g+hg^2-fhg)S_1^* + (bg^2+fg^2+g^2h+2beg+2gef+2geh+b^2g+2bfg+2bgh+f^2g+2fgh+gh^2)I_1^* + (g^3-fg^2)S_1^*I_1^* + b^2(e+f+h) + 2bef + 2beh + e^2(b+f+h) + (b+e)(f^2+h^2) + 2bfh + 2efh$.

Proof. According to the theory in (Bosi and Desmarchelier 2019) and the characteristic Equation (9), we found that Hopf bifurcations occur if $-C = B(-A)$. It is fulfilled if the value of d satisfies the quadratic equation $Pd^2 + Qd + R = 0$ where $P = (a-m)S_1^*V_1^* - (b+h)V_1^{*^2} - gS_1^*V_1^{*^2}$, $Q = (ag+gm-bm+ab-em-fm+fa+ah)S_1^* - (g^2+eg)S_1^*V_1^* - (2bf+ef+b^2+2bh+fh+h^2)V_1^* - mgS_1^*I_1^* - g^2S_1^*V_1^*I_1^* - (2bg+fg+2gh)V_1^*I_1^*$, and $R = (eg^2-efg+fg^2-f^g+hg^2-fhg)S_1^* + (bg^2+fg^2+g^2h+2beg+2gef+2geh+b^2g+2bfg+2bgh+f^2g+2fgh+gh^2)I_1^* + (g^3-fg^2)S_1^*I_1^* + b^2(e+f+h) + 2bef + 2beh + e^2(b+f+h) + (b+e)(f^2+h^2) + 2bfh + 2efh$.

Codimension-two Bifurcation

Codimension-two bifurcation is obtained through continuation of bifurcation point related to bifurcation value (Verhulst 1996) that found in codimension-one bifurcation. Some Generalized Hopf, Bogdanov-Takens, or Zero Hopf bifurcations are found when we make a continuation of the non-neutral Hopf bifurcation point as susceptible-Coronavirus interaction rate (d) and one of the following parameter, i.e. susceptible-infected interaction rate (g), infected subpopulation recovery rate (f), or Coronavirus increasing rate from infected subpopulation (a) vary. The existence of Bogdanov-Takens and Zero hopf bifurcations are explained analytically, but the existence of Generalized Hopf bifurcations are shown numerically, because of its complexity.

The existence of Bogdanov-Takens bifurcations is shown in the following theorem.

Theorem 10. Bogdanov-Takens bifurcations occur if $d = \frac{bg[(f-g)S_1^*-(f+h)I_1^*-(f+h)}{[a(g-e)+m(g+h)]S_1^*+(bV_1^*-aI_1^*)gS_1^*+bhV_1^*}$ and $d = \frac{(fg-g^2)S_1^*-g(b+f+h)I_1^*-b(e+f+h)-e(f+h)}{gS_1^*V_1^*+(m-a)S_1^*+(b+h)V_1^*}$.

Proof. According to the theory in (Bosi and Desmarchelier 2019) and the characteristic Equation (9), we found that Bogdanov-Takens bifurcations occur if $-C = 0$ and $-B = 0$. They are equivalent with $d = \frac{bg[(f-g)S_1^*-(f+h)I_1^*-(f+h)}{[a(g-e)+m(g+h)]S_1^*+(bV_1^*-aI_1^*)gS_1^*+bhV_1^*}$ and $d = \frac{(fg-g^2)S_1^*-g(b+f+h)I_1^*-b(e+f+h)-e(f+h)}{gS_1^*V_1^*+(m-a)S_1^*+(b+h)V_1^*}$ respectively.

The existence of Zero Hopf bifurcation is presented in the following theorem.

Theorem 11. Zero-Hopf bifurcation occurs if $d = \frac{bg[(f-g)S_1^*-(f+h)I_1^*-(f+h)}{[a(g-e)+m(g+h)]S_1^*+(bV_1^*-aI_1^*)gS_1^*+bhV_1^*}$, $d = -(gI_1^*+b+e+f+h)$, and $d > \frac{(fg-g^2)S_1^*-g(b+f+h)I_1^*-b(e+f+h)-e(f+h)}{gS_1^*V_1^*+(m-a)S_1^*+(b+h)V_1^*}$ where $gS_1^*V_1^* + (m-a)S_1^* + (b+h)V_1^* > 0$.

Proof. According to the theory in (Bosi and Desmarchelier 2019) and the characteristic Equation (9), we found that Zero Hopf bifurcations occur if $-C = 0$, $-A = 0$, and $B > 0$. They are equivalent with $d = \frac{bg[(f-g)S_1^*-(f+h)I_1^*-(f+h)}{[a(g-e)+m(g+h)]S_1^*+(bV_1^*-aI_1^*)gS_1^*+bhV_1^*}$, $d = -(gI_1^*+b+e+f+h)$, and $d > \frac{(fg-g^2)S_1^*-g(b+f+h)I_1^*-b(e+f+h)-e(f+h)}{gS_1^*V_1^*+(m-a)S_1^*+(b+h)V_1^*}$ where $gS_1^*V_1^* + (m-a)S_1^* + (b+h)V_1^* > 0$ respectively.

NUMERICAL SIMULATION

Susceptible-Coronavirus interaction rate (d), susceptible-infected interaction rate (g), infected subpopulation recovery rate (f), and Coronavirus increasing rate from infected subpopulation (a) vary numerically by using MATCONT (Wiraya and Adi-Kusumo 2023; Adi *et al.* 2023), then the impact of the variations in the dynamics of Covid-19 transmission in the population that become the characteristics of the transmission is identified. We set initial parameter values as written in Table 2.

Fold and Hopf Bifurcations

Continuation of $E_2 = (12.12660541, 1753.700767, -8.647237780)$ as susceptible-Coronavirus interaction rate (d) decreases generates a Fold bifurcation and three Hopf bifurcations which consist of two neutral saddle and one non-neutral saddle Hopf bifurcations, see Figure 2.

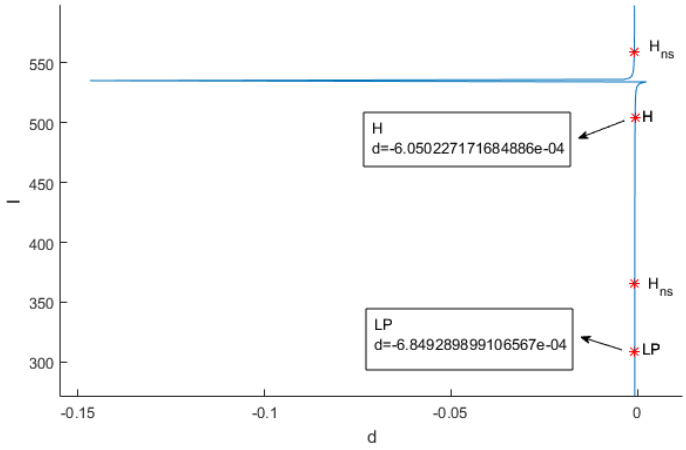

Figure 2 Bifurcation diagram generated by continuing E_2 as susceptible-Coronavirus interaction rate (d) decreases.

Two infection equilibrium points collide at the Fold bifurcation point and vanish when the prevention of Coronavirus infection through non-living objects has the same rate as the infection. A cycle is found at the non-neutral saddle Hopf bifurcation point which represents a fluctuation cycle of Coronavirus, susceptible, and infected subpopulations when the rate of the infection by Coronavirus that exists in non-living objects is less than its prevention rate. We make a continuation of the non-neutral saddle Hopf

bifurcation point to generate some codimension-two bifurcations which are explained in the next section.

Generalized Hopf, Zero Hopf, and Bogdanov-Takens Bifurcations

Continuations of the non-neutral saddle Hopf bifurcation point as susceptible-Coronavirus interaction rate (d), susceptible-infected interaction rate (g), infected subpopulation recovery rate (f), and Coronavirus increasing rate from infected subpopulation (a) vary are conducted, see Figure 3, Figure 4, and Figure 5.

Continuation of the non-neutral saddle Hopf bifurcation point as susceptible-Coronavirus interaction rate (d) and susceptible-infected interaction rate (g) decrease generates two Generalized Hopf and one Bogdanov-Takens bifurcations, see Figure 3.

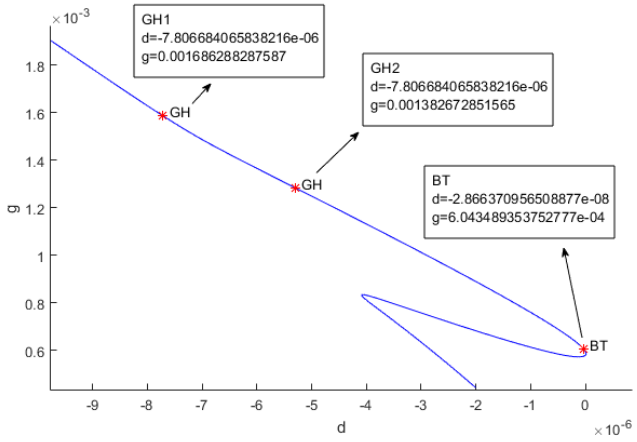

Figure 3 Bifurcation diagram generated by continuing the Fold point as susceptible-Coronavirus interaction rate (d) and susceptible-infected interaction rate (g) decrease.

The other codimension-two bifurcations are found by making continuation of the non-neutral saddle Hopf bifurcation point as the susceptible-Coronavirus interaction rate (d) decreases and infected subpopulation recovery rate (f) increases. It generates four Generalized Hopf, one Bogdanov-Takens, and two Zero Hopf bifurcations which consist of one non-neutral saddle and one neutral saddle Zero Hopf bifurcation, see Figure 4.

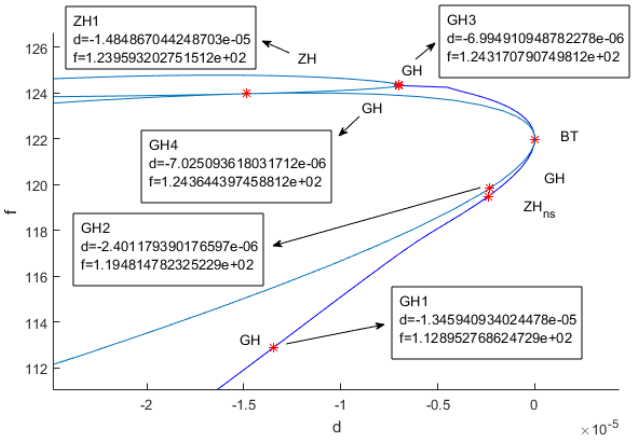

Figure 4 Bifurcation diagram generated by continuing the non-neutral Hopf bifurcation point as the Coronavirus interaction rate (d) decreases and the infected subpopulation recovery rate (f) increases.

We also make a continuation of the non-neutral saddle Hopf bifurcation point as susceptible-Coronavirus interaction rate (d) and Coronavirus increasing rate from infected subpopulation (a) decrease. It generates a Generalized Hopf bifurcation, see Figure 5.

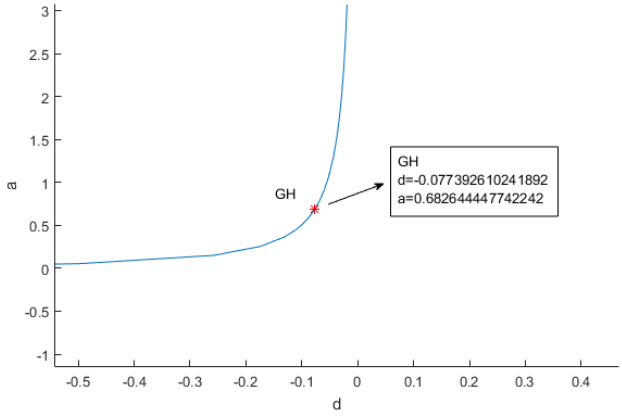

Figure 5 Bifurcation diagram generated by continuing the non-neutral Hopf bifurcation point as susceptible-Coronavirus interaction rate (d) and Coronavirus increasing rate from infected subpopulation (a) decrease.

Some phenomena are found around the Generalized Hopf bifurcation points, such as strange attractors and catastrophe which are discussed in the next section. The phenomena become some characteristics of Covid-19 transmission based on the varied parameters that can become an indicator to predict the dynamics of Covid-19 in the population.

Strange Attractors Generated by Generalized Hopf Bifurcations

We choose a value of (d, g) around the GH1 and GH2 points in Figure 3, and also (d, f) around the GH1 point in Figure 4. Then, we choose an initial value around the equilibrium which was found by choosing those parameters, then we found three strange attractors as shown in Figure 6(a), Figure 6(b), and Figure 6(c). We also calculate the Lyapunov exponent (Dieci *et al.* 1997) of the strange attractors to investigate their characteristic.

In Figure 6(a), we choose $(d, g) = (-7.806684065838216e-06, 0.001686288287587)$ around GH1 in Figure 3 and an initial value $(V, S, I) = (1.815098324208333e+04., 1.159155421086804e+03, 1.757552288703374e+02)$ generated by choosing those parameters. In Figure 6(b), we choose $(d, g) = (5.591353065874137e-06, 0.001482672851565)$ around GH2 in Figure 3 and an initial value $(V, S, I) = (1.918856995532746e+04, 1.125005746177521e+03, 1.862583288670330e+02)$ generated by choosing those parameters. In Figure 5, we choose $(d, f) = (-1.345940934024478e-05, 1.028952768624729e+02)$ around GH1 in Figure 4 and an initial value $(V, S, I) = (8.152543256535453e+03, 1.486804434008352e+03, 74.09169434849883)$ generated by choosing those parameters.

Lyapunov exponent of each variable generating the strange attractor shown in Figure 6(a), Figure 6(b), and Figure 6(c) are presented in Figure 6(c), Figure 6(d), and Figure 6(e) respectively. Based on the Lyapunov exponents, we found that all of the strange attractors are non-chaotic as all of the variable's Lyapunov exponents have a negative value (Wiraya and Adi-Kusumo 2023).

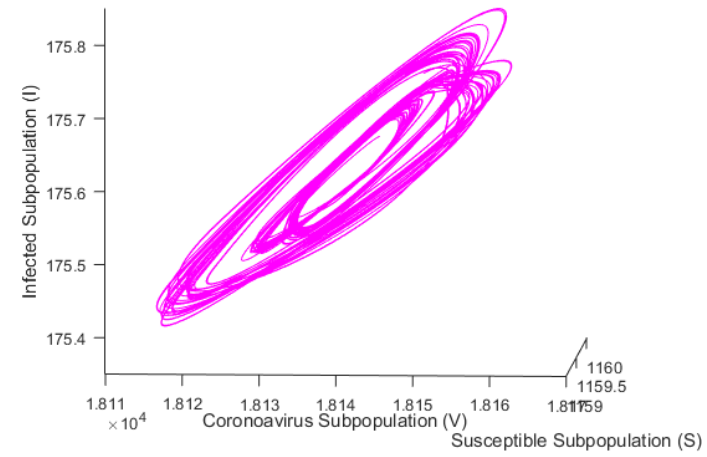

(a)

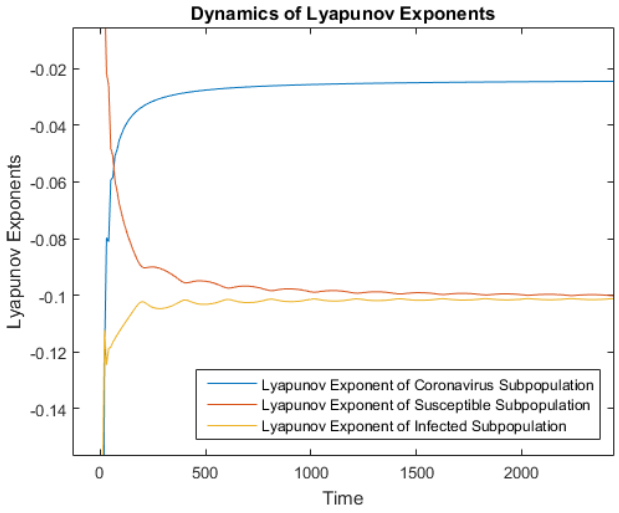

(d)

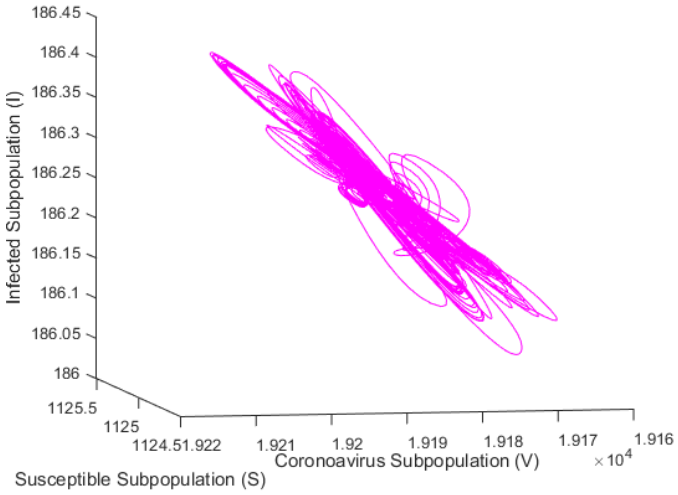

(b)

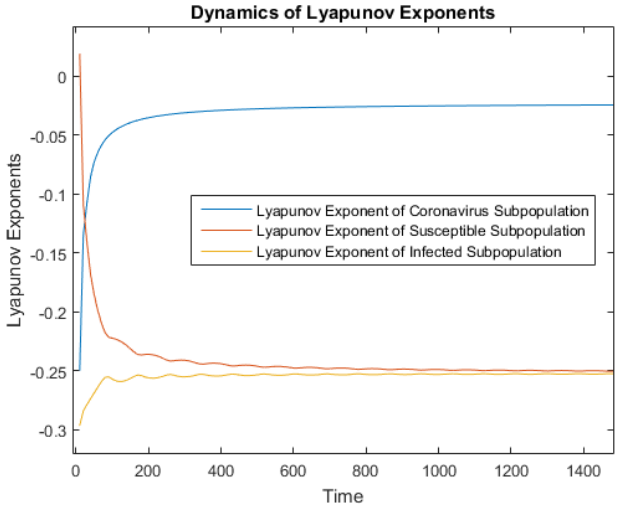

(e)

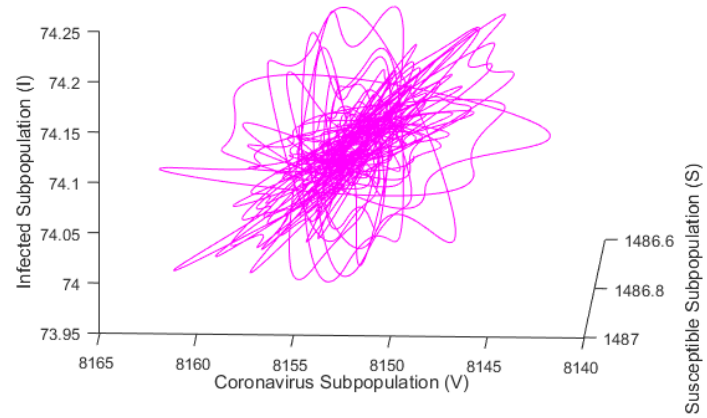

(c)

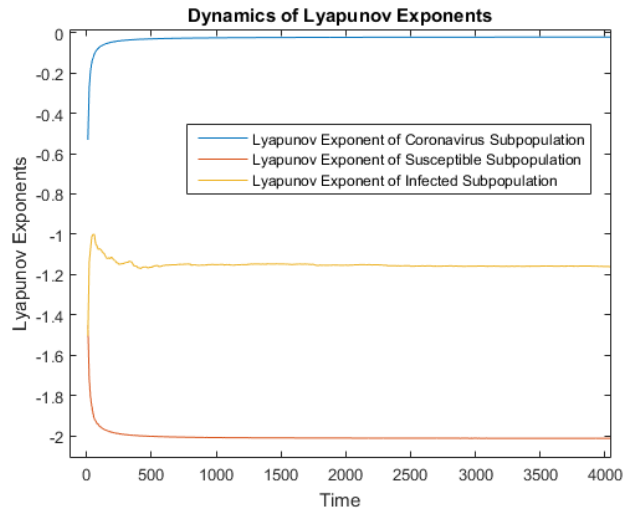

(f)

Figure 6 Strange attractors around GH1, GH2 in Figure 3 and GH1 in Figure 4 and the Lyapunov exponent of the variables which generate the strange attractors: (a) Strange attractor around GH1 in Figure 3, (b) Strange attractor around GH2 in Figure 3, (c) Strange attractor around GH1 in Figure 4, (d) Lyapunov exponent of the strange attractor around GH1 in Figure 3, (e) Lyapunov exponent of the strange attractor around GH2 in Figure 3, (f) Lyapunov exponent of the strange attractor around GH1 in Figure 4

The non-chaotic strange attractors represent a complex but predictable fluctuation of Coronavirus, susceptible, and infected subpopulations (Wiraya and Adi-Kusumo 2023) as one of the following variations occurs: i) susceptible-Coronavirus and susceptible-infected interaction rate decrease; ii) susceptible-Coronavirus interaction rate decrease and infected subpopulation recovery rate increases; iii) susceptible-Coronavirus interaction rate and Coronavirus increasing rate from infected subpopulation decrease.

Catastrophe Phenomenon

We choose a value of (d, a) around the GH point in Figure 5 and an initial value around the equilibrium found by choosing those parameters. Then, we found a catastrophe phenomenon generated by the attractor and repeller of the solution started by a smooth solution and then colliding at a region having a transformation of the solution pattern become chaotic confirmed by the Lyapunov exponent of each variable generates the attractor and repeller. The catastrophe phenomenon is presented in Figure 7 and Figure 8.

We choose $(d, a) = (-0.077392610241892, 0.682644447742242)$ around GH and an initial value $(V, S, I) = (3.943299602340211e+02, 1.020277404117016e+02, 5.026599969563091e+02)$ generated by choosing those parameters. Then, we plot the solution for forward time generating an attractor and backward time generating a repeller after a smooth solution. The attractor and repeller collide at a region constructing the chaotic part of the catastrophe phenomenon as shown in Figure 7. Chaotic part of the catastrophe phenomenon is presented in Figure 8.

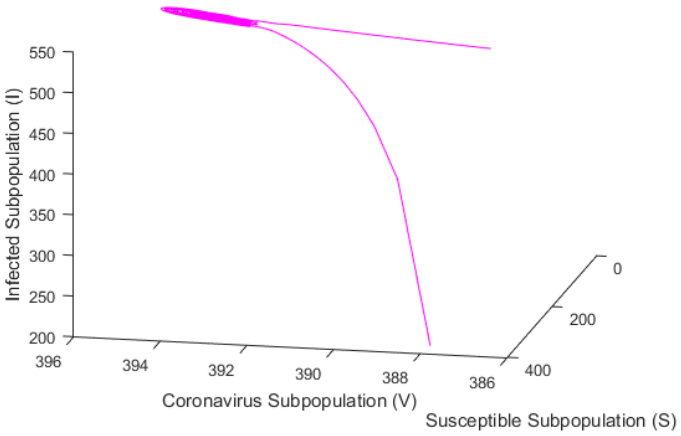

Figure 7 Catastrophe phenomenon around GH

Lyapunov exponent of each variable which generates the attractor and repeller is calculated to confirm the transition of the solution pattern from smooth to chaotic and vice versa. Calculations of the Lyapunov exponent of each variable which generates the attractor and repeller are presented in Figure 9 and Figure 10 respectively.

We investigate the catastrophe phenomenon further through the Lyapunov exponents of the variables in the attractor and repeller, especially the existence of their transition from negative to positive value which represents the transformation of the solution pattern. We found that the attractor and repeller are chaotic as the Lyapunov exponents of Coronavirus have a positive value (Wiraya and Adi-Kusumo 2023; Cencini *et al.* 2009) as time goes by, but they have a momentary negative value (dashed black circle) which

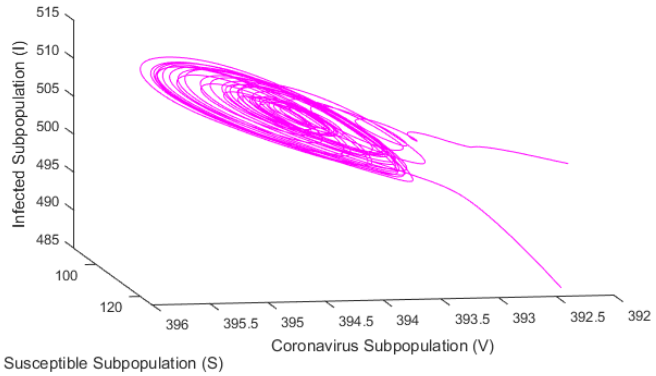

Figure 8 Chaotic part of the catastrophe phenomenon around GH

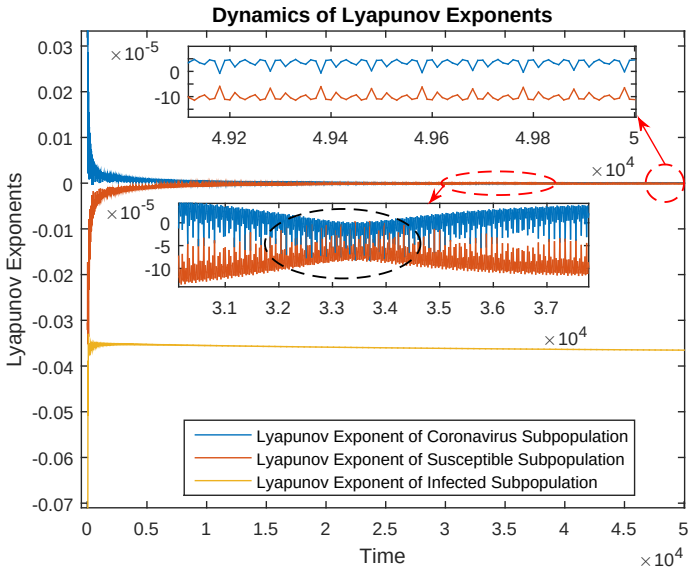

Figure 9 Lyapunov exponent of the variables in the attractor of the catastrophe phenomenon around GH

represents the smooth solution before they tend to a positive value. These phenomena illustrate the transformation of the solution pattern, i.e. smooth-chaotic-smooth solution which represents the catastrophe phenomenon.

Fluctuation of Coronavirus, susceptible, and infected subpopulations that start from a smooth, then change to a chaotic, then change back to a smooth pattern indicates the appearance of catastrophe phenomenon which represents a momentary complex and unpredictable fluctuation of them as susceptible-Coronavirus interaction rate Coronavirus increasing rate from infected subpopulation decrease.

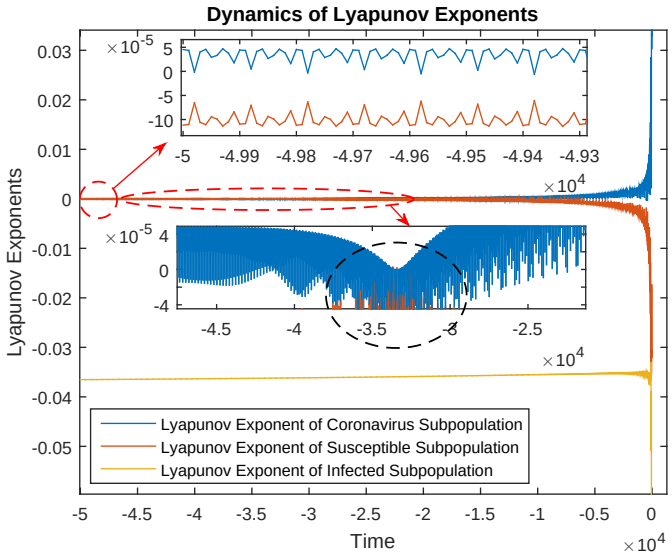

Figure 10 Lyapunov of the variables in the repeller of the catastrophe phenomenon around GH.

CONCLUSION

A three-dimensional ordinary differential equation system has been constructed as a new mathematical model of Covid-19 transmission in the population by considering two factors, i.e. non-living objects as one of the Coronavirus transmission media together with the susceptible subpopulation as one of the Coronavirus carriers. The model represents interactions between Coronavirus that exists on non-living objects, susceptible, and infected subpopulations. Analysis of the model reveals some results, such as equilibrium points along with their local stability and bifurcation analysis which consists of the finding of many interesting phenomena.

One disease-free and two infection equilibrium points are found in the model. The disease-free equilibria describes extinction of Coronavirus infection, so that the population is free from Covid-19. The infection equilibrium points describe the existence of Coronavirus infection in the population. Local stability conditions of disease-free equilibria should be fulfilled in order to make the population free from Covid-19 when initial subpopulations are around the disease-free equilibria. The population can also be free from Covid-19 for any initial condition of the subpopulations if the global stability conditions of the disease-free equilibria are fulfilled. Local stability conditions of infection equilibrium points should not be fulfilled so that Coronavirus infection in the population can be avoided when initial subpopulations are around the infection equilibrium points.

Codimension-one and codimension-two bifurcation analysis of the model gives some results that have a related biological meaning so they become some characteristics of Coronavirus transmission in the population relative to the parameter variations. Codimension-one bifurcation analysis has some results, i.e. the finding of Fold and non-neutral saddle Hopf bifurcation. Two infection equilibrium points collide at the Fold bifurcation point and then they vanish when the prevention of Coronavirus infection through non-living objects has the same rate as the infection. A cycle is found at the non-neutral saddle Hopf bifurcation point which represents a fluctuation cycle of Coronavirus, susceptible, and infected subpopulation when the eradication of Coronavirus by susceptible subpopulation is more vigorous than the infection.

Codimension-two bifurcation analysis shows that the model undergoes Generalized Hopf bifurcations. Those bifurcations trigger rich dynamics, i.e. strange attractors and catastrophe phenomena. Strange attractors which represent some complex and predictable fluctuation of Coronavirus, susceptible, and infected subpopulations are found as the susceptible-Coronavirus interaction rate decreases and one of these two variations occurs, i.e. susceptible-infected interaction rate decreases or the infected subpopulation recovery rate increases. Catastrophe phenomenon which represents a momentary complex and unpredictable fluctuation of Coronavirus, susceptible, and infected subpopulation is found as susceptible-Coronavirus interaction rate Coronavirus increasing rate from infected subpopulation decrease.

We also found some other codimension-two bifurcations, such as Bogdanov-Takens and Zero Hopf bifurcations. Bogdanov-Takens bifurcation has the potential to trigger the existence of homoclinic orbit or homoclinic bifurcations (Wiraya *et al.* 2024). Zero Hopf bifurcation can also become a trigger for strange attractor or repeller occurrence. Those two phenomena can become chaotic dynamics indicators. But recently, we still have not found those phenomena in this research. Therefore, investigation of homoclinic orbit and homoclinic bifurcations that can be triggered by the Bogdanov-Takens bifurcation, and also strange attractor or repeller that can be generated by the Zero Hopf bifurcation are our future research directions.

Acknowledgments

We would like to express our gratitude to Universitas Sebelas Maret who has funded this research through "Hibah Penelitian dan Pengabdian kepada Masyarakat (P2M) Penerimaan Negara Bukan Pajak (PNBP) Universitas Sebelas Maret 2023 (228/UN27.22/PT.01.03/2023)".

Availability of data and material

Not applicable.

Conflicts of interest

The authors declare that there is no conflict of interest regarding the publication of this paper.

Ethical standard

The authors have no relevant financial or non-financial interests to disclose.

LITERATURE CITED

Adi, Y., N. Irsalinda, A. Wiraya, S. Sugiyarto, and Z. Rafsanjani, 2023 Mathematical Modeling and Computing **10**: 311–325, DOI: 10.23939/mmc2023.02.311.

AlQadi, H. and M. Bani-Yaghoub, 2022 Incorporating global dynamics to improve the accuracy of disease models: Example of a covid-19 sir model. PloS one **17**: e0265815, DOI: 10.1371/journal.pone.0265815.

Bosi, S. and D. Desmarchelier, 2019 Local bifurcations of three and four-dimensional systems: A tractable characterization with economic applications. Mathematical Social Sciences **97**: 1–1, DOI: 10.1016/j.mathsocsci.2018.11.001.

Carraturo, F., C. Giudice, M. Morelli, V. Cerullo, G. Libralato, *et al.*, 2020 Persistence of sars-cov-2 in the environment and covid-19 transmission risk from environmental matrices and surfaces. Environmental Pollution **265**, DOI: 10.1016/j.envpol.2020.

Castillo-Garsow, C. and C. Castillo-Chavez, 2020 *A tour of the basic reproductive number and the next generation of researchers*. Springer International Publishing, Berlin/Heidelberg, Germany.

Cencini, M., F. Cecconi, and A. Vulpiani, 2009 *Chaos: from Simple Models to Complex Systems*. World Scientific, Singapore.

Dieci, L., R. Russell, and E. Van Vleck, 1997 SIAM Journal on Numerical Analysis **34**: 402–423, https://api.semanticscholar.org/CorpusID:18204582.

Din, R. and E. Algehyne, 2021 Mathematical analysis of covid-19 by using sir model with convex incidence rate. Results in Physics **23**, DOI: 10.1016/j.rinp.2021.103970.

for Disease Prevention, E. C. and Control, 2020 Using face masks in the community reducing covid-19 transmission from potentially asymptomatic or pre-symptomatic people through the use of face masks. Technical report, Stockholm.

Gandhi, M., D. Yokoe, and D. Havlir, 2020 Asymptomatic transmission, the achilles' heel of current strategies to control covid-19. The New England Journal of Medicine **382**: 2158–2160, DOI: 10.1056/NEJMe2009758.

He, F., Y. Deng, and W. Li, 2020 Coronavirus disease 2019: What we know? Journal of Medical Virology **92**: 719–725, DOI: 10.1002/jmv.25766.

Kuznetsov, Y., 1998 *Element of Applied Bifurcation Theory*. Springer-Verlag, Inc., New York.

LaSalle, J. and S. Lefschetz, 1961 *Stability by Lyapunov's Direct Method with Applications*. Academic Press, New York.

Mondal, B., A. Thirthar, N. Sk, M. Alqudah, and T. Abdeljawad, 2024 Complex dynamics in a two species system with crowley–martin response function: Role of cooperation, additional food and seasonal perturbations. Mathematics and Computers in Simulation **221**: 415–434, DOI: 10.1016/j.matcom.2024.03.015.

Obi, O. and D. Odoh, 2021 Transmission of coronavirus (sars-cov-2) by presymptomatic and asymptomatic covid-19 carriers? European Journal of Medical and Educational Technologies **14**, DOI: 10.30935/ejmets/11060.

Pakhira, R., B. Mondal, A. Thirthar, M. Alqudah, and T. Abdeljawad, 2024 Developing a fuzzy logic-based carbon emission cost-incorporated inventory model with memory effects. Ain Shams Engineering Journal p. 102746, DOI: 10.1016/j.asej.2024.102746.

Pedersen, S. and Y. Ho, 2020 Sars-cov-2: a storm is raging. The Journal of Clinical Investigation **130**: 2202–2205, DOI: 10.1172/JCI137647.

Perko, L., 2001 *Differential Equations and Dynamical Systems*. Springer-Verlag, Inc., New York, NY.

Ramesh, N., A. Siddaiah, and B. Joseph, 2020 Tackling coronavirus disease 2019 (covid 19) in workplaces. Indian Journal of Occupational and Environmental Medicine **24**: 16–18.

Sender, R., Y. Bar-On, S. Gleizer, B. Bernshtein, A. Flamholz, *et al.*, 2021 The total number and mass of sars-cov-2 virions. Proceedings of the National Academy of Sciences of the United States of America **118**, DOI: 10.1073/pnas.2024815118.

Sk, N., B. Mondal, A. Thirthar, M. Alqudah, and T. Abdeljawad, 2023 Bistability and tristability in a deterministic prey–predator model: Transitions and emergent patterns in its stochastic counterpart. Chaos, Solitons and Fractals **176**: 114073, DOI: 10.1016/j.matcom.2024.03.015.

Thirthar, A., 2023 A mathematical modelling of a plant-herbivore community with additional effects of food on the environment. Iraqi Journal of Science **64**: 3551–3566, DOI: 10.24996/ijs.2023.64.7.34.

Thirthar, A., N. Sk, B. Mondal, M. Alqudah, and T. Abdeljawad, 2023 Utilizing memory effects to enhance resilience in disease-driven prey-predator systems under the influence of global warming. Journal of Applied Mathematics and Computing **69**: 4617–4643, DOI: 10.1007/s12190-023-01936-x.

van Doremalen, N., T. Bushmaker, D. Morris, M. Holbrook, A. Gamble, *et al.*, 2020 Aerosol and surface stability of sars-cov-2 as compared with sars-cov-1. The New England Journal of Medicine **382**: 1564–1567, DOI: 10.1056/NEJMc2004973.

Verhulst, F., 1996 *Nonlinear differential equation and dynamical systems*. Springer-Verlag, Inc., New York.

Vermund, S. and V. Pitzer, 2021 Asymptomatic transmission and the infection fatality risk for covid-19: Implications for school reopening. Clinical Infectious Diseases **7**: 1493–1496, DOI: 10.1093/cid/ciaa855.

WHO, 2020 Website of the who coronavirus (covid-19) dashboard. Technical report, World Health Organization.

Wiggins, S., 2003 *Introduction To Applied Nonlinear Dynamical Systems And Chaos*. Springer-Verlag, Inc., New York.

Wiraya, A., Y. Adi, L. Fitriana, Triyanto, and S. Khoirunnisa, 2022 Global stability of latency equilibria on mathematical model for human inflammatory response to coronavirus infection. In *Internationa Conference of Mathematics and Mathematics Education (I-CMME) 2021, I-CMME 2021, Surakarta, Indonesia*, pp. 030009–1–030009–9.

Wiraya, A. and F. Adi-Kusumo, 2023 Torus and homoclinic bifurcations on a cells repair regulations model of the metastatic nasopharyngeal carcinoma. Journal of Nonlinear Science **33**: 1–21, DOI: 10.1007/s00332-023-09925-x.

Wiraya, A., L. Fitriana, Triyanto, Y. Adi, Y. Kusumadewi, *et al.*, 2024 Bifurcation analysis of the dynamics in covid-19 transmission through living and nonliving media. Journal of Applied Mathematics **2024**: 1–15, DOI: 10.1155/2024/5669308.

Yang, C. and J. Wang, 2020 A mathematical model for the novel coronavirus epidemic in wuhan, china. Mathematical Biosciences and Engineering **17**: 2708–2724, DOI: 10.3934/mbe.2020148.

Zu, Z., M. Jiang, P. Xu, W. Chen, Q. Ni, *et al.*, 2020 Coronavirus disease 2019 (covid-19): A perspective from china. Radiology **296**: E15–E25, DOI: 10.1148/radiol.2020200490.

How to cite this article: Wiraya, A., Adi, A. Y., Fitriana, L., Triyanto., Kusumadewi, Y. A., Safitri, A. N., and Nurmalitasari, A. Birth of Catastrophe and Strange Attractors through Generalized Hopf Bifurcations in Covid-19 Transmission Mathematical Model. *Chaos Theory and Applications*, 6(3), 159-169, 2024.

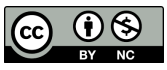

CHAOS
Theory and Applications
in Applied Sciences and Engineering

e-ISSN: 2687-4539
RESEARCH ARTICLE
Vol.6 / No.3 / 2024 / pp.170-179
https://doi.org/10.51537/chaos.1424487

Chaotic Spread-Spectrum Communication: A Comparative Study between Chaotic Synchronization and Matched Filtering

Nikolajs Tihomorskis *,1, **Andreas Ahrens** α,2 **and Arturs Aboltins** *,3

*Institute of Photonics, Electronics and Telecommunications, Faculty of Computer Science and Power Engineering, Riga Technical University, 12 Azenes Street, LV-1048, Riga, Latvia, αFaculty of Engineering, Hochschule Wismar, University of Applied Sciences, Technology, Business and Design, Philipp-Muller-Straße 14, 23966 Wismar, Germany.

ABSTRACT This publication investigates the performance of demodulation methods utilized in spread spectrum chaotic communication systems in order to understand conditions at which advanced demodulation methods, such as chaotic synchronization, provide tangible benefits over classical, matched filtering-based approaches. We conduct simulations and comparisons of three different communication systems: classic direct sequence spread spectrum (DSSS), chaotic signal fragment-based pseudo-chaotic spread spectrum (PCSS), and chaotic synchronization-based antipodal chaos shift keying (ACSK). These systems possess similar spectral and time domain characteristics, allowing us to shed light on their fundamental differences and limitations in chaos-based communication. Additionally, we assess the impact of frequency modulation (FM) on these modulation methods, as FM allows the creation of simplified non-coherent modulation schemes. Our findings, based on the analysis of bit error ratio (BER) curves, demonstrate that in the case of a non-dispersive communication channel, the utilization of chaotic synchronization does not allow to achieve performance of correlation-based receivers. Additionally, the utilization of chaotic synchronization for multiple access poses certain challenges due to malicious synchronization between users. As a supplementary finding, we show that in systems with matched filter-based demodulation, discrete-time quantized spreading sequences confer an advantage over analogous, continuous-time spreading waveforms.

KEYWORDS
Spread spectrum communication
Chaotic communication
Chaos
Multiple access interference
Correlation
Chaotic synchronization

INTRODUCTION

With the increasing deployments of internet of things (IoT) and other wireless services, the mutual interference between services is increasing, leading to the necessity to improve existing solutions and move to higher frequencies. Spread spectrum (SS) systems, which are widely employed in wireless sensor networks (WSNs), are robust against low signal-to-noise ratio (SNR) and poor signal propagation conditions. However, this comes at the cost of increased frequency bandwidth, leading to the need to share frequencies among many users.

Chaotic modulation exhibits a natural resistance to multi-path propagation due to the significantly reduced cross-correlation among segments of chaotic waveforms compared to periodic signals. Additionally, it provides a method for the physical layer security considering the unpredictability of the chaotic signals. Finally, chaotic synchronization can be used to deal with multiple synchronization tasks present in any practical communication system. This paper is devoted to comparing the main detection methods employed in chaos-based spread-spectrum systems: matched filtering and chaotic synchronization. The comparison is made using analytical derivations and modeling implemented in MATLAB Simulink. The main contribution and novelty of this research are the following: Firstly, a fair comparison between well-known and experimental chaos-based communication systems, such as

Manuscript received: 23 January 2024,
Revised: 10 March 2024,
Accepted: 5 April 2024.

[1]nikolajs.tihomorskis@rtu.lv (**Corresponding author**)
[2]andreas.ahrens@hs-wismar.de
[3]aboltins@rtu.lv

chaotic direct sequence spread spectrum (DSSS) and antipodal chaos shift keying (ACSK) is provided in terms of noise resistance and multiple access interference (MAI). The provided unique comparison allows us to understand both technologies' similarities, differences and limitations and their suitability for different single-user and multi-user communication scenarios. In this research, we also demonstrate that employing quantized chaotic waveforms in conjunction with matched filtering-based demodulation provides significant advantages over signals with continuous amplitude.

Studies of the chaotic communication system are rooted deeply in the 1990s when significant discoveries regarding the properties of chaos-based systems were made. The majority of chaos-based communication systems employ one of two mechanisms for the demodulation of the information: matched filtering (correlation) (Parlitz and Ergezinger 1994) and chaotic synchronization (Parlitz *et al.* 1996), initially proposed in works of Parlitz et al. Additionally, such systems as chaotic on-off keying (COOK) (Sangeetha and Bhaskar 2020; Mesloub *et al.* 2017; Andreyev 2023) rely on the simple envelope detection of the chaotic carrier.

The case of matched filtering does not significantly differ from non-chaotic SS systems. Namely, the transmitter uses a piece of chaotic waveform or a signal derived from a chaotic waveform to spread the data bits. Typical examples of such systems are chaos-based DSSS (Hasjuks *et al.* 2022; Cai *et al.* 2021; Yuan *et al.* 2021), which usually employ discrete-time quantized binary chaotic sequences produced by the chaotic maps. In this case, the receiver usually uses a locally stored chaotic sequence for the matched filtering. Another bright example is differential chaos shift keying (DCSK) and its derivatives (Quyen 2017; Que *et al.* 2021; Ma *et al.* 2022), where pieces of discrete-time chaotic sequences are embedded into the waveform so that the receiver can use cross-correlation between adjacent fragments of the waveform, to estimate the encoded data symbol. Another system that employs matched filtering is correlation delay shift keying (CDSK) (Zhang *et al.* 2015; Mukherjee and Ghosh 2014), where reference is delayed by a certain time and super-imposed into a chaotic payload sequence. In many cases, the chaotic sequences are modified by quantization (Litvinenko and Aboltins 2016), orthogonalization (Aboltins *et al.* 2022) and essentially lose their chaotic characteristics. In all systems mentioned above, the demodulator is implemented either as finite impulse response (FIR) filter or cross-correlation followed by strobe (Litvinenko and Aboltins 2016) or energy-based (Andreyev 2023; Aboltins *et al.* 2023) detection and all these systems possess essentially similar characteristics, such as processing gain, due to nature of correlation-based demodulator. Digital matched filtering is resource-demanding because it requires a large number of multiplications.

If the locally stored sequence is used for the matching, timing synchronization at the symbol and chip levels is necessary. Rake receiver (Patel *et al.* 2015a) employing multiple branches aids synchronization and allows to benefit from maximum-ratio combining (MRC). In publication (Berber and Gandhi 2016), it was shown that binary chaotic sequences do not improve bit error ratio (BER) compared to classical spreading sequences because BER is determined solely by bit energy and correlation properties of the sequences. In research work (Liu 2019), authors propose a direct synchronization acquisition method that relies on the chaotic nature of the spreading sequence. In DCSK, the symbol synchronization is unnecessary because reference sequences are transmitted between the payload symbols.

The second group of chaos-based communication systems relies on chaotic synchronization, a natural phenomenon observable in many physical systems (Parlitz *et al.* 1996). This type of system does not need external synchronization. In systems like chaos shift keying (CSK) and its derivatives like quadrature chaos phase-shift keying (QCPSK) (Jovic 2017; Babajans *et al.* 2021), encoding of the information is based on the alternating of the chaotic waveform in a way that does not affect chaotic features of the carrier so that at receiver, the signal is recognized by the slave chaotic oscillator and observer-based synchronization takes place. For example, in ACSK (Litvinenko *et al.* 2019), the waveform is just inverted depending on the data bit value for transmission. As practical experiments have shown (Aboltins and Tihomorskis 2023), chaotic synchronization is a very robust process and can withstand noise and interference. However, special attention must be paid to generating the chaotic signals as they are not always purely chaotic (Candido *et al.* 2015). In the more advanced system proposed in (Hassan and Hammuda 2019), the parameters of the chaotic oscillator are periodically changed to increase security. The constrained Smoothed Regularized Least Square observer method is used to demodulate the rapidly changing signal. Research (Li and Wang 2017) employs drive-response-based adaptive chaotic synchronization in the Mackey-Glass system for recovering the transmitted messages. The system uses Walsh spreading codes before chaotic modulation to improve detection robustness.

In systems that employ chaotic synchronization, continuous-time, non-quantized chaotic waveforms must be used in contrast to matched-filter-based systems where discrete chaotic sequences prevail. In some recent publications, which inspired us for the given investigation, the researchers propose to employ pieces of chaotic waveforms instead of discrete sequences for systems with matched filtering-based demodulation. For example, in (Yao *et al.* 2019), authors have implemented a prototype that demonstrated excellent characteristics of continuous-time chaotic waveforms used in matched-filtering based DCSK communication system. In (Aboltins *et al.* 2022), authors use pieces of orthogonalized chaotic waveforms from continuous-time Chua oscillator model for precoding of orthogonal frequency division multiplexing (OFDM) signal. This approach allows improvement in the diversity of OFDM link and the potential use of chaotic synchronization for symbol timing in OFDM. A similar approach with multi-level CSK is used in research (Yang *et al.* 2017).

Communication systems can employ chaotic carrier directly (Sushchik *et al.* 2000; Andreyev 2023) or use up-conversion to the sinusoidal carrier (Jovic 2017). In the case of up-conversion, one of the significant problems of wireless communication systems arises—carrier frequency synchronization. In the case of carrier frequency offset (CFO), the chaotic signal will be modulated by low-frequency harmonic waveform, leading to the loss of chaotic features and substantial change of the waveform. One of the easiest ways to fight with CFO is the use of frequency modulation (FM) on top of chaotic modulation (Cirjulina *et al.* 2022; Hasjuks *et al.* 2022; Yao *et al.* 2019; Ma *et al.* 2022). Since FM is frequently used for mitigation of CFO, in current research, we explore the impact of FM on the BER of chaos-based communication systems.

Chaotic spreading signals or sequences can provide excellent means for code-based multiple access (Sumith Babu and Kumar 2020). The amount of multiple user interference (MUI) primarily depends on cross-correlation among spreading codes at various time delays. Practical experiments of our research group with software-defined radio (SDR) (Aboltins and Tihomorskis 2023) have shown that chaotic synchronization-based have relatively

high MUI due to limited orthogonality among signals from the same chaotic generator with different parameters. Performance analysis of chaotic sequences based code division multiple access (CDMA) system with frequency-selective channel and antenna diversity is presented in (Patel *et al.* 2015b). This paper explores the impact of the synchronization mechanism and quantization on the performance of multi-user chaos-based communication systems.

SPREAD SPECTRUM MODULATION SCHEMES

Matched filtering-based chaotic spread spectrum systems

A general block scheme of implemented matched filtering-based SS system is presented in Figure 1. SS system spreads each data bit $b\,(t)$ with period T_b, which is represented by "–1" and "1", with chaos-based spreading sequence $c\,(t)$ via multiplication. The entire sequence's period equals T_b, and one spreading sequence's element is called a chip, which has period T_c. Spreading sequence inverts when it is multiplied by data bit $b\,(t)$ is "–1" and is left intact when data bit $b\,(t)$ is "1". Spread signal from the transmitter is then passed through a communication channel that adds additive white Gaussian noise (AWGN) $\eta\,(t)$ to the spread signal. Equation (1) describes received signal $r\,(t)$ at the input of the receiver in the case of ideal timing synchronization.

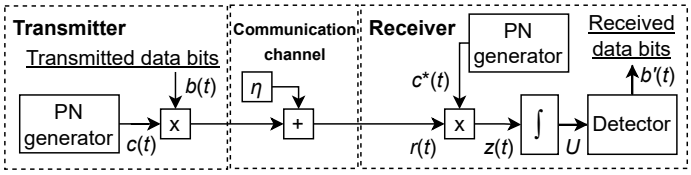

Figure 1 Block-scheme of baseband matched filtering-based chaotic spread spectrum system

$$r\,(t) = b\,(t)\,c\,(t) + \eta\,(t)\ . \tag{1}$$

By adding more users to the channel, each employing a unique spreading sequence $c_i\,(t)$ to transmit different data bits $b_i\,(t)$, the received input signal $r\,(t)$ from Equation (1) at every user's receiver is defined in Equation (2):

$$r\,(t) = \sum_{i=1}^{n} b_i\,(t)\,c_i\,(t) + \eta\,(t)\ , \tag{2}$$

where n is the total number of transmitting users in the communication channel.

In the receiver, received signal $r\,(t)$ is down-converted and then despread using correlation. This means that received signal $r\,(t)$ is multiplied with local spreading sequence $c^*\,(t)$ that is the complex conjugate of the sequence $c\,(t)$ used in the transmitter, counting in possible delay between the systems, resulting in despread signal $z\,(t)$ that is defined in Equation (3):

$$z\,(t) = r\,(t)\,c^*\,(t) = b\,(t)\,c\,(t)\,c^*\,(t) + c^*\,(t)\,\eta\,(t)\ . \tag{3}$$

Multiplying spreading sequence $c\,(t)$ by $c^*\,(t)$ will produce $|c\,(t)\,|^2$ that is always 1, which means that Equation (3) can be rewritten as Equation (4):

$$z\,(t) = b\,(t) + c^*\,(t)\,\eta\,(t)\ , \tag{4}$$

where we can see that signal containing data bits $b\,(t)$ is present separately in despread signal $z\,(t)$. In the case of multiple users, despread signal $z\,(t)$ is the combination of k user's useful data, noise $\eta\,(t)$ and additional noise from MAI, i.e. signals from other users, as defined in Equation (5):

$$z_k\,(t) = b_k\,(t) + \sum_{\substack{1\le i\le n\\ i\neq k}} b_i\,(t)\,c_i\,(t)\,c_k^*\,(t) + c_k^*\,(t)\,\eta\,(t)\ , \tag{5}$$

where k is the number of a chosen user.

By applying integration to the Equation (4) it is possible to recover data bit $b\,(t)$ as shown in Equation (6):

$$U = \int_0^{T_b} b\,(t) + c^*\,(t)\,\eta\,(t)\,\mathrm{d}t\,. \tag{6}$$

The threshold detector converts signal U into received data bits $b'\,(t)$, which compares U signal's values to "0". Since an ideal timing synchronization is assumed, adjusting the detection point in time is unnecessary.

Classical 2-level DSSS communication system can be implemented as binary phase shift keying (BPSK). BPSK system's BER probability can be expressed via Q-function as Equation (7):

$$P_b = \mathrm{Q}\left(\sqrt{2\frac{E_b}{N_0}}\right)\ , \tag{7}$$

where P_b is probability of an error or theoretical BER, E_b is energy per bit and N_0 is noise power spectral density. Q is a complementary cumulative distribution function (CCDF) of normal distribution defined as Equation (8):

$$\mathrm{Q}\,(x) = \frac{1}{\sqrt{2\pi}}\int_x^{\infty} \mathrm{e}^{-\frac{x^2}{2}}\,\mathrm{d}x\,. \tag{8}$$

Chaotic synchronization-based spread spectrum system

Block-scheme of implemented ACSK system (Litvinenko *et al.* 2019), which employs chaotic synchronization for the demodulation, is presented in Figure 2.

ACSK system consists of three chaos generators based on a fourth-order modified Chua's oscillator. One master chaos generator is in the transmitter, whereas two slave chaos generators are in the receiver. Fourth-order modified Chua's oscillator is described by four continuous-time differential equations in Equation (9):

$$\begin{cases} \dfrac{\mathrm{d}p_1}{\mathrm{d}t} = -\mathrm{g}\,(p_1, p_3)\,(p_1 - p_3) - p_2 \\ \dfrac{\mathrm{d}p_2}{\mathrm{d}t} = p_1 + \gamma p_2 \\ \dfrac{\mathrm{d}p_3}{\mathrm{d}t} = \theta\,(\mathrm{g}\,(p_1, p_3)\,(p_1 - p_3) - p_4) \\ \dfrac{\mathrm{d}p_4}{\mathrm{d}t} = \sigma p_3 \end{cases}\ , \tag{9}$$

where p_1, p_2, p_3, p_4 are system's state variables given in Table 1, $\mathrm{g}\,(p_1, p_3)$ is a piecewise linear function and γ, θ, σ are system coefficients that are given in Table 2.

The difference between generators in the transmitter and receiver is in the absence of piece-wise linear function $\mathrm{g}(p_1, p_3)$ in the receiver's generators that are defined in Equation (10):

$$\mathrm{g}\,(p_1, p_3) = \begin{cases} c\,(p_1 - p_3 - d) & (p_1 - p_3) > d \\ 0 & (p_1 - p_3) \le d \end{cases}\ , \tag{10}$$

where c, d are system coefficients that are given in Table 2.

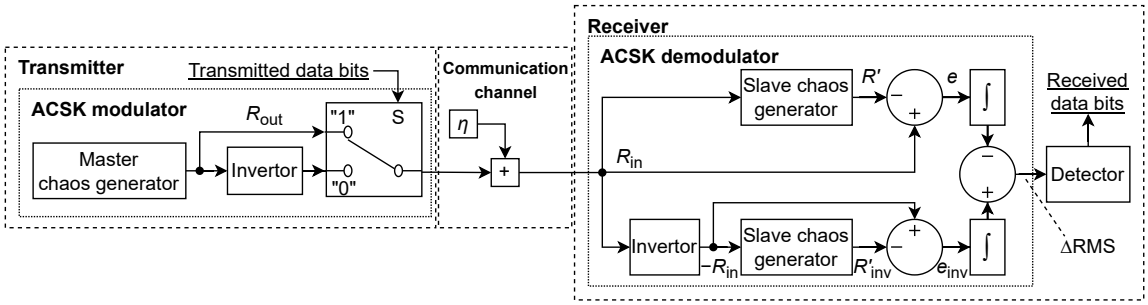

Figure 2 Block-scheme of baseband ACSK system

Table 1 Two ACSK master-slave generator pairs state variables' initial values

	Master chaos generator (transmitter)				Slave chaos generators (receiver)			
User	p_1	p_2	p_3	p_4	p'_1	p'_2	p'_3	p'_4
1	0.05	0.06	0.07	0.08	0.5	0.6	0.7	0.8
2	0.2386	–2.3058	–0.5283	1.3338	0.2386	–2.3058	–0.5283	1.3338

Table 2 Two ACSK master-slave generator pairs' coefficients of differential equations

	System coefficients					Weight coefficients			
User	γ	θ	σ	c	d	k_1	k_2	k_3	k_4
1	0.5	10	1.5	3	1	–2.6302	–0.6054	0.587	0.7763
2	0.25	7	1.4	3	1	–2.0302	–0.2054	1.587	0.0763

In an antipodal modulator, chaotic signal R_{out} is generated by passing the direct or inverted chaotic signal through the switch, depending on the data bit value. The chaotic signal is inverted when the "0" data bit is spread. The generated chaotic signal at the output of ACSK modulator is expressed in Equation (11):

$$R_{\text{out}} = \sum_{i=1}^{4} p_i k_i + \mathrm{g}\left(p_1, p_3\right) , \tag{11}$$

where p_i are system's state variables and k_i are weight coefficients from Table 2 that define output signal's R_{out} waveform variation.

In the receiver's ACSK demodulator, two chaotic slave generators are used to synchronize with input signal R_{in}, one for direct and one for inverted chaotic signal. Chaotic synchronization is a complex phenomenon caused by the trend of the chaotic oscillator settling on a stable orbit if one of the state variables is forced from the outside (Parlitz *et al.* 1996). Therefore, sufficient conditions for the synchronization are as follows:

- Drive and response systems are similar in terms of stable orbits. Effectively, drive and response systems must have the same design and similar parameters (Cirjulina *et al.* 2019).
- Signal from the drive to the response system is not distorted too much (Anstrangs *et al.* 2019) still leads to the same stable orbit.

.

Using signal R_{in} as an input for both generators, it is possible to restore piece-wise linear function $\mathrm{g}'(p_1, p_3)$ with additional use of local state variables as shown in Equation (12):

$$\mathrm{g}'\left(p_1, p_3\right) = R_{\text{in}} - \sum_{i=1}^{4} p'_i k_i \,, \tag{12}$$

where p'_i are slave chaos generators' state variables initialized by values from Table 1. The output signal R' in Equation (13) is generated similarly to master chaos generator's signal R_{out} from Equation (11).

$$R' = \sum_{i=1}^{4} p'_i k_i + \left|\mathrm{g}'\left(p_1, p_3\right)\right| , \tag{13}$$

where $|\mathrm{g}'\left(p_1, p_3\right)|$ is restored piece-wise linear function in absolute form to negate the recovery of incorrect negative values. The calculation of synchronization errors e and e_{inv} from both slave chaos generators' output signals R' and R'_{inv} is shown in Equation (14):

$$\begin{aligned} e &= R_{\text{in}} - R' \\ e_{\text{inv}} &= -R_{\text{in}} - R'_{\text{inv}} \end{aligned} , \tag{14}$$

where R' chaos generators' output signals, e are chaos generators' synchronization errors and index $_{\text{inv}}$ denotes signals associated

with inverted slave chaos generator. After synchronization errors are obtained, integration is applied for each error, and the difference is calculated in Equation (15):

$$\Delta\mathrm{RMS}(e) = \sqrt{\frac{1}{T_b}\int_{t_n}^{t_n+T_b}[e_{\mathrm{inv}}(t)]^2\,\mathrm{d}t} - \sqrt{\frac{1}{T_b}\int_{t_n}^{t_n+T_b}[e(t)]^2\,\mathrm{d}t}\ , \tag{15}$$

where T_b is the data bit period in seconds, and t_n is the time at the moment of calculation in seconds.

This difference ΔRMS is used as an input of an energy detector (Aboltins and Tihomorskis 2023) that detects data bits by calculating the mean value of the whole symbol interval.

SIMULATION ENVIRONMENT

In this paper, all simulations of the tested communication systems were conducted in MATLAB Simulink environment. The following subsections provide simulated SS systems' descriptions, parameters and visual representation of signals in time and frequency domains.

Spread spectrum systems

To be able to compare two different approaches of received signal synchronization in ideal circumstances, two distinct SS systems are implemented: correlation-based DSSS and chaotic synchronization-based ACSK systems. Implemented ACSK system's chaotic signal, which varies in time, spreads data bits according to the description from the previous section.

In previously conducted research (Hasjuks *et al.* 2022), it was concluded that a predefined signal provides similar performance as a pseudo-noise (PN) generated signal, so in DSSS system PN generator, that was shown in Figure 1, was swapped for the generated signal of a constant number of samples. In total, three different but mutually related spreading signals were generated.

The first signal is a fragment of a master chaos generator recorded output signal R_{out} from an ACSK modulator's part before the switch and inverter blocks that were shown in Figure 2. DSSS system employing this signal is named pseudo-chaotic spread spectrum (PCSS), as this signal becomes a discrete periodic signal, repeating a predefined sequence, that is not dependant on any parameters that are used in the generation of the signal in the transmitter.

The second, analogous direct sequence spread spectrum (A-DSSS) system's signal is a continuous-amplitude, discrete-time signal obtained using the Poincare section of the phase portrait created from PCSS signal and its derivative. The resulting signal is up-sampled to the PCSS signal's sample rate.

In the third case, 2-DSSS waveform is obtained by passing A-DSSS signal through a threshold, defined in Equation (16), that selects between two values—"1" and "–1".

$$y_n = \begin{cases} 1 & x_n > \Theta \\ -1 & x_n \leq \Theta \end{cases}, \tag{16}$$

where n is a signal sample's sequence number, y is a 2-DSSS signal, x is an A-DSSS signal before up-sampling and $\Theta = 0$ is a threshold. After the quantization, the binary 2-DSSS signal is up-sampled to the PCSS and A-DSSS signals' sample rate.

These PCSS, A-DSSS and 2-DSSS signals are used as spreading sequences in a single DSSS system that was modeled in Simulink according to the description from the previous section. None of the parameters of DSSS system are altered after changing between generated SS signals.

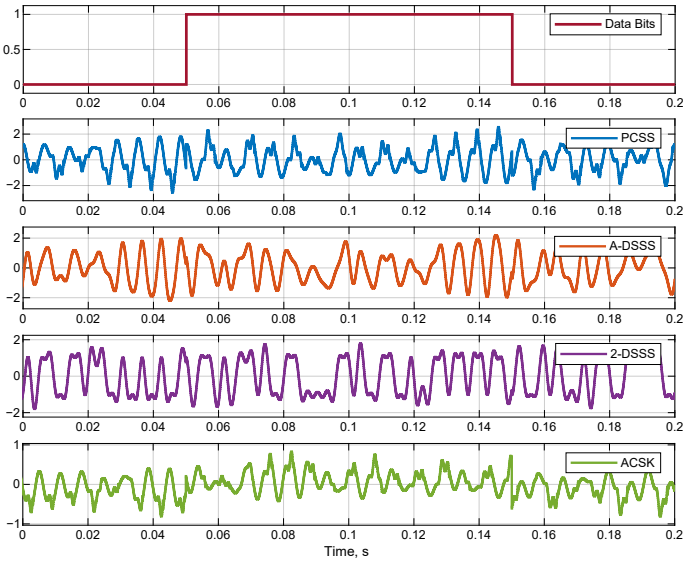

Figure 3 Baseband signals of chaotic spread spectrum modulations. All spread-spectrum signals have the same bit energy

SS systems' simulation parameters are compiled in Table 3. Spread data bits using implemented SS systems are presented in Figure 3.

Table 3 Spread spectrum systems' simulation parameters

Parameter	Value
Data bit frequency $1/T_b$, Hz	10
Chip frequency $1/T_c$, kHz	17.05
Spreading sequence's samples per data bit	1705
AWGN channel sample rate, kHz	68.2
Receiver's LPF cut-off frequency, kHz	10

In DSSS system, spreading sequences of defined lengths and values are used. Thus, it is possible to calculate auto and cross-correlations of given sequences. Auto and cross-correlations are presented in Figure 4 and Figure 5, respectively, showing used spreading sequences' correlations. ACSK system's spreading signal is non-repeating, meaning that the signal's auto-correlation and cross-correlation functions are non-constant. Despite this, only at one exact time instant correlation is equal to the PCSS signal's correlation when the spreading sequence was recorded.

As seen from these correlation function figures Fig. 4 and Fig. 5, all signals are related, having similar oscillation patterns at time shifts with varying similarity. It is worth noticing that the correlation function of 2-DSSS decreases more rapidly compared to other systems.

Figure 6 shows the power spectra of the transmitted signals of all compared systems. These systems have similar bandwidth and occupied areas; thus, they can be compared.

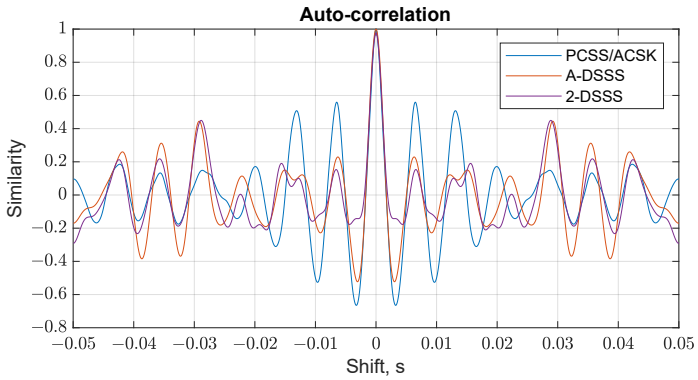

Figure 4 Auto-correlation function of selected chaotic spreading sequences

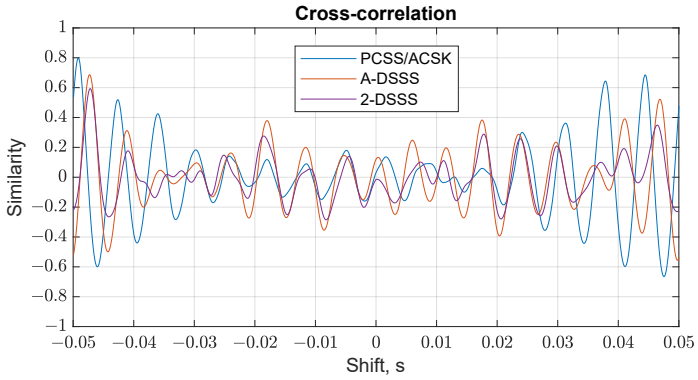

Figure 5 Cross-correlation between two selected chaotic spreading sequences of the same kind corresponding to different users

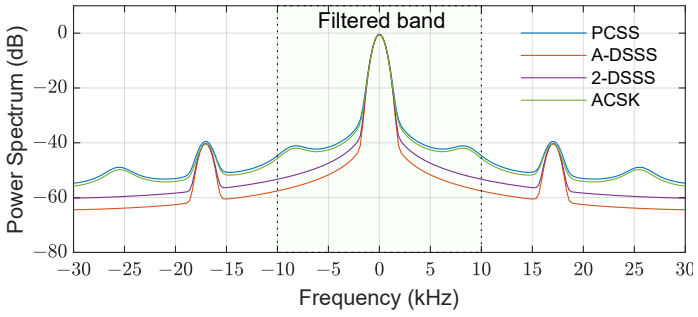

Figure 6 Power spectra of chaotic spread spectrum systems

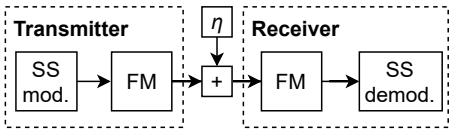

Figure 7 Block-scheme of frequency modulated spread spectrum systems

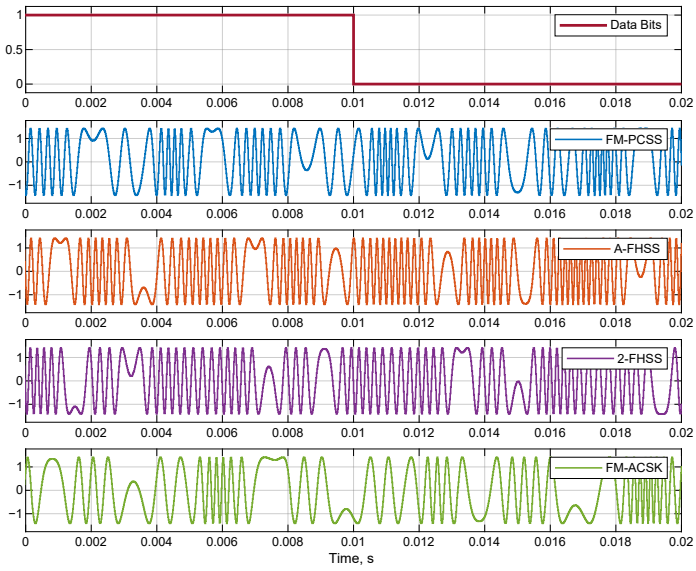

Figure 8 Baseband signals of frequency-modulated chaotic spread spectrum modulations

Before demodulation, DSSS and ACSK receivers filter incoming signal that was carried through AWGN channel. It is done by using low-pass filter (LPF) that has a cut-off frequency equal to 10 kHz, as marked by the green area labeled "Filtered band" in Figure 6.

Frequency modulated spread spectrum systems

One of the drawbacks of previously explored direct SS systems is the variable bit energy of the baseband signal. Bit energy can be unified by adding FM after SS modulation in the transmitter, as seen in Figure 7. Moreover, employment of FM significantly eases the practical implementation of the communication system as non-coherent FM does not require precise carrier frequency synchronization as in the case of coherent modulation formats, such as phase shift keying (PSK).

By adding FM to DSSS system, frequency hopping spread spectrum (FHSS) system is created. In FHSS systems, carrier frequency changes between multiple predefined frequencies in some defined order. In this paper, signals employed in FHSS system will be called frequency modulated pseudo-chaotic spread spectrum (FM-PCSS), analogous frequency hopping spread spectrum (A-FHSS) and 2-FHSS, which are FM versions of PCSS, A-DSSS and 2-DSSS signals. ACSK system's FM version is called frequency modulated antipodal chaos shift keying (FM-ACSK).

Simulated FM-SS systems' spread signals are depicted in Figure 8. FM-SS systems have equal bandwidth of $\approx$ 10 kHz and occupy similar area as seen in Figure 9. Comparing spread signals of FM-SS from Figure 8 with direct SS from Figure 3, it can be noted that FM increased the frequency bandwidth of the modulated signals. This is also confirmed by power spectra of FM-SS systems (see Figure 9) are $\approx$ 4 times wider than those of SS systems (see Figure 6), nearly occupying full LPF frequency band until 10 kHz cut-off frequency of receiver's LPF. To achieve equal bandwidth for both FHSS and FM-ACSK systems, different FM deviation values shown in Table 4 were used for each modulation format. In 2-FHSS system, two well-defined peaks at $\approx$ 3.6 kHz are seen, which means that primarily two frequencies are used in spreading, which is also marked in the name of the signal—2-FHSS.

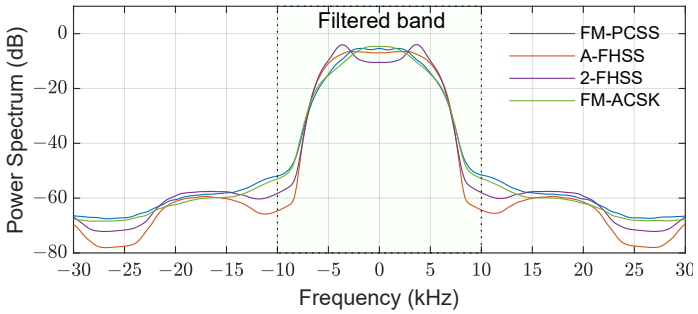

Figure 9 Power spectra of FM-SS systems

Table 4 FM-SS systems' FM deviations

System	FM deviation
FM-PCSS	0.95
A-FHSS	1.05
2-FHSS	3.5
FM-ACSK	7.8

SIMULATION RESULTS

In this research, three distinct experiments for both SS and FM-SS systems were conducted—data transmission in the single-user scenario, two-user scenario and two-user scenario with receiving user's constant transmitter power and variable transmitter power for interfering user.

Performance comparison of direct spread-spectrum systems

Results for SS systems in the single-user scenario are presented in Figure 10 and for a two-user scenario in Figure 11. In a two-user scenario, mean BER is provided at the Y-axis, calculated by dividing the sum of both users' BER by 2.

As it can be seen, DSSS system, using any of the previously generated spreading sequences, outperforms ACSK system in both cases. Looking at DSSS system's signals, 2-DSSS outperforms both PCSS and A-DSSS, but PCSS comes in second place, insignificantly surpassing A-DSSS.

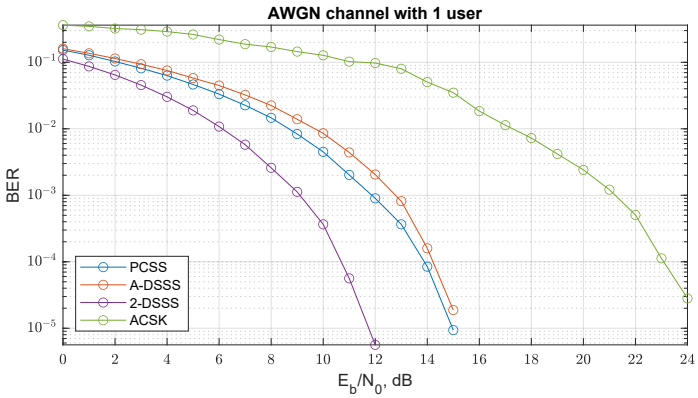

Figure 10 BER versus E_b/N_0 for chaotic spread spectrum systems in single-user scenario

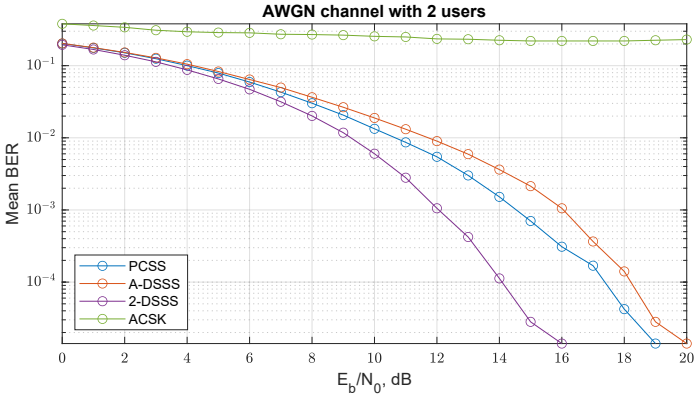

Figure 11 BER versus E_b/N_0 for chaotic spread spectrum systems in two-user scenario

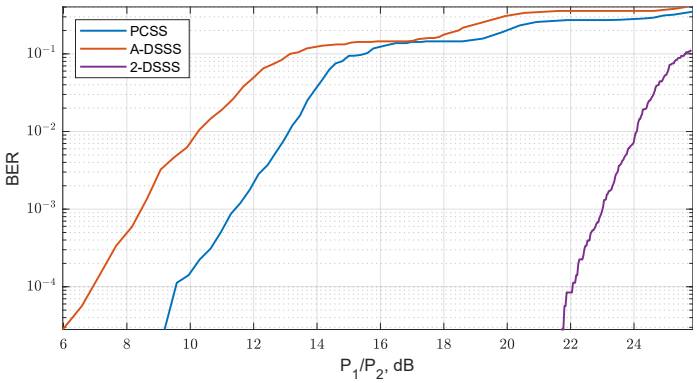

Figure 12 Receiving user's BER versus P_1/P_2 at $E_b/N_0 = 20$ dB

In the two-user scenario, mean BER results show that communication using two ACSK transmitter/receiver pairs at exactly equal center frequency leads to both users being unable to receive their transmitted data. This means that both ACSK receivers are synchronizing with each user's transmitted signal despite having different initial state conditions and coefficients. In DSSS system, all used signals lead to similar results but lower system performance at equal E_b/N_0 values compared to the single-user scenario.

MUI simulations were carried out, where one of the user's transmitter power P_1 was varied, whereas the receiving user's transmitter power P_2 was constant in all simulations. This power ratio P_1/P_2 is displayed in dB, and the results of these simulations are depicted in Figure 12. The communication channel between the users is noise-free.

These results mirror previously presented results from Figure 11, showing that better performing spreading signal in DSSS also has a better resistance to MAI.

At higher E_b/N_0 or without any noise present in the communication channel, when lowering the interfering transmitter's power, drop from BER $> 10^{-1}$ to immeasurable BER, at a given number of transmitted data bits, will be instant. To show a gradual decrease in BER, AWGN with $E_b/N_0 = 20$ dB was used.

Performance comparison of FM spread-spectrum systems

Results depicted in Figure 13 show that in a single-user scenario, similarly to the direct SS systems, 2-FHSS significantly outperforms other systems. Moreover, the FHSS system employing FM-PCSS signal has slightly worse performance than one using A-FHSS signal. Despite this, with any of the used spreading signals, FHSS

systems manage to outperform FM-ACSK system, but with a more negligible difference of E_b/N_0 between the worst performing FHSS and FM-ACSK, comparing to results of SS systems from Figure 10.

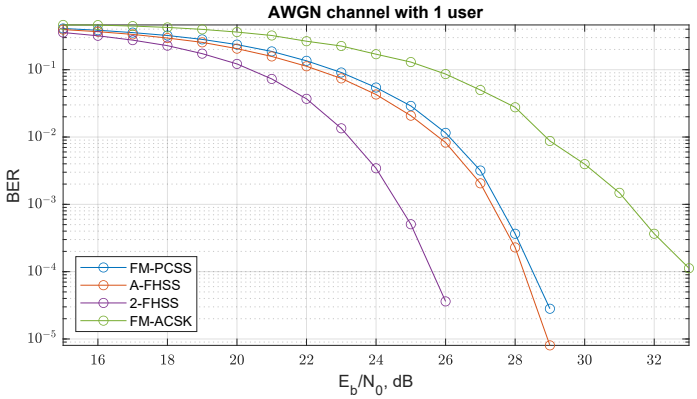

Figure 13 BER versus E_b/N_0 for FM-SS systems in single-user scenario

In the case of two-user, FHSS system with 2-FHSS spreading signal has a gradual decrease in mean BER, as seen in Figure 14. Both FM-PCSS and A-FHSS signals in FHSS system hit a threshold at BER $\approx 10^{-6}$ and BER $\approx 10^{-5}$ respectively. These signals have an equal mean BER at $E_b/N_0 \leq 27$, but at $E_b/N_0 > 27$ employment of FM-PCSS in FHSS system shows an improvement in system's performance over the use of A-FHSS signal. Similarly to the results of ACSK system in the two-user scenario from Figure 11, FM-ACSK system's users can not communicate on the same carrier frequency.

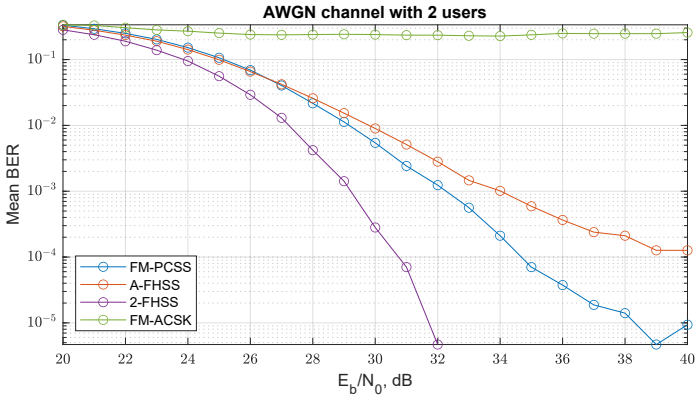

Figure 14 BER versus E_b/N_0 for FM-SS systems in two-user scenario

In Figure 15 BER versus power ratio P_1/P_2 is shown where P_1 is interfering with the transmitter's power and P_2 is receiving the user's transmitter's power. As in Figure 12, this graph mirrors results previously depicted in Figure 14. Receiving user's BER increases when the interfering transmitter's power increases.

CONCLUSION

This research aimed to compare matched filtering and chaotic synchronization SS systems. For this purpose, four SS systems were implemented—DSSS, ACSK and their FM variants—FHSS and FM-ACSK. Simulations have shown that DSSS and FHSS systems both outperform ACSK and FM-ACSK systems. In all cases, DSSS and FHSS systems employing binary spreading signal generated

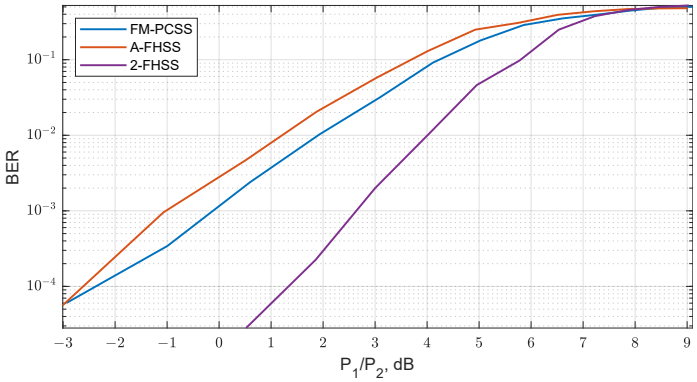

Figure 15 Receiving user's BER versus P_1/P_2 at $E_b/N_0 = 30$ dB

by applying a threshold to the quantized version of the recorded sample of the chaotic signal have improved performance over these systems with multi-level spreading signal. In most cases, the continuous-time spreading signal recorded at ACSK master chaos generator's output provided slightly better performance than its sampled version.

As it turns out, the implemented Chua oscillator-based ACSK system can not be used in multi-user scenarios because of malicious synchronization between different users, even with unique parameters of the chaotic oscillator. To solve this problem, chaos generators based on other circuits can be examined. Another solution, as well as potential future research, can be the application of advanced algorithms, including machine learning, to find implemented fourth-order modified Chua's oscillator ACSK chaotic generators' parameter combinations that could prove this ACSK system's usability in a multi-user environment.

In the real application of matched filtering-based systems, the local spreading sequence must be synchronized with the received signal's spreading sequence at a given delayed time, which can be done by the FIR matched filter. ACSK system based on chaotic synchronization, on the other hand, ensures the synchronization of the transmitter's and receiver's chaos generators, which facilitates the development and integration of the chaotic synchronization in the communication systems. Exciting look experiments with ultra-wideband (UWB) pulse synchronization (Chong and Yong 2008; Mesloub *et al.* 2017; Andreyev 2023), or employment of strongly-quantized signals for the chaotic synchronization.

Author contributions

Arturs Aboltins designed and supervised the project; Arturs Aboltins developed the concept and designed the methodology; Andreas Ahrens developed the concept; Nikolajs Tihomorskis made the simulations, performed the experiments, visualized results and curated data; Arturs Aboltins validated results; Both Nikolajs Tihomorskis and Arturs Aboltins contributed to the final version of the manuscript.

Acknowledgments

This work has been supported by the Riga Technical University 2022/2023 project for strengthening scientific personnel capacity Nr. ZM-2023/28, "Implementation of chaos-based data transmission systems in software-defined radio".

Availability of data and material

The data collected in this study are available from the corresponding author upon reasonable request.

Conflicts of interest

The authors declare that there is no conflict of interest regarding the publication of this paper.

Ethical standard

The authors have no relevant financial or non-financial interests to disclose.

LITERATURE CITED

Aboltins, A., F. Capligins, N. Hasjuks, and A. Ahrens, 2023 Implementation of chaotic frequency modulation based spread spectrum communication system in software-defined radio. In *IEEE Wireless Communications and Networking Conference, WCNC*, volume 2023-March, pp. 1–6, IEEE.

Aboltins, A., A. Litvinenko, M. Terauds, and A. Ahrens, 2022 Use of Chaotic Oscillations for Precoding and Synchronization in OFDM. Advances in Electrical and Electronic Engineering **20**: 260 – 271.

Aboltins, A. and N. Tihomorskis, 2023 Software-Defined Radio Implementation and Performance Evaluation of Frequency-Modulated Antipodal Chaos Shift Keying Communication System †. Electronics (Switzerland) **12**: 1240.

Andreyev, Y., 2023 Analytical Model of an Energy Detector for Ultra-Wideband Chaotic Communications. Electronics (Switzerland) **12**: 954.

Anstrangs, D. D., D. Cirjulina, R. Babajans, A. Litvinenko, and D. Pikulins, 2019 Noise Immunity of Chaotic Synchronization in Master-Slave System. In *Advances in Information, Electronic and Electrical Engineering, AIEEE 2019 - Proceedings of the 7th IEEE Workshop*, volume 2019-Novem, pp. 1–5, IEEE.

Babajans, R., D. Cirjulina, J. Grizans, A. Aboltins, D. Pikulins, *et al.*, 2021 Impact of the Chaotic Synchronization's Stability on the Performance of QCPSK Communication System. Electronics **10**: 640.

Berber, S. M. and A. K. Gandhi, 2016 Inherent diversity combining techniques to mitigate frequency selective fading in chaos-based DSSS systems. Physical Communication **19**: 30–37.

Cai, X., W. Xu, S. Hong, and L. Wang, 2021 A Trinal-Code Shifted Differential Chaos Shift Keying System. IEEE Communications Letters **25**: 1000–1004.

Candido, R., D. C. Soriano, M. T. Silva, and M. Eisencraft, 2015 Do chaos-based communication systems really transmit chaotic signals? Signal Processing **108**: 412–420.

Chong, C. C. and S. K. Yong, 2008 UWB direct chaotic communication technology for low-rate WPAN applications. IEEE Transactions on Vehicular Technology **57**: 1527–1536.

Cirjulina, D., D. D. Anstrangs, R. Babajans, A. Litvinenko, and S. Tjukovs, 2019 Influence of element nominal values on chaos oscillator dynamics and synchronization. In *Advances in Information, Electronic and Electrical Engineering, AIEEE 2019 - Proceedings of the 7th IEEE Workshop*, volume 2019-Novem, pp. 1–5, IEEE.

Cirjulina, D., D. Pikulins, R. Babajans, M. Zeltins, D. Kolosovs, *et al.*, 2022 Experimental Study on FM-CSK Communication System for WSN. Electronics (Switzerland) **11**: 1517.

Hasjuks, N., H. Hellbruck, and A. Aboltins, 2022 Performance study of chaos-based DSSS and FHSS multi-user communication systems. In *Proceedings of 2022 Workshop on Microwave Theory and Techniques in Wireless Communications, MTTW 2022*, pp. 23–28, IEEE.

Hassan, M. F. and M. Hammuda, 2019 A new approach for constrained chaos synchronization with application to secure data communication. Journal of the Franklin Institute **356**: 6697–6723.

Jovic, B., 2017 Class of novel broadband chaos-based coherent communication systems. IET Communications **11**: 1970–1984.

Li, A. and C. Wang, 2017 Efficient Data Transmission Based on a Scalar Chaotic Drive-Response System. Mathematical Problems in Engineering **2017**: 1–9.

Litvinenko, A. and A. Aboltins, 2016 Use of cross-correlation minimization for performance enhancement of chaotic spreading sequence based asynchronous DS-CDMA system. In *2016 IEEE 4th Workshop on Advances in Information, Electronic and Electrical Engineering (AIEEE)*, pp. 1–6, IEEE.

Litvinenko, A., A. Aboltins, D. Pikulins, A. Ahrens, F. Capligins, *et al.*, 2019 Advanced Chaos Shift Keying Based on a Modified Chua's Circuit. In *2019 IEEE Microwave Theory and Techniques in Wireless Communications (MTTW)*, pp. 17–22, IEEE.

Liu, F., 2019 Unconventional direct acquisition method for chaotic DSSS signals. AEU - International Journal of Electronics and Communications **99**: 293–298.

Ma, H., Y. Fang, P. Chen, and Y. Li, 2022 Reconfigurable Intelligent Surface-aided *M*-ary FM-DCSK System: a New Design for Non-coherent Chaos-based Communication. IEEE Transactions on Vehicular Technology pp. 1–15.

Mesloub, A., A. Boukhelifa, O. Merad, S. Saddoudi, A. Younsi, *et al.*, 2017 Chip Averaging Chaotic ON-OFF Keying: A New Non-Coherent Modulation for Ultra Wide Band Direct Chaotic Communication. IEEE Communications Letters **21**: 2166–2169.

Mukherjee, S. and D. Ghosh, 2014 Design and performance analysis of a novel FM-chaos based modulation technique. In *IEEE Wireless Communications and Networking Conference, WCNC*, pp. 594–599, IEEE.

Parlitz, U. and S. Ergezinger, 1994 Robust communication based on chaotic spreading sequences. Physics Letters A **188**: 146–150.

Parlitz, U., L. Kocarev, T. Stojanovski, and H. Preckel, 1996 Encoding messages using chaotic synchronization. Physical review. E, Statistical physics, plasmas, fluids, and related interdisciplinary topics **53**: 4351–4361.

Patel, M. K., S. M. Berber, and K. W. Sowerby, 2015a Adaptive RAKE receiver in chaos based pilot-added DS-CDMA system. Physical Communication **16**: 37–42.

Patel, M. K., S. M. Berber, and K. W. Sowerby, 2015b Performance Analysis of Adaptive Chaos Based CDMA System with Antenna Diversity in Frequency Selective Channel. Wireless Personal Communications **84**: 1439–1448.

Que, D. T., N. X. Quyen, and T. M. Hoang, 2021 Performance of Improved-DCSK system over land mobile satellite channel under effect of time-reversed chaotic sequences. Physical Communication **47**: 101342.

Quyen, N. X., 2017 On the Study of a Quadrature DCSK Modulation Scheme for Cognitive Radio. International Journal of Bifurcation and Chaos **27**: 1750135.

Sangeetha, M. and V. Bhaskar, 2020 Improved Non-coherent Communication Systems Using Noise Reduction Chaotic ON–OFF Keying (NR-COOK) Techniques. Wireless Personal Communications **113**: 1297–1314.

Sumith Babu, S. B. and R. Kumar, 2020 A High Capacity 1D-Chaotic-Collaborative-CDMA Scheme for Shared Band 5G-IoT Operation. Wireless Personal Communications **115**: 307–314.

Sushchik, M., N. Rulkov, L. Larson, L. Tsimring, H. Abarbanel, *et al.*, 2000 Chaotic Pulse Position Modulation: A Robust Method of Communicating with Chaos. IEEE Communications Letters **4**: 128–130.

Yang, H., W. K. S. Tang, G. Chen, and G.-P. Jiang, 2017 Multi-Carrier Chaos Shift Keying: System Design and Performance Analysis.

IEEE Transactions on Circuits and Systems I: Regular Papers pp. 1–13.

Yao, J. L., Y. Z. Sun, H. P. Ren, and C. Grebogi, 2019 Experimental wireless communication using chaotic baseband waveform. IEEE Transactions on Vehicular Technology **68**: 578–591.

Yuan, G., Z. Chen, X. Gao, and Y. Zhang, 2021 Enhancing the Security of Chaotic Direct Sequence Spread Spectrum Communication through WFRFT. IEEE Communications Letters **25**: 2834–2838.

Zhang, G., N. Cui, and T. Zhang, 2015 System Based on Walsh Code. Journal of Electrical and Computer Engineering **2015**.

How to cite this article: Tihomorskis, N., Ahrens, A. and Aboltins, A. Chaotic Spread-Spectrum Communication: A Comparative Study between Chaotic Synchronization and Matched Filtering. *Chaos Theory and Applications*, 6(3), 170-179, 2024.

CHAOS
Theory and Applications
in Applied Sciences and Engineering

e-ISSN: 2687-4539
RESEARCH ARTICLE
Vol.6 / No.3 / 2024 / pp.180-191
https://doi.org/10.51537/chaos.1414782

Application of the New Mapping Method to Complex Three Coupled Maccari's System Possessing M-Fractional Derivative

Muhammad Bilal Riaz *,α,1, **Aziz Ur Rehman** β,2 **and Jan Martinovic** *,3

*VSB – Technical University of Ostrava, Ostrava, Czech Republic, αDepartment of Computer Science and Mathematics, Lebanese American University, Byblos, Lebanon, βDepartment of Mathematics, University of Management and Technology, Lahore, Pakistan.

ABSTRACT In this academic investigation, an innovative mapping approach is applied to complex three coupled Maccari's system to unveil novel soliton solutions. This is achieved through the utilization of M-Truncated fractional derivative with employing the new mapping method and computer algebraic syatem (CAS) such as Maple. The derived solutions in the form of hyperbolic and trigonometric functions. Our study elucidates a variety of soliton solutions such as periodic, singular, dark, kink, bright, dark-bright solitons solutions. To facilitate comprehension, with certain solutions being visually depicted through 2-dimensional, contour, 3-dimensional, and phase plots depicting bifurcation characteristics utilizing Maple software. Furthermore, the incorporation of M-Truncated derivative enables a more extensive exploration of solution patterns. Our study establishes a connection between computer science and soliton physics, emphasizing the pivotal role of soliton phenomena in advancing simulations and computational modelling. Analytical solutions are subsequently generated through the application of the new mapping method. Following this, a thorough examination of the dynamic nature of the equation is conducted from various perspectives. In essence, understanding the dynamic characteristics of systems is of great importance for predicting outcomes and advancing new technologies. This research significantly contributes to the convergence of theoretical mathematics and applied computer science, emphasizing the crucial role of solitons in scientific disciplines.

KEYWORDS
Complex three coupled Maccari's system
A new mapping method
Soliton patterns
Bifurcation
M-Truncated fractional derivative

INTRODUCTION

In this contemporary era of innovations and development, remarkable advancements have been noted in the field of soliton theory. Soliton phenomena, crucial for augmenting computational capabilities in computer systems, hold particular relevance in applications such as image processing, data analysis and simulations within diverse domains of computer science together with numerous applications in nonlinear optics, engineering, deep water waves, fiber optics, plasma physics, fluid mechanics, mathematical physics, and particularly in scenarios involving the propagation of nonlinear waves. Soliton models play a crucial role in various applications, including solitary wave-based communication links, fiber-optic, optical pulse compressors, amplifiers, and numerous other mechanisms. Optical solitons play a important role in the realm of telecommunications, serving as a fundamental cornerstone of the industry. Their importance in nonlinear optics is underscored by this distinctive characteristic. Solitons are essentially the outcome of the interplay between non-linearity, which inclines towards increasing the wave slope, and dispersion, which tends to stabilize the wave. Nonlinear physical phenomena is significantly enriched by the presence of precise moving wave solutions in nonlinear partial differential equations (PDEs). Numerous researchers have unveiled a diverse range of solutions across various nonlinear models, including rogue wave solutions, dromion wave solutions, soliton solutions, multi soliton solutions, lumps, and breather solutions. Many efficient techniques have been developed for acquiring precise wave solutions in case of study the

Manuscript received: 5 January 2024,
Revised: 4 April 2024,
Accepted: 4 April 2024.

[1]muhammad.bilal.riaz@vsb.cz (**Corresponding author**)
[2]prof.azizkhan@gmail.com
[3]jan.martinovic@vsb.cz

non-linear models, such as, the coupled nonlinear Schrödinger equations (NSEs) and derived the optical soliton solutions by using the Kudryashov R function technique (Das and Saha Ray 2023), for time-fractional perturbed (NSEs) obtained some new soliton solutions with application of the generalized Kudryashov scheme (Das and Saha Ray 2022), for (NSEs) by the application of modified auxiliary technique derived optical solutions and some new optical wave solutions gained by employing the improved $tan(\phi(\zeta/2))$-expansion technique to perturbed (NSEs) (Saha Ray and Das 2022), the F-expantion method (A. Filiz and Sonmezoglu 2014; W. B. Rabie and Hamdy 2023), the Jacobi eliptic function expansion method (Zayed and AlurrÖ 2015; Zheng and Feng 2014), and many others have been used in the past.

We employ the new mapping method in our research, a robust approach for addressing nonlinear evolution equations. This method, when applied with specific parameter values, enables the derivation of soliton solutions. New exact soliton solutions derived through this approach align with those obtained through the trial equation method, the first integral method, and the functional variable method. Numerous new results are identified, encompassing in the form of transcendental functions. The versatility of this method is evident through its widespread applications in the literature. For instance, some soliton solutions for two (NSEs) by the application of new mapping method are investigated by Zayed et.al (Zayed and AlurrÖ 2017). Zeng et.al (X. Zeng 2008) developed A new mapping method and discussed its applications to nonlinear partial differential equations. Zayed et.al (E. M. Zayed and Alshehr 2022) investigated Optical wave solutions having Kudryashovís self-phase modulation by using new mapping approach.

The versatile and valuable impacts of fractional calculus in the field of electrical engineering, electrochemistry, control theory, electromagnetism, mechanics, image processing, bioengineering, physics, finance, fluid dynamics, and many others make it a valuable tool for study. Fractional derivatives not only keep the record of the present but also the past, so they are very suitable and accurate when the system has long-term memory. It has several applications in physical science as well as in other areas such as biology, astrophysics, ecology, geology and chemistry. The mechanism of non-Newtonian models is elaborated successfully with the fractional calculus in the past decades due to its simple and elegant description of the complexity of its behaviour. One of the important feature and most commonly known name of non-Newtonian fluid is viscoelastic fluid that which exhibit the behaviour of elasticity and viscosity. Such types of fluid models have great implications in various fields namely polymerization, industrial as well as mechanical engineering and also in the field of auto mobile industry due to its significance.

Fractional calculus is very helpful in the interpretation of the viscoelastic nature of the materials. Taking into account the enormous mentioned properties, many researchers paid attention to analyse the fractional behaviour of different models directly or indirectly in case of derivatives when it is considered as non-integer order from. Fractional calculus, emerging from the traditional calculus such as derivative and integral operators, much like fractional exponents evolving from integer values, constitutes a distinct field of mathematical study. Certainly. Real-world processes, by and large, exhibit characteristics of fractional-order systems. The effectiveness of Fractional Calculus (FC) applications can be attributed to the heigh accuracy of these innovative fractional-order models as compared to traditional models. The fractional order model introduces greater degrees of freedom than the corresponding classical model, contributing to its superior performance. A differential equation containing fractional integrals, derivatives or both is described as a Fractional Equation (FE).

Recognition of the importance of such equations has steadily increased over the past decade. Diverse applications have surfaced, including wave propagation in porous media or complex (Zaslavsky 2002), fractional order modified Duffing systems (Ge and Ou 2008), Ginzburg–Landau model (Zhu and Gao 2023), regularized symmetric long wave equation flow models in deep water (Senol 2020), in physical and engineering sciences fractional Boussinesq type equations (Ellahi and Khan 2018), and Korteweg–de Vries equations taking coefficients variable (Wang and Li 2018). The spectrum of fractional derivative operators encompasses various types, such as Beta-fractional derivative (Rafiq and Kamran 2022), Atangana–Baleanu–Riemann fractional derivative (Khater and Kumar 2020), Caputo–Fabrizio derivative (Naeem and Zaland 2022), and truncated M-fractional derivatives (Mohammed and Abouelregal 2023; Alabedalhadi and Alhazmi 2023).

The aim of this paper is to clarify how the soliton solutions of the complex three coupled Maccari's system are influenced by the M-fractional derivative operator, by using the New Mapping Method. The importance of the M-fractional derivative lies in its capacity to incorporate the features of both fractional and integer order derivatives. This serves as a generalization of numerous fractional derivatives, preserving essential characteristics of integer-order derivatives. Our findings reveal that employing straightforward schemes and solvable ordinary differential equations (ODEs) facilitates the easy derivation of various exact-wave solutions for complex NLFPDEs.

Notably, the solution of this ODE has been achieved using the New mapping method technique, the obtained results are novel compared to existing literature to examine soliton patterns. Following this, we have explored the dynamics of the analyzed equation by employing bifurcation theory. As a result, phase portraits illustrates the bifurcation features of the model under various initial conditions has been conducted. A bifurcation theory refers to a qualitative transformation to unveil the dynamical system characteristics, provides the modification of involving parameters. The primary objective of this study is to unveil novel exact soliton solutions for the considerd system with employing the new mapping method and analyzed the behaviour of differential equations (DEs) through the bifurcation analysis.

This manuscript is structured as follows: Described the basic definition and properties of M-fractional derivative in Section 2. Section 3 presented the fractional model being studied. Section 4 provides an overview of the renowned new mapping method. In Section 5, wave solutions discovered by employing this method along with several figures displayed. Section 6 involves the illustration of bifurcation analysis and discussed the behaviour of fixed points through phase portraits.Finally, Section 7 presents the comprehensive summary of the obtained results from the study.

FUNDAMENTAL CONCEPTS OF FRACTIONAL CALCULUS

In this part, some basic concepts of the fractional operator used in this article are given.

Truncated-M Fractional Derivative

Definition 1 The truncated one parameter Mittag-Leffler function is given below (Vanterler 2018):

$$ {}_{i}E_{\varpi}(G) = \sum_{j=0}^{i} \frac{G^{j}}{\Gamma(\varpi j + 1)}, $$

where $\varpi > 0$ and $G \in \mathbb{C}$.

Definition 2 Let $R : [0, \infty) \to \mathbb{R}$ and $\delta \in (0, 1)$. The truncated M-derivative of function R of order ϑ is defined by:

$$\mathcal{D}_M^{\vartheta,\varpi} R(t) = \lim_{\varepsilon \to 0} \frac{R(t + {}_iE_\varpi(\varepsilon t^{-\vartheta})) - R(t)}{\varepsilon},$$

for $t > 0$ and ${}_iE_\varpi(.)$, where $\varpi > 0$.

Theorem 1 Suppose that R is a differentiable function of order ϑ at $t_0 > 0$, where $\vartheta \in (0, 1]$ and $\varpi > 0$. Then, R is continuous at t_0.

Theorem 2 Assuming $\vartheta \in (0, 1]$, $\varpi > 0$, $\alpha, \beta \in \mathbb{R}$, and R, S are ϑ-differentiable at $t > 0$, then:

1- ${}_i\mathcal{D}_M^{\vartheta,\varpi}(\alpha\, R(t) + \beta\, S(t)) = r\mathcal{D}_M^{\vartheta,\varpi}(R(t)) + s\mathcal{D}_M^{\vartheta,\varpi}(S(t))$.

2- ${}_i\mathcal{D}_M^{\vartheta,\varpi}(R(t).S(t)) = R(t)\mathcal{D}_M^{\vartheta,\varpi}(S(t)) + S(t)\mathcal{D}_M^{\vartheta,\varpi}(R(t))$.

3- ${}_i\mathcal{D}_M^{\vartheta,\varpi}(\frac{R(t)}{S(t)}) = \frac{R(t)\mathcal{D}_M^{\vartheta,\varpi}(S(t)) - S(t)\mathcal{D}_M^{\vartheta,\varpi}(R(t))}{[S(t)]^2}$.

4- ${}_i\mathcal{D}_M^{\vartheta,\varpi}(\delta) = 0$, where δ is a constant.

5- If $R(t)$ is differentiable, then ${}_i\mathcal{D}_M^{\vartheta,\varpi}(R)(t) = \frac{t^{1-\vartheta}}{\Gamma(\varpi+1)}\frac{dR(t)}{dt}$.

FRACTIONAL GOVERNING MODEL WITH MATHEMATICAL ANALYSIS

The M-fractional three-coupled nonlinear Maccari's system, as depicted in (Emad and Lanre 2021), elucidates the propagation of isolated waves within a limited spatial domain. This phenomenon is relevant to various fields such as hydrodynamics, optical communications and plasma physics.

$$\begin{cases} iD_{M,t}^{\chi,\gamma}\Psi + \Psi_{xx} + \Pi\Psi = 0, \\ iD_{M,t}^{\chi,\gamma}\Phi + \Phi_{xx} + \Pi\Phi = 0, \\ iD_{M,t}^{\chi,\gamma}\Omega + \Omega_{xx} + \Pi\Omega = 0, \\ iD_{M,t}^{\chi,\gamma}\Pi + \Pi_y + \left(|\Psi + \Phi + \Omega|^2\right)_x = 0. \end{cases} \tag{1}$$

Let us consider the following transformations:

$$\begin{cases} \Psi(x,y,t) &= \Psi(\zeta) \times \exp\left(\iota\left(\kappa_1 x + \nu y + \theta\frac{\Gamma(\gamma+1)}{\alpha}t^\alpha\right) + \kappa\right), \\ \Phi(x,y,t) &= \Phi(\zeta) \times \exp\left(\iota\left(\kappa_1 x + \nu y + \theta\frac{\Gamma(\gamma+1)}{\alpha}t^\alpha\right) + \kappa\right), \\ \Omega(x,y,t) &= \Omega(\zeta) \times \exp\left(\iota\left(\kappa_1 x + \nu y + \theta\frac{\Gamma(\gamma+1)}{\alpha}t^\alpha\right) + \kappa\right), \\ \Pi(x,y,t) &= \Pi(\zeta) \quad \text{where} \quad \zeta = \lambda\left(x + y - 2\beta\frac{\Gamma(\gamma+1)}{\alpha}t^\alpha\right). \end{cases} \tag{2}$$

In this context, the variables κ_1, θ, ν, and β represent the unknowns, with κ serving as the arbitrary constant. Upon substituting Equation (2) into Equation (1), both the real and imaginary components are derived such as, Real parts:

$$\begin{cases} \lambda^2\Psi'' - \left(\theta + \kappa_1^2\right)\Psi + \Psi\Pi = 0, \\ \lambda^2\Phi'' - \left(\theta + \kappa_1^2\right)\Phi + \Phi\Pi = 0, \\ \lambda^2\Omega'' - \left(\theta + \kappa_1^2\right)\Omega + \Omega\Pi = 0, \\ \lambda(1 - 2\beta)\Pi' + \lambda\left((\Psi + \Phi + \Omega)^2\right)' = 0. \end{cases} \tag{3}$$

and its imaginary parts:

$$(-2\beta + 2\kappa_1)\Psi' = 0, (-2\beta + 2\kappa_1)\Phi' = 0, (-2\beta + 2\kappa_1)\Omega' = 0. \tag{4}$$

By Equation Eq.(4), imply $\beta = \kappa_1$. Integrating the fourth equation of system (3) yields

$$\Pi = -\frac{(\Psi + \Phi + \Omega)^2}{1 - 2\kappa_1} \tag{5}$$

Replacing (5) in the system (3), yields

$$\begin{cases} \lambda^2\Psi'' - \left(\theta + \kappa_1^2\right)\Psi - \frac{(\Psi+\Phi+\Omega)^2}{1-2\kappa_1}\Psi = 0, \\ \lambda^2\Phi'' - \left(\theta + \kappa_1^2\right)\Phi - \frac{(\Psi+\Phi+\Omega)^2}{1-2\kappa_1}\Phi = 0, \\ \lambda^2\Omega'' - \left(\theta + \kappa_1^2\right)\Omega - \frac{(\Psi+\Phi+\Omega)^2}{1-2\kappa_1}\Omega = 0. \end{cases} \tag{6}$$

Taking $\Phi = \kappa_2\Psi$ and $\Omega = c\Psi$ in the system (6), we obtain

$$\lambda^2\Psi'' - \left(\theta + \kappa_1^2\right)\Psi - \frac{(1 + \kappa_2 + c)^2}{1 - 2\kappa_1}\Psi^3 = 0 \tag{7}$$

OVERVIEW OF THE RECENTLY INTRODUCED NEW MAPPING METHOD

Consider the non-linear PDE :

$$P\left(\Psi, \Psi_x, \Psi_t, \Psi_{xx}, \Psi_t, \ldots\right) = 0 \tag{8}$$

In this context, where P is a polynomial in Ψ involving its partial derivatives, specifically the highest order derivatives and nonlinear terms and Ψ is a function of x and t, i.e, $\Psi = \Psi(x, t)$ which is an unknown function. The fundamental procedures of the widely recognized new mapping method (X. Zeng 2008) can be outlined as follows:

Step 1. The transformation of travelling wave

$$\Psi(x, t) = \Psi(\varsigma), \quad \varsigma = x - ct \tag{9}$$

where c represent a constant, after applying the transformation, Eq. (8) reduces into to the following non-linear (ODE):

$$G\left(\Psi, \Psi', \Psi'', \ldots\right) = 0 \tag{10}$$

Here, G represents a polynomial involving $\Psi(\varsigma)$ and its derivatives with respect to ς.

Step 2. We assume that the solution to Equation (10) written in the following form:

$$\Psi(\varsigma) = \sum_{i=0}^{2N} \alpha_i F^i(\varsigma) \tag{11}$$

Here, $F(\varsigma)$ fulfills a first-order nonlinear ordinary differential equation:

$$\left(F'\right)^2(\varsigma) = pF^2(\varsigma) + \frac{1}{2}qF^4(\varsigma) + \frac{1}{3}sF^6(\varsigma) + r \tag{12}$$

In this context, constants α_i (where i ranges from 0 to $2N$), along with the constants p, q, s, and r, are to be determined, but both s and α_{2N} must be non-zero.

Step 3. We ascertain the balancing number N for Equation (11) by equating the highest-order derivatives with the highest nonlinear terms in Equation (10).

Step 4. By substituting Eq.(11) together with Eq. (12) into Eq. (10) and aggregating all the coefficients of $F^m\left(F'\right)^n$ (where $m = 0, 1, 2, \ldots$) and $(n = 0, 1)$, subsequent setting of these coefficients to zero leads to a system of algebraic equations. These equations can be effectively solved using Maple software to determine the values of unknowns such as, α_i (where $i = 0, 1, 2, \ldots, 2N$), p, q, s, r, and c.

Step 5. It is widely acknowledged (Zayed and AlurrÖ 2017; X. Zeng 2008; E. M. Zayed and Alshehr 2022) that Eq. (12) possesses sets of solutions, outlined as follows:

$$F_1(\varsigma) = 4\left(-\frac{p\tanh^2\left(\epsilon\sqrt{-\frac{p}{3}}\varsigma\right)}{3q\left(3+\tanh^2\left(\epsilon\sqrt{-\frac{p}{3}}\varsigma\right)\right)}\right)^{\frac{1}{2}}, \quad p<0, q>0, s=\frac{3q^2}{16p}, r=\frac{16p^2}{27q},$$

$$F_2(\varsigma) = 4\left(-\frac{p\coth^2\left(\epsilon\sqrt{-\frac{p}{3}}\varsigma\right)}{3q\left(3+\coth^2\left(\epsilon\sqrt{-\frac{p}{3}}\varsigma\right)\right)}\right)^{\frac{1}{2}}, \quad p<0, q>0, s=\frac{3q^2}{16p}, r=\frac{16p^2}{27q},$$

$$F_3(\varsigma) = 4\left(\frac{p\tan^2\left(\epsilon\sqrt{\frac{p}{3}}\varsigma\right)}{3q\left(3-\tan^2\left(\epsilon\sqrt{\frac{p}{3}}\varsigma\right)\right)}\right)^{\frac{1}{2}}, \quad p>0, q<0, s=\frac{3q^2}{16p}, r=\frac{16p^2}{27q},$$

$$F_4(\varsigma) = 4\left(\frac{p\cot^2\left(\epsilon\sqrt{\frac{\epsilon}{3}}\varsigma\right)}{3q\left(3-\cot^2\left(\epsilon\sqrt{\frac{p}{3}}\varsigma\right)\right)}\right)^{\frac{4}{2}}, \quad p>0, q<0, s=\frac{3q^2}{16p}, r=\frac{16p^2}{27q},$$

$$F_5(\varsigma) = \left(-\frac{2p}{q}(1+\tanh(\epsilon\sqrt{p}\varsigma))\right)^{\frac{1}{2}}, p>0, s=\frac{3q^2}{16p}, r=0,$$

$$F_6(\varsigma) = \left(-\frac{2p}{q}(1+\coth(\epsilon\sqrt{p}\varsigma))\right)^{\frac{1}{2}}, p>0, s=\frac{3q^2}{16p}, r=0,$$

$$F_7(\varsigma) = \left(-\frac{6pq\,\mathrm{sech}^2(\sqrt{p}\varsigma)}{3q^2-4ps(1+\epsilon\tanh(\sqrt{p}\varsigma))^2}\right)^{\frac{4}{2}}, p>0, r=0,$$

$$F_8(\varsigma) = \left(\frac{6pq\,\mathrm{csch}^2(\sqrt{p}\varsigma)}{3q^2-4ps(1+\epsilon\coth(\sqrt{p}\varsigma))^2}\right)^{\frac{1}{2}}, p>0, r=0,$$

$$F_9(\varsigma) = \left(-\frac{6p\,\mathrm{sech}^2(\sqrt{p}\varsigma)}{3q+4\epsilon\sqrt{3ps}\tanh(\sqrt{p}\varsigma)}\right)^{\frac{1}{2}}, p>0, s>0, r=0,$$

$$F_{10}(\varsigma) = \left(\frac{6p\,\mathrm{csch}^2(\sqrt{p}\varsigma)}{3q+4\epsilon\sqrt{3ps}\coth(\sqrt{p}\varsigma)}\right)^{\frac{1}{2}}, p>0, s>0, r=0,$$

$$F_{11}(\varsigma) = \left(-\frac{6p\sec^2(\sqrt{-p}\varsigma)}{3q+4\epsilon\sqrt{-3ps}\tan(\sqrt{-p}\varsigma)}\right)^{\frac{1}{2}}, p<0, s>0, r=0,$$

$$F_{12}(\varsigma) = \left(-\frac{6p\,\mathrm{csc}^2(\sqrt{-p}\varsigma)}{3q+4\epsilon\sqrt{-3ps}\cot(\sqrt{-p}\varsigma)}\right)^{\frac{1}{2}}, p<0, s>0, r=0$$

$$F_{13}(\varsigma) = 2\left(\frac{3p\,\mathrm{sech}^2(\epsilon\sqrt{p}\varsigma)}{2\sqrt{M}-(\sqrt{M}+3q)\,\mathrm{sech}^2(\epsilon\sqrt{p}\varsigma)}\right)^{\frac{1}{2}}, \quad p>0, q<0, s<0, M>0, r=0 \tag{13}$$

$$F_{14}(\varsigma) = 2\left(\frac{3p\,\mathrm{csch}^2(\epsilon\sqrt{p}\varsigma)}{2\sqrt{M}+(\sqrt{M}-3q)\,\mathrm{csch}^2(\epsilon\sqrt{p}\varsigma)}\right)^{\frac{1}{2}}, \quad p>0, q<0, s<0, M>0, r=0,$$

$$F_{15}(\varsigma) = 2\left(\frac{-3p\sec^2(\epsilon\sqrt{-p}\varsigma)}{2\sqrt{M}-(\sqrt{M}-3q)\sec^2(\epsilon\sqrt{-p}\varsigma)}\right)^{\frac{1}{2}}, \quad p<0, q>0, s<0, M>0, r=0,$$

$$F_{16}(\varsigma) = 2\left(\frac{3p\,\mathrm{csc}^2(\epsilon\sqrt{-p}\varsigma)}{2\sqrt{M}-(\sqrt{M}+3q)\,\mathrm{csc}^2(\epsilon\sqrt{-p}\varsigma)}\right)^{\frac{1}{2}}, \quad p<0, q>0, s<0, M>0, r=0,$$

$$F_{17}(\varsigma) = 2\left(\frac{3p}{\epsilon\sqrt{M}\cosh(2\sqrt{p}\varsigma)-3q}\right)^{\frac{1}{2}}, p>0, M>0, r=0,$$

$$F_{18}(\varsigma) = 2\left(\frac{3p}{\epsilon\sqrt{M}\cos(2\sqrt{-p}\varsigma)-3q}\right)^{\frac{1}{2}}, p<0, M>0, r=0,$$

$$F_{19}(\varsigma) = 2\left(\frac{3p}{\epsilon\sqrt{M}\sin(2\sqrt{-p}\varsigma)-3q}\right)^{\frac{1}{2}}, p<0, M>0, r=0$$

$$F_{20}(\varsigma) = 2\left(\frac{3p}{\epsilon\sqrt{-M}\sinh(2\sqrt{p}\varsigma)-3q}\right)^{\frac{1}{2}}, p>0, M<0, r=0,$$

where $M = 9q^2 - 48ps$ and $\epsilon = \pm 1$.

Step 6. By substituting the values of α_i, p, q, s, r, and c, along with the solutions of Eq. (12) provided in Step 5, into Eq. (11), we obtain the precise solutions for Eq. (8).

EXPLICIT SOLUTIONS OF THE EQUATION

In this section the primary objective to obtain the precise solutions for the model under examination. Calculating the value of N involves the application of the homogeneous balancing principle to Eq. (7). By setting Ψ'' and Ψ^3 in Eq. (7) equal to each other, yielding $3N = N + 2$, we deduce that $N = 1$. Consequently, for $N = 1$, the solution of the system can be expressed as follows:

$$\Psi(\zeta) = \Lambda_0 + \Lambda_1 F(\zeta) + \Lambda_2 F^2(\zeta). \tag{14}$$

By substituting Eq. (14) into Eq. (7) along with Eq. (12), a system of equations is formed by equating the coefficients of various powers of $F(\zeta)$ to zero. The utilization of Maple software in solving this system yields the following efficacious solution:

$$p = -\left(\frac{A+3B\kappa^2}{4}\right), \quad q = \mp\frac{2\kappa\sqrt{-6Bs}}{3}, \tag{15}$$
$$\Lambda_0 = \Theta, \Lambda_1 = 0, \quad \Lambda_2 = \pm\frac{2\sqrt{-6Bs}}{3B}$$

where,

$$\Theta=\frac{\left(\left(3\sqrt{3}\sqrt{\frac{A^3-72sr^2}{B}}B+18\sqrt{-6Bs}r\right)B\right)^{\frac{2}{3}}-3AB}{3B\left(\left(3\sqrt{3}\sqrt{\frac{A^3-72sr^2}{B}}B+18\sqrt{-6BS}r\right)B\right)^{\frac{1}{3}}},$$
$$A=-\frac{(\theta+\kappa_1^2)}{\lambda^2},\quad B=-\frac{(1+\kappa_2+c)^2}{\lambda^2(1-2\kappa_1)}.$$

By plugging above values in Eq.(14) which becomes $\Psi(\zeta)=\Theta\pm\frac{2\sqrt{-6Bs}}{3B}F^2(\zeta)$ and employing the transformation mentioned in Eq.(12), the solutions of system (1) are as follows,

• **Type 1:** For $p<0,q>0,s=\frac{3q^2}{16p}$ and $r=\frac{16p^2}{27q}$, we have

$$\begin{cases}\Psi_1(x,y,t)=\left[\Theta\pm\frac{32\sqrt{-6Bs}}{3B}\left(-\frac{p\tanh^2\left(\epsilon\sqrt{-\frac{p}{3}}\varsigma\right)}{3q\left(3+\tanh^2\left(\epsilon\sqrt{-\frac{p}{3}}\varsigma\right)\right)}\right)\right]\\ \qquad\times\left(\exp\left(\iota\left(\kappa_1x+\nu y+\theta\frac{\Gamma(\gamma+1)}{\alpha}t^\alpha\right)\right)+\kappa\right),\\ \Phi_1(x,y,t)=\kappa_2\left[\Theta\pm\frac{32\sqrt{-6Bs}}{3B}\left(-\frac{p\tanh^2\left(\epsilon\sqrt{-\frac{p}{3}}\varsigma\right)}{3q\left(3+\tanh^2\left(\epsilon\sqrt{-\frac{p}{3}}\varsigma\right)\right)}\right)\right]\\ \qquad\times\left(\exp\left(\iota\left(\kappa_1x+\nu y+\theta\frac{\Gamma(\gamma+1)}{\alpha}t^\alpha\right)\right)+\kappa\right),\\ \Omega_1(x,y,t)=c\left[\Theta\pm\frac{32\sqrt{-6Bs}}{3B}\left(-\frac{p\tanh^2\left(\epsilon\sqrt{-\frac{p}{3}}\varsigma\right)}{3q\left(3+\tanh^2\left(\epsilon\sqrt{-\frac{p}{3}}\varsigma\right)\right)}\right)\right]\\ \qquad\times\left(\exp\left(\iota\left(\kappa_1x+\nu y+\theta\frac{\Gamma(\gamma+1)}{\alpha}t^\alpha\right)\right)+\kappa\right),\end{cases}\tag{16}$$

• **Type 2:** For $p<0,q>0,s=\frac{3q^2}{16p}$ and $r=\frac{16p^2}{27q}$, we have

$$\begin{cases}\Psi_1(x,y,t)=\left[\Theta\pm\frac{32\sqrt{-6Bs}}{3B}\left(-\frac{pcoth^2\left(\epsilon\sqrt{-\frac{p}{3}}\varsigma\right)}{3q\left(3+coth^2\left(\epsilon\sqrt{-\frac{p}{3}}\varsigma\right)\right)}\right)\right]\\ \qquad\times\left(\exp\left(\iota\left(\kappa_1x+\nu y+\theta\frac{\Gamma(\gamma+1)}{\alpha}t^\alpha\right)\right)+\kappa\right),\\ \Phi_1(x,y,t)=\kappa_2\left[\Theta\pm\frac{32\sqrt{-6Bs}}{3B}\left(-\frac{pcoth^2\left(\epsilon\sqrt{-\frac{p}{3}}\varsigma\right)}{3q\left(3+coth^2\left(\epsilon\sqrt{-\frac{p}{3}}\varsigma\right)\right)}\right)\right]\\ \qquad\times\left(\exp\left(\iota\left(\kappa_1x+\nu y+\theta\frac{\Gamma(\gamma+1)}{\alpha}t^\alpha\right)\right)+\kappa\right),\\ \Omega_1(x,y,t)=c\left[\Theta\pm\frac{32\sqrt{-6Bs}}{3B}\left(-\frac{pcoth^2\left(\epsilon\sqrt{-\frac{p}{3}}\varsigma\right)}{3q\left(3+coth^2\left(\epsilon\sqrt{-\frac{p}{3}}\varsigma\right)\right)}\right)\right]\\ \qquad\times\left(\exp\left(\iota\left(\kappa_1x+\nu y+\theta\frac{\Gamma(\gamma+1)}{\alpha}t^\alpha\right)\right)+\kappa\right),\end{cases}\tag{17}$$

• **Type 3:** For $p>0,q<0,s=\frac{3q^2}{16p}$ and $r=\frac{16p^2}{27q}$, we have

$$\begin{cases}\Psi_1(x,y,t)=\left[\Theta\pm\frac{32\sqrt{-6Bs}}{3B}\left(\frac{p\tan^2\left(\epsilon\sqrt{\frac{p}{3}}\varsigma\right)}{3q\left(3-\tan^2\left(\epsilon\sqrt{\frac{p}{3}}\varsigma\right)\right)}\right)\right]\\ \qquad\times\left(\exp\left(\iota\left(\kappa_1x+\nu y+\theta\frac{\Gamma(\gamma+1)}{\alpha}t^\alpha\right)\right)+\kappa\right),\\ \Phi_1(x,y,t)=\kappa_2\left[\Theta\pm\frac{32\sqrt{-6Bs}}{3B}\left(\frac{p\tan^2\left(\epsilon\sqrt{\frac{p}{3}}\varsigma\right)}{3q\left(3-\tan^2\left(\epsilon\sqrt{\frac{p}{3}}\varsigma\right)\right)}\right)\right]\\ \qquad\times\left(\exp\left(\iota\left(\kappa_1x+\nu y+\theta\frac{\Gamma(\gamma+1)}{\alpha}t^\alpha\right)\right)+\kappa\right),\\ \Omega_1(x,y,t)=c\left[\Theta\pm\frac{32\sqrt{-6Bs}}{3B}\left(\frac{p\tan^2\left(\epsilon\sqrt{\frac{p}{3}}\varsigma\right)}{3q\left(3-\tan^2\left(\epsilon\sqrt{\frac{p}{3}}\varsigma\right)\right)}\right)\right]\\ \qquad\times\left(\exp\left(\iota\left(\kappa_1x+\nu y+\theta\frac{\Gamma(\gamma+1)}{\alpha}t^\alpha\right)\right)+\kappa\right),\end{cases}\tag{18}$$

• **Type 4:** For $p>0,q<0,s=\frac{3q^2}{16p}$ and $r=\frac{16p^2}{27q}$, we have

$$\begin{cases}\Psi_4(x,y,t)=\left[\Theta\pm\frac{32\sqrt{-6Bs}}{3B}\left(\frac{p\cot^2\left(\epsilon\sqrt{\frac{p}{3}}\varsigma\right)}{3q\left(3-\cot^2\left(\epsilon\sqrt{\frac{p}{3}}\varsigma\right)\right)}\right)\right]\\ \qquad\times\left(\exp\left(\iota\left(\kappa_1x+\nu y+\theta\frac{\Gamma(\gamma+1)}{\alpha}t^\alpha\right)\right)+\kappa\right),\\ \Phi_4(x,y,t)=\kappa_2\left[\Theta\pm\frac{32\sqrt{-6Bs}}{3B}\left(\frac{p\cot^2\left(\epsilon\sqrt{\frac{p}{3}}\varsigma\right)}{3q\left(3-\cot^2\left(\epsilon\sqrt{\frac{p}{3}}\varsigma\right)\right)}\right)\right]\\ \qquad\times\left(\exp\left(\iota\left(\kappa_1x+\nu y+\theta\frac{\Gamma(\gamma+1)}{\alpha}t^\alpha\right)\right)+\kappa\right),\\ \Omega_4(x,y,t)=c\left[\Theta\pm\frac{32\sqrt{-6Bs}}{3B}\left(\frac{p\cot^2\left(\epsilon\sqrt{\frac{p}{3}}\varsigma\right)}{3q\left(3-\cot^2\left(\epsilon\sqrt{\frac{p}{3}}\varsigma\right)\right)}\right)\right]\\ \qquad\times\left(\exp\left(\iota\left(\kappa_1x+\nu y+\theta\frac{\Gamma(\gamma+1)}{\alpha}t^\alpha\right)\right)+\kappa\right),\end{cases}\tag{19}$$

• **Type 5:** For $p>0,s=\frac{3q^2}{16p}$ and $r=0$, we have

$$\begin{cases}\Psi_5(x,y,t)=\left[\Theta\pm\frac{2\sqrt{-6Bs}}{3B}\left(-\frac{2p}{q}\left(1+\tanh\left(\epsilon\sqrt{p}\varsigma\right)\right)\right)\right]\\ \qquad\times\left(\exp\left(\iota\left(\kappa_1x+\nu y+\theta\frac{\Gamma(\gamma+1)}{\alpha}t^\alpha\right)\right)+\kappa\right),\\ \Phi_5(x,y,t)=\kappa_2\left[\Theta\pm\frac{2\sqrt{-6Bs}}{3B}\left(-\frac{2p}{q}\left(1+\tanh\left(\epsilon\sqrt{p}\varsigma\right)\right)\right)\right]\\ \qquad\times\left(\exp\left(\iota\left(\kappa_1x+\nu y+\theta\frac{\Gamma(\gamma+1)}{\alpha}t^\alpha\right)\right)+\kappa\right),\\ \Omega_5(x,y,t)=c\left[\Theta\pm\frac{2\sqrt{-6Bs}}{3B}\left(-\frac{2p}{q}\left(1+\tanh\left(\epsilon\sqrt{p}\varsigma\right)\right)\right)\right]\\ \qquad\times\left(\exp\left(\iota\left(\kappa_1x+\nu y+\theta\frac{\Gamma(\gamma+1)}{\alpha}t^\alpha\right)\right)+\kappa\right),\end{cases}\tag{20}$$

• **Type 6:** For $p>0,s=\frac{3q^2}{16p}$ and $r=0$, we have

$$\begin{cases}\Psi_6(x,y,t)=\left[\Theta\pm\frac{2\sqrt{-6Bs}}{3B}\left(-\frac{2p}{q}\left(1+coth\left(\epsilon\sqrt{p}\varsigma\right)\right)\right)\right]\\ \qquad\times\left(\exp\left(\iota\left(\kappa_1x+\nu y+\theta\frac{\Gamma(\gamma+1)}{\alpha}t^\alpha\right)\right)+\kappa\right),\\ \Phi_6(x,y,t)=\kappa_2\left[\Theta\pm\frac{2\sqrt{-6Bs}}{3B}\left(-\frac{2p}{q}\left(1+coth\left(\epsilon\sqrt{p}\varsigma\right)\right)\right)\right]\\ \qquad\times\left(\exp\left(\iota\left(\kappa_1x+\nu y+\theta\frac{\Gamma(\gamma+1)}{\alpha}t^\alpha\right)\right)+\kappa\right),\\ \Omega_6(x,y,t)=c\left[\Theta\pm\frac{2\sqrt{-6Bs}}{3B}\left(-\frac{2p}{q}\left(1+coth\left(\epsilon\sqrt{p}\varsigma\right)\right)\right)\right]\\ \qquad\times\left(\exp\left(\iota\left(\kappa_1x+\nu y+\theta\frac{\Gamma(\gamma+1)}{\alpha}t^\alpha\right)\right)+\kappa\right),\end{cases}\tag{21}$$

• **Type 7:** For $p>0$ and $r=0$, we have

$$\begin{cases}\Psi_7(x,y,t)=\left[\Theta\pm\frac{2\sqrt{-6Bs}}{3B}\left(-\frac{6pq\ sech^2\left(\sqrt{p}\varsigma\right)}{3q^2-4ps\left(1+\epsilon\tanh\left(\sqrt{p}\varsigma\right)^2\right)}\right)\right]\\ \qquad\times\left(\exp\left(\iota\left(\kappa_1x+\nu y+\theta\frac{\Gamma(\gamma+1)}{\alpha}t^\alpha\right)\right)+\kappa\right),\\ \Phi_7(x,y,t)=\kappa_2\left[\Theta\pm\frac{2\sqrt{-6Bs}}{3B}\left(-\frac{6pq\ sech^2\left(\sqrt{p}\varsigma\right)}{3q^2-4ps\left(1+\epsilon\tanh\left(\sqrt{p}\varsigma\right)^2\right)}\right)\right]\\ \qquad\times\left(\exp\left(\iota\left(\kappa_1x+\nu y+\theta\frac{\Gamma(\gamma+1)}{\alpha}t^\alpha\right)\right)+\kappa\right),\\ \Omega_7(x,y,t)=c\left[\Theta\pm\frac{2\sqrt{-6Bs}}{3B}\left(-\frac{6pq\ sech^2\left(\sqrt{p}\varsigma\right)}{3q^2-4ps\left(1+\epsilon\tanh\left(\sqrt{p}\varsigma\right)^2\right)}\right)\right]\\ \qquad\times\left(\exp\left(\iota\left(\kappa_1x+\nu y+\theta\frac{\Gamma(\gamma+1)}{\alpha}t^\alpha\right)\right)+\kappa\right),\end{cases}\tag{22}$$

• **Type 8:** For $p>0$ and $r=0$, we have

$$\begin{cases}\Psi_8(x,y,t)=\left[\Theta\pm\frac{2\sqrt{-6Bs}}{3B}\left(\frac{6pqcsch^2\left(\sqrt{p}\varsigma\right)}{3q^2-4ps\left(1+\epsilon coth\left(\sqrt{p}\varsigma\right)^2\right)}\right)\right]\\ \qquad\times\left(\exp\left(\iota\left(\kappa_1x+\nu y+\theta\frac{\Gamma(\gamma+1)}{\alpha}t^\alpha\right)\right)+\kappa\right),\\ \Phi_8(x,y,t)=\kappa_2\left[\Theta\pm\frac{2\sqrt{-6Bs}}{3B}\left(\frac{6pqcsch^2\left(\sqrt{p}\varsigma\right)}{3q^2-4ps\left(1+\epsilon coth\left(\sqrt{p}\varsigma\right)^2\right)}\right)\right]\\ \qquad\times\left(\exp\left(\iota\left(\kappa_1x+\nu y+\theta\frac{\Gamma(\gamma+1)}{\alpha}t^\alpha\right)\right)+\kappa\right),\\ \Omega_8(x,y,t)=c\left[\Theta\pm\frac{2\sqrt{-6Bs}}{3B}\left(\frac{6pqcsch^2\left(\sqrt{p}\varsigma\right)}{3q^2-4ps\left(1+\epsilon coth\left(\sqrt{p}\varsigma\right)^2\right)}\right)\right]\\ \qquad\times\left(\exp\left(\iota\left(\kappa_1x+\nu y+\theta\frac{\Gamma(\gamma+1)}{\alpha}t^\alpha\right)\right)+\kappa\right),\end{cases}\tag{23}$$

• **Type 9:** For $p>0,s>0$ and $r=0$, we have

$$\begin{cases}\Psi_9(x,y,t)=\left[\Theta\pm\frac{2\sqrt{-6Bs}}{3B}\left(-\frac{6psech^2\left(\sqrt{p}\varsigma\right)}{3q+4\epsilon\sqrt{3ps}\tanh\left(\sqrt{p}\varsigma\right)}\right)\right]\\ \qquad\times\left(\exp\left(\iota\left(\kappa_1x+\nu y+\theta\frac{\Gamma(\gamma+1)}{\alpha}t^\alpha\right)\right)+\kappa\right),\\ \Phi_9(x,y,t)=\kappa_2\left[\Theta\pm\frac{2\sqrt{-6Bs}}{3B}\left(-\frac{6psech^2\left(\sqrt{p}\varsigma\right)}{3q+4\epsilon\sqrt{3ps}tanh\left(\sqrt{p}\varsigma\right)}\right)\right]\\ \qquad\times\left(\exp\left(\iota\left(\kappa_1x+\nu y+\theta\frac{\Gamma(\gamma+1)}{\alpha}t^\alpha\right)\right)+\kappa\right),\\ \Omega_9(x,y,t)=c\left[\Theta\pm\frac{2\sqrt{-6Bs}}{3B}\left(-\frac{6psech^2\left(\sqrt{p}\varsigma\right)}{3q+4\epsilon\sqrt{3ps}tanh\left(\sqrt{p}\varsigma\right)}\right)\right]\\ \qquad\times\left(\exp\left(\iota\left(\kappa_1x+\nu y+\theta\frac{\Gamma(\gamma+1)}{\alpha}t^\alpha\right)\right)+\kappa\right),\end{cases}\tag{24}$$

• **Type 10:** For $p>0,s>0$ and $r=0$, we have

$$\begin{cases}\Psi_{10}(x,y,t)=\left[\Theta\pm\frac{2\sqrt{-6Bs}}{3B}\left(\frac{6pcsch^2\left(\sqrt{p}\varsigma\right)}{3q+4\epsilon\sqrt{3ps}coth\left(\sqrt{p}\varsigma\right)}\right)\right]\\ \qquad\times\left(\exp\left(\iota\left(\kappa_1x+\nu y+\theta\frac{\Gamma(\gamma+1)}{\alpha}t^\alpha\right)\right)+\kappa\right),\\ \Phi_{10}(x,y,t)=\kappa_2\left[\Theta\pm\frac{2\sqrt{-6Bs}}{3B}\left(\frac{6pcsch^2\left(\sqrt{p}\varsigma\right)}{3q+4\epsilon\sqrt{3ps}coth\left(\sqrt{p}\varsigma\right)}\right)\right]\\ \qquad\times\left(\exp\left(\iota\left(\kappa_1x+\nu y+\theta\frac{\Gamma(\gamma+1)}{\alpha}t^\alpha\right)\right)+\kappa\right),\\ \Omega_{10}(x,y,t)=c\left[\Theta\pm\frac{2\sqrt{-6Bs}}{3B}\left(\frac{6pcsch^2\left(\sqrt{p}\varsigma\right)}{3q+4\epsilon\sqrt{3ps}coth\left(\sqrt{p}\varsigma\right)}\right)\right]\\ \qquad\times\left(\exp\left(\iota\left(\kappa_1x+\nu y+\theta\frac{\Gamma(\gamma+1)}{\alpha}t^\alpha\right)\right)+\kappa\right),\end{cases}\tag{25}$$

• **Type 11:** For $p<0,s>0$ and $r=0$, we have

$$\begin{cases}\Psi_{11}(x,y,t)=\left[\Theta\pm\frac{2\sqrt{-6Bs}}{3B}\left(-\frac{6p\sec^2\left(\sqrt{-p}\varsigma\right)}{3q+4\epsilon\sqrt{-3ps}\tan\left(\sqrt{-p}\varsigma\right)}\right)\right]\\ \qquad\times\left(\exp\left(\iota\left(\kappa_1x+\nu y+\theta\frac{\Gamma(\gamma+1)}{\alpha}t^\alpha\right)\right)+\kappa\right),\\ \Phi_{11}(x,y,t)=\kappa_2\left[\Theta\pm\frac{2\sqrt{-6Bs}}{3B}\left(-\frac{6p\sec^2\left(\sqrt{-p}\varsigma\right)}{3q+4\epsilon\sqrt{-3ps}\tan\left(\sqrt{-p}\varsigma\right)}\right)\right]\\ \qquad\times\left(\exp\left(\iota\left(\kappa_1x+\nu y+\theta\frac{\Gamma(\gamma+1)}{\alpha}t^\alpha\right)\right)+\kappa\right),\\ \Omega_{11}(x,y,t)=c\left[\Theta\pm\frac{2\sqrt{-6Bs}}{3B}\left(-\frac{6p\sec^2\left(\sqrt{-p}\varsigma\right)}{3q+4\epsilon\sqrt{-3ps}\tan\left(\sqrt{-p}\varsigma\right)}\right)\right]\\ \qquad\times\left(\exp\left(\iota\left(\kappa_1x+\nu y+\theta\frac{\Gamma(\gamma+1)}{\alpha}t^\alpha\right)\right)+\kappa\right),\end{cases}\tag{26}$$

• **Type 12:** For $p<0,s>0$ and $r=0$, we have

$$\begin{cases}\Psi_{12}(x,y,t)=\left[\Theta\pm\frac{2\sqrt{-6Bs}}{3B}\left(-\frac{6p\csc^2\left(\sqrt{-p}\varsigma\right)}{3q+4\epsilon\sqrt{-3ps}\cot\left(\sqrt{-p}\varsigma\right)}\right)\right]\\ \qquad\times\left(\exp\left(\iota\left(\kappa_1x+\nu y+\theta\frac{\Gamma(\gamma+1)}{\alpha}t^\alpha\right)\right)+\kappa\right),\\ \Phi_{12}(x,y,t)=\kappa_2\left[\Theta\pm\frac{2\sqrt{-6Bs}}{3B}\left(-\frac{6p\csc^2\left(\sqrt{-p}\varsigma\right)}{3q+4\epsilon\sqrt{-3ps}\cot\left(\sqrt{-p}\varsigma\right)}\right)\right]\\ \qquad\times\left(\exp\left(\iota\left(\kappa_1x+\nu y+\theta\frac{\Gamma(\gamma+1)}{\alpha}t^\alpha\right)\right)+\kappa\right),\\ \Omega_{12}(x,y,t)=c\left[\Theta\pm\frac{2\sqrt{-6Bs}}{3B}\left(-\frac{6p\csc^2\left(\sqrt{-p}\varsigma\right)}{3q+4\epsilon\sqrt{-3ps}\cot\left(\sqrt{-p}\varsigma\right)}\right)\right]\\ \qquad\times\left(\exp\left(\iota\left(\kappa_1x+\nu y+\theta\frac{\Gamma(\gamma+1)}{\alpha}t^\alpha\right)\right)+\kappa\right),\end{cases}\tag{27}$$

• **Type 13:** For $p>0,q<0,s<0,M>0$ and $r=0$, we have

$$\begin{cases}\Psi_{13}(x,y,t)=\left[\Theta\pm\frac{2\sqrt{-6Bs}}{3B}\left(\frac{12p\ sech^2\left(\epsilon\sqrt{p}\varsigma\right)}{2\sqrt{M}-\left(\sqrt{M}+3q\right)\ sech^2\left(\epsilon\sqrt{p}\varsigma\right)}\right)\right]\\ \qquad\times\left(\exp\left(\iota\left(\kappa_1x+\nu y+\theta\frac{\Gamma(\gamma+1)}{\alpha}t^\alpha\right)\right)+\kappa\right),\\ \Phi_{13}(x,y,t)=\kappa_2\left[\Theta\pm\frac{2\sqrt{-6Bs}}{3B}\left(\frac{12p\ sech^2\left(\epsilon\sqrt{p}\varsigma\right)}{2\sqrt{M}-\left(\sqrt{M}+3q\right)\ sech^2\left(\epsilon\sqrt{p}\varsigma\right)}\right)\right]\\ \qquad\times\left(\exp\left(\iota\left(\kappa_1x+\nu y+\theta\frac{\Gamma(\gamma+1)}{\alpha}t^\alpha\right)\right)+\kappa\right),\\ \Omega_{13}(x,y,t)=c\left[\Theta\pm\frac{2\sqrt{-6Bs}}{3B}\left(\frac{12p\ sech^2\left(\epsilon\sqrt{p}\varsigma\right)}{2\sqrt{M}-\left(\sqrt{M}+3q\right)\ sech^2\left(\epsilon\sqrt{p}\varsigma\right)}\right)\right]\\ \qquad\times\left(\exp\left(\iota\left(\kappa_1x+\nu y+\theta\frac{\Gamma(\gamma+1)}{\alpha}t^\alpha\right)\right)+\kappa\right),\end{cases}\tag{28}$$

• **Type 14:** For $p>0,q<0,s<0,M>0$ and $r=0$, we

have

$$\begin{cases}\Psi_{14}(x,y,t) = \left[\Theta \pm \frac{2\sqrt{-6Bs}}{3B}\left(\frac{12pcsch^2\left(\epsilon\sqrt{p}\varsigma\right)}{2\sqrt{M}+\left(\sqrt{M}-3q\right)csch^2\left(\epsilon\sqrt{p}\varsigma\right)}\right)\right] \\ \qquad \times\left(\exp\left(\iota\left(\kappa_1 x+\nu y+\theta\frac{\Gamma(\gamma+1)}{\alpha}t^{\alpha}\right)\right)+\kappa\right), \\ \Phi_{14}(x,y,t) = \kappa_2\left[\Theta \pm \frac{2\sqrt{-6Bs}}{3B}\left(\frac{12pcsch^2\left(\epsilon\sqrt{p}\varsigma\right)}{2\sqrt{M}+\left(\sqrt{M}-3q\right)csch^2\left(\epsilon\sqrt{p}\varsigma\right)}\right)\right] \\ \qquad \times\left(\exp\left(\iota\left(\kappa_1 x+\nu y+\theta\frac{\Gamma(\gamma+1)}{\alpha}t^{\alpha}\right)\right)+\kappa\right), \\ \Omega_{14}(x,y,t) = c\left[\Theta \pm \frac{2\sqrt{-6Bs}}{3B}\left(\frac{12pcsch^2\left(\epsilon\sqrt{p}\varsigma\right)}{2\sqrt{M}+\left(\sqrt{M}-3q\right)csch^2\left(\epsilon\sqrt{p}\varsigma\right)}\right)\right] \\ \qquad \times\left(\exp\left(\iota\left(\kappa_1 x+\nu y+\theta\frac{\Gamma(\gamma+1)}{\alpha}t^{\alpha}\right)\right)+\kappa\right),\end{cases} \tag{29}$$

• **Type 15:** For $p<0, q>0, s<0, M>0$ and $r=0$, we have

$$\begin{cases}\Psi_{15}(x,y,t) = \left[\Theta \pm \frac{2\sqrt{-6Bs}}{3B}\left(\frac{-12p\sec^2\left(\epsilon\sqrt{-p}\varsigma\right)}{2\sqrt{M}-\left(\sqrt{M}-3q\right)\sec^2\left(\epsilon\sqrt{-p}\varsigma\right)}\right)\right] \\ \qquad \times\left(\exp\left(\iota\left(\kappa_1 x+\nu y+\theta\frac{\Gamma(\gamma+1)}{\alpha}t^{\alpha}\right)\right)+\kappa\right), \\ \Phi_{15}(x,y,t) = \kappa_2\left[\Theta \pm \frac{2\sqrt{-6Bs}}{3B}\left(\frac{-12p\sec^2\left(\epsilon\sqrt{-p}\varsigma\right)}{2\sqrt{M}-\left(\sqrt{M}-3q\right)\sec^2\left(\epsilon\sqrt{-p}\varsigma\right)}\right)\right] \\ \qquad \times\left(\exp\left(\iota\left(\kappa_1 x+\nu y+\theta\frac{\Gamma(\gamma+1)}{\alpha}t^{\alpha}\right)\right)+\kappa\right), \\ \Omega_{15}(x,y,t) = c\left[\Theta \pm \frac{2\sqrt{-6Bs}}{3B}\left(\frac{-12p\sec^2\left(\epsilon\sqrt{-p}\varsigma\right)}{2\sqrt{M}-\left(\sqrt{M}-3q\right)\sec^2\left(\epsilon\sqrt{-p}\varsigma\right)}\right)\right] \\ \qquad \times\left(\exp\left(\iota\left(\kappa_1 x+\nu y+\theta\frac{\Gamma(\gamma+1)}{\alpha}t^{\alpha}\right)\right)+\kappa\right),\end{cases} \tag{30}$$

• **Type 16:** For $p<0, q>0, s<0, M>0$ and $r=0$, we have

$$\begin{cases}\Psi_{16}(x,y,t) = \left[\Theta \pm \frac{2\sqrt{-6Bs}}{3B}\left(\frac{12p\csc^2\left(\epsilon\sqrt{-p}\varsigma\right)}{2\sqrt{M}-\left(\sqrt{M}+3q\right)\csc^2\left(\epsilon\sqrt{-p}\varsigma\right)}\right)\right] \\ \qquad \times\left(\exp\left(\iota\left(\kappa_1 x+\nu y+\theta\frac{\Gamma(\gamma+1)}{\alpha}t^{\alpha}\right)\right)+\kappa\right), \\ \Phi_{16}(x,y,t) = \kappa_2\left[\Theta \pm \frac{2\sqrt{-6Bs}}{3B}\left(\frac{12p\csc^2\left(\epsilon\sqrt{-p}\varsigma\right)}{2\sqrt{M}-\left(\sqrt{M}+3q\right)\csc^2\left(\epsilon\sqrt{-p}\varsigma\right)}\right)\right] \\ \qquad \times\left(\exp\left(\iota\left(\kappa_1 x+\nu y+\theta\frac{\Gamma(\gamma+1)}{\alpha}t^{\alpha}\right)\right)+\kappa\right), \\ \Omega_{16}(x,y,t) = c\left[\Theta \pm \frac{2\sqrt{-6Bs}}{3B}\left(\frac{12p\csc^2\left(\epsilon\sqrt{-p}\varsigma\right)}{2\sqrt{M}-\left(\sqrt{M}+3q\right)\csc^2\left(\epsilon\sqrt{-p}\varsigma\right)}\right)\right] \\ \qquad \times\left(\exp\left(\iota\left(\kappa_1 x+\nu y+\theta\frac{\Gamma(\gamma+1)}{\alpha}t^{\alpha}\right)\right)+\kappa\right),\end{cases} \tag{31}$$

• **Type 17:** For $p>0, M>0$ and $r=0$, we have

$$\begin{cases}\Psi_{17}(x,y,t) = \left[\Theta \pm \frac{2\sqrt{-6Bs}}{3B}\left(\frac{12p}{\epsilon\sqrt{M}\cosh\left(2\sqrt{p}\varsigma\right)-3q}\right)\right] \\ \qquad \times\left(\exp\left(\iota\left(\kappa_1 x+\nu y+\theta\frac{\Gamma(\gamma+1)}{\alpha}t^{\alpha}\right)\right)+\kappa\right), \\ \Phi_{17}(x,y,t) = \kappa_2\left[\Theta \pm \frac{2\sqrt{-6Bs}}{3B}\left(\frac{12p}{\epsilon\sqrt{M}\cosh\left(2\sqrt{p}\varsigma\right)-3q}\right)\right] \\ \qquad \times\left(\exp\left(\iota\left(\kappa_1 x+\nu y+\theta\frac{\Gamma(\gamma+1)}{\alpha}t^{\alpha}\right)\right)+\kappa\right), \\ \Omega_{17}(x,y,t) = c\left[\Theta \pm \frac{2\sqrt{-6Bs}}{3B}\left(\frac{12p}{\epsilon\sqrt{M}\cosh\left(2\sqrt{p}\varsigma\right)-3q}\right)\right] \\ \qquad \times\left(\exp\left(\iota\left(\kappa_1 x+\nu y+\theta\frac{\Gamma(\gamma+1)}{\alpha}t^{\alpha}\right)\right)+\kappa\right),\end{cases} \tag{32}$$

• **Type 18:** For $p<0, M>0$ and $r=0$, we have

$$\begin{cases}\Psi_{18}(x,y,t) = \left[\Theta \pm \frac{2\sqrt{-6Bs}}{3B}\left(\frac{12p}{\epsilon\sqrt{M}\cos(2\sqrt{-p}\varsigma)-3q}\right)\right] \\ \qquad \times\left(\exp\left(\iota\left(\kappa_1 x+\nu y+\theta\frac{\Gamma(\gamma+1)}{\alpha}t^{\alpha}\right)\right)+\kappa\right), \\ \Phi_{18}(x,y,t) = \kappa_2\left[\Theta \pm \frac{2\sqrt{-6Bs}}{3B}\left(\frac{12p}{\epsilon\sqrt{M}\cos(2\sqrt{-p}\varsigma)-3q}\right)\right] \\ \qquad \times\left(\exp\left(\iota\left(\kappa_1 x+\nu y+\theta\frac{\Gamma(\gamma+1)}{\alpha}t^{\alpha}\right)\right)+\kappa\right), \\ \Omega_{18}(x,y,t) = c\left[\Theta \pm \frac{2\sqrt{-6Bs}}{3B}\left(\frac{12p}{\epsilon\sqrt{M}\cos(2\sqrt{-p}\varsigma)-3q}\right)\right] \\ \qquad \times\left(\exp\left(\iota\left(\kappa_1 x+\nu y+\theta\frac{\Gamma(\gamma+1)}{\alpha}t^{\alpha}\right)\right)+\kappa\right),\end{cases} \tag{33}$$

• **Type 19:** For $p<0, M>0$ and $r=0$, we have

$$\begin{cases}\Psi_{19}(x,y,t) = \left[\Theta \pm \frac{2\sqrt{-6Bs}}{3B}\left(\frac{12p}{\epsilon\sqrt{M}\sin(2\sqrt{-p}\varsigma)-3q}\right)\right] \\ \qquad \times\left(\exp\left(\iota\left(\kappa_1 x+\nu y+\theta\frac{\Gamma(\gamma+1)}{\alpha}t^{\alpha}\right)\right)+\kappa\right), \\ \Phi_{19}(x,y,t) = \kappa_2\left[\Theta \pm \frac{2\sqrt{-6Bs}}{3B}\left(\frac{12p}{\epsilon\sqrt{M}\sin(2\sqrt{-p}\varsigma)-3q}\right)\right] \\ \qquad \times\left(\exp\left(\iota\left(\kappa_1 x+\nu y+\theta\frac{\Gamma(\gamma+1)}{\alpha}t^{\alpha}\right)\right)+\kappa\right), \\ \Omega_{19}(x,y,t) = c\left[\Theta \pm \frac{2\sqrt{-6Bs}}{3B}\left(\frac{12p}{\epsilon\sqrt{M}\sin(2\sqrt{-p}\varsigma)-3q}\right)\right] \\ \qquad \times\left(\exp\left(\iota\left(\kappa_1 x+\nu y+\theta\frac{\Gamma(\gamma+1)}{\alpha}t^{\alpha}\right)\right)+\kappa\right),\end{cases} \tag{34}$$

• **Type 20:** For $p>0, M<0$ and $r=0$, we have

$$\begin{cases}\Psi_{20}(x,y,t) = \left[\Theta \pm \frac{2\sqrt{-6Bs}}{3B}\left(\frac{12p}{\epsilon\sqrt{-M}\sinh\left(2\sqrt{p}\varsigma\right)-3q}\right)\right] \\ \qquad \times\left(\exp\left(\iota\left(\kappa_1 x+\nu y+\theta\frac{\Gamma(\gamma+1)}{\alpha}t^{\alpha}\right)\right)+\kappa\right), \\ \Phi_{20}(x,y,t) = \kappa_2\left[\Theta \pm \frac{2\sqrt{-6Bs}}{3B}\left(\frac{12p}{\epsilon\sqrt{-M}\sinh\left(2\sqrt{p}\varsigma\right)-3q}\right)\right] \\ \qquad \times\left(\exp\left(\iota\left(\kappa_1 x+\nu y+\theta\frac{\Gamma(\gamma+1)}{\alpha}t^{\alpha}\right)\right)+\kappa\right), \\ \Omega_{20}(x,y,t) = c\left[\Theta \pm \frac{2\sqrt{-6Bs}}{3B}\left(\frac{12p}{\epsilon\sqrt{-M}\sinh\left(2\sqrt{p}\varsigma\right)-3q}\right)\right] \\ \qquad \times\left(\exp\left(\iota\left(\kappa_1 x+\nu y+\theta\frac{\Gamma(\gamma+1)}{\alpha}t^{\alpha}\right)\right)+\kappa\right),\end{cases} \tag{35}$$

Dark, periodic, bright, kink, and singular solitons have been observed in the context of $\Psi_3(x,y,t)$, $\Psi_9(x,y,t)$, $\Psi_4(x,y,t)$, as well as $\Psi_5(x,y,t)$ and $\Psi_6(x,y,t)$. The outcomes acquired from the experiments are exhibited in Figs.(1)-(8).

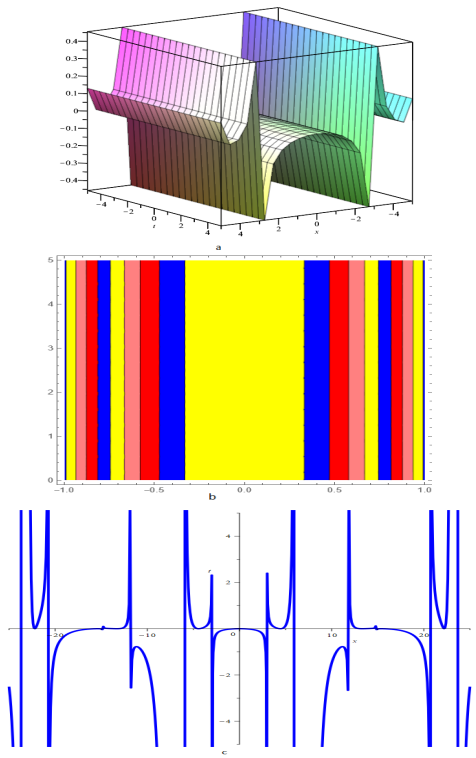

Figure 1 Figures (a),(b) and (c) represents 3D, Contour and 2D plots respectively for $\Psi_3(x,y,t)$ corresponding to the values $\kappa = 0.5$,$\epsilon = 0$,$y = 0$, $c = 1$,$\lambda = 0.4$, $\kappa_1 = 0$ and $\kappa_2 = 0$.

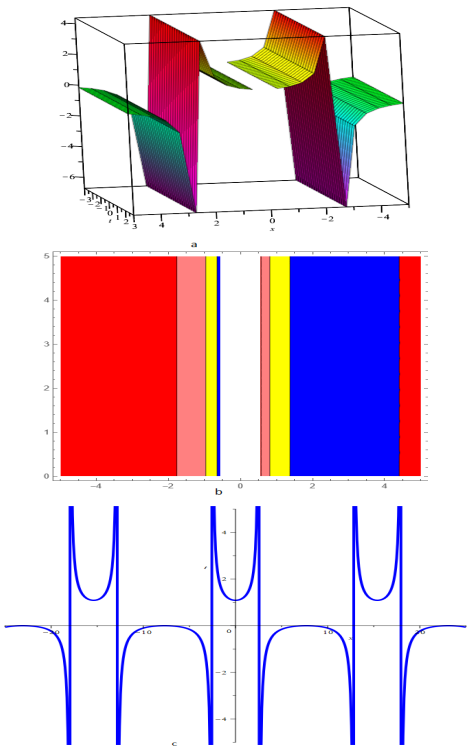

Figure 3 Figures (a),(b) and (c) represents 3D, Contour and 2D plots respectively $\Psi_4(x,y,t)$ corresponding to the values $\kappa = 0.5$,$\epsilon = 0$,$y = 0$, $c = 1$,$\lambda = 0.4$, $\kappa_1 = 0$ and $\kappa_2 = 0$

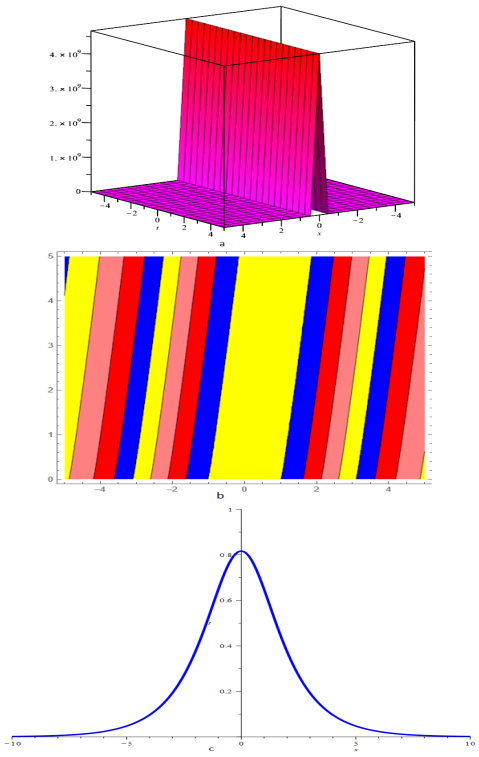

Figure 2 Figures (a),(b) and (c) represents 3D, Contour and 2D plots respectively $\Psi_9(x,y,t)$ corresponding to the values $\kappa = 0.5$,$\epsilon = 0$,$y = 0$, $c = 1$,$\lambda = 0.4$, $\kappa_1 = 0$ and $\kappa_2 = 0$.

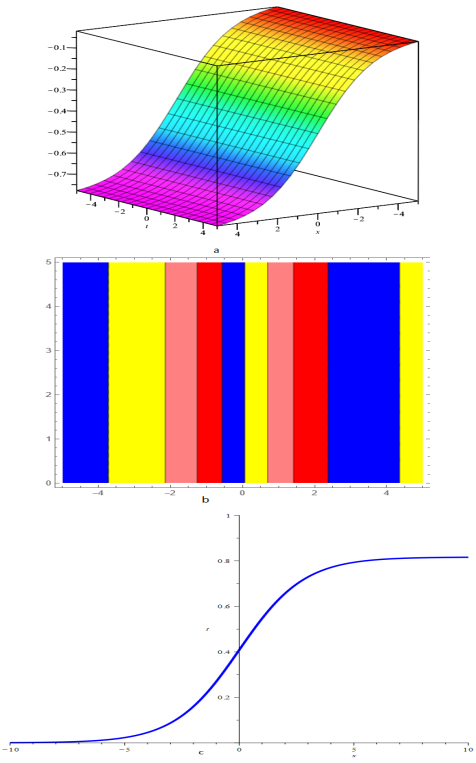

Figure 4 Figures (a),(b) and (c) represents 3D, Contour and 2D plots respectively $\Psi_5(x,y,t)$ corresponding to the values $\kappa = 0.5$,$\epsilon = 0$,$y = 0$, $c = 1$,$\lambda = 0.4$, $\kappa_1 = 0$ and $\kappa_2 = 0$

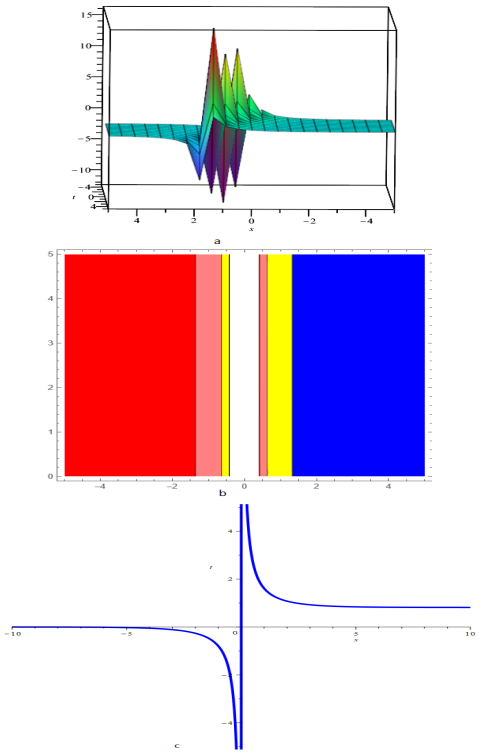

Figure 5 Figures (a),(b) and (c) represents 3D, Contour and 2D plots respectively $\Psi_6(x,y,t)$ corresponding to the values $\kappa = 0.5$,$\epsilon = 0$,$y = 0$, $c = 1$,$\lambda = 0.4$, $\kappa_1 = 0$ and $\kappa_2 = 0$

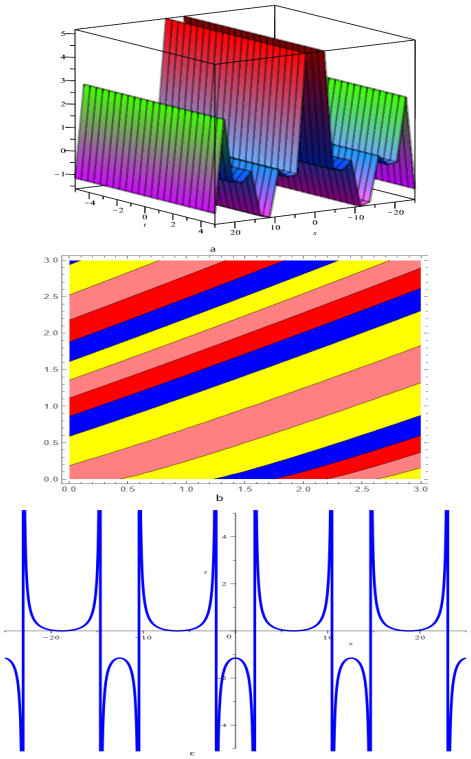

Figure 7 Figures (a),(b) and (c) represents 3D, Contour and 2D plots respectively $\Psi_4(x,y,t)$ corresponding to the values $\kappa = 0.5$,$\epsilon = 0$,$y = 0$, $c = 1$,$\lambda = 0.4$, $\kappa_1 = 0$ and $\kappa_2 = 0.5$

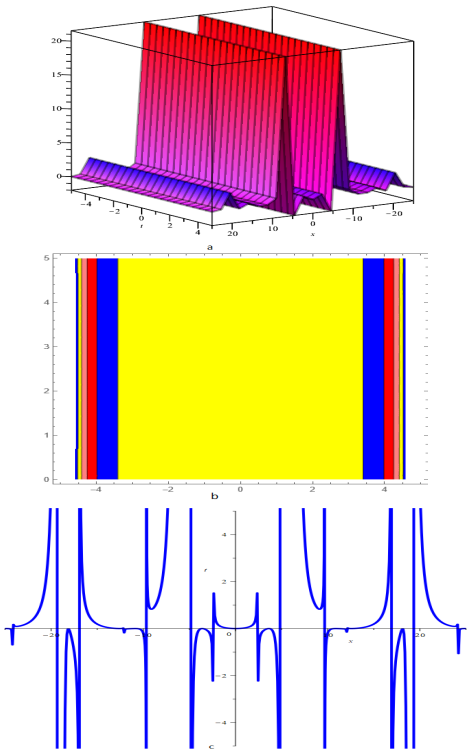

Figure 6 Figures (a),(b) and (c) represents 3D, Contour and 2D plots respectively $\Psi_3(x,y,t)$ corresponding to the values $\kappa = 0.5$,$\epsilon = 0$,$y = 0$, $c = 1$,$\lambda = 0.4$, $\kappa_1 = 0$ and $\kappa_2 = 0.5$

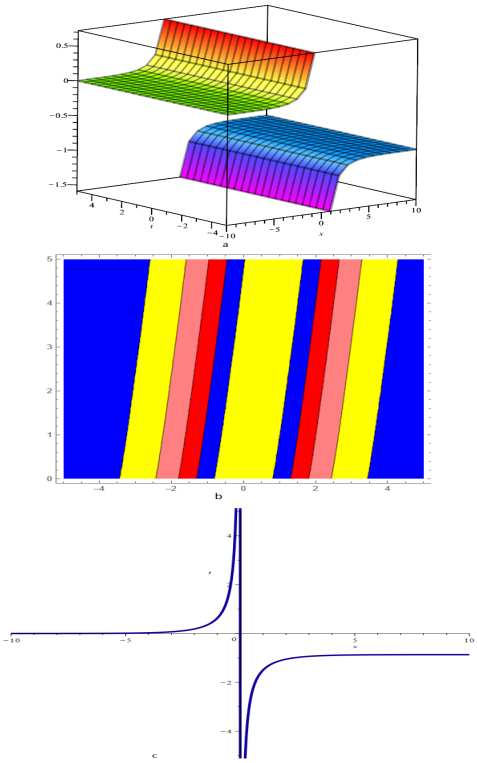

Figure 8 Figures (a),(b) and (c) represents 3D, Contour and 2D plots respectively $\Psi_6(x,y,t)$ corresponding to the values $\kappa = 0.5$,$\epsilon = 0$,$y = 0$, $c = 1$,$\lambda = 0.4$, $\kappa_1 = 0$ and $\kappa_2 = 0.5$

BIFURCATION ANALYSIS OF THE MODEL

For the sake of bifurcation analysis through phase portrait of Eq.(7), suppose that $\Psi' = \chi$ then Eq.(7) transform into the first order dynamical system of the following form:

$$\begin{cases} \frac{d\Psi}{d\zeta} = \chi, \\ \frac{d\chi}{d\zeta} = \eta_1 \Psi - \eta_2 \Psi^3, \end{cases} \tag{36}$$

where $\eta_1 = \frac{\theta+\kappa_1^2}{\lambda^2}$, and $\eta_2 = \frac{(1+\kappa_2+c)^2}{\lambda^2(2\kappa_1-1)}$. Hamiltonian function for the dynamical system (36) is defined as:

$$L(\Psi,\chi) = \frac{\chi^2}{2} - \eta_1 \frac{\Psi^2}{2} + \eta_2 \frac{\Psi^4}{4}. \tag{37}$$

The dynamical system (36) has the following equilibrium points:

$$Y_1 = (0,0), \quad Y_2 = (\sqrt{\frac{\eta_1}{\eta_2}},0), \quad Y_3 = (-\sqrt{\frac{\eta_1}{\eta_2}},0).$$

Furthermore, the Jacobian of (36) is:

$$J(\Psi,\chi) = \begin{vmatrix} 0 & 1 \\ \eta_1 - 3\eta_2\Psi^2 & 0 \end{vmatrix}$$

$$= -\eta_1 + 3\eta_2\Psi^2,$$

thus (Ψ,χ) is a saddle point for $J(\Psi,\chi) < 0$, a center for $J(\Psi,\chi) > 0$ and a cusp if $J(\Psi,\chi) = 0$.
To investigate the characteristics of the system (36), we consider the different possible cases by taking various values of parameters and observe the corresponding critical points, the following cases are observed and analysed as:

• **Case 1:** Let $\eta_1 > 0$, and $\eta_2 > 0$.
For $\theta = 0.5$, $c = 1$,$\lambda = 0.4$, $\kappa_1 = 0$ and $\kappa_2 = 0$, system (36),then critical points $Y_1 = (0,0)$, $Y_2 = (-0.57735,0)$, and $Y_3 = (0.57735,0)$. In this case, Y_1 is **saddle point** and Y_2, Y_3 are **central points**. The phase plots are displayed for different values ofλ in Fig.(9).

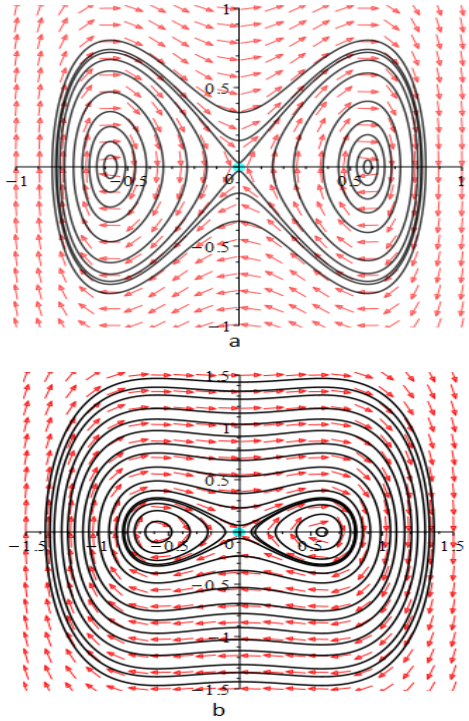

Figure 9 Phase Portarait visualization of the planar system (36) corresponding to the parameter values for Fig.(a) $\theta = 0.5$, $c = 1$,$\lambda = 0.4$, $\kappa_1 = 0$, $\kappa_2 = 0$ and Fig.(b) $\theta = 0.5$, $c = 1$,$\lambda = 0.9$, $\kappa_1 = 0$, $\kappa_2 = 0$

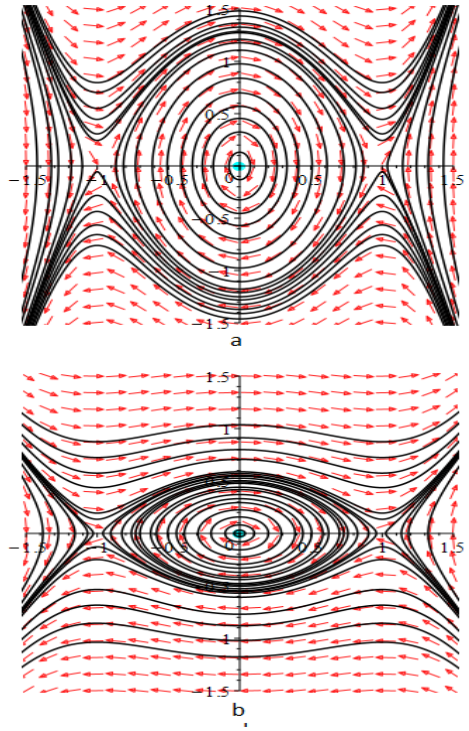

Figure 10 Phase Portarait visualization of the planar system (36) corresponding to the parameter values for Fig.(a) $\theta = -0.5$, $c = 1$,$\lambda = 0.4$, $\kappa_1 = 0$ and $\kappa_2 = 0$. and Fig.(b) $\theta = -0.5$, $c = 1$,$\lambda = 0.9$, $\kappa_1 = 0$, $\kappa_2 = 0$.

• **Case 2:** Let $\eta_1 < 0$, and $\eta_2 < 0$.
For $\theta = -0.5$, $c = 1$,$\lambda = 0.4$, $\kappa_1 = 0$ and $\kappa_2 = 0$, system (36) exhibits three fixed points $Y_1 = (0,0)$, $Y_2 = (-1,0)$, and $Y_3 = (1,0)$. In this case, Y_1 is **center** and Y_2, Y_3 are **saddle points**. Also the phase plots are displayed for different values of λ in Fig.(10).

CONCLUSION

In this study, we effectively explored a novel mapping method to complex three coupled Maccari's system to unveil novel soliton solutions. This is achieved through the utilization of M-Truncated fractional derivative with employing the new mapping method and Maple software. Our study elucidates a variety of soliton solutions.These versatile soliton classifications provide flexible tools for both modeling and simulation purposes. To the best of our understanding, this technique has been employed for the first time on this model, resulting in entirely novel solutions not previously documented in the existing literature. To facilitate comprehension, with certain solutions being visually depicted through 2-dimensional, contour, 3-dimensional plots and phase portraits depicting bifurcation characteristics that explored comprehensively its dynamical nature at equilibrium points utilizing Maple software. Fundamentally, grasping the dynamic characteristics of systems holds significant value in predicting results and propelling advancements in emerging technologies. In summary, the results of this investigation are not only intriguing but also highlight the effectiveness of the suggested methodologies in evaluating the dynamics of solitons and phase patterns across various nonlinear models.

Author's Contribution

Writing original draft, M.B.R. and A.R; Writing review and editing, Methodlogy, Conceptualization, formal analysis A.R. and M.B.R.; Software, Supervision, Funding, M.B.R.; Project administration, Visualization, Formal analysis A.J.

Acknowledgments

This article has been produced with the financial support of the European Union under the REFRESH – Research Excellence For Region Sustainability and High-tech Industries project number CZ.10.03.01/00/22_003/0000048 via the Operational Programme Just Transition.

Availability of data and material

Not applicable.

Conflicts of interest

The authors declare that there is no conflict of interest regarding the publication of this paper.

Ethical standard

The authors have no relevant financial or non-financial interests to disclose.

LITERATURE CITED

A. Filiz, M. E. and A. Sonmezoglu, 2014 F-expansion method and new exact- solution of the Schrödinger-KdV equation . Sci. World J. **2014**.

Alabedalhadi, A.-O. S.-A.-S.-M., M. and S. Alhazmi, 2023 Traveling Wave Solutions for Time-Fractional mKdV-ZK Equation of Weakly Nonlinear Ion-Acoustic Waves in Magnetized Electron–Positron Plasma . Symmetry **15**.

Das, N. and S. Saha Ray, 2022 Dispersive optical soliton wave solutions for the time-fractional perturbed nonlinear Schrödinger equation with truncated M-fractional conformable derivative in the nonlinear optical fibers. Opt. Quantum Electron **54**.

Das, N. and S. Saha Ray, 2023 Dispersive optical soliton solutions of the (2+1)-dimensional cascaded system governing by coupled nonlinear Schrödinger equation with Kerr law nonlinearity in plasma. Opt. Quantum Electron **55**.

E. M. Zayed, R. M. S. A. B. Y. Y. A. S. A., M. E. Alngar and H. M. Alshehr, 2022 Optical solitons having Kudryashovís self-phase modulation with multiplicative white noise via ItÙ Calculus using new mapping approach. Optik **264**.

Ellahi, M.-D. S., R. and U. Khan, 2018 Exact traveling wave solutions of fractional order Boussinesq-like equations by applying Exp-function method. Results in Phys **8**: 114–120.

Emad, Z.-M. S. S. M.-A. M., H.M. and A. Lanre, 2021 Exact propagation of the isolated waves model described by the three coupled nonlinear Maccari's system with complex structure. . Int. J. Mod. Phys. B **35**.

Ge, Z.-M. and C.-Y. Ou, 2008 Chaos synchronization of fractional order modified Duffing systems with parameters excited by a chaotic signal. Chaos Solitons Fractals **35**: 705–717.

Khater, B. N. K., M.M.A. Ghanbari and D. Kumar, 2020 Novel exact solutions of the fractional Bogoyavlensky–Konopelchenko equation involving the Atangana-Baleanu-Riemann derivative. Alex. Eng. J. **59**: 2957–2967.

Mohammed, E.-M. M. M. A.-A. E. B. M., W.W. and A. Abouelregal, 2023 Effects of M-Truncated Derivative and Multiplicative Noise on the Exact Solutions of the Breaking Soliton Equation. . Symmetry **15**.

Naeem, R.-H. K. A. S.-R., M. and S. Zaland, 2022 Analysis of the fuzzy fractional-order solitary wave solutions for the KdV equation in the sense of Caputo-Fabrizio derivative. . J. Math. **2022**: 2957–2967.

Rafiq, M.-A. I. M., M.N. and M. Kamran, 2022 New traveling wave solutions for space-time fractional modified equal width equation with beta derivative. Phys. Lett. A **446**: 411–425.

Saha Ray, S. and N. Das, 2022 Novel optical soliton solutions for time-fractional resonant nonlinear Schrödinger equation in optical fiber. . Mod.Phys. Lett. B **36**.

Senol, M., 2020 New analytical solutions of fractional symmetric regularized-long-wave equation. Rev. Mex. Fís. **66**: 297–307.

Vanterler, D. C. E. O.-D., J.; Sousa, 2018 A new truncated M-fractional derivative type unifying some fractional derivative types with classical properties. Int. J. Anal. Appl **16**: 83–96.

W. B. Rabie, H. M. A. and W. Hamdy, 2023 Exploration of new optical solitons in magnetooptical waveguide with coupled system of nonlinear BiswasñMilovic equation via Kudryashovís law using extended F-expansion method. . Mathematics **11**.

Wang, S. C.-Q. L.-X.-Q., Y.-Y. and J.-G. Li, 2018 Nonautonomous solitons for an extended forced Korteweg-de Vries equation with variable coefficients in the fluid or plasma. Waves Random Complex Media **3**: 411–425.

X. Zeng, X. Y., 2008 A new mapping method and its applications

to nonlinear partial differential equations. Phys. Lett. A **372**: 6602–6607.
Zaslavsky, G., 2002 Chaos, fractional kinetics, and anomalous transport. Phys. Rep. **371**: 461–580.
Zayed, E. M. and K. A. AlurrÖ, 2017 Solitons and other solutions for two nonlinear Schrödinger equations using the new mapping method. Optik **11**: 132–148.
Zayed, E. M. E. and K. A. E. AlurrÖ, 2015 A new Jacobi elliptic function expansion method for solving a nonlinear PDE describing the nonlinear low-pass electrical lines, Chaos, Solitons and Fractals. . Mathematics **78**: 148–155.
Zheng, B. and Q. Feng, 2014 The Jacobi elliptic equation method for solving fractional partial di§erential equations . Abs. Appl. Anal. **2014**.
Zhu, L. Z. X.-Y., W. and M. Gao, 2023 Bifurcations and the Exact Solutions of the Time-Space Fractional Complex Ginzburg-Landau Equation with Parabolic Law Nonlinearity. Fractal Fract. **7**.

How to cite this article: Riaz, M. B., Rehman, A. U., and Martinovic, J. Application of the New Mapping Method to Complex Three Coupled Maccari's System Possessing M-Fractional Derivative. *Chaos Theory and Applications*, 6(3), 180-191, 2024.

CHAOS
Theory and Applications
in Applied Sciences and Engineering

e-ISSN: 2687-4539
RESEARCH ARTICLE
Vol.6 / No.3 / 2024 / pp.192-204
https://doi.org/10.51537/chaos.1300754

Chaotic Dynamics of the Fractional Order Predator-Prey Model Incorporating Gompertz Growth on Prey with Ivlev Functional Response

Md. Jasim Uddin *,[1], **P. K. Santra** α,[2], **Sarker Md. Sohel Rana** *,[3] **and G. S. Mahapatra** §,[4]

*Department of Mathematics, University of Dhaka, Dhaka-1000, Bangladesh, αAbada Nsup School, Abada, Sankrail-711313, Howrah, India, §Department of Mathematics, National Institute of Technology Puducherry, Karaikal-609609, India.

ABSTRACT This paper examines dynamic behaviours of a two-species discrete fractional order predator-prey system with functional response form of Ivlev along with Gompertz growth of prey population. A discretization scheme is first applied to get Caputo fractional differential system for the prey-predator model. This study identifies certain conditions for the local asymptotic stability at the fixed points of the proposed prey-predator model. The existence and direction of the period-doubling bifurcation, Neimark-Sacker bifurcation, and Control Chaos are examined for the discrete-time domain. As the bifurcation parameter increases, the system displays chaotic behaviour. For various model parameters, bifurcation diagrams, phase portraits, and time graphs are obtained. Theoretical predictions and long-term chaotic behaviour are supported by numerical simulations across a wide variety of parameters. This article aims to offer an OGY and state feedback strategy that can stabilize chaotic orbits at a precarious equilibrium point.

KEYWORDS
Prey-predator model
Fractional order
Bifurcations
Maximum Lyapunov Exponents
Fractal dimensions
Chaos control

INTRODUCTION

In the ecology, predation and prey behaviors are frequent occurrences. Since Volterra and Lotka developed the predator-prey paradigm in the 20th century, several academics have expressed worry about it. Numerous researchers have made significant adjustments to the system by including ecological elements such functional responses, emigration and immigration (Kangalgil and Işık 2022), time delays (Li *et al.* 2022b), diffusion (Sun *et al.* 2022), and the Allee effect (Zhao and Du 2016) because this system has disregarded many real-world scenarios. The study of the intricate dynamical behaviors of predator-prey systems has recently attracted growing interest (Atabaigi 2020; Din 2017; Işık 2019; Kartal 2014, 2017). In any prey-predator encounter, the functional response in population dynamics is a key component as it refers to the quantity of prey consumed by a predator based on the density of the prey in per unit of time. The Holling type II Holling (1965) is suitable for the majority of arthropod predators as the functional response compare to others form Holling type I, III, IV. In the first quadratic, these functional responses are uniformly bounded functions in addition to being monotonically increasing. Ivlev Ivlev (1961) proposed a different functional response, known as the Ivlev functional response, to study the dynamical interaction between prey and predator species: $p(x) = b(1 - e^{-ax})y$, where the maximal rate of predation and the decline in hunting drive are represented by the positive constants b and a, respectively.

Numerous studies have been done to examine the predator-prey relationship with Ivlev-type functional responses. The findings suggested that Ivlev-type relation between the species have several systems in ecological applications, including dynamics in predator-prey systems (Cheng *et al.* 1982; Guo *et al.* 2013; Kooij and Zegeling 1996; Wang *et al.* 2010), host-parasite systems (Preedy *et al.* 2007), and animal coat patterns (Uriu and Iwasa 2007). The authors investigated the presence and uniqueness of limit cycles as well as the numerical calculation of phase portraits in these empirical studies. In a predator-prey system (Wei *et al.* 2023), this work examines the dynamical balance and Markov-switching-induced stochastic P-bifurcation.A theoretical foundation for comprehending the spatiotemporal evolution characteristics of plant systems is provided by the findings presented in (Li *et al.* 2022b; Sun *et al.* 2022).

Manuscript received: 22 May 2023,
Revised: 25 February 2024,
Accepted: 5 April 2024.

[1]jasimu00@gmail.com
[2]prasunsantra5@gmail.com (**Corresponding author**)
[3]srana.mthdu@gmail.com
[4]gs.mahapatra@nitpy.ac.in

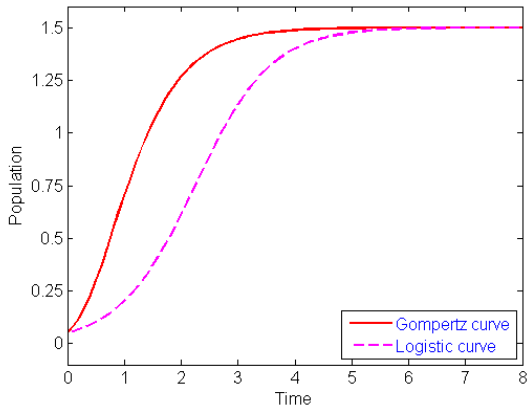

(a)

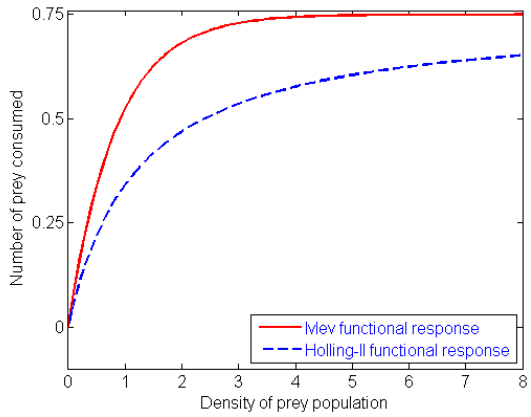

(b)

Figure 1 (a) Growth curves (b) Functional responses for $r = 1.5, k = 1.5, a = 1.2, d = 0.4$

When a third party distracts their predators, prey can lessen the burden of exploitation, such type prey-predator model is discussed in (Revilla and Křivan 2022). On the basis of the generalized Klausmeier-Gray-Scott model, authors Li *et al.* (2022a) build an extended vegetation-water model with infiltration delay and discuss dynamic behavior of this model. The long-term coevolution of the giving-up rates of the model of reckless prey and patient predator is studied by Cecilia B. et al. in (Berardo and Geritz 2021) using adaptive dynamics. The majority of predator-prey systems with various functional responses take into account the logistic growth of the prey, according to academics.

Gompertz (1825) created a different prey birth rate interpretation similar to logistic growth to study the dynamics of a community made up of populations of several interacting species. The comparison of functional responses and growth curves are shown in Figure 1. The Gompertz curve expands more rapidly than the logistic curve, we discover. Moreover, the point of inflection for the Gompertz curve occurs earlier than for the logistic curve, and thus reaches carrying capacity a little bit early. Also, compared to the Holling type II functional response, the predation rate reaches its peak significantly earlier in the Ivlev-type functional response. In terms of biology, this suggests that the predation rate is proportionate to the prey population while the prey population is low and saturates to a constant 1 when the prey population is high.

The concept of Gompertz growth on prey will be taken into consideration with accounting of Ivlev functional response for the formulation of the following predator-prey system (Rosenzweig 1971):

$$\begin{aligned} \dot{x} &= rx \ln \frac{k}{x} - (1 - e^{-ax})y, \\ \dot{y} &= (1 - e^{-ax})y - dy. \end{aligned} \tag{1}$$

Here, prey and predator population densities are represented by the time-dependent variables $x(t)$ and $y(t)$, respectively. The carrying capacity is described by the parameter k. The value r represents the growth rate of the prey and the death rate of the predator is represented by the constant d. In this prey-predator model, it is presumed that all variables and parameters are non-negative real numbers.

Fractional calculus is the additional idea used in the creation of our model. Fractional-order differential equations (FD) (Kilbas *et al.* 1993; Connolly 2004; Dzieliński *et al.* 2010) are the most widely used because of their similarities to memory-based systems, which are present in most biological systems (Elsadany and Matouk 2015). In many disciplines, including science, engineering, finance, economics, and epidemiology (Huang *et al.* 2017a, 2018, 2017b; M. *et al.* 2011), fractional-order differential equations can be successfully explained. The description of phenomena that integer order differential equations (IDEs) can't fully simulate can be done using fractional differential equations (Ichise *et al.* 1971).

A nonlinear fractional differential system exhibits the complicated dynamics like a nonlinear differential system does in bifurcation and chaos analysis. It is fascinating to study chaos in fractional-order dynamical systems (Elsadany and Matouk 2015; Abdelaziz *et al.* 2018; Ahmad and Sprott 2003). There are various methods for applying the differentiation notion to arbitrary order. The frequently employed definitions are those proposed by Caputo, Riemann-Liouville, and Grünwald-Letnikov (Podlubny 1999). Academics are interested in a variety of discrete models and demonstrating dynamics of those systems through various bifurcations and chaotic attractors (Khan *et al.* 2022; Rana and Kulsum 2017; Rana 2019). Mathematical quantification of these events is possible.

In this work, we employ the Caputo fractional derivatives on the continuous system (1) to theoretically explain the bifurcation occurrences. Fractional derivatives are defined in many ways. Among the most well-known definitions of fractional derivatives is Caputo's (Čermák *et al.* 2015; Abdeljawad 2011), which is widely applied in practical contexts.

Consider

$$D^{\alpha} g(t) = K^{l-\alpha} g^{(l)}(t), \quad \alpha > 0$$

where g^l denotes the $l-$order derivative of $g(t)$, $l = [\alpha]$ is the rounded nearest integer value of α, and K^q is the $q-$ order operator for the Riemann-Liouville integral.

$$K^q f(t) = \frac{\int_0^t (t - \tau_e)^{q-1} f(\tau_e) d\tau_e}{\Gamma(q)}, \quad q > 0$$

where $\Gamma(.)$ is the Euler gamma function. The "α–order Caputo differential operator is expressed by D^{α}.

The following is the model (1)'s fractional order form

$$\begin{aligned} D^{\alpha} x(t) &= rx(t) \ln \frac{k}{x(t)} - (1 - e^{-ax(t)})y(t) \\ D^{\alpha} y(t) &= (1 - e^{-ax(t)})y(t) - dy(t) \end{aligned} \tag{2}$$

There are many methods for converting the model (1) into discrete form. The piecewise constant approximation (PCA) (Uddin *et al*. 2023) is one among them. The model is discretized using PCA method. Here are the steps:

Assume that model (2) initial conditions are $x(0) = x_0, y(0) = y_0$. The discretized version of model (2) is given as:

$$\begin{aligned} D^{\alpha}x(t) &= rx([\frac{t}{\rho}])\ln\frac{k}{x([\frac{t}{\rho}])} - (1-e^{-ax([\frac{t}{\rho}])})y([\frac{t}{\rho}]) \\ D^{\alpha}y(t) &= (1-e^{-ax([\frac{t}{\rho}])})y([\frac{t}{\rho}]) - dy([\frac{t}{\rho}]) \end{aligned}$$

Initially consider $t \in [0,\rho)$, so $\frac{t}{\rho} \in [0,1)$. Then, we get

$$\begin{aligned} D^{\alpha}x(t) &= rx_0\ln\frac{k}{x_0} - (1-e^{-ax_0})y_0 \\ D^{\alpha}y(t) &= (1-e^{-ax_0})y_0 - dy_0 \end{aligned} \tag{3}$$

The solution of (3) can be written as

$$\begin{aligned} x_1(t) &= x_0 + J^{\alpha}\left(rx_0\ln\frac{k}{x_0} - (1-e^{-ax_0})y_0\right) \\ &= x_0 + \frac{t^{\alpha}}{\alpha\Gamma(\alpha)}\left(rx_0\ln\frac{k}{x_0} - (1-e^{-ax_0})y_0\right), \\ y_1(t) &= y_0 + J^{\alpha}\left((1-e^{-ax_0})y_0 - dy_0\right) \\ &= y_0 + \frac{t^{\alpha}}{\alpha\Gamma(\alpha)}\left((1-e^{-ax_0})y_0 - dy_0\right). \end{aligned}$$

Then consider $t \in [\rho,2\rho)$, so $\frac{t}{\rho} \in [1,2)$. Then

$$\begin{aligned} D^{\alpha}x(t) &= rx_1\ln\frac{k}{x_1} - (1-e^{-ax_1})y_1 \\ D^{\alpha}y(t) &= (1-e^{-ax_1})y_1 - dy_1 \end{aligned} \tag{4}$$

which have the following solution

$$\begin{aligned} x_2(t) &= x_1(\rho) + J^{\alpha}_{\rho}\left(rx_1\ln\frac{k}{x_1} - (1-e^{-ax_1})y_1\right) \\ &= x_1(\rho) + \frac{(t-\rho)^{\alpha}}{\alpha\Gamma(\alpha)}\left(rx_1\ln\frac{k}{x_1} - (1-e^{-ax_1})y_1\right), \\ y_2(t) &= y_1(\rho) + J^{\alpha}_{\rho}\left((1-e^{-ax_1})y_1 - dy_1\right) \\ &= y_1(\rho) + \frac{(t-\rho)^{\alpha}}{\alpha\Gamma(\alpha)}\left((1-e^{-ax_1})y_1 - dy_1\right), \end{aligned} \tag{5}$$

where $J^{\alpha}_{\rho} \equiv \frac{1}{\Gamma(\alpha)}\int_{\rho}^{t}(t-\tau_e)^{\alpha-1}d\tau_e, \quad \alpha > 0$. After repeating n times, we get

$$\begin{aligned} x_{n+1}(t) &= x_n(n\rho) + \frac{(t-n\rho)^{\alpha}}{\alpha\Gamma(\alpha)}\left(rx_n(n\rho)\ln\frac{k}{x_n(n\rho)}\right. \\ &\left.-(1-e^{-ax_n(n\rho)})y_n(n\rho)\right), \\ y_{n+1}(t) &= y_n(n\rho) + \frac{(t-n\rho)^{\alpha}}{\alpha\Gamma(\alpha)}\left((1-e^{-ax_n(n\rho)})y_n(n\rho) - dy_n(n\rho)\right), \end{aligned} \tag{6}$$

where $t \in [n\rho,(n+1)\rho)$. For $t \longrightarrow (n+1)\rho$, model (6) becomes

$$\begin{aligned} x_{n+1} &= x_n + \frac{\rho^{\alpha}}{\Gamma(\alpha+1)}\left(rx_n\ln\frac{k}{x_n} - (1-e^{-ax_n})y_n\right), \\ y_{n+1} &= y_n + \frac{\rho^{\alpha}}{\Gamma(\alpha+1)}\left((1-e^{-ax_n})y_n - dy_n\right). \end{aligned} \tag{7}$$

In this context, ρ represents the step size, while α represents the fractional order. Both parameter values are selected from the interval $(0,1]$. The remaining parameters have the same range and meaning as defined in equation (1). The Fractional Order Predator-Prey Model incorporating Gompertz growth on prey with Ivlev functional response is a mathematical model designed to capture the dynamics of predator-prey interactions in a more nuanced and realistic way. Let's break down the components and motivations behind this model:

Fractional Order Dynamics: Traditional predator-prey models often use ordinary differential equations (ODEs) with integer-order derivatives. However, fractional calculus allows for the consideration of non-integer order derivatives, offering a more flexible and accurate representation of complex systems. Fractional order models are particularly useful in capturing long-term memory effects and non-local interactions, making them suitable for describing ecological systems with delayed responses.

Gompertz Growth on Prey: The Gompertz growth model is commonly used to describe the growth of biological populations, where the growth rate decreases exponentially over time. Incorporating Gompertz growth in the prey population allows the model to account for the realistic limitation on prey population growth as it reaches carrying capacity. This is especially relevant in ecological systems where resources are finite.

Ivlev Functional Response: Motivation: The functional response describes how the feeding rate of predators changes with the abundance of prey. The Ivlev functional response is one of the many functional response forms, and it considers the saturation of a predator's feeding rate as prey abundance increases. This is crucial for capturing realistic predator-prey interactions, where a predator's feeding rate is not constant but saturates as prey becomes more abundant.

Integration of Components: Motivation: By combining fractional order dynamics, Gompertz growth on prey, and the Ivlev functional response, the model aims to provide a more comprehensive representation of the complex and dynamic nature of predator-prey interactions. This integration allows for a more realistic portrayal of ecological systems by accounting for memory effects, finite resources, and the nonlinear nature of predation.

In summary, the motivation behind the Fractional Order Predator-Prey Model incorporating Gompertz growth on prey with Ivlev functional response lies in the desire to create a more accurate and nuanced mathematical representation of ecological systems. By considering fractional order dynamics, realistic prey growth dynamics, and a biologically relevant functional response, the model aims to improve our understanding of the intricate interplay between predators and prey in natural ecosystems.

While there may not be specific studies or examples explicitly using the exact combination of a Fractional Order Predator-Prey Model with Gompertz growth on prey and Ivlev functional response, you can envision scenarios where such a model might find application. Here are two hypothetical examples:

Fisheries Management: Consider a marine ecosystem where a specific fish species (predator) preys on a population of smaller fish (prey). The fractional order dynamics help account for historical fishing pressures and the impact of environmental changes on the predator-prey relationship. The Gompertz growth model is applied to the prey population, considering resource limitations and environmental factors. The Ivlev functional response reflects the saturation of the predator's feeding rate as the prey becomes more abundant.

Fisheries managers could use this model to predict the effects of fishing quotas, environmental changes, or other interventions on the stability and sustainability of the fishery. It provides a more nuanced understanding of the dynamics involved, aiding in the development of effective management strategies.

Agricultural Pest Control: In an agricultural setting, consider a scenario where a certain insect species (prey) is damaging crops, and a predator species (such as a bird or insect) is introduced for pest control. The fractional order dynamics capture the long-term impact of past pest control measures on predator-prey interactions. The Gompertz growth model represents the natural growth constraints of the pest population due to resource limitations. The Ivlev functional response reflects the saturation in the predator's consumption rate as the pest population increases.

Farmers and pest control agencies could use this model to optimize the introduction of natural predators for pest management. By understanding how past interventions, environmental factors, and prey-predator interactions interact, they can implement more targeted and sustainable pest control strategies.

These examples illustrate how the combination of fractional order dynamics, Gompertz growth on prey, and Ivlev functional response could be applied in different ecological and management contexts to gain insights and inform decision-making.

The remaining sections are arranged as follows. The presence and stability of fixed points are discussed in Section 2. The conditions for codimension-one bifurcations are established such as Neimark-Sacker and period-doubling bifurcations in Section 3. Section 4 presents the prerequisites for Marottos chaos to exist. The results of numerical simulations are presented in Section 5 to demonstrate new and rich dynamic behavior to validate the theoretical analysis. In Section 6, we employ the OGY (Edward *et al.* (1990)) and state feedback control strategies to reduce the chaos of the unmanaged system. Finally, Section 7 provides a conclusion to this article.

EXISTENCE CONDITIONS AND FIXED POINT'S STABILITY ANALYSIS

Existence of Fixed points

A quick algebraic calculation reveals that the proposed system (7) has two fixed points for any value of the permitted parameters:

(i) The fixed point of the boundary $E_1(k,0)$. According to biology, when there are no predators, the population of prey achieves its carrying limit k.

(ii) If $0 < d < 1$, then the unique coexistence fixed point $E_2(x^*,y^*)$ exists, where $x^* = -\frac{1}{a}\ln[1-d], y^* = -\frac{r\ln[1-d]\ln[-\frac{ak}{\ln[1-d]}]}{ad}$.

Analysis of local stability for fixed points

At fixed points obtained in section 2.1, we examine the system's stability of the system (7). The magnitude of the eigenvalues calculated at the fixed point $E(x^*,y^*)$, it should be noted that estimated eigenvalues affect the fixed point's local stability.

Then

$$J(x^*,y^*) = \begin{pmatrix} \tilde{j_{11}} & \tilde{j_{12}} \\ \tilde{j_{21}} & \tilde{j_{22}} \end{pmatrix} \tag{8}$$

where

$$\tilde{j_{11}} = 1 - \left(r + ay^*e^{-ax^*} - r\ln[\frac{k}{x^*}]\right)\frac{\rho^\alpha}{\Gamma(\alpha+1)},$$
$$\tilde{j_{12}} = \left(-1 + e^{-ax^*}\right)\frac{\rho^\alpha}{\Gamma(\alpha+1)},$$
$$\tilde{j_{21}} = ay^*e^{-ax^*}\frac{\rho^\alpha}{\Gamma(\alpha+1)},$$
$$\tilde{j_{22}} = 1 + \left(1 - d - e^{-ax^*}\right)\frac{\rho^\alpha}{\Gamma(\alpha+1)}.$$

The Jacobian Matrix's characteristic polynomial can be expressed as follows:

$$F(\lambda) := \lambda^2 + \widehat{p_{ee}}(x,y)\lambda + \widehat{q_{ee}}(x,y) = 0 \tag{9}$$

where $\widehat{p_{ee}}(x,y) = -(\tilde{j_{11}} + \tilde{j_{22}})$ and $\widehat{q_{ee}}(x,y) = \tilde{j_{11}}\tilde{j_{22}} - \tilde{j_{12}}\tilde{j_{21}}$. The following stability conditions of fixed points are stated based on the concept of the Jury's criterion.

The Jacobian matrix (8) at $E_1(k,0)$ can be found as

$$J(E_1) = \begin{pmatrix} 1 - r\frac{\rho^\alpha}{\Gamma(\alpha+1)} & (-1+e^{-ak})\frac{\rho^\alpha}{\Gamma(\alpha+1)} \\ 0 & 1 + \left(1 - d - e^{-ak}\right)\frac{\rho^\alpha}{\Gamma(\alpha+1)} \end{pmatrix} \tag{10}$$

The eigenvalues are $\lambda_1 = 1 - r\frac{\rho^\alpha}{\Gamma(\alpha+1)}$ and $\lambda_2 = 1 + \left(1 - d - e^{-ak}\right)\frac{\rho^\alpha}{\Gamma(\alpha+1)}$

The following topological categorization is valid for the predator-free equilibrium point $E_1(k,0)$:

(a) if $d > (1 - e^{-ak})$ then $E_1(k,0)$ is
- sink if $0 < \rho < min\{\left(\frac{2}{r}\Gamma(1+\alpha)\right)^{\frac{1}{\alpha}}, \left(\frac{2}{d-(1-e^{-ak})}\Gamma(1+\alpha)\right)^{\frac{1}{\alpha}}\}$
- source if $\rho > max\{\left(\frac{2}{r}\Gamma(1+\alpha)\right)^{\frac{1}{\alpha}}, \left(\frac{2}{d-(1-e^{-ak})}\Gamma(1+\alpha)\right)^{\frac{1}{\alpha}}\}$
- non-hyperbolic if $\rho = \left(\frac{2}{r}\Gamma(1+\alpha)\right)^{\frac{1}{\alpha}}$ or $\rho = \left(\frac{2}{d-(1-e^{-ak})}\Gamma(1+\alpha)\right)^{\frac{1}{\alpha}}$

(b) if $d < (1 - e^{-ak})$ then the fixed point $E_1(k,0)$ is
- source if $\rho > \left(\frac{2}{r}\Gamma(1+\alpha)\right)^{\frac{1}{\alpha}}$
- saddle if $\rho < \left(\frac{2}{r}\Gamma(1+\alpha)\right)^{\frac{1}{\alpha}}$
- non-hyperbolic if $\rho = \left(\frac{2}{r}\Gamma(1+\alpha)\right)^{\frac{1}{\alpha}}$

(c) if $d = (1 - e^{-ak})$ then the fixed point $E_1(k,0)$ is non-hyperbolic

Naturally, one of the eigenvalues of the above mentioned jacobian matrix is -1, and the remaining eigenvalues are different from ± 1 when $\rho = \left(\frac{2}{r}\Gamma(1+\alpha)\right)^{\frac{1}{\alpha}}$ or $\rho = \left(\frac{2}{d-(1-e^{-ak})}\Gamma(1+\alpha)\right)^{\frac{1}{\alpha}}$.

Therefore, if parameters change in a limited area around $\widehat{PDF}^1_{E_1}$ or $\widehat{PDF}^2_{E_1}$, a flip bifurcation may happen.

$$\widehat{PDF}^1_{E_1} = \{(r,a,k,d,\rho,\alpha) \in (0,+\infty) : \rho = \left(\frac{2}{r}\Gamma(1+\alpha)\right)^{\frac{1}{\alpha}},$$
$$\rho \neq \left(\frac{2\Gamma(1+\alpha)}{d-(1-e^{-ak})}\right)^{\frac{1}{\alpha}}, d > (1 - e^{-ak})\}$$

or

$$\widehat{PDF}^2_{E_1} = \{(r,a,k,d,\rho,\alpha) \in (0,+\infty) : \rho = \left(\frac{2\Gamma(1+\alpha)}{d-(1-e^{-ak})}\right)^{\frac{1}{\alpha}},$$

$$\rho \neq \left(\tfrac{2}{r}\Gamma(1+\alpha)\right)^{\frac{1}{\alpha}}, d > (1-e^{-ak})\}$$

At $E_2(x^*,y^*)$, the characteristic equation can be written as

$$F_e(\lambda) := \lambda^2 - (2+\tilde{M}_a\tilde{\mu_e})\lambda + (1+\tilde{M}_a\tilde{\mu_e} + \tilde{N}_a\tilde{\mu_e}^2) = 0 \qquad (11)$$

where

$$\tilde{\mu_e} = \frac{\rho^\alpha}{\Gamma(\alpha+1)}$$

$$\tilde{M}_a = e^{-ax^*}\left(-1-e^{ax^*}(-1+d+r)-ay^*\right) + r\ln[\frac{k}{r}]$$

$$\tilde{N}_a = e^{-ax^*}\left(r-e^{ax^*}r(1-d)+ady^*-(1+(-1+d)e^{ax^*})r\ln[\frac{k}{x}]\right)$$

So $F_e(1) = \tilde{M}_a\tilde{\mu_e}^2 > 0$ and $F_e(-1) = 4+2\tilde{M}_a\tilde{\mu_e}+\tilde{N}_a\tilde{\mu_a}^2$. Regarding the stability criterion of E_2, we state the following lemma.

The fixed point E_2 with any arbitrary selection of parameter values is a

(i) source if

$(i.i)$ $\tilde{M_a}^2 - 4\tilde{N_a} \geq 0$ and $\tilde{\mu_e} > \frac{-\tilde{M_a}+\sqrt{\tilde{N_a}^2-4\tilde{N_a}}}{\tilde{N_a}}$

$(i.ii)$ $\tilde{M_a}^2 - 4\tilde{N_a} < 0$ and $\tilde{\mu_e} > \frac{-\tilde{M_a}}{\tilde{N_a}}$

(ii) sink if

$(ii.i)$ $\tilde{M_a}^2 - 4\tilde{N_a} \geq 0$ and $\tilde{\mu_e} < \frac{-\tilde{M_a}-\sqrt{\tilde{N_a}^2-4\tilde{N_a}}}{\tilde{N_a}}$

$(ii.ii)$ $\tilde{M_a}^2 - 4\tilde{N_a} < 0$ and $\tilde{\mu_e} < \frac{-\tilde{M_a}}{\tilde{N_a}}$

(iii) non-hyperbolic if

$(iii.i)$ $\tilde{M_a}^2 - 4\tilde{N_a} \geq 0$ and $\tilde{\mu_e} = \frac{-\tilde{M_a}\pm\sqrt{\tilde{M_a}^2-4\tilde{N_a}}}{\tilde{N_a}}; \tilde{\mu_e} \neq \frac{-2}{\tilde{M_a}}, \frac{-4}{\tilde{M_a}}$

$(iii.ii)$ $\tilde{M_a}^2 - 4\tilde{N_a} < 0$ and $\tilde{\mu_e} = \frac{-4}{\tilde{M_a}}$.

(iv) saddle if otherwise

Let,

$$\widehat{PD}_{E_2} = \left\{(r,a,k,d,\rho,\alpha) : \rho = \left(\frac{-\tilde{M_a}\pm\sqrt{\tilde{M_a}^2-4\tilde{N_a}}}{\tilde{N_a}}\Gamma(1+\alpha)\right)^{\frac{1}{\alpha}} = \rho_\pm,\right\}$$

with $\tilde{M_a}^2 - 4\tilde{N_a} \geq 0, \tilde{\mu_e} \neq \frac{-2}{\tilde{M_a}}, \frac{-4}{\tilde{M_a}}$

The system (7) at E_2 undergoes a flip bifurcation, when the parameters (r,a,k,d,ρ,α) fluctuate within a narrow region of $\widehat{PD}_{E_2}$.

Also, let

$$\widehat{NS}_{E_2} = \left\{(r,a,k,d,\rho,\alpha) : \rho = \left(\Gamma(1+\alpha)\frac{-\tilde{M_a}}{\tilde{N_a}}\right)^{\frac{1}{\alpha}} = \rho_{NS}, \tilde{M_a}^2 - 4\tilde{N_a} < 0\right\}$$

If the parameters (r,a,k,d,ρ,α) vary around the set $\widehat{NS}_{E_2}$, system (7) will suffer an NS bifurcation at that point.

BIFURCATION ANALYSIS

This section introduces to investigate the Neimark–Sacker (NS) bifurcation and Period-Doubling (PD) bifurcation at the equilibrium point $E_2(x^*,y^*)$ of the system taking ρ as the parameter of bifurcation for this study.

Neimark–Sacker bifurcation

For the formulated predator-prey system (7) in discrete fractional, the bifurcation analysis of the research of Gompertz growth on prey with exposure to Ivlev functional response has been conducted through the NS bifurcation. For the parameters that fall under the following set:

$$\widehat{NS}_{E_2} = \left\{(r,a,k,d,\rho,\alpha) : \rho = \left(\Gamma(1+\alpha)\frac{A_{1e}}{A_{2e}}\right) = \rho_{NS}, \mathfrak{L} < 0\right\},$$

Let ρ^* is the perturbation of ρ where $|\rho^*| \lll 1$. Therefore, the model perturbation is

$$\begin{aligned} x_{n+1} &= x_n + \frac{(\rho+\rho^*)^\alpha}{\Gamma(\alpha+1)}\left(rx_n\ln\frac{k}{x_n} - (1-e^{-ax_n})y_n\right) \equiv f(x_n,y_n,\rho^*), \quad (12)\\ y_{n+1} &= y_n + \frac{(\rho+\rho^*)^\alpha}{\Gamma(\alpha+1)}\left((1-e^{-ax_n})y_n - dy_n\right) \equiv g(x_n,y_n,\rho^*). \end{aligned}$$

If $u_n = x_n - x^*, v_n = y_n - y^*$, then equilibrium is $E_2(x^*,y^*)$ becomes the origin , and by using Taylor series at $(u_n,v_n) = (0,0)$ expanding f and g to the third order, the model (12) becomes

$$\begin{aligned} u_{n+1} &= \alpha_1 u_n + \alpha_2 v_n + \alpha_{11}u_n^2 + \alpha_{12}u_nv_n + \alpha_{22}v_n^2 + \alpha_{111}u_n^3 + \quad (13)\\ &\quad \alpha_{112}u_n^2v_n + \alpha_{122}u_nv_n^2 + \alpha_{222}v_n^3 + O((|u_n|+|v_n|)^4),\\ v_{n+1} &= \beta_1 u_n + \beta_2 v_n + \beta_{11}u_n^2 + \beta_{12}u_nv_n + \beta_{22}v_n^2 + \beta_{111}u_n^3 +\\ &\quad \beta_{112}u_n^2v_n + \beta_{122}u_nv_n^2 + \beta_{222}v_n^3 + O((|u_n|+|v_n|)^4), \end{aligned}$$

where

$$\begin{aligned} \alpha_1 &= \frac{d - dr\frac{\rho^\alpha}{\Gamma(\alpha+1)} + r\frac{\rho^\alpha}{\Gamma(\alpha+1)}\left(d-(-1+d)\ln[1-d]\right)\ln\left[\frac{-ak}{\ln[1-d]}\right]}{d},\\ \alpha_2 &= -d\frac{\rho^\alpha}{\Gamma(\alpha+1)},\\ \alpha_{11} &= \frac{ar\frac{\rho^\alpha}{\Gamma(\alpha+1)}\left(d+(-1+d)\ln[1-d]^2\ln\left[\frac{-ak}{\ln[1-d]}\right]\right)}{d\ln[1-d]},\\ \alpha_{12} &= a(-1+d)\frac{\rho^\alpha}{\Gamma(\alpha+1)},\\ \alpha_{22} &= 0,\\ \alpha_{111} &= \frac{a^2r\frac{\rho^\alpha}{\Gamma(\alpha+1)}\left(1-\frac{(-1+d)\ln[1-d]^3\ln\left[\frac{-ak}{\ln[1-d]}\right]}{\ln[1-d]^2}\right)}{\ln[1-d]^2},\\ \alpha_{112} &= -a^2(-1+d)\frac{\rho^\alpha}{\Gamma(\alpha+1)},\\ \alpha_{122} &= 0,\\ \alpha_{222} &= 0,\\ \beta_1 &= \frac{(-1+d)r\frac{\rho^\alpha}{\Gamma(\alpha+1)}\ln[1-d]\ln\left[\frac{-ak}{\ln[1-d]}\right]}{d},\\ \beta_2 &= 1,\\ \beta_{11} &= -\frac{a(-1+d)r\frac{\rho^\alpha}{\Gamma(\alpha+1)}\ln[1-d]\ln\left[\frac{-ak}{\ln[1-d]}\right]}{d},\\ \beta_{22} &= 0,\\ \beta_{111} &= \frac{a^2(-1+d)r\frac{\rho^\alpha}{\Gamma(\alpha+1)}\ln[1-d]\ln\left[\frac{-ak}{\ln[1-d]}\right]}{d},\\ \beta_{112} &= a^2(-1+d)\frac{\rho^\alpha}{\Gamma(\alpha+1)},\\ \beta_{122} &= 0,\\ \beta_{222} &= 0. \end{aligned} \qquad (14)$$

The characteristic equation of the model (13) is $\lambda^2 + p(\rho^*)\lambda + q(\rho^*) = 0$,
where

$$p(\rho^*) = -\frac{d(2-r\frac{(\rho+\rho^*)^\alpha}{\Gamma(\alpha+1)})+r\frac{(\rho+\rho^*)^\alpha}{\Gamma(\alpha+1)}(d-(-1+d)\ln[1-d])\ln[\frac{-ak}{\ln[1-d]}]}{d},$$

and

$$q(\rho^*) = \frac{d(1-r\frac{(\rho+\rho^*)^\alpha}{\Gamma(\alpha+1)})+r\frac{(\rho+\rho^*)^\alpha}{\Gamma(\alpha+1)}\left(d+(-1+d)(-1+d\frac{(\rho+\rho^*)^\alpha}{\Gamma(\alpha+1)})\ln[1-d]\right)\ln[\frac{-ak}{\ln[1-d]}]}{d}.$$

The roots of the characteristic equation are $\lambda_{1,2}(\rho^*) = \frac{-p(\rho^*)\pm i\sqrt{4q(\rho^*)-(p(\rho^*))^2}}{2}$.

where

$$\begin{aligned}
&4q(\rho^*)-(p(\rho^*))^2 \\
=\ & \frac{4\left(d-dr\frac{(\rho+\rho^*)^\alpha}{\Gamma(\alpha+1)}+r\frac{(\rho+\rho^*)^\alpha}{\Gamma(\alpha+1)}\left(d+(-1+d)(-1+d\frac{(\rho+\rho^*)^\alpha}{\Gamma(\alpha+1)})\ln[1-d]\right)\ln\left[\frac{-ak}{\ln[1-d]}\right]\right)}{d} \\
-\ & \frac{\left(d(2-r\frac{(\rho+\rho^*)^\alpha}{\Gamma(\alpha+1)})+r\frac{(\rho+\rho^*)^\alpha}{\Gamma(\alpha+1)}(d-(-1+d)\ln[1-d])\ln[\frac{-ak}{\ln[1-d]}]\right)^2}{d^2}
\end{aligned}$$

For $0<d<1$, $4q(\rho^*)-(p(\rho^*))^2$ is always less than zero.

From $|\lambda_{1,2}(\rho^*)|=1$, and $\rho^*=0$, we have $|\lambda_{1,2}(\rho^*)| = [q(\rho^*)]^{\frac{1}{2}}$ and

$$l = \left[\frac{d|\lambda_{1,2}(\rho^*)|}{d\rho^*}\right]_{\rho^*=0}$$
$$= \frac{r\left(-d+(d+(-1+d)(-1+2d\frac{\rho^\alpha}{\Gamma(\alpha+1)})\ln[1-d])\ln\left[\frac{-ak}{\ln[1-d]}\right]\right)}{2d\sqrt{\frac{d-dr\frac{\rho^\alpha}{\Gamma(\alpha+1)}+r\frac{\rho^\alpha}{\Gamma(\alpha+1)}\left(d+(-1+d)(1+d\frac{\rho^\alpha}{\Gamma(\alpha+1)})\ln[1-d]\right)\ln\left[\frac{-ak}{\ln[1-d]}\right]}{d}}} \neq 0.$$

Additionally, it is necessary that when $\rho^*=0$, $\lambda_{1,2}^i \neq 1$, $i=1,2,3,4$, which is equivalent to $p(0)\neq\pm2,0,1$.

For normal form study, let $\gamma = Im(\lambda_{1,2})$ and $\delta = Re(\lambda_{1,2})$. We define $T=\begin{bmatrix}0 & 1\\ \gamma & \delta\end{bmatrix}$, and using the transformation $\begin{bmatrix}u_n\\ v_n\end{bmatrix} = T\begin{bmatrix}\overline{x}_n\\ \overline{y}_n\end{bmatrix}$, the model (13) becomes

$$\begin{aligned}
\overline{x}_{n+1} &= \delta\overline{x}_n - \gamma\overline{y}_n + f_{11}(\overline{x}_n,\overline{y}_n), \\
\overline{y}_{n+1} &= \gamma\overline{x}_n + \delta\overline{y}_n + g_{11}(\overline{x}_n,\overline{y}_n),
\end{aligned} \tag{17}$$

where the variables $(\overline{x}_n,\overline{y}_n)$ with the order at least two are denoted the terms in the model (17) by the functions f_{11} and g_{11}, respectively.

The following discriminatory amount Ω must be nonzero in order to undergo NSB:

$$\Omega = -Re\left[\frac{(1-2\overline{\lambda})\overline{\lambda}^2}{1-\lambda}\xi_{11}\xi_{20}\right] - \frac{1}{2}|\xi_{11}|^2 - |\xi_{02}|^2 + Re(\overline{\lambda}\xi_{21}),$$

where

$$\begin{aligned}
\xi_{20} &= \frac{\delta}{8}\left(2\beta_{22}-\delta\alpha_{22}-\alpha_{12}+4\gamma\alpha_{22}+i\left(4\gamma\alpha_{22}-2\alpha_{22}-2\delta\alpha_{22}\right)\right) \\
&+ \frac{\gamma}{4}\alpha_{12} + \frac{\beta_{12}}{8} + \frac{\delta\alpha_{11}-2\beta_{11}+\delta^3\alpha_{22}-\delta^2\beta_{22}-\delta^2\alpha_{12}+\delta\beta_{12}}{4\gamma}, \\
&+ i\frac{1}{8}\left(4\gamma\beta_{22}+2\gamma^2\alpha_{22}-2\alpha_{11}\right) \\
\xi_{11} &= \frac{\gamma}{2}(\beta_{22}-\delta\alpha_{22}) + i\frac{1}{2}(\gamma^2\alpha_{22}+\alpha_{11}+\delta\alpha_{12}+\delta^2\alpha_{22}) \\
&+ \frac{\beta_{11}-\delta\alpha_{11}+\delta\beta_{12}-\delta^2\alpha_{12}-2\delta^2\beta_{22}+2\delta^3\alpha_{22}}{2\gamma},
\end{aligned} \tag{15}$$

$$\begin{aligned}
\xi_{02} &= \frac{1}{4}\gamma(2\delta\alpha_{22}+\alpha_{12}+\beta_{22}) + i\frac{1}{4}(\beta_{12}+2\delta\beta_{22}-2\delta\alpha_{12}-\alpha_{11}) \\
&- \frac{\beta_{11}-\delta\alpha_{11}+\delta\beta_{12}-\delta^2\alpha_{12}+\delta^2\beta_{22}-\delta^3\alpha_{22}}{4\gamma} + \frac{1}{4}\alpha_{22}i(\gamma^2-3\delta^2),
\end{aligned}$$

$$\begin{aligned}
\xi_{21} &= \frac{3}{8}\beta_{222}(\gamma^2+\delta^2) + \frac{\beta_{112}}{8} + \frac{\delta}{4}\alpha_{112} + \frac{\delta}{4}\beta_{122} + \alpha_{122}(\frac{\gamma^2}{8}+\frac{3\delta^2}{8}-\frac{\delta}{4}) \\
&+ \frac{3}{8}\alpha_{111} + i\frac{3}{8}\alpha_{222}(\gamma^2+2\delta^2) + i\frac{3\gamma\delta}{8}\alpha_{122} - \frac{1}{8}\beta_{122}\gamma i - i\frac{3\gamma\delta}{8}\beta_{222} \\
&- i\frac{3\beta_{111}-3\delta\alpha_{111}}{8\gamma} - i\frac{3\delta\beta_{112}-3\delta^2\alpha_{112}}{8\gamma} - i\frac{3\delta^2\beta_{122}-3\delta^3\alpha_{122}}{8\gamma} \\
&- i\frac{3\delta^3\beta_{222}-3\delta^4\alpha_{222}}{8\gamma}.
\end{aligned} \tag{16}$$

The following theorem can be used to demonstrate the direction and stability of the NS bifurcation in light of the explanation above.

If $\Omega\neq0$, the system undergoes NS bifurcation at E_2 for the parameter ρ varies in neighborhood of $\widehat{NS}_{E_2}$. If $\Omega<0$ ($\Omega>0$), then there is a smooth closed invariant curve that can bifurcate from the positive fixed point E_2, and the bifurcation is sub-critical (resp. super-critical).

Period-Doubling bifurcation

The one eigenvalue is $\lambda_1 = -1$ of the positive fixed point $E_2(x^*,y^*)$, and the other one (λ_2) neither 1 nor -1, if the following set contains the model's parameters

$$\widehat{PD}_{E_2} = \left\{(r,a,k,d,\rho,\alpha) : \rho = \left(\Gamma(1+\alpha)\frac{A_{1e}\pm\sqrt{\mathfrak{L}}}{A_{2e}}\right)^{\frac{1}{\alpha}} = \rho_\pm, \mathfrak{L}\geq0\right\}.$$

Here, we address the PD bifurcation of the system at $E_2(x^*,y^*)$ when a limited fluctuation of parameters in the area of $\widehat{PD}_{E_2}$. The parameter (ρ) is utilized to analyze the NS bifurcation.

Let ρ^* ($|\rho^*| \lll 1$,) is the perturbation of ρ and taking a model perturbation like this

$$\begin{aligned}
x_{n+1} &= x_n + \frac{(\rho+\rho^*)^\alpha}{\Gamma(\alpha+1)}\left(rx_n\ln\frac{k}{x_n} - \left(1-e^{-ax_n}\right)y_n\right) \equiv f(x_n,y_n,\rho^*), \\
y_{n+1} &= y_n + \frac{(\rho+\rho^*)^\alpha}{\Gamma(\alpha+1)}\left(\left(1-e^{-ax_n}\right)y_n - dy_n\right) \equiv g(x_n,y_n,\rho^*).
\end{aligned} \tag{18}$$

If $u_n = x_n - x^*$, $v_n = y_n - y^*$, then equilibrium $E_2(x^*,y^*)$ is becomes the origin, and by using Taylor series about $(u_n,v_n)=(0,0)$ expanding to the third order of f and g, the model (18) becomes

$$\begin{aligned}
u_{n+1} &= \alpha_1u_n + \alpha_2v_n + \alpha_{11}u_n^2 + \alpha_{12}u_nv_n + \alpha_{13}u_n\rho^* + \\
&\alpha_{23}v_n\rho^* + \alpha_{111}u_n^3 + \alpha_{112}u_n^2v_n + \alpha_{113}u_n^2\rho^* + \\
&\alpha_{123}u_nv_n\rho^* + O((|u_n|+|v_n|+|\rho^*|)^4), \\
v_{n+1} &= \beta_1u_n + \beta_2v_n + \beta_{11}u_n^2 + \beta_{12}u_nv_n + \beta_{22}v_n^2 + \beta_{13}u_n\rho^* + \\
&\beta_{23}v_n\rho^* + \beta_{111}u_n^3 + \beta_{112}u_n^2v_n + \beta_{113}u_n^2\rho^* + \beta_{123}u_nv_n\rho^* + \\
&\beta_{223}v_n^2\rho^* + O((|u_n|+|v_n|+|\rho^*|)^4),
\end{aligned} \tag{19}$$

where

$$\begin{aligned}
\alpha_{13} &= -\frac{r\left(d+(-d+(-1+d)\ln[1-d])\ln\left[\frac{-ak}{\ln[1-d]}\right]\right)}{d}\frac{\alpha\rho^{\alpha-1}}{\Gamma(\alpha+1)},\\
\alpha_{23} &= -d\frac{\alpha\rho^{\alpha-1}}{\Gamma(\alpha+1)},\\
\alpha_{113} &= \frac{ar\left(d+(-1+d)\ln[1-d]^2\ln\left[\frac{-ak}{\ln[1-d]}\right]\right)}{d\ln[1-d]}\frac{\alpha\rho^{\alpha-1}}{\Gamma(\alpha+1)},\\
\alpha_{123} &= a(-1+d)\frac{\alpha\rho^{\alpha-1}}{\Gamma(\alpha+1)},\\
\beta_{13} &= \frac{(-1+d)r\ln[1-d]\ln\left[\frac{-ak}{\ln[1-d]}\right]}{d}\frac{\alpha\rho^{\alpha-1}}{\Gamma(\alpha+1)},\\
\beta_{23} &= 0,\\
\beta_{113} &= -\frac{a(-1+d)r\ln[1-d]\ln\left[\frac{-ak}{\ln[1-d]}\right]}{d}\frac{\alpha\rho^{\alpha-1}}{\Gamma(\alpha+1)},\\
\beta_{123} &= a(1-d)\frac{\alpha\rho^{\alpha-1}}{\Gamma(\alpha+1)},\\
\beta_{223} &= 0.
\end{aligned} \tag{20}$$

We define $T=\begin{bmatrix}\alpha_2 & \alpha_2\\ -1-\alpha_1 & \lambda_2-\alpha_1\end{bmatrix}$ which is invertible. Now, applying the transformation $\begin{bmatrix}u_n\\ v_n\end{bmatrix}=T\begin{bmatrix}\overline{x}_n\\ \overline{y}_n\end{bmatrix}$, the system (19) becomes

$$\begin{aligned}
\overline{x}_{n+1} &= -\overline{x}_n+f_{11}(u_n,v_n,b^*),\\
\overline{y}_{n+1} &= \lambda_2\overline{y}_n+g_{11}(u_n,v_n,b^*),
\end{aligned} \tag{21}$$

where the variables $(\overline{x}_n,\overline{y}_n)$ having the order at least two are denoted the terms in the model (21) by the functions f_{11} and g_{11}, respectively.

Using the center manifold theorem, it can be derived that the system (21) has a center manifold $W^c(0,0,0)$ at $(0,0)$ in a very closed neighbourhood of $\rho^*=0$, which may roughly be stated as follows:
$W^c(0,0,0)=\{(\overline{x}_n,\overline{y}_n,\rho^*)\,\epsilon R^3:\overline{y}_{n+1}=\overline{\alpha}_1\overline{x}_n^2+\overline{\alpha}_2\overline{x}_n\rho^*$
$+O((|\overline{x}_n|+|\rho^*|)^3)\}$

$$\begin{aligned}
\overline{\alpha}_1 &= \frac{\alpha_2[(1+\alpha_1)\alpha_{11}+\alpha_2\beta_{11}]}{1-\lambda_2^2}+\frac{\beta_{22}(1+\alpha_1)^2}{1-\lambda_2^2}-\\
&\quad\frac{(1+\alpha_1)[\alpha_{12}(1+\alpha_1)+\alpha_2\beta_{12}]}{1-\lambda_2^2},\\
\overline{\alpha}_2 &= \frac{(1+\alpha_1)[\alpha_{23}(1+\alpha_1)+\alpha_2\beta_{23}]}{\alpha_2(1+\lambda_2)^2}-\frac{(1+\alpha_1)\alpha_{13}+\alpha_2\beta_{13}]}{(1+\lambda_2)^2}.
\end{aligned}$$

The center manifold $W^c(0,0,0)$ restricted the model (21) has the following form:
$\overline{x}_{n+1}=-\overline{x}_n+h_1\overline{x}_n^2+h_2\overline{x}_n\rho^*+h_3\overline{x}_n^2\rho^*+h_4\overline{x}_n\rho^{*2}+h_5\overline{x}_n^3+O((|\overline{x}_n|+|\rho^*|)^3)\equiv F(\overline{x}_n,\rho^*)$

where

$$\begin{aligned}
h_1 &= \frac{\overline{\alpha}_2[(\lambda_2-\overline{\alpha}_1)\alpha_{11}-\overline{\alpha}_2\beta_{11}]}{1+\lambda_2}-\frac{\beta_{22}(1+\overline{\alpha}_1)^2}{1+\lambda_2}-\\
&\quad\frac{(1+\overline{\alpha}_1)[(\lambda_2-\overline{\alpha}_1)\alpha_{12}-\overline{\alpha}_2\beta_{12}]}{1+\lambda_2},\\
h_2 &= \frac{(\lambda_2-\overline{\alpha}_1)\alpha_{13}-\overline{\alpha}_2\beta_{13}}{1+\lambda_2}-\frac{(1+\overline{\alpha}_1)[(\lambda_2-\overline{\alpha}_1)\alpha_{23}-\overline{\alpha}_2\beta_{23}]}{\overline{\alpha}_2(1+\lambda_2)},\\
h_3 &= \frac{(\lambda_2-\alpha_1)\overline{\alpha}_1\alpha_{13}-\alpha_2\beta_{13}}{1+\lambda_2}+\frac{[(\lambda_2-\alpha_1)\alpha_{23}-\alpha_2\beta_{23}](\lambda_2-\alpha_1)\overline{\alpha}_1}{\alpha_2(1+\lambda_2)}-\\
&\quad\frac{(1+\alpha_1)[(\lambda_2-\alpha_1)\alpha_{123}-\alpha_2\beta_{123}]}{1+\lambda_2}+\frac{\alpha_2[(\lambda_2-\alpha_1)\alpha_{113}-\alpha_2\beta_{113}]}{1+\lambda_2}+\\
&\quad\frac{2\alpha_2\overline{\alpha}_2[(\lambda_2-\alpha_1)\alpha_{11}-\alpha_2\beta_{11}]}{1+\lambda_2}-\frac{2\beta_{22}\overline{\alpha}_2(1+\alpha_1)(\lambda_2-\alpha_1)}{1+\lambda_2}-\\
&\quad\frac{\beta_{223}(1+\alpha_1)^2}{1+\lambda_2}+\frac{\overline{\alpha}_2[(\lambda_2-\alpha_1)\alpha_{12}-\alpha_2\beta_{12}](\lambda_2-1-2\alpha_1)}{1+\lambda_2},\\
h_4 &= \frac{\overline{\alpha}_2[(\lambda_2-\alpha_1)\alpha_{13}-\alpha_2\beta_{13}]}{1+\lambda_2}+\frac{[(\lambda_2-\alpha_1)\alpha_{23}-\alpha_2\beta_{23}](\lambda_2-\alpha_1)\overline{\alpha}_2}{\alpha_2(1+\lambda_2)}+\\
&\quad\frac{2\alpha_2\overline{\alpha}_2[(\lambda_2-\alpha_1)\alpha_{11}-\alpha_2\beta_{11}]}{1+\lambda_2}+\frac{2\beta_{22}\overline{\alpha}_2(1+\alpha_1)(\lambda_2-\alpha_1)}{1+\lambda_2}+\\
&\quad\frac{\overline{\alpha}_2[(\lambda_2-\alpha_1)\alpha_{12}-\alpha_2\beta_{12}](\lambda_2-1-2\alpha_1)}{1+\lambda_2},\\
h_5 &= \frac{2\alpha_2\overline{\alpha}_1[(\lambda_2-\alpha_1)\alpha_{11}-\alpha_2\beta_{11}]}{1+\lambda_2}+\frac{2\beta_{22}\overline{\alpha}_1(\lambda_2-\alpha_1)(1+\alpha_1)}{1+\lambda_2}-\\
&\quad\frac{\overline{\alpha}_2(1+\alpha_1)[(\lambda_2-\alpha_1)\alpha_{112}-\alpha_2\beta_{112}]}{1+\lambda_2}+\frac{\overline{\alpha}_2^2[(\lambda_2-\alpha_1)\alpha_{111}-\alpha_2\beta_{111}]}{1+\lambda_2}\\
&\quad+\frac{[(\lambda_2-\alpha_1)\alpha_{11}-\alpha_2\beta_{11}](\lambda_2-1-2\alpha_1)\overline{\alpha}_1}{1+\lambda_2}.
\end{aligned}$$

For PD bifurcation, the two differentiating quantities ξ_1 and ξ_2 be nonzero,
$\xi_1 = \left(\frac{\partial^2F}{\partial\overline{x}\partial\rho^*}+\frac{1}{2}\frac{\partial F}{\partial\rho^*}\frac{\partial^2F}{\partial\overline{x}^2}\right)\Big|_{(0,0)}$ and $\xi_2 = \left(\frac{1}{6}\frac{\partial^3F}{\partial\overline{x}^3}+\left(\frac{1}{2}\frac{\partial^2F}{\partial\overline{x}^2}\right)^2\right)\Big|_{(0,0)}$.

The following theorem contains a succinct statement of the previously discussed topic.

If $\xi_1\neq0$ and $\xi_2\neq0$ then the system undergoes PD bifurcation at $E_2(x^*,y^*)$ for varies of ρ in a small neighborhood of b_{PDB}. Further, the period-two orbits for $\xi_2>0$ ($\xi_2<0$) that bifurcate from $E_2(x^*,y^*)$ is stable (unstable).

EXISTENCE OF MAROTTOS CHAOS

This section presents the condition under which the system (7) will be chaotic in the sense of Marotto (1978, 2005). Fixed point z of system f is repelling if all of the eigenvalues of $Df(z)$ are greater than 1. A repelling fixed point z is snap-back repeller of system f if there is a point $x_0\neq z$ in the repelling vicinity of z, such that $x_M=z$ and $det(Df(x_k))\neq0$ for $1\leq k\leq M$, where $x_k=f^k(x_0)$. A snap-back repeller indicates that system f is chaotic.

$E_2(x^*,y^*)$ is an repelling fixed point of $F(X_n)$ if $p^2(x^*,y^*)-4q(x^*,y^*)<0$ and $q(x^*,y^*)-1>0$

For map $F(X_n)=\begin{pmatrix}x_n+\frac{\rho^\alpha}{\Gamma(\alpha+1)}\left(rx_n\ln\frac{k}{x_n}-\left(1-e^{-ax_n}\right)y_n\right)\\ y_n+\frac{\rho^\alpha}{\Gamma(\alpha+1)}\left(\left(1-e^{-ax_n}\right)y_n-dy_n\right)\end{pmatrix}$,
$X_n=(x_n\ \ y_n)^T$

The eigenvalues that match the fixed point $E_2(x^*,y^*)$ are given by $\lambda_{1,2}=\frac{-\widehat{p}(x^*,y^*)\pm\sqrt{\widehat{p}^2(x^*,y^*)-4\widehat{q}(x^*,y^*)}}{2}$, where

$\widehat{p}(x^*,y^*) = -(2 - \frac{r\rho^\alpha}{\Gamma(\alpha+1)}) - \frac{r\rho^\alpha}{d\Gamma(\alpha+1)}(d-(-1+d)\ln[1-d])\ln\left[\frac{-ak}{\ln[1-d]}\right]$,

$\widehat{q}(x^*,y^*) = (1 - \frac{r\rho^\alpha}{\Gamma(\alpha+1)}) + \frac{r\rho^\alpha}{d\Gamma(\alpha+1)}(d+(-1+d)(-1+\frac{d\rho^\alpha}{\Gamma(\alpha+1)})\ln[1-d])\ln\left[\frac{-ak}{\ln[1-d]}\right]$.

As a result, the fixed point $E_2(x^*,y^*)$ has two complex eigenvalues, and their norm is greater than unity if

$p^2(x^*,y^*) - 4q(x^*,y^*) < 0$ and $q(x^*,y^*) - 1 > 0$

As a result, we can assert the following inference.

$E_2(x^*,y^*)$ is a snap-back repeller of $F(X_n)$ if $|DF^2(E(x_0,y_0))| \neq 0$.

Let $E(x_0,y_0) \neq E_2(x^*,y^*)$ be a point in a repelling neighborhood of $E_2(x^*,y^*)$, such that $F^2(E(x_0,y_0)) = E_2(x^*,y^*)$.

Therefore

$$x_1 = x_0 + \frac{\rho^\alpha}{\Gamma(\alpha+1)}\left(rx_0\ln\frac{k}{x_0} - (1-e^{-ax_0})y_0\right) \text{ and}$$

$$y_1 = y_0 + \frac{\rho^\alpha}{\Gamma(\alpha+1)}\left((1-e^{-ax_0})y_0 - dy_0\right) \tag{22}$$

and

$$x^* = x_1 + \frac{\rho^\alpha}{\Gamma(\alpha+1)}\left(rx_1\ln\frac{k}{x_1} - (1-e^{-ax_1})y_1\right) \text{ and}$$

$$y^* = y_1 + \frac{\rho^\alpha}{\Gamma(\alpha+1)}\left((1-e^{-ax_1})y_1 - dy_1\right). \tag{23}$$

We will calculate the value of x_0 and y_0 by solving equations (22) and (23)

By simple calculations, we get

$$|DF^2(E(x_0,y_0))| = |DF(E(x_0,y_0))|\,|DF(F(E(x_0,y_0)))|$$

$$= (CH-DG)\begin{bmatrix} 1+\{1-d-r-(1+aB)e^{-aA}+r\ln\frac{k}{A}\}\frac{\rho^\alpha}{\Gamma(\alpha+1)} \\ +\{d(r+aBe^{-aA}-r\ln\frac{k}{A})-r(1-e^{-aA})(1-\ln\frac{k}{A})\}\left(\frac{\rho^\alpha}{\Gamma(\alpha+1)}\right)^2 \end{bmatrix}$$

where $A = x_0 + \frac{\rho^\alpha}{\Gamma(\alpha+1)}\left(rx_0\ln\frac{k}{x_0} - (1-e^{-ax_0})y_0\right)$, $B = y_0 + \frac{\rho^\alpha}{\Gamma(\alpha+1)}\left((1-e^{-ax_0})y_0 - dy_0\right)$,

$C = 1 - \frac{\rho^\alpha}{\Gamma(\alpha+1)}\left(r + ay_0e^{-ax_0} - r\ln\frac{k}{x_0}\right)$, $D = \frac{\rho^\alpha}{\Gamma(\alpha+1)}\left(-1+e^{-ax_0}\right)$,

$G = \frac{\rho^\alpha}{\Gamma(\alpha+1)}\left(ay_0e^{-ax_0}\right)$, $H = 1 + \frac{\rho^\alpha}{\Gamma(\alpha+1)}\left(1-d-e^{-ax_0}\right)$.

Therefore $E_2(x^*,y^*)$ is a snap-back repeller of $F(X_n)$ when $|DF^2(E(x_0,y_0))| \neq 0$ Further, the following inference can claim as a result of the chaotic nature. $F(X_n)$ is chaotic under the condition $p^2(x^*,y^*) - 4q(x^*,y^*) < 0$, $q(x^*,y^*) - 1 > 0$ and $|DF^2(E(x_0,y_0))| \neq 0$. Since $F(X_n)$ has a repelling fixed point $E_2(x^*,y^*)$ if $p^2(x^*,y^*) - 4q(x^*,y^*) < 0$, $q(x^*,y^*) - 1 > 0$, and further from Theorem-5, the same fixed point $E_2(x^*,y^*)$ is a snap-back repeller if $|DF^2(E(x_0,y_0))| \neq 0$.
Therefore $F(X_n)$ is chaotic.

NUMERICAL SIMULATIONS

The Lyapunov exponent, bifurcation diagram, phase portrait and fractal dimension are shown for various parameter values in this section to illustrate the qualitative dynamical characteristic of the discrete fractional system. To support our theoretical conclusions for the system (7), we shall run numerical simulations. These parameter values were picked: $r = 1.2$, $k = 1.5$, $a = 0.5$, $\alpha = 0.75$, $d = 0.1$ and ρ varies between $1.9 \leq \rho \leq 2.73$. We locate a fixed point $E(x^*,y^*) = (1.02165, 3.36309)$ and assess the bifurcation point for the system (7) at $\rho_- = 2.08616$. The eigenvalues are $\lambda_{1,2} = -1, 0.937016$.

The system trajectory is shown in Figure 2 as changing from a fixed point to a Flip bifurcation and finally to a chaotic attractor. The computed MLEs and FDs associated with Figure 2(a-b) are shown in Figure 2 (c-d). In reference of the bifurcation Figure 2, the phase portraits are displayed in Figure 3, which effectively illustrates the bifurcation of a smooth, invariant closed curve into a chaotic attractor from a stable fixed point.

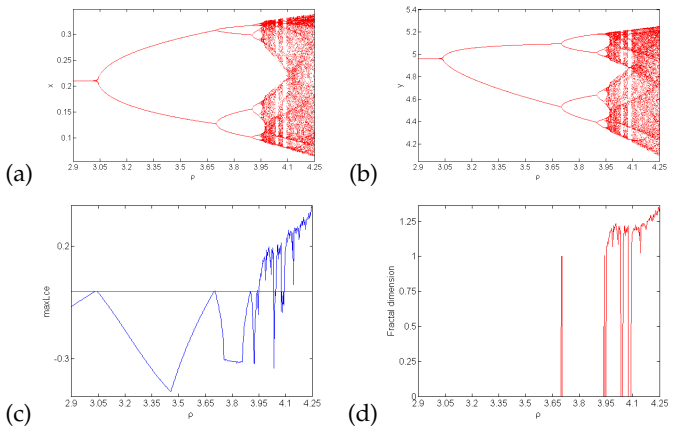

Figure 2 Flip Bifurcation diagram, MLEs and FDs for varying parameter ρ

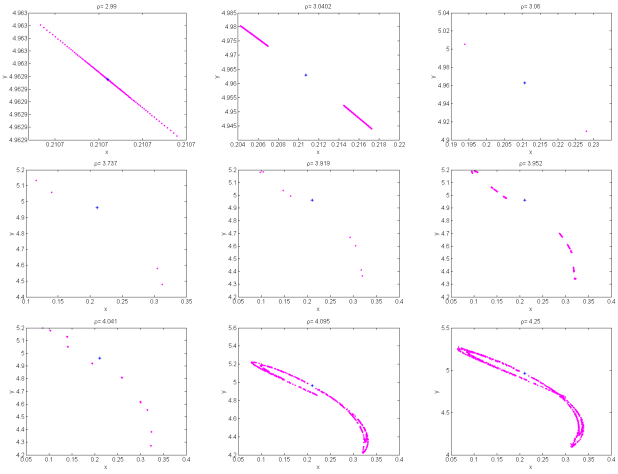

Figure 3 Phase picture for varying ρ with matching to Figure 2 a,b. Blue $*$ is the fixed point E_0.

In Figure 4, the orbit diagram of the prey and predator populations is shown together with other fixed parameter values are $r = 1.2, k = 1.5, a = 1.0, \alpha = 0.5, d = 0.4$ and ρ varies between $2.5 \leq \rho \leq 3.25$. We establish a fixed point $E(x^*,y^*) = (0.510826, 3.30154)$ and assess the bifurcation point for the system (7) at $\rho_{NS} = 2.65984$. The eigenvalues are $\lambda_{1,2} = -0.0173315 \pm 0.99985i$. This figure showing transition of trajectory from a fixed point to NSB and finally to chaotic attractor. The phase portrait, MLEs and FD of Figure 4 (a-b) are shown in Figure 5 and Figure 4 (c-d) respectively. All bifurcation processes for both prey and predator have three distinct periodic windows.

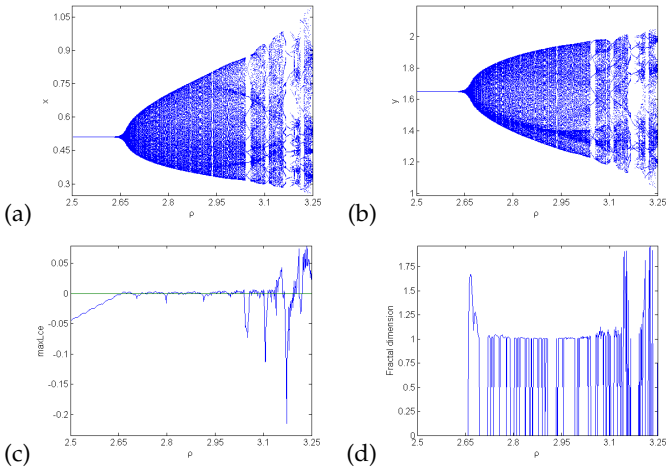

Figure 4 Visual representation of NS Bifurcation, MLEs and FDs of species for varying parameter ρ

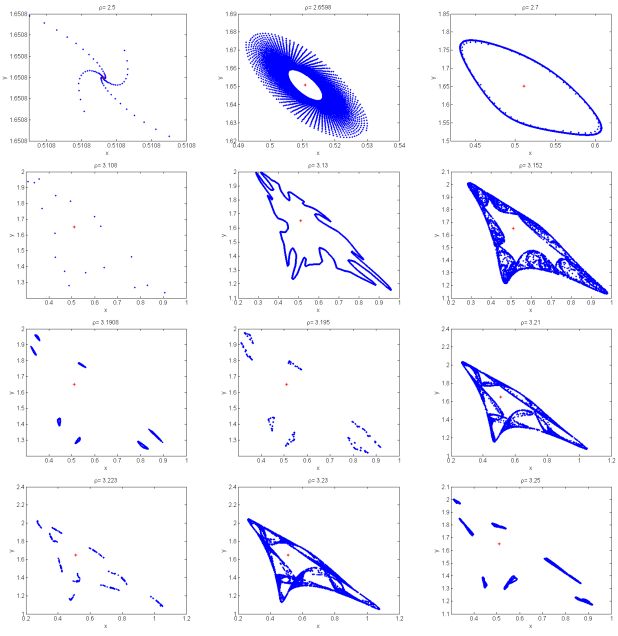

Figure 5 Phase picture for changing input of ρ matching to Figure 4 a,b. Red $*$ is the fixed point E_0.

We have also investigated NS bifurcation by varying the fractional order α in the range $0.65 \leq \alpha \leq 0.985$ and fixed all other parameter discussed above for Figure 4 with $\rho = 2.65984$. The visual representation of Figure 6 is displayed in Figure 7.

The prey-predator model may behave more dynamically in the Neimark-Sacker bifurcation diagram as other parameter values vary (for example, parameter a). When the parameter values are set as $r = 1.2$, $k = 1.5$, $\alpha = 0.75$, $d = 0.4$ with $\rho = 2.65984$ and a range between $0.5 \leq a \leq 1.33$, as illustrated in Figure 8 (a-b), a new Neimark-Sacker bifurcation diagram is produced. At $a = a_{NS} = 1.0$, the system encounters a Neimark-Sacker bifurcation. Figures 9 and 8 (c-d) illustrate, respectively, the phase portrait, MLEs, and FD of Figure 8(a-b). Figure 10 (a) shows the 3D bifurcation diagrams in (ρ, b, x)-space. The plot of the maximal Lyapunov exponents is shown in Figure 10 (b) for two control parameters through a 2D projection onto the (ρ, a) plane.

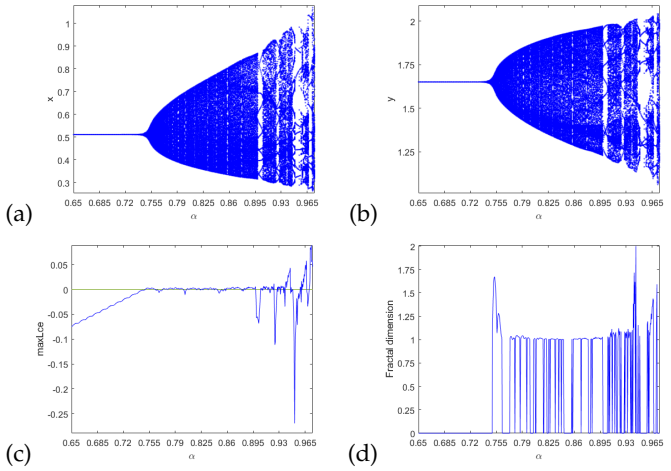

Figure 6 Diagram of NS Bifurcation in (a) (α, x) plane, (b) (α, y) plane, (c) MLEs , (d) FDs

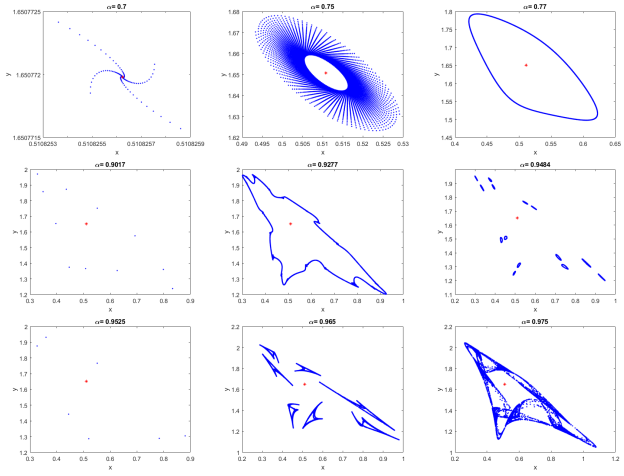

Figure 7 Phase picture for different inputs of α matching to Figure 6 a,b. Red $*$ is the fixed point E_2.

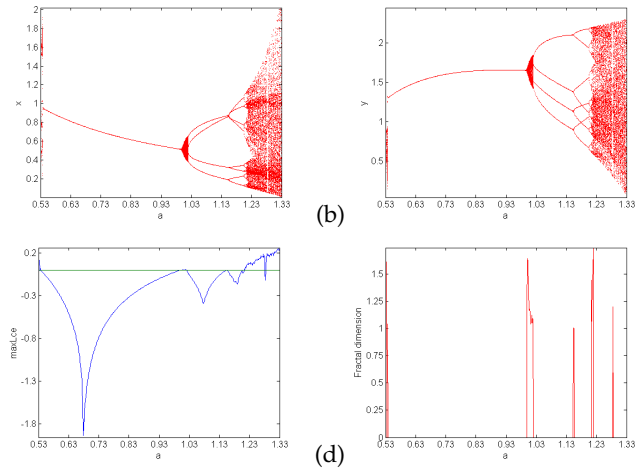

Figure 8 Diagram of NS Bifurcation in (a) (a, x) plane, (b) (a, y) plane, (c) MLEs , (d) FDs

Fractal Dimension

To determine chaotic attractors of a system, the fractal dimensions (FD) measurement is used and is defined by Cartwright (1999)

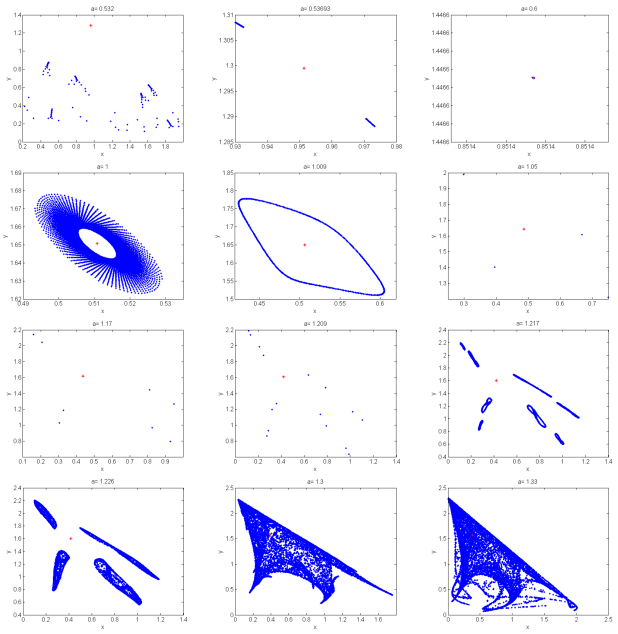

Figure 9 Phase picture for different inputs of a matching to Figure 8 a,b. Red $*$ is the fixed point E_2.

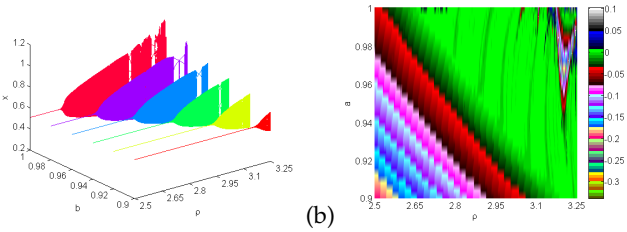

Figure 10 (a) 3D Bifurcation diagram in (ρ, b, x) space (b) Maximum Lyapunov exponents projected in two dimensions onto the (ρ, a) plane

$$\widehat{D}_{FD} = k + \frac{\sum_{j=1}^{k} \mathrm{tt}_j}{|\mathrm{tt}_{k+1}|} \tag{24}$$

where the largest integer is k such that $\sum_{j=1}^{k} \mathrm{tt}_j \geq 0$ and $\sum_{j=1}^{k+1} \mathrm{tt}_j < 0$ and t_j's are Lyapunov exponenets.

Now, the system's fractal dimensions (7) have the following structure:

$$\widehat{D}_{FD} = 2 + \frac{\mathrm{tt}_1}{|\mathrm{tt}_2|} \tag{25}$$

It is certain that the dynamics of the fractional order prey-predator system become unstable as the value of the parameter ρ rises since the chaotic dynamics of the system (7) (ref. Figure 5) are quantified with the sign of FD (ref. Figure 4 (d)).

CHAOS CONTROL

Dynamical systems are thought to be optimal in reference to a performance criterion and will avert chaos. Chaotic behavior is investigated in physics, biology, ecology, telecommunications, and other domains. Additionally, useful chaos management approaches can be used to a wide range of sectors, including communication systems, physics labs, biochemistry, turbulence, and cardiology. The challenge of regulating chaos dynamics in discrete-time systems has recently piqued the interest of many academics.

The four approaches for researching chaos control in discrete-time models most frequently referenced to take the challenge of controlling chaos are the state feedback method, pole-placement methodology, OGY technique, and hybrid control approach. We introduce OGY (Edward *et al.* 1990) and state feedback (Lynch 2007) for managing chaos in the fractional order prey-predator model. We are unable to use ρ as a control parameter in the OGY technique. To implement the OGY approach, a serves as a control parameter.

To apply the OGY approach, we can rewrite the system (7) as shown below.

$$\begin{aligned} x_{n+1} &= x_n + \frac{\rho^\alpha}{\Gamma(\alpha+1)}\left(r x_n \ln\frac{k}{x_n} - (1-e^{-a x_n}) y_n\right) = \tilde{f_{e1}}(x,y,a), \\ y_{n+1} &= y_n + \frac{\rho^\alpha}{\Gamma(\alpha+1)}\left((1-e^{-a x_n}) y_n - d y_n\right) = \tilde{f_{e2}}(x,y,a) \end{aligned} \tag{26}$$

where a is the parameter for chaos control. Additionally, let us assume that the chaotic regions are defined by $|a - a_0| < \tilde{v}$, where $\tilde{v} > 0$ and a_0 symbolizes the nominal parameter. Our stabilizing feedback control system steers the trajectory toward the desired orbit. If the system (7) has an unstable fixed point at (x^+, y^+) in a chaotic zone created by the development of a Neimark-Sacker bifurcation, the following linear map can represent the system (26) in the vicinity of the unstable fixed point at (x^+, y^+).

$$\begin{bmatrix} x_{n+1} - x^+ \\ y_{n+1} - y^+ \end{bmatrix} \approx \tilde{A_{ee}} \begin{bmatrix} x_n - x^+ \\ y_n - y^+ \end{bmatrix} + \tilde{B_{ee}}\,[a - a_0] \tag{27}$$

where

$$\tilde{A_{ee}} = \begin{bmatrix} \frac{\partial \tilde{f_{e1}}(x,y,a)}{\partial x} & \frac{\partial \tilde{f_{e1}}(x,y,a)}{\partial y} \\ \frac{\partial \tilde{f_{e2}}(x,y,a)}{\partial x} & \frac{\partial \tilde{f_{e2}}(x,y,a)}{\partial y} \end{bmatrix}$$

$$= \begin{bmatrix} 1 + r\tilde{\mu_e}\left(-1 + \ln\frac{k}{x^+} - a\tilde{R_{e1}}\right) & (-1 + e^{-a x^+})\tilde{\mu_e} \\ a r \tilde{\mu_e} \tilde{R_{e1}} & 1 + \tilde{\mu_e}(1 - d - e^{-a x^+}) \end{bmatrix}$$

and

$$\tilde{B_{ee}} = \begin{bmatrix} \frac{\partial \tilde{f_{e1}}(x,y,a)}{\partial a} \\ \frac{\partial \tilde{f_{e2}}(x,y,a)}{\partial a} \end{bmatrix} = \begin{bmatrix} -\tilde{R_{e2}} \\ \tilde{R_{e2}} \end{bmatrix}$$

For convenience, here we let $\frac{\rho^\alpha}{\Gamma(\alpha+1)} = \tilde{\mu_e}$, $\tilde{R_{e1}} = \frac{e^{-a x^+} x^+ \ln\frac{-ak}{\ln[1-d]}}{d}$ and $\tilde{R_{e2}} = \frac{e^{-a x^+} r x^{+2} \tilde{\mu_e} \ln\frac{-ak}{\ln[1-d]}}{d}$

The system's (26) controllability matrix, is therefore defined as follows:

$$\tilde{C_{ee}} = [\tilde{B_{ee}} : \tilde{A_{ee}}\tilde{B_{ee}}]$$

$$= \begin{bmatrix} -\tilde{R_{e2}} & \frac{e^{-2a x^+} r x^{+2} \ln\frac{-ak}{\ln[1-d]} \left(d(\tilde{\mu_e} + e^{a x^+}(-1+(-1+r)\tilde{\mu_e}) - d e^{a x^+} r \ln\frac{k}{x^+}) + a r x^+ \tilde{\mu_e} \ln\frac{-ak}{\ln[1-d]}\right)}{d^2} \\ \tilde{R_{e2}} & \frac{e^{-2a x^+} r x^{+2} \ln\frac{-ak}{\ln[1-d]} \left(d(\tilde{\mu_e} + e^{a x^+}(-1+(-1+r)\tilde{\mu_e}) + a r x^+ \tilde{\mu_e} \ln\frac{-ak}{\ln[1-d]}\right)}{d^2} \end{bmatrix}$$

It is then clear to determine that the rank of $\tilde{C_{ee}}$ is 2. Assume that $[a - a_0] = -\tilde{K_{ee}} \begin{bmatrix} x_n - x^+ \\ y_n - y^+ \end{bmatrix}$ where $\tilde{K_{ee}} = [\tilde{\sigma_{e1}} \quad \tilde{\sigma_{e2}}]$, then system (26) becomes

$$\begin{bmatrix} x_{n+1}-x^+ \\ y_{n+1}-y^+ \end{bmatrix} \approx [\tilde{A_{ee}}-\tilde{B_{ee}}\tilde{K_{ee}}] \begin{bmatrix} x_n-x^+ \\ y_n-y^+ \end{bmatrix}$$

Additionally, (7) offers the appropriate controlled system.

$$\begin{aligned} x_{n+1} &= x_n+\tilde{\mu_e}\left(rx_n\ln\frac{k}{x_n}-(1-e^{-(a_0-\tilde{\sigma_{e1}}(x_n-x^+)-\tilde{\sigma_{e2}}(y_n-y^+))x_n})y_n\right)\\ y_{n+1} &= y_n+\tilde{\mu_e}\left((1-e^{-(a_0-\tilde{\sigma_{e1}}(x_n-x^+)-\tilde{\sigma_{e2}}(y_n-y^+))x_n})y_n-dy_n\right) \end{aligned} \tag{28}$$

Additionally, the fixed point (x^+,y^+) is locally asymptotically stable iff both eigenvalues $(\tilde{A_{ee}}-\tilde{B_{ee}}\tilde{K_{ee}})$ of the matrix are situated inside an open unit disk.

Also,

$$\tilde{A_{ee}}-\tilde{B_{ee}}\tilde{K_{ee}}=$$

$$\begin{bmatrix} 1+\tilde{\mu_e}\left(r\ln\frac{k}{x^+}-ar\tilde{R_{e1}}-r\right)+\tilde{R_{e2}}\tilde{\sigma_{e1}} & (e^{-ax^+}-1)\tilde{\mu_e}+\tilde{R_{e2}}\tilde{\sigma_{e2}} \\ ar\tilde{R_{e1}}-\tilde{R_{e2}}\tilde{\sigma_{e1}} & 1+(d-e^{-ax^+}-1)\tilde{\mu_e}-\tilde{R_{e2}}\tilde{\sigma_{e2}} \end{bmatrix}$$

Also

$$\begin{aligned} &\lambda_e{}^2-\left(2+(1-d-e^{ax^+})\tilde{\mu_e}+\tilde{\mu_e}(r\ln\frac{k}{x^+}-r-ar\tilde{R_{e1}})+(\tilde{R_{e2}}\tilde{\sigma_{e1}}-\tilde{R_{e2}}\tilde{\sigma_{e2}})\right)\lambda_e\\ &+\frac{e^{-ax^+}}{d}\left(d\tilde{\mu_e}(r\tilde{\mu_e}-1)+de^{ax^+}(1+\tilde{\mu_e}(1-d-r-r\tilde{\mu_e}(1-d)))\right)\\ &+\frac{1}{d}e^{-ax^+}\left(dr\tilde{\mu_e}\ln\frac{k}{x^+}(e^{x^+}-\tilde{\mu_e}(1-e^{ax^+}(1-d)))\right)+\\ &\frac{e^{-ax^+}}{d}\left(rx^+\tilde{\mu_e}\ln\frac{-ak}{\ln[1-d]}(a\tilde{\mu_e}-a+x^+(1-d\tilde{\mu_e})\tilde{\sigma_{e1}}-x^+(1-r\tilde{\mu_e}+r\tilde{\mu_e}\ln\frac{k}{x^+})\tilde{\sigma_{e2}})\right)=0. \end{aligned} \tag{29}$$

The lines of marginal stability can then be obtained by solving the equations $\lambda_{e1}=\pm1$ and $\lambda_{e1}\lambda_{e2}=1$. Furthermore, these restrictions ensure that the open unit disc has both eigenvalues. Let us consider $\lambda_{e1}\lambda_{e2}=1$ and from (29), we get

$$\begin{aligned} L_{e1} &= \frac{-1}{d}e^{-ax^+}\tilde{\mu_e}\left(d(1-r\tilde{\mu_e})-de^{ax^+}(1-d-r-r\tilde{\mu_e}(1-d))\right)\\ &+\frac{-1}{d}e^{-ax^+}\tilde{\mu_e}\left(dr\ln\frac{k}{x^+}(-e^{ax^+}+\tilde{\mu_e}(1-e^{ax^+}+de^{ax^+}))\right)-\\ &\frac{e^{-ax^+}}{d}\tilde{\mu_e}\left(rx^+\ln\frac{-ak}{\ln[1-d]}(a-ad\tilde{\mu_e}+x^+(1-d\tilde{\mu_e})\tilde{\sigma_{e1}}+x^+(1-r\tilde{\mu_e}+r\tilde{\mu_e}\ln\frac{k}{x^+})\tilde{\sigma_{e2}})\right). \end{aligned}$$

Next, if we assume that $\lambda_{e1}=1$, we obtain

$$\begin{aligned} L_{e2} &= \frac{1}{d}e^{-ax^+}\left(d\tilde{\mu_e}(-2+\tilde{\mu_e})+de^{ax^+}(4+2\tilde{\mu_e}-2d\tilde{\mu_e}-r\tilde{\mu_e}(2+r\tilde{\mu_e}-dr\tilde{\mu_e}))\right)\\ &+\frac{1}{d}e^{-ax^+}\left(dr\tilde{\mu_e}\ln\frac{k}{x^+}(2e^{ax^+}-\tilde{\mu_e}(1-e^{ax^+}-de^{ax^+}))\right)+\\ &\frac{1}{d}e^{-ax^+}\left(rx^+\tilde{\mu_e}\ln\frac{-ak}{\ln[1-d]}(-2a+ad\tilde{\mu_e}+x^+(2-d\tilde{\mu_e})\tilde{\sigma_{e1}}+x^+(-2+r\tilde{\mu_e}-r\tilde{\mu_e}\ln\frac{k}{x^+})\tilde{\sigma_{e2}})\right). \end{aligned}$$

Also, if $\lambda_{e1}=-1$, then

$$\begin{aligned} L_{e3} &= \frac{e^{-ax^+}r\tilde{\mu_e}^2}{d}\left(d(e^{ax^+}-de^{ax^+}-1+(1+(-1+d)e^{ax^+})\ln\frac{k}{x^+}-ax^+\ln\frac{-ak}{\ln[1-d]})\right)\\ &+\frac{1}{d}e^{-ax^+}r\tilde{\mu_e}^2\ln\frac{-ak}{\ln[1-d]}x^{+2}\left(d\tilde{\sigma_{e1}}+r(-1+\frac{k}{x^+}\tilde{\sigma_{e2}})\right). \end{aligned}$$

For a given parametric value, the stable eigenvalues are located in the triangle in the $\tilde{\sigma_{e1}},\tilde{\sigma_{e2}}$ plane encircled by the straight lines L_{e1},L_{e2},L_{e3}.

Chaos is stabilized at the point where the system's (7) unstable trajectories through a technique known as state feedback control. By introducing a feedback control law as the control force u_{ee}, and using the following formula, the system (7) may be made to take on a controlled form.

$$\begin{aligned} x_{n+1} &= x_n+\frac{\rho^\alpha}{\Gamma(\alpha+1)}\left(rx_n\ln\frac{k}{x_n}-(1-e^{-ax_n})y_n\right)+u_{ee}\\ y_{n+1} &= y_n+\frac{\rho^\alpha}{\Gamma(\alpha+1)}\left((1-e^{-ax_n})y_n-dy_n\right)\\ u_{ee} &= -k_1(x_n-x^+)-k_2(y_n-y^+) \end{aligned} \tag{30}$$

where the nonnegative equilibrium point of the system (7) is represented by (x^+,y^+). The feedback gains are represented by the numbers k_1 and k_2.

Example: To implement the feedback control OGY mechanism for the system (7), we utilize $(a_0,r,k,d,\alpha,\rho)=(1.33,1.2,1.5,0.4,0.75,2.65984)$. In this situation, the unstable system (7) has a single non-negative fixed point $(x^+,y^+)=(0.384079,1.56978)$. Then, based on these parametric values, we offer the controlled system below.

$$\begin{aligned} x_{n+1} &= x_n+2.2662\left(1.2x_n\ln\frac{1.5}{x_n}-(1-e^{-(1.33-\tilde{\sigma_{e1}}(x_n-0.384079)-\tilde{\sigma_{e2}}(y_n-1.56978))x_n})y_n\right),\\ y_{n+1} &= y_n+2.2662\left((1-e^{-(1.33-\tilde{\sigma_{e1}}(x_n-0.384079)-\tilde{\sigma_{e2}}(y_n-1.56978))x_n})y_n-0.4y_n\right). \end{aligned} \tag{31}$$

where the gain matrix is $\tilde{K}=[\tilde{\sigma_{e1}}\quad\tilde{\sigma_{e2}}]$. We also get,

$$\tilde{A_{ee}}=\begin{bmatrix} -0.85338 & -0.90648 \\ 2.83883 & 1 \end{bmatrix}$$

$$\tilde{B_{ee}}=\begin{bmatrix} -0.819801 \\ 0.819801 \end{bmatrix}$$

$$\tilde{C_{ee}}=\begin{bmatrix} -0.819801 & -0.0435314 \\ 0.819801 & -1.50747 \end{bmatrix}$$

Consequently, it is easy to confirm that the matrix's $\tilde{C_{ee}}$ rank is 2. As a result, it is possible to control the system (31), and the Jacobian matrix of its controlled system is given by.

$$\tilde{A_{ee}}-\tilde{B_{ee}}\tilde{K_{ee}}=\begin{bmatrix} -0.85338+0.819801\tilde{\sigma_{e1}} & -0.90648+0.819801\tilde{\sigma_{e2}} \\ 2.83883-0.819801\tilde{\sigma_{e1}} & 1-0.819801\tilde{\sigma_{e2}} \end{bmatrix}$$

The lines L_{e1}, L_{e2} and L_{e3} are offered by for marginal stability.

$$\begin{aligned} L_{e1} &= 0.719959+0.0766677\tilde{\sigma_{e1}}-1.62767\tilde{\sigma_{e2}}=0\\ L_{e2} &= 2.86658+0.896468\tilde{\sigma_{e1}}-2.44747\tilde{\sigma_{e2}}=0\\ L_{e3} &= -2.57334+0.743133\tilde{\sigma_{e1}}+0.807869\tilde{\sigma_{e2}}=0 \end{aligned}$$

The controlled system(31)'s stable triangular region is defined by the marginal lines L_{e1}, L_{e2} and L_{e3}, which are shown in Figure 11.

To investigate the operation of the applied feedback control influence as a controller of chaos in an unstable condition, we performed numerical simulations (see Figure 11). The parameter values will be the same as the OGY method that we select. The chosen feedback increases are $k_1=-0.3$ and $k_2=-0.25$.

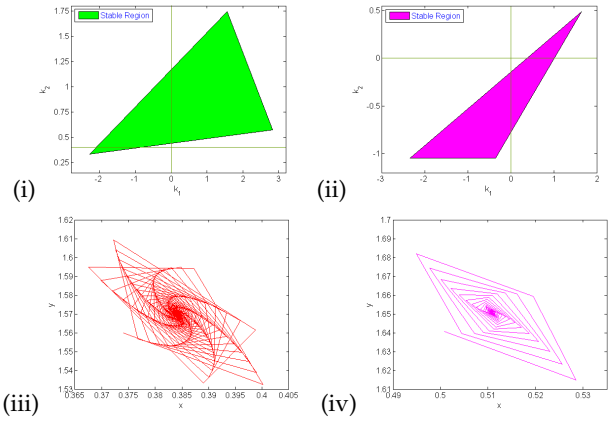

Figure 11 (i-ii) OGY method and State feedback method's stable region (iii-iv) Trajectories of a stable system

CONCLUSION

The present study investigates the dynamics of a model system and identifies two equilibrium points under specific parametric conditions. Our work provides a comprehensive stability analysis of these equilibrium points, which is presented in detail in the paper. In addition, we demonstrate the occurrence of a flip bifurcation and a Neimark-Sacker bifurcation in the model system, both analytically and numerically, under certain conditions. Notably, our results indicate that increasing values of the parameters ρ and a destabilize the system, resulting in a transition from a stable state to chaotic behavior via bifurcation. We observe the resulting chaotic behavior in the models. However, we also demonstrate that the OGY technique can be used to control the chaotic behavior, both numerically and analytically.

Furthermore, our main finding is that the degree of memory represented by the parameter α plays a crucial role in determining the system's behavior. Specifically, our results indicate that strong memory, corresponding to α approaching zero, stabilizes the system, while weak memory, corresponding to α approaching one, leads to chaotic behavior. These findings highlight the importance of memory in the dynamics of the model system.

In summary, this study presents a comprehensive analysis of the dynamics of a model system and demonstrates the occurrence of bifurcations and chaos under specific parametric conditions. Additionally, we show the effectiveness of the OGY technique in controlling the chaotic behavior and highlight the impact of memory on the system's behavior. Our work contributes to a better understanding of the dynamics of the model system and provides insights into the role of memory in the system's behavior.

Availability of data and material

Not applicable.

Conflicts of interest

The authors declare that there is no conflict of interest regarding the publication of this paper.

Ethical standard

The authors have no relevant financial or non-financial interests to disclose.

LITERATURE CITED

Abdelaziz, M., A. Ismail, F. Abdullah, and M. Mohd, 2018 Bifurcations and chaos in a discrete si epidemic model with fractional order. Advances in Difference Equations pp. 1–19.

Abdeljawad, T., 2011 On riemann and caputo fractional differences. Computers & Mathematics with Applications **62**: 1602–1611.

Ahmad, W. and J. Sprott, 2003 Chaos in fractional-order autonomous nonlinear systems. Chaos, Solitons & Fractals **16**: 339–351.

Atabaigi, A., 2020 Multiple bifurcations and dynamics of a discrete time predator-prey system with group defense and non-monotonic functional response. Differential Equations and Dynamical Systems **28**: 107–132.

Berardo, C. and S. Geritz, 2021 Coevolution of the reckless prey and the patient predator. Journal of Theoretical Biology **530**: 110873.

Cartwright, J., 1999 Nonlinear stiffness, lyapunov exponents, and attractor dimension. Physics Letters A **264**: 298–302.

Čermák, J., I. Győri, and L. Nechvátal, 2015 On explicit stability conditions for a linear fractional difference system. Fractional Calculus and Applied Analysis **18**: 651–672.

Cheng, K., S. Hsu, and S. Lin, 1982 Some results on global stability of a predator-prey system. Journal of Mathematical Biology **12**: 115–126.

Connolly, J. A., 2004 The numerical solution of fractional and distributed order differential equations .

Din, Q., 2017 Neimark-sacker bifurcation and chaos control in hassell-varley model. Journal of Difference Equations and Applications **23**: 741–762.

Dzieliński, A., D. Sierociuk, and G. Sarwas, 2010 Some applications of fractional order calculus. Bulletin of the Polish Academy of Sciences: Technical Sciences **4**.

Edward, O., G. Celso, and A. James, 1990 Controlling chaos. Physical Review Letters **64**: 1196–1199.

Elsadany, A. and A. Matouk, 2015 Dynamical behaviors of fractional-order lotka–volterra predator–prey model and its discretization. Journal of Applied Mathematics and Computing **49**: 269–283.

Gompertz, B., 1825 On the nature of the function expressive of the law of human mortality, and on a new mode of determining the value of life contingencies. in a letter to francis baily, esq. frs &c. Philosophical transactions of the Royal Society of London **115**: 513–583.

Guo, G., B. Li, and X. Lin, 2013 Qualitative analysis on a predator-prey model with ivlev functional response. Advances in Difference Equations .

Holling, C., 1965 The functional response of predators to prey density and its role in mimicry and population regulation. The Memoirs of the Entomological Society of Canada **97**: 5–60.

Huang, C., J. Cao, M. Xiao, A. Alsaedi, and F. Alsaadi, 2017a Controlling bifurcation in a delayed fractional predator–prey system with incommensurate orders. Applied Mathematics and Computation **293**: 293–310.

Huang, C., J. Cao, M. Xiao, A. Alsaedi, and T. Hayat, 2018 Effects of time delays on stability and hopf bifurcation in a fractional ring-structured network with arbitrary neurons. Communications in Nonlinear Science and Numerical Simulation **57**: 1–13.

Huang, C., Y. Meng, J. Cao, A. Alsaedi, and F. Alsaadi, 2017b New bifurcation results for fractional bam neural network with leakage delay. Chaos, Solitons & Fractals **100**: 31–44.

Ichise, M., Y. Nagayanagi, and T. Kojima, 1971 An analog simulation of non-integer order transfer functions for analysis of electrode processes. Journal of Electroanalytical Chemistry and

Interfacial Electrochemistry **33**: 253–265.
Işık, S., 2019 A study of stability and bifurcation analysis in discrete-time predator–prey system involving the allee effect. International Journal of Biomathematics **12**: 1950011.
Ivlev, V., 1961 *Experimental ecology of the feeding of fishes*. Yale Univ.
Kangalgil, F. and S. Işık, 2022 Effect of immigration in a predator-prey system: Stability, bifurcation and chaos. AIMS Mathematics **7**: 14354–14375.
Kartal, S., 2014 Mathematical modeling and analysis of tumor-immune system interaction by using lotka-volterra predator-prey like model with piecewise constant arguments. Periodicals of Engineering and Natural Sciences (PEN) **2**.
Kartal, S., 2017 Flip and neimark–sacker bifurcation in a differential equation with piecewise constant arguments model. Journal of Difference Equations and Applications **23**: 763–778.
Khan, A., S. Bukhari, and M. Almatrafi, 2022 Global dynamics, neimark-sacker bifurcation and hybrid control in a leslie's prey-predator model. Alexandria Engineering Journal **61**: 11391–11404.
Kilbas, A., O. Marichev, and S. Samko, 1993 *Fractional integrals and derivatives (theory and applications)*.
Kooij, R. and A. Zegeling, 1996 A predator–prey model with ivlev's functional response. Journal of Mathematical Analysis and Applications **198**: 473–489.
Li, J., G. Sun, and Z. Guo, 2022a Bifurcation analysis of an extended klausmeier–gray–scott model with infiltration delay. Studies in Applied Mathematics **148**: 1519–1542.
Li, J., G. Sun, and Z. Jin, 2022b Interactions of time delay and spatial diffusion induce the periodic oscillation of the vegetation system. Discrete and Continuous Dynamical Systems-B **27**: 2147–2172.
Lynch, S., 2007 *Dynamical systems with applications using Mathematica*. Springer.
M., R., M. D.O., I. P., and J. T., 2011 On the fractional signals and systems. Signal Processing **91**: 350–371.
Marotto, F., 1978 Snap-back repeller imply chaos in rn. J. Math. Anal. Appl. **63**: 199–223.
Marotto, F., 2005 On redefining a snap-back repeller. Chaos, Solit. Fract. **25**: 25–28.
Podlubny, I., 1999 *Fractional Differential Equations*. New York: Academic Press.
Preedy, K., P. Schofield, M. Chaplain, and S. Hubbard, 2007 Disease induced dynamics in host–parasitoid systems: chaos and coexistence. Journal of the Royal Society Interface **4**: 463–471.
Rana, S., 2019 Dynamics and chaos control in a discrete-time ratio-dependent holling-tanner model. Journal of the Egyptian Mathematical Society **27**: 1–16.
Rana, S. and U. Kulsum, 2017 Bifurcation analysis and chaos control in a discrete-time predator-prey system of leslie type with simplified holling type iv functional response. Discrete Dynamics in Nature and Society .
Revilla, T. and V. Křivan, 2022 Prey–predator dynamics with adaptive protection mutualism. Applied Mathematics and Computation **433**: 127368.
Rosenzweig, M., 1971 Paradox of enrichment: Destabilization of exploitation ecosystems in ecological time. Science **171**: 385–387.
Sun, G., H. Zhang, Y. Song, L. Li, and Z. Jin, 2022 Dynamic analysis of a plant-water model with spatial diffusion. Journal of Differential Equations **329**: 395–430.
Uddin, M., S. Rana, S. Işık, and F. Kangalgil, 2023 On the qualitative study of a discrete fractional order prey–predator model with the effects of harvesting on predator population. Chaos, Solitons & Fractals **175**: 113932.
Uriu, K. and Y. Iwasa, 2007 Turing pattern formation with two kinds of cells and a diffusive chemical. Bulletin of mathematical biology **69**: 2515–2536.
Wang, W., L. Zhang, H. Wang, and Z. Li, 2010 Pattern formation of a predator–prey system with ivlev-type functional response. Ecological Modelling **221**: 131–140.
Wei, W., W. Xu, J. Liu, Y. Song, and S. Zhang, 2023 Stochastic bifurcation and break-out of dynamic balance of predator-prey system with markov switching. Applied Mathematical Modelling .
Zhao, M. and Y. Du, 2016 Stability of a discrete-time predator-prey system with allee effect. Nonlinear Analysis and Differential Equations **4**: 225–233.

How to cite this article: Uddin, M. J., Santra, P. K., Rana, S. S., and Mahapatra, G. S. Chaotic Dynamics of the Fractional Order Predator-Prey Model Incorporating Gompertz Growth on Prey with Ivlev Functional Response. *Chaos Theory and Applications*, 6(3), 192-204, 2024.

CHAOS
Theory and Applications
in Applied Sciences and Engineering

e-ISSN: 2687-4539
RESEARCH ARTICLE
Vol.6 / No.3 / 2024 / pp.205-217
https://doi.org/10.51537/chaos.1396823

Bio-Inspired Jumping Spider Optimization for Controller Tuning/Parameter Estimation of an Uncertain Aerodynamic MIMO System

David Mohammed Ezekiel [*,1], **Ravi Samikannu** [*,2] **and Oduetse Matsebe** [β,3]

*Department of Electrical and Communications Systems Engineering, Botswana International University of Science & Technology (BIUST), Private bag 16, Palapye, Botswana, βDepartment of Mechanical Energy and Industrial Engineering, Botswana International University of Science & Technology (BIUST), Private bag 16, Palapye, Botswana.

ABSTRACT The practical near impossibility of empirical attempts in estimating optimal controller gains makes the use of metaheuristics strategies inevitable to automatically obtain these gains by an iterative heuristic simulation procedure. The convergence of the gain values to the local or global solutions occur with ease. In designing controllers for the Twin-Rotor MIMO System (TRMS) Jumping Spider Optimization Algorithm (JSOA), a novel neoteric population-based bio-inspired metaheuristic approach is used to obtain optimum values for the Proportional Integral and Derivative (PID) controllers. With the k_p, k_i, k_d controller gains as the decision variables, the JSOA solution to a nonlinear multi-objective optimization problem subject to some intrinsic constraints spawned optimal values for the controllers' variables. Counter to other algorithms (deterministic and stochastic) that get caught in local minima, JSOA evolved a solution after searchingly rummaging the entire solution search space in a vectorized fashion for an optimal value. Compared with several other versatile controllers (using GA, PSO, Pattern Search, and Simulated Annealing), statistical results obtained showed JSOA technique provided a unique solution and found the gains of the PID controllers marginally in relation to the others (optimization methods).

KEYWORDS
Jumping Spider Optimization Algorithm (JSOA), Meta-heuristics, Optimization, PID, Intelligent control, Dynamic system, Nonlinear system, Linearization, Pitch and Yaw, Twin-Rotor MIMO System (TRMS)

INTRODUCTION

Recent advances in computerized/computing technology have revolutionized the aerospace industry, putting flying vessels and equipment at the cutting-edge. Flying vessels or maneuvering vehicles designed for Vertical Take-Off and Landing (VTOL) like helicopters, drones, Unmanned Aerial Vehicles (UAVs) are advantageous over fixed-wing types (e.g., airplanes) in that they can maneuver and hover around in confined and limited spaces (Toha and Tokhi 2010). To carry out research on the helicopters and drones, control laboratories around the world are equipped with a laboratory-scaled version of the helicopter model, the TRMS. Essentially, it is an electromechanical, electrodynamic, and aerodynamic equipment prototype which models the dynamics of a typical true-life helicopter (Ezekiel *et al.* 2020a; Mones and Diaa-Eldeen 2017; Toha and Tokhi 2011). It is a unique equipment with fewer Degrees of Freedom (DoF) than a true-life helicopter, and its Angle Of Attack (AOA) in piercing through space and air is fixed (see Table 1 for comparison). Since it is an equipment fixed to the workbench in the laboratory, it most important function is to develop control strategies to control and maintain the testbed in a hovering posture (Ezekiel *et al.* 2020b; Choudhary 2017), signifying a helicopter position when airlifting humans and equipment during emergency rescues, etc.

The challenge to control multivariable systems (SIMO, MISO, MIMO systems) has attracted numerous researches over the past few centuries. This is owing to the problem of cross-linkages or dynamic couplings which are significant, and pairing issues between the input-output variables/channels. The best practice is not to trivialize these coupling and dynamic effects in modeling

Manuscript received: 27 November 2023,
Revised: 31 January 2024,
Accepted: 7 March 2024.

[1]ed18100190@studentmail.biust.ac.bw (**Corresponding author**)
[2]ravis@biust.ac.bw
[3]matsebeo@biust.ac.bw

Table 1 Similar and contrasting features between a Helicopter and its Prototype/Model (Basturk 2006)

Attributes	Helicopter	TRMS
Locus of pivot point	Main rotor head	Three-fifth way between twin-rotor
Vertical control	Main rotor's pitch angle	Main rotor Speed control
Horizontal control	Tail rotor's yaw angle	Tail rotor Speed control
Degrees-of-Freedom	3-DOF yaw, pitch, and roll axes	1 or 2-DOF pitch and/or yaw
Angle of Attack (AOA)	AOA changes (variable)	Fixed AOA

and design because in so doing results in degraded controller's performance and in unrealized control objectives (Ezekiel *et al.* 2020b; Choudhary 2017; Raghavan and Thomas 2017). The all-purpose PID controllers uniquely designed for linear systems are applicable for only SISO systems, which may not be adequate for multivariable MIMO systems due to the aforementioned problem involved, even if the channels are decoupled. Hence the need for an efficient strategy to handle these effects.

Poised with this challenge, therefore, authors and researchers have proposed a vast number of methodologies using Classical, Optimal, Robust, Adaptive, and Intelligent control strategies. The investigation of deadbeat control as a strategy capable of controlling the TRMS as a decoupled subsystem (of vertical and horizontal) was carried out in (Wen and Lu 2008). Simulations were performed on the decoupled system, which is a linearized system. It can be inferred that errors due to approximations were systematically introduced on the system due to decoupling as reflected in the final system's simulations results. Ghellab et al. designed a multistage fuzzy gain-scheduled feedback linearization-based controller using the nonlinear TRMS model to stabilize the beam of the TRMS to its horizontal posture (Ghellab *et al.* 2018). The effects of cross-couplings were incorporated in the design of the control laws. The proposed controller was implemented real-time. However, the use of output feedback linearization inherently introduced disturbance as presented in the simulations results obtained therein.

The robust and adaptive Sliding Mode Control (SMC) is a controller designed on 2 sliding control surfaces on the control plane (Mondal 2012a; Butt and Aschemann 2015; Mondal and Mahanta 2012; Mondal 2012b; Dimassi *et al.* 2019). The main benefits of SMC as a controller are robust system robustness against nonlinearities, modeling errors, and parametric uncertainty (variations) as well as being very effective in rejecting disturbances. In (Mondal and Mahanta 2012), a terminal sliding mode controller was implemented on the linearized nonlinear TRMS plant. In (Mondal 2012a; Mondal and Mahanta 2012; Mondal 2012b), the 2nd order SMC was proposed to control the TRMS plant while a MIMO Integral SMC of a 2-DOF helicopter was proposed in (Butt and Aschemann 2015). A Fuzzy-Sliding and Fuzzy-Integral-Sliding Controller (FS/FISC) for the TRMS were presented in (Mondal 2012a). The main challenge in the use of SMC is the chattering phenomenon that exists in the control signals owing to the discontinuous control action that may excite un-modeled high-frequency dynamics powerful enough to damage the actuators. Although the undesired effects of chattering were reduced to a barest in simulations in (Mondal 2012a; Mondal and Mahanta 2012), yet the effect still persisted and the control signal was still discontinuous and not smooth enough for practical purposes.

Parallel distributed fuzzy LQR controllers were utilized in (Tao *et al.* 2010) to accommodate different regions of operation for the decoupled system to separately control the pitch and yaw angles in pure simulations without any real-time applications on the system. Particle Swarm Optimisation (PSO) invented by Kennedy & Eberhard in the 90's, one of the most recent intelligent optimization strategies, was employed to augment the tuning process of the popular PID controller in (Toha and Tokhi 2011; Al-Mahturi and Wahid 2017). It is a population-based stochastic search global optimisation technique inspired by nature. It is based on simulating the phenomenon of a swarm of schools of fishes or flocks of birds competing for food (Toha and Tokhi 2011). PSO is designed to operate on a swarm of particles where each particle represents a candidate solution to the optimization problem (Al-Mahturi and Wahid 2017). These particles are arranged in an n-dimensional search space and a randomized selection of positions and velocities for their best values. The flying experience of each particle swarm automatically adjusts the velocity of the individual alongside the other particles in the swarm. The drawback to this technique is that it cannot directly handle multi-objective optimization problems and may not converge for large parametric modeling (large variables).

Juang et al. proposed an evolutionary algorithm methodology using Real-coded Genetic Algorithm (R-GA) for the parametrized modeling and optimization of PID controller gains to control the TRMS (Juang *et al.* 2008). The simulations results were not satisfactorily optimal due to the bang-bang inputs used and the highly oscillatory results obtained. Intelligent systems are employed to intelligently tune or determine the best possible values of the system parameters (decision variables) for optimum system performance. Some of the techniques used have been mentioned above already under "Intelligence control schemes". Mostly these schemes are nature-inspired or biologically inspired (bio-inspired) from living organisms or natural processes. In this paper, a Multi-Objective GA (MOGA) algorithm is employed for tuning custom-designed PID controller parameters for optimized performance. The preponderating advantage of the simple design reposes/stands in the compromise on the various control performance requirements or preconditions. The paper organization is as follows: Section 1 introduces the TRMS and control strategies developed by researchers; Section 2 reviews related literature; Section 3 focuses on the mathematical modelling; while section 4 discusses the intelligent bio-inspired JSOA-PID controller design and tuning process utilized; Section 5 presents and discusses simulation and experimental results obtained and the further discussions of the results; with a conclusion drawn at the end in Section 6.

MATHEMATICAL/ANALYTICAL MODELLING OF THE TRMS

The mathematical models used are based on the rotations of the asymmetrically weight-distributed beam of the TRMS owing to the unequal weights of the main and tail rotor assemblages placed end to end. The TRMS as a dynamic system is modelled (i.e. described by equations) using the phenomenological model (Instruments 2000; Agrawal 2013).

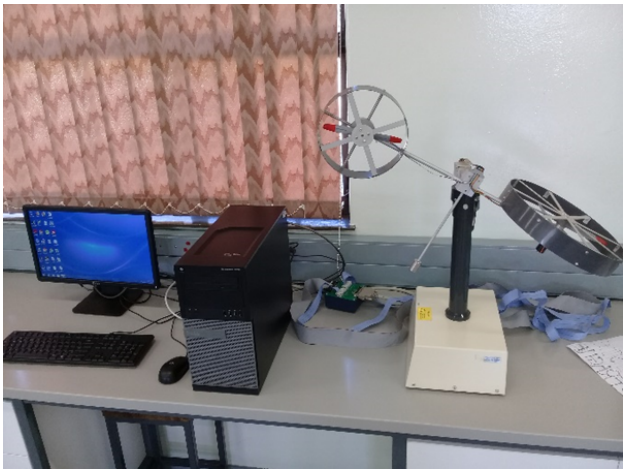

(a) A setup of the TRMS in the Measurements Control and Instrumentation Laboratory of the Botswana International University of Science and Technology (BIUST)

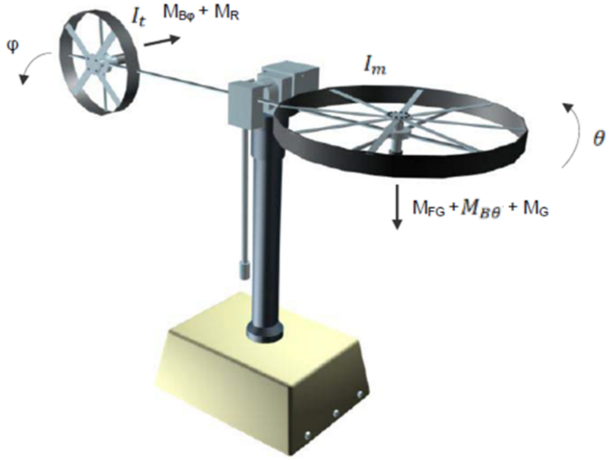

(b) Phenomenological model of the TRMS (Instruments 2006)

Figure 1 (a) A setup of the TRMS and (b) Phenomenological model of the TRMS

Equations of Motion governing the TRMS Based on Newton-Euler Approach

Let u_1, u_2 represent the two DC Stepper motors input voltages (for the pitch and yaw channels) respectively and τ_1, τ_2 represent their corresponding output torques. The torque-developed equations due to the resulting rotations can be modelled as:

$$\begin{aligned} \tau_1 &= \frac{K_1}{T_{11}s + T_{10}} u_1 \\ \tau_2 &= \frac{K_2}{T_{21}s + T_{20}} u_2 \end{aligned} \tag{1}$$

where $K_1, K_2, T_{10}, T_{11}, T_{21}, T_{20}$ are some lumped-parameter motor constants (motor torque constants, back emf constants, etc.) that have been determined experimentally (Instruments 2006).

Summing moments and forces acting on the system about the pitch axis for vertical motion yields the general form of the torque-developed equation of motion about the pitch plane (Raghavan and Thomas 2017; Instruments 2006; Chaudhary and Kumar 2019a,b; Sodhi and Kar 2014) as:

$$I_m\ddot{\theta} = M_m - M_{FF} - M_{B\theta} - M_G \tag{2}$$

$$M_m = \alpha_1\tau_1^2 + b_1\tau_1 \quad \text{(nonlinear static characteristic)} \tag{3}$$

$$M_{B\theta} = B_{1\theta}\dot{\theta} - B_{2\theta}\sin(2\theta)\dot{\varphi}^2 \quad \text{(friction forces momentum)} \tag{4}$$

$$M_{FF} = M_g\sin(\theta) \quad \text{(gravity momentum)} \tag{5}$$

$$M_G = K_{gy}M_m\dot{\varphi}\cos(\theta) \quad \text{(gyroscopic momentum)} \tag{6}$$

Equations (3-6) are the momentum equations acting on the vertical plane.

Similarly, summing moments and forces acting on the system about the yaw axis yields the general form of the developed torque equation for motion about the yaw plane (Raghavan and Thomas 2017; Instruments 2006; Chaudhary and Kumar 2019a,b) as:

$$I_t\ddot{\phi} = M_t - M_{B\phi} - M_{CR} \tag{7}$$

where

$$M_t = \alpha_2\tau_2^2 + b_2\tau_2 \quad \text{- nonlinear static characteristics} \tag{8}$$

$$M_{B\phi} = B_1\phi\phi + B_2\theta\text{sign}\dot{\phi} \quad \text{- fric. forces momentum} \tag{9}$$

$$M_{CR} = K_c\left(\frac{T_os+1}{T_ps+1}\right)M_m \quad \text{- approx. cross-reactn momentum} \tag{10}$$

Where equations (8-10) are the momentums acting on the horizontal plane due to the rotational dynamics of the twin rotors.

Substituting equations (3-6) into (2) and (8-10) into (7) result in 2 differential algebraic equations with $\ddot{\theta}$ and $\ddot{\phi}$ numerically given by:

$$\begin{aligned} \ddot{\theta} &= \frac{1}{I_m}\Big(\alpha_1\tau_1^2 + b_1\tau_1 - Mg\sin\theta \\ &\quad - \left(B_{1\theta}\dot{\theta} - B_{2\theta}\sin(2\theta)\dot{\phi}^2\right) \\ &\quad - K_{gy}M_m\dot{\phi}\cos\theta\Big) \\ &= \frac{1}{I_m}\Big(\alpha_1\tau_1^2 + b_1\tau_1 - Mg\sin\theta \\ &\quad - B_{1\theta}\dot{\theta} + B_{2\theta}\sin(2\theta)\dot{\phi}^2 \\ &\quad - K_{gy}(\alpha_1\tau_1^2 + b_1\tau_1)\dot{\phi}\cos\theta\Big) \end{aligned} \tag{11}$$

$$\begin{aligned} \ddot{\phi} &= \frac{1}{I_t}\Big(\alpha_2\tau_2^2 + b_2\tau_2 - B_{1\phi}\dot{\phi} \\ &\quad - \frac{K_c(T_Ds+1)}{T_Ps+1}M_m\Big) \\ &= \frac{1}{I_t}\Big(\alpha_2\tau_2^2 + b_2\tau_2 - B_{1\phi}\dot{\phi} \\ &\quad - \frac{K_c(T_Ds+1)}{T_Ps+1}(\alpha_1\tau_1^2 + b_1\tau_1)\Big) \end{aligned} \tag{12}$$

These wholly define the equations of motion for the TRMS. The MATLAB/Simulink implementation of these equations for modeling, simulations, and control purposes is shown below:

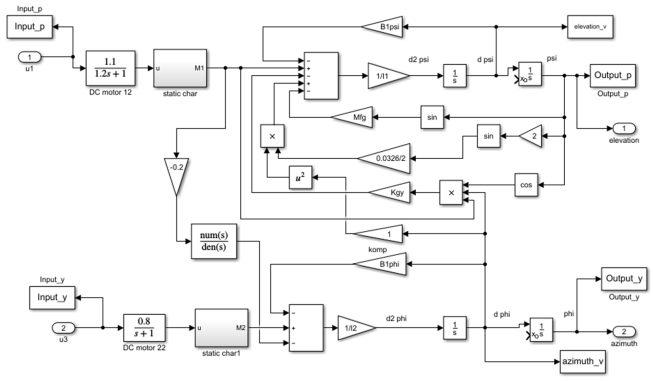

Figure 2 TRMS full implementation in Simulink

State-Space Models

The dynamic state of the linear plant given by the state-space representation (Chaudhary and Kumar 2019a) using dynamic equation is:

$$\dot{x} = Ax + Bu, \quad y = Cx + Du \tag{13}$$

The state vector x, input vector u, and output vector y for the system are given by equations (14-16)

$$x = \begin{bmatrix} \theta & \phi & \dot{\theta} & \dot{\phi} & \tau_1 & \tau_2 & M_{CR} \end{bmatrix}^T \tag{14}$$

$$u = \begin{bmatrix} u_1 & u_2 \end{bmatrix}^T \tag{15}$$

$$y = \begin{bmatrix} \theta & \phi \end{bmatrix}^T \tag{16}$$

Modelling of the 2-DOF TRMS

Using the state, input and output vectors (equations (14-16)), the complete 2-DOF TRMS dynamic equations for the system can be modelled and in state-variable form by:

$$\begin{cases} \frac{d}{dt}\dot{\theta} = \dot{\theta} \\ \frac{d}{dt}\dot{\phi} = \dot{\phi} \\ \frac{d}{dt}\dot{\theta} = -\frac{Mg}{I_m}\sin\theta - \frac{B_{1\theta}}{I_m}\dot{\theta} + \frac{B_{2\theta}}{I_m}\sin(2\theta)\dot{\phi}^2 \\ \qquad + \left(1 - K_{gy}\dot{\phi}\cos\theta\right)\frac{\alpha_1\tau_1^2}{I_m} + \left(1 - K_{gy}\dot{\phi}\cos\theta\right)\frac{b_1\tau_1}{I_m} \\ \frac{d}{dt}\dot{\phi} = -\frac{B_{1\phi}}{I_t}\dot{\phi} + \left(1 - \frac{K_c(T_Ds+1)}{T_ps+1}\right)\frac{\alpha_2\tau_1^2}{I_t} \\ \qquad + \left(1 - \frac{K_c(T_Ds+1)}{T_ps+1}\right)\frac{b_2\tau_1}{I_t} \\ \frac{d}{dt}\tau_1 = -\frac{T_{10}}{T_{11}}\tau_1 + \frac{K_1}{T_{11}}u_1 \\ \frac{d}{dt}\tau_2 = -\frac{T_{20}}{T_{21}}\tau_2 + \frac{K_2}{T_{21}}u_2 \\ \frac{d}{dt}M_{CR} = \frac{d}{dt}\left(\frac{K_c(T_os+1)}{T_ps+1}\alpha_1\tau_1^2\right) + \frac{d}{dt}\left(\frac{K_c(T_os+1)}{T_ps+1}b_1\tau_1\right) \\ \qquad = 2\alpha_1\frac{K_c(T_os+1)}{T_ps+1}\tau_1\dot{\tau}_1 + b_1\frac{K_c(T_os+1)}{T_ps+1}\dot{\tau}_1 \end{cases} \tag{17}$$

or,

$$\dot{x} = \begin{bmatrix} x_3 \\ x_4 \\ -\frac{Mg}{I_m}\sin x_1 - \frac{B_{1x_1}}{I_m}x_2 + \frac{B_{2x_1}}{I_m}\sin(2x_1)x_4^2 \\ \quad + \frac{b_1}{I_m}x_6 - K_{gy}\frac{b_1}{I_m}\cos x_1 x_4 x_6 + \frac{\alpha_1}{I_m}x_6^2 \\ \quad - K_{gy}\frac{\alpha_1}{I_m}\cos x_1 x_4 x_6^2 \\ -\frac{B_{1x_3}}{I_t}x_4 + \left(1 - \frac{K_c(T_Ds+1)}{T_ps+1}\right)\frac{b_2}{I_t}x_6 \\ \quad + \left(1 - \frac{K_c(T_Ds+1)}{T_ps+1}\right)\frac{\alpha_2}{I_t}x_6^2 \\ -\frac{T_{10}}{T_{11}}x_6 \\ -\frac{T_{20}}{T_{21}}x_7 \\ 2\alpha_1\frac{K_c(T_os+1)}{T_ps+1}x_6\dot{x}_6 + \frac{K_c(T_os+1)}{T_ps+1}b_1\dot{x}_6 \end{bmatrix} + \begin{bmatrix} 0 & 0 & 0 & 0 & 0 & \frac{K_1}{T_{11}} & 0 \\ 0 & 0 & 0 & 0 & 0 & 0 & \frac{K_2}{T_{21}} \end{bmatrix}^T u$$

$$y = \begin{bmatrix} x_1 & x_2 \end{bmatrix}^T \tag{18}$$

INTELLIGENT CONTROL DESIGN

Bio-Inspired/Nature-Inspired Algorithm Design Based on a novel metaheuristic Jumping Spider Optimization Algorithm (JSOA)

In this research, the novel metaheuristic technique called Jumping Spider Optimization Algorithm (JSOA) is used as the optimization strategy for controllers' tuning. It is a Biologically-Inspired and Nature-Inspired optimization strategy inspired by the hunting habits of Arachnida Salticidae spider species (Peraza-Vázquez *et al.* 2022). JSOA mimics the behaviour of spiders in nature, modelling how it hunts for food/prey using a search, persecution, and jumping prowess and artistry (skills) to catch and kill (or prey) for its meal. Just like other evolutionary metaheuristics, this strategic hunting scheme or ruse of search, persecution, and jumping are harnessed to strike a balance over the entire solution space (search space) between exploitation and exploration. This is intended in solving a global optimization problem.

In this study, JSOA is used as an optimization algorithm to parametrically tune the PID controllers' gains in a decentralized control system architecture of the underactuated TRMS plant. In addition to the algorithm globally converging for the multi-objective problem, its performance is tested by comparing against several notable, popular, and well-established metaheuristics algorithms of Genetic Algorithm (GA), Pattern Search, Simulated Annealing, and Particle Swarm Optimization (PSO). The results (in tables and graphs) revealed that the proposed algorithm outperforms the aforementioned algorithms and is capable of solving real-world problems that can be considered very challenging with unknown search or solution spaces.

In the TRMS controller design, an optimization problem is setup where the gains of the PID controllers are set as the parameters to be optimized by the JSOA metaheuristic optimizer.

Modelling of the JSOA Optimization Algorithm

The proposed JSOA considers four hunting strategies of the spiders: attacking by persecution, search, jumping on prey and pheromone rate.

Attacking by Persecution The stealthy jumping to catch movements made by the spider in attacking its prey is modelled using Newton's third equation for linear or rectilinear motion. The spider moves along its coordinate axis with increasing or decreasing velocity at constant/uniform velocity linearly with time and given by:

$$x_i = \frac{1}{2}at^2 + v_o t \tag{19}$$

where x_i is the position of the ith follower spider, v_o, a, and t follow the usual conventional definition for the initial speed, acceleration, and time respectively. The optimization procedure is an iterative procedure where each iteration $x_i(t)$ is defined in terms of position with disparity in iterations equalling 1. The initial velocity $v_o = 0$.

$$\vec{x}_i(t+1) = \vec{x}_i(t) - \vec{x}_r(t) \tag{20}$$

where $\vec{x}_i(t+1)$ is the updated displacement of the jumping spider Search Agent (SA) of $(t+1)$ generation, $\vec{x}_i(t)$ is the prevailing or current ith SA in the tth generation, and $\vec{x}_r(t)$ is the rth SA for a randomly selected $r \neq i$ where r is a randomized integer in the interval between 1 and the maximum size of SAs. This is depicted as shown in Figure 3.

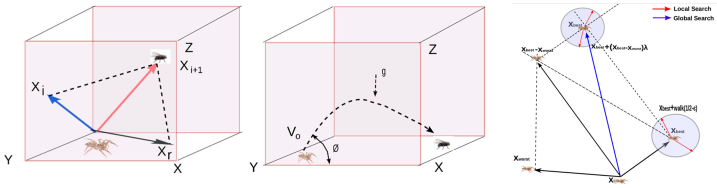

Figure 3 (a) Jumping Spider performing persecution (b) Jumping on prey under a projectile-like motion (c) The local and global search vectorizations (Peraza-Vázquez *et al.* 2022)

Jumping on Prey The jumping spider attacks and pounces on its prey in a projectile motion fashion. It is decomposed into its horizontal and vertical components and given by:

$$\begin{cases} \vec{x}_i = v_o(a)t\vec{i} \\ \dfrac{dx}{dt} = \vec{V}_x = v_o(a)\vec{i} \end{cases} \tag{21}$$

$$\begin{cases} \vec{y}_l = \left(v_o \sin(a)t - \dfrac{1}{2}gt^2\right)\vec{i} \\ \dfrac{dy}{dt} = \vec{V}_y = (v_o \sin(a) - gt)\,\vec{i} \end{cases} \tag{22}$$

Where equations (21) and (22) represent the horizontal and vertical components respectively. Therefore the equation for the trajectory is given as:

$$y = x\tan(a) - \frac{gx^2}{2V_o^2\cos^2(a)} \tag{23}$$

The trajectory w.r.t the iterations in the succeeding generations is therefore given by:

$$\vec{x}_l(t+1) = \vec{x}_l(t)\tan(a) - \frac{g\vec{x}_l^2(t)}{2V_o^2\cos^2(a)} \tag{24}$$

where $\vec{x}_l(t+1)$= the new displacement/position of the new search agent, $\vec{x}_l(t)$= the current ith search agent, $\vec{V}_x$=100 mm/sec, g=9.80665 m/s^2 is the acceleration due to gravity and a is the angle determined by a randomly generated ϕ angle lying between the interval (0, 1).

$$a = \phi\pi/180 \tag{25}$$

Searching for Prey JSOA in searching for prey executes a random search within the search space in order to locate its prey. Both the local and global search models have been developed and used in the JSOA approach. The local search is modelled as:

$$\vec{x}_l(t+1) = \vec{x}_{\text{best}}(t) + \text{walk}\left(\frac{1}{2} - \epsilon\right) \tag{26}$$

where $\vec{x_{best}}(t)$ is the best SA/solution from the preceding generation (or iteration), walk is a pseudo-random number (PRBS) generated with a Gaussian distribution in the interval $[-2, 2]$, and ϵ is a PRBS generated in the interval $[0, 1]$. The formulation for the global search model is given by:

$$\vec{x}_i(t+1) = \vec{x_{best}}(t) + \beta\left(\vec{x_{best}}(t) - \vec{x_{worst}}(t)\right) \tag{27}$$

where $\vec{x_{worst}}(t)$ is the worst SA (or solution) found in the preceding generation/ iteration, β is a Cauchy random number with mean $\mu = 0$ and variance $\sigma = 1$.

Pheromone's Rate Pheromone is a chemical substance/secretion secreted externally by the body of an individual jumping spider which is being perceived by the olfactory lobes of another individual that influences the physiology or behavior of the other individual animal of the same species. Pheromone is not unique to the jumping spider alone but a biological process shared with many animals particularly insects or arachnids. The modeling of the rate of pheromone production in jumping spider is given as:

$$\text{pheromone}(i) = \frac{\text{Fitness}_{best} - \text{Fitness}(i)}{\text{Fitness}_{best} - \text{Fitness}_{worst}} \tag{28}$$

where Fitness_{best}, Fitness_{worst} are the best and worst fitness values in the current generation/iteration respectively. The fitness values are normalized in the interval $(0, 1)$, the bounds corresponding to the worst and best pheromone rates respectively. For low or subjacent pheromone rates (pheromone$(i) \leq 0.3$) the position/displacement is recalculated by:

$$\vec{x}_l(t) = \vec{x}_{\text{best}}(t) + \gamma\left(\vec{x}_{r_1}(t) - (-1)^{\sigma}\vec{x}_{r_2}(t)\right) \tag{29}$$

where $\vec{x}_l(t)$ is the SA (but this time with low pheromone rate for updating, r_1, r_2 are random integers numbers randomized within the interval of $[1, \text{maximum size of SAs}]$, $r_1 \neq r_2$, $\vec{x}_{r_1}(t), \vec{x}_{r_2}(t)$ represent the r_1th r_2th search agents randomly selected, σ is binary random number generated i.e. $\sigma \in [0, 1]$.

SIMULATIONS RESULTS AND DISCUSSIONS

Design, modeling, simulations, and algorithms optimizations were carried out. The following results were obtained as explained in this section.

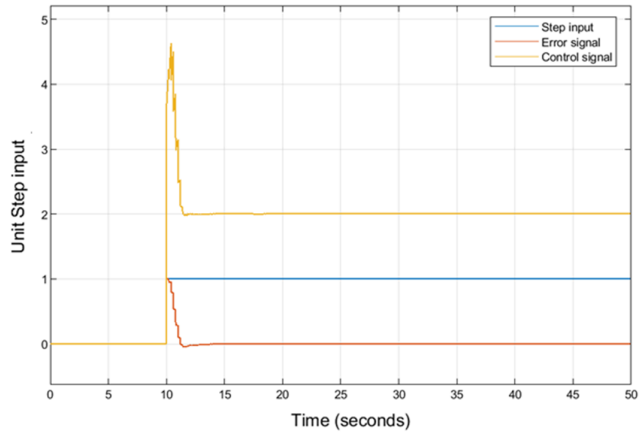

Figure 4 Control & error signals compared against step input signal

The PID controller configuration shows the control action of the controller in response to non-zero input and the error (Figure 4). The basic task of intelligent control is the controller-tuning design problem where satisfactory values for the adjustable parameters like the proportional gain, normalized gain, and integral time must be found to satisfy or achieve the desired closed loop requirements for a given system or process.

Results from Linearization of the TRMS Plant

Using the formulations presented in Klee and Allen (2018) for linearizing a nonlinear system about an operating point based on the Jacobian matrix of the vector-valued function $f(t, \underline{x}, \underline{u})$ which defines the state derivatives in MATLAB/SIMULINK software, the following useful results were directly obtained:

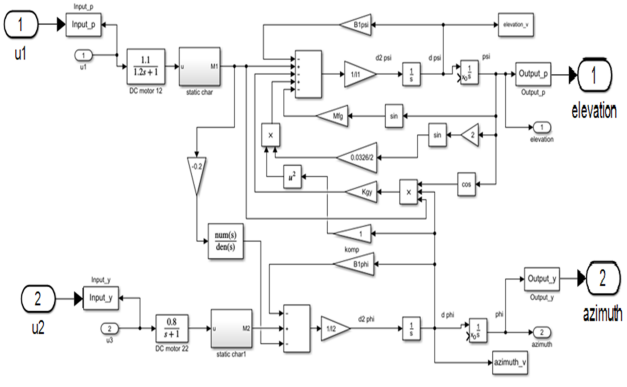

Figure 5 TRMS Simulink Nonlinear model prepared for linearization

Note: u_1, u_2 are the step inputs to the TRMS system while elevation and azimuth are the pitch & yaw outputs. The A, B, C, D system matrices were obtained to be:

$$A = \begin{bmatrix} 0 & 0 & 1 & 0 & 0 & 0 & 0 \\ 0 & 0 & 0 & 1 & 0 & 0 & 0 \\ -4.706 & 0 & -0.08824 & 0 & 1.246 & 0 & 0 \\ 0 & 0 & 0 & -5 & 1.482 & 3.6 & 18.75 \\ 0 & 0 & 0 & 0 & -0.8333 & 0 & 0 \\ 0 & 0 & 0 & 0 & 0 & -1 & 0 \\ 0 & 0 & 0 & 0 & -0.01694 & 0 & -0.5 \end{bmatrix},$$

$$B = \begin{bmatrix} 0 & 0 \\ 0 & 0 \\ 0 & 0 \\ 0 & 0 \\ 1 & 0 \\ 0 & 1 \\ 0 & 0 \end{bmatrix},$$

$$C = \begin{bmatrix} 1 & 0 & 0 & 0 & 0 & 0 & 0 \\ 0 & 1 & 0 & 0 & 0 & 0 & 0 \end{bmatrix},$$

$$D = \begin{bmatrix} 0 & 0 \\ 0 & 0 \end{bmatrix} \tag{30}$$

Representing the system matrices in transfer function transform the continuous-time state-space system matrices to the following equations in the frequency-domain:

$$\begin{cases} G_{11} = \dfrac{1.246}{s^3 + 0.9215s^2 + 4.78s + 3.922} \\ G_{21} = \dfrac{1.482s + 0.4234}{s^4 + 6.333s^3 + 7.083s^2 + 2.083s} \\ G_{12} = 0 \\ G_{22} = \dfrac{3.6}{s^3 + 6s^2 + 5s} \end{cases} \tag{31}$$

As can be seen from the 4 transfer functions obtained (equation 31) for our particular TRMS plant, there are main rotor - yaw plane or axis i.e., G_{21} interactions or cross couplings but there seems to be no interaction at all between the tail rotor and the pitch axis or pitch plane, i.e., G_{12}. There is therefore the need to design a decoupler to eliminate or reduce to the barest the G_{21} interactions offered by the tail rotor (powered by its DC motor) which serves as disturbance to the movements/ rotations about the yaw axis.

Let G_m and G_t represent the pitch & yaw planes' transfer functions respectively of the decoupled system. Making substitutions for $G_{11}, G_{12}, G_{21}, G_{22}$ to obtain G_m and G_t respectively, in MATLAB, as:

$$\begin{cases} G_m = \dfrac{1.246}{s^3 + 0.9215s^2 + 4.78s + 3.922} \\ G_t = \dfrac{3.66}{s^3 + 6s^2 + 45s} \end{cases} \tag{32}$$

Optimizing the pitch model of the TRMS is tasking and very involved because of the system complexity and the cross-correlational existing between the main and tail rotors' effects.

Results from Decoupling the TRMS

Accordingly, from equation 34 it follows that

$$\begin{cases} G_{\text{inv}11}(s) = 0.8026s^3 + 0.74s^2 + 3.2s + 3.144 \\ G_{\text{inv}12}(s) = 0 \\ G_{\text{inv}21}(s) = \dfrac{-0.3304s^7 - 2.381s^6 - 5.711s^5 - 13.74s^4 - 19.18s^3}{s^4 + 6.333s^3 + 7.083s^2 + 2.083s + 2.637 \cdot 10^{-13}} \\ \qquad\qquad + \dfrac{-10.96s^2 - 1.851s + 1.982 \cdot 10^{-12}}{s^4 + 6.333s^3 + 7.083s^2 + 2.083s + 2.637 \cdot 10^{-13}} \\ G_{\text{inv}22}(s) = 0.2778s^3 + 1.667s^2 + 1.389s \end{cases} \tag{33}$$

Using the simplified decoupling technique/methodology based on the generalized procedure of matrix inversion formula (Yang *et al.* 2016), the decoupling plant transfer matrix $G_R(s)$ as presented in (Yang *et al.* 2016) is expressed as:

$$G_R(s) = \begin{bmatrix} G_m(s) & 0 \\ 0 & G_t(s) \end{bmatrix} \tag{34}$$

where $G_m(s)$, $G_t(s)$ are the decoupled transfer functions for the main and tail rotors subsystems respectively and given by equation (32). To obtain the decoupling matrix, we apply equations given in (Yang *et al.* 2016) to get:

$$G_D(s) = \begin{bmatrix} G_{D11}(s) & G_{D12}(s) \\ G_{D21}(s) & G_{D22}(s) \end{bmatrix} \tag{35}$$

So that

$$\begin{cases} G_{D11}(s) = \dfrac{s^3 + 0.9215s^2 + 4.78s + 3.922}{s^3 + 0.9215s^2 + 4.78s + 3.922} = 1 \\ G_{D12}(s) = 0 \\ G_{D21}(s) = \dfrac{-0.4117s^7 - 2.967s^6 - 7.116s^5 - 17.12s^4 - 23.9s^3}{s^7 + 7.255s^6 + 17.7s^5 + 42.8s^4 + 60.61s^3} \ldots, \\ \qquad\qquad \dfrac{-13.65s^2 - 2.306s + 2.47 \times 10^{-12}}{37.74s^2 + 8.17s + 1.034 \times 10^{-12}} \\ G_{D22}(s) = \dfrac{s^3 + 6s^2 + 5s}{s^3 + 6s^2 + 5s} = 1 \end{cases} \tag{36}$$

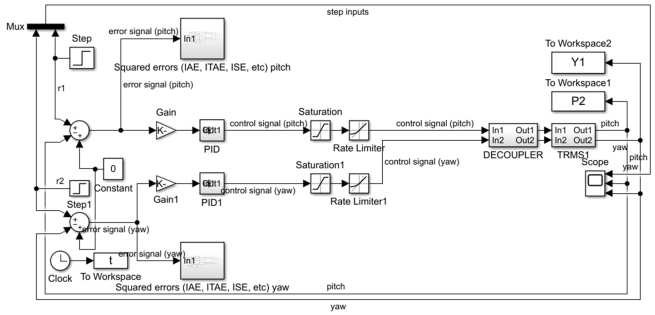

(a) Control system designed for optimizing with JSOA intelligent scheme

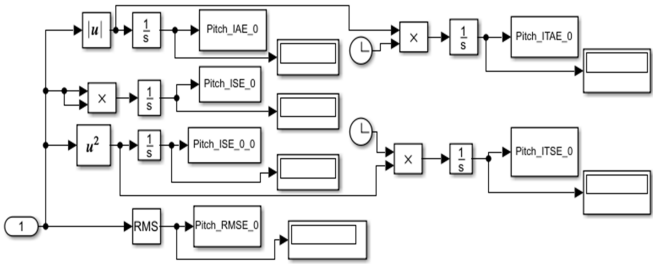

(b) Squared errors (IAE, ITAE, ISE, etc.) pitch

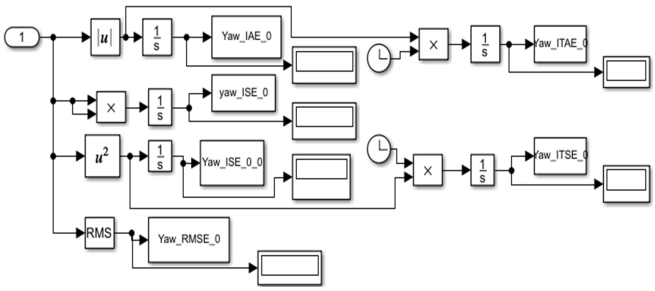

(c) Squared errors (IAE, ITAE, ISE, etc.) yaw

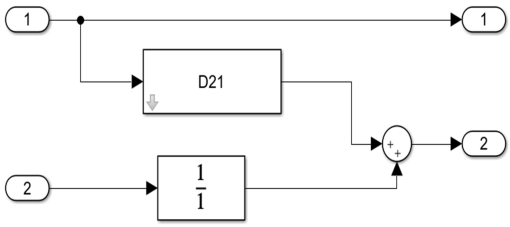

(d) Decoupler

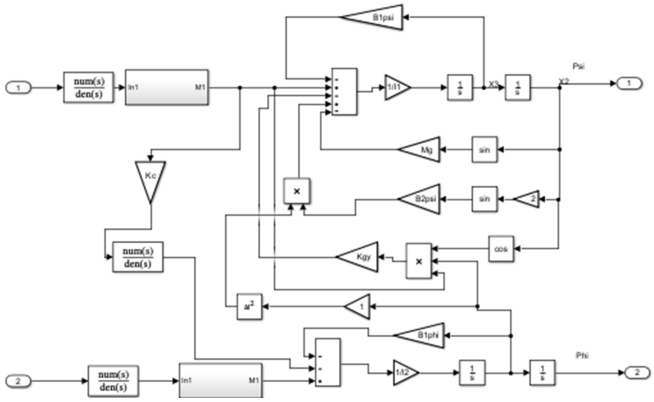

(e) TRMS1

Figure 6 (a) Control system designed for optimizing with JSOA intelligent scheme, (b) Squared errors (IAE, ITAE, ISE, etc.) pitch, (c) Squared errors (IAE, ITAE, ISE, etc.) yaw, (d) Decoupler, (e) TRMS1

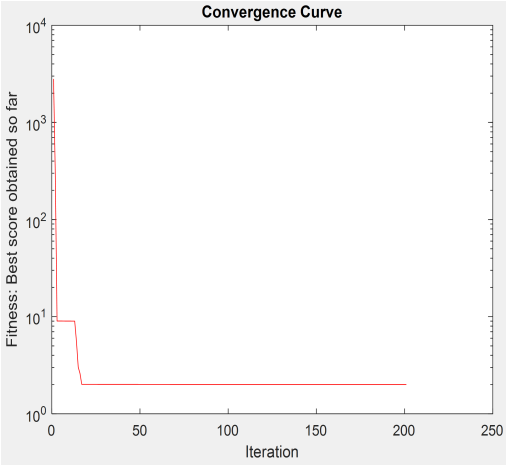

Figure 7 JSOA-PID Optimization convergence graph for 30 search agents (jumping spiders) and 200 generations

JSOA-PID Optimization Simulations Results

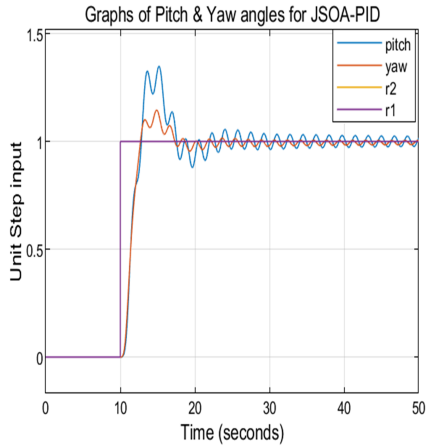

(a) With dead time

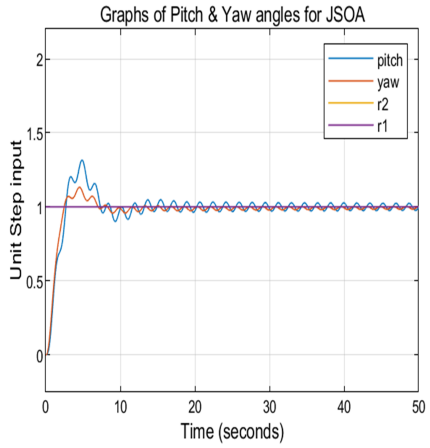

(b) Without dead time

Figure 8 Set-point tracking responses of pitch and yaw angles using JSOA-based controllers (a) With dead time (b) Without dead time

Multi-objective optimization algorithm was written and used with the JSOA code for faster convergence. JSOA is a slow converging procedure taking several hours or even days to converge depending on the size of the design variables, search agents/ number of iterations, population size, and other design settings used. An exponential relationship exists between number of search agents or population size and time to converge (the larger the population size, the more time required to converge). Also, another factor here is the size of the population. The visible vibrations or ripples seen on the plot resulted from the fact that the plant (i.e., TRMS) is a very stiff system as well as the significant cross-couplings. For this design, 30 search agents were employed.

Table 2 Baseline JSOA-PID controller's parameters/gains values

Parameters	K_p	K_i	K_d
Main	-1.2171	-1.2432	-2.3345
Tail	-2.3897	-0.0485	-2.026

Six (6) other methods or strategies were compared against JSOA strategy.

Performance Indices

The parameter tuning rules are based on the following performance measures: Integral of the Absolute Error (IAE), Integral of Time Absolute Error (ITAE), Integral Squared Error (ISE), Integral Time Squared Error (ITSE), and Root Mean Squared Error (RMSE). These measures or indicators are indices that show or indicate how well the system performed during the execution/run).

Objective Function

The objective function used is given by:

$$J(K_p, K_i, K_d, \theta, \phi) = 2 * (\omega_1 * \text{pitch (ISE)} + \omega_2 * \text{yaw (ISE)}) \quad (37)$$

where ω_1, ω_2 are some carefully chosen weighting coefficients. In this study, $\omega_1 = \omega_2 = 0.5$.

Fitness Function

The error signal minimization is achieved by the use of the PID controller via performance index minimization in the objective function value J. And we know that the smaller the J value of performance index of the corresponding search agent, the fitter the search agent will be and vice versa. Hence, J varies inversely to the fitness of the chromosomes. Therefore, the fitness of the chromosomes is defined as:

$$\text{Fitness function} = \frac{1}{J} = \frac{1}{2} * \frac{1}{\omega_1 * \text{pitch(ISE)} + \omega_2 * \text{yaw(ISE)}} \quad (38)$$

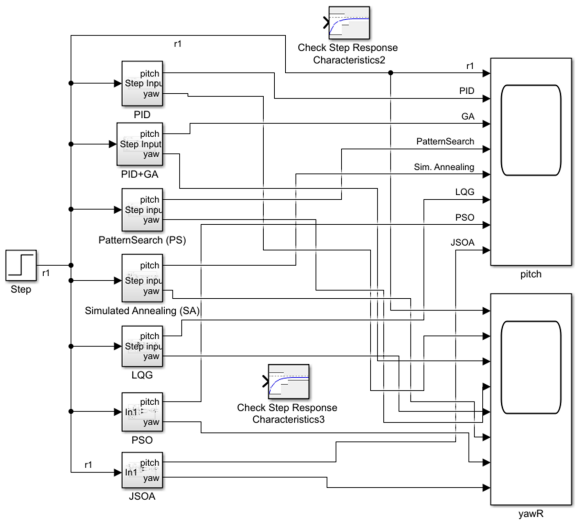

(a) Combined Simulink Model

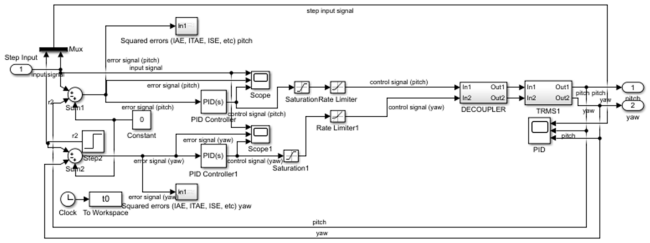

(b) PID Controllers

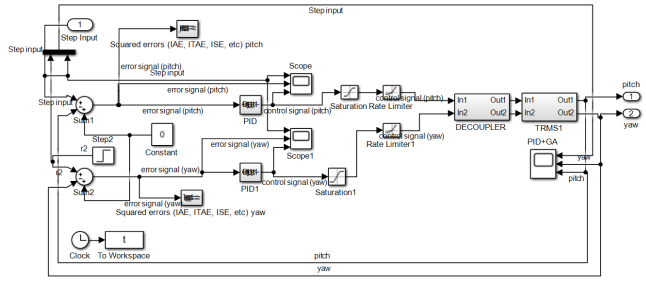

(c) PID+GA Controllers

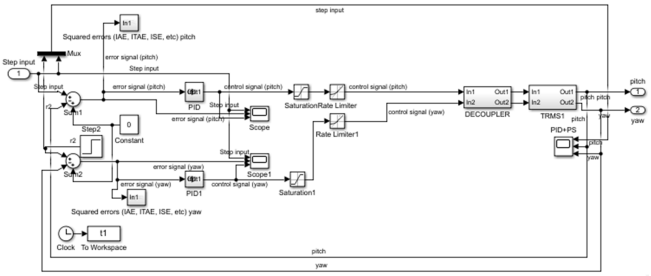

(d) PID+Pattern Search Controllers

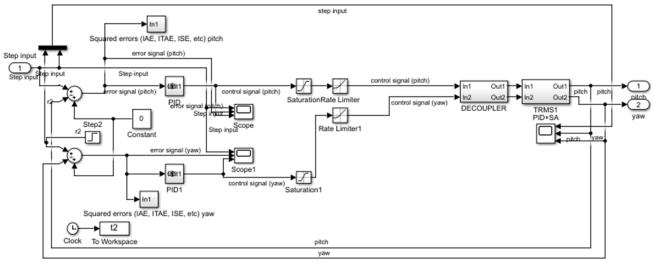

(e) PID+Simulated Annealing Controllers

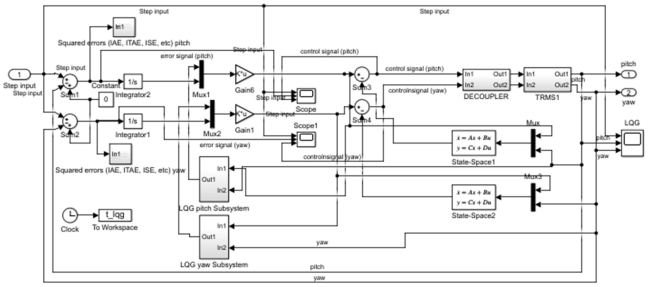

(f) LQG Controllers

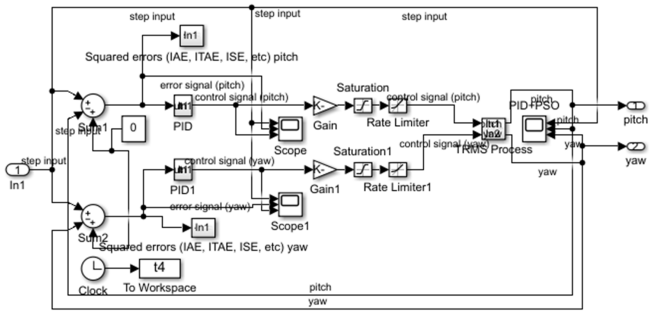

(g) PID+PSO Controllers

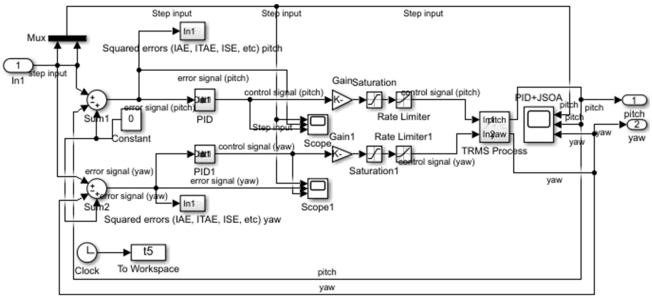

(h) PID+JSOA-based Controllers

Figure 9 Set-point tracking responses of the seven methods: (a) Combined Simulink Model, (b) PID Controllers, (c) PID+GA Controllers, (d) PID+Pattern Search Controllers, (e) PID+Simulated Annealing Controllers, (f) LQG Controllers, (g) PID+PSO Controllers, (h) PID+JSOA-based Controllers

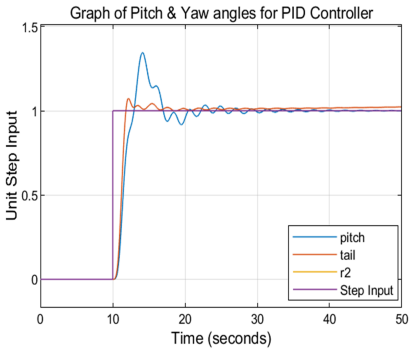

(a) Results for PID Controllers

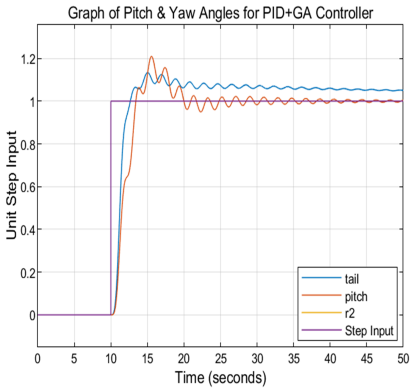

(b) Results for PID+GA Controllers

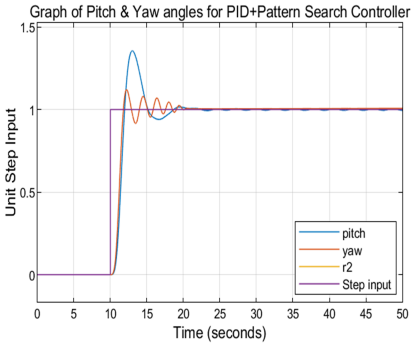

(c) Results for PID+Pattern Search Controllers

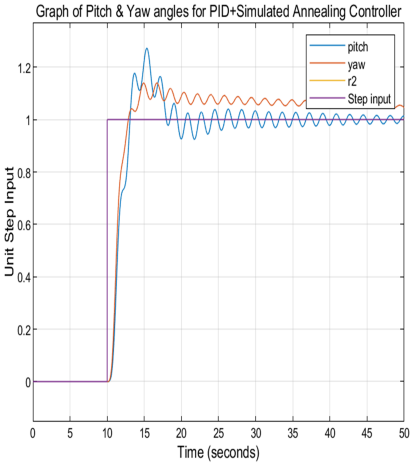

(d) Results for PID+Simulated Annealing Controllers

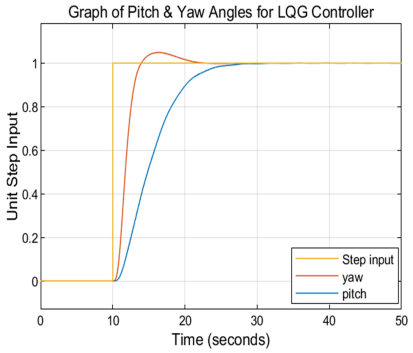

(e) Results for LQG Controllers

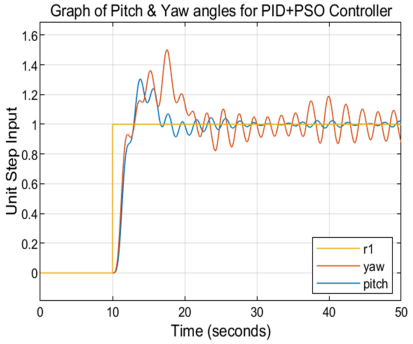

(f) Results for PID+PSO Controllers

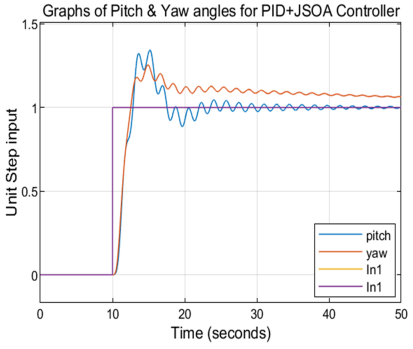

(g) Results for PID+JSOA-based Controllers

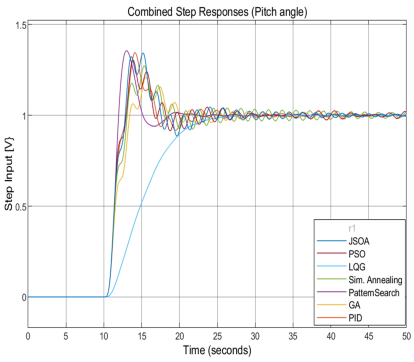

(h) Results for Combined Pitch Angles

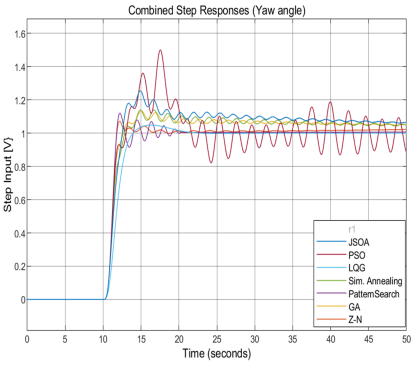

(i) Results for Combined Yaw Angles

Figure 10 (a) Results for PID Controllers, (b) Results for PID+GA Controllers, (c) Results for PID+Pattern Search Controllers, (d) Results for PID+Simulated Annealing Controllers, (e) Results for LQG Controllers, (f) Results for PID+PSO Controllers, (g) Results for PID+JSOA-based Controllers, (h) Results for Combined Pitch Angles, (i) Results for Combined Yaw Angles

Table 3 Summary of PID parameters for six methods

Method	Horizontal plane K_p	Horizontal plane K_i	Horizontal plane K_d	Vertical plane K_p	Vertical plane K_i	Vertical plane K_d
PID	7.5803	-0.2479	9.7221	1.7053	2.1643	3.0066
GA	4.9553	0.0693	5.2448	2.1593	1.5238	3.9310
LQG	–	–	–	–	–	–
Pattern Search	11.7969	-0.2656	19.2324	1.2267	2.5595	1.7598
Simulated Annealing	4.7778	0.0835	5.8484	2.6264	2.0038	4.5171
PSO	-8.2211	-2.6907	-19.9187	-12.8273	-12.0269	-19.9996
JSOA	-2.3897	-0.04852	-2.026	-1.2171	-1.2432	-2.3345

Table 4 Quantitative comparison of the proposed JSOA-PID controller and six other controllers design strategies with performance indices for pitch & yaw angles

Controller Method	Horizontal plane ϕ angle IAE	Horizontal plane ϕ angle ITAE	Horizontal plane ϕ angle ISE	Horizontal plane ϕ angle ITSE	Horizontal plane ϕ angle RMSE	Vertical plane θ angle IAE	Vertical plane θ angle ITAE	Vertical plane θ angle ISE	Vertical plane θ angle ITSE	Vertical plane θ angle RMSE
PID	1.787	31.32	0.997	10.72	0.02268	2.583	35.38	1.364	15.3	0.0009143
GA	3.78	87.21	1.193	15.58	0.04985	2.858	43.47	1.417	15.92	0.008896
LQG	2.068	24.49	1.384	15.02	0.000004	5.501	76.03	3.645	45.38	0.000003
Pattern Search	1.638	21.5	1.007	10.7	0.004712	2.29	30.04	1.327	14.63	0.003673
Simulated Annealing	3.946	90.81	1.243	16.47	0.04331	3.278	58.43	1.382	16.08	0.03074
PSO	4.109	76.61	1.551	20.9	0.002231	2.723	41.4	1.318	14.84	0.0008534
JSOA	2.008	14.6	0.904	0.7934	0.002157	3.138	28.47	1.194	2.041	0.003753

CONCLUSION

The score or performance of JSOA alongside other techniques used in this study are quantified in tables and graphs. It is seen that the optimum solution for the controller parameters K_p, K_i, and K_d values for the pitch are -1.2171, -1.2432, & -2.3345 while for the yaw are -2.3897, 0.0485, & -2.026 respectively. These global solutions converged after about 22 hrs of simulation time in MATLAB/Simulink software. For PID, Pattern Search and Simulated Annealing, the values obtained were: ZN: 7.5803, -0.2479, 9.7221, 1.7053, 2.1643, & 3.0066, Pattern Search: 11.7969, -0.2656, 19.2324, 1.2267, 2.5595, 1.7598; Simulated Annealing: 4.7778, 0.0835, 5.8484, 2.6264, 2.0038, 4.5171 respectively for the pitch and yaw. In terms of performance on a comparative scale, the fitness function for JSOA is 0.953288847 or 95.3%.

From the final plot (figure 9), a cursory look suggests that GA did not perform well (worst performing) while JSOA was the best performing among the optimization techniques in spite of the stiffness offered by the system, though the yawning action has an unresolved error that continued at the steady state, which is not surprising. This is because of the computational effort required (figure 4). The graphs confirm that methods like GA are unsuitable for optimizing nonlinear systems.

The physical significance of these results is that with a PID controller, the derivative gain (D) can have a different sign from the integral gain (I), in order to return a stable controller even if one or more gains are negative. This is in order for phase adjustment in the loop, if the plant is non-minimum phase. The TRMS is clearly a non-minimum phase system, having a pole or zero at the origin and so can be made asymptotically stable. This means the system

Table 5 Objective function values against Controller design strategy for the seven methods

Controller Method	Yaw plane (ϕ angle) ISE	Pitch plane (θ angle) ISE	Objective function
PID	0.997	1.364	1.1805
GA	1.193	1.417	1.305
LQG	1.384	3.645	2.5145
Pattern Search	1.007	1.327	1.167
Simulated Annealing	1.243	1.382	1.3125
PSO	1.551	1.318	1.2309
JSOA	0.904	1.194	1.049

Table 6 Fitness function (or score) against Controller Design Strategy (Method) for the seven methods

Controller Method	Yaw plane (ϕ angle) ISE	Pitch plane (θ angle) ISE	Fitness score
PID	0.997	1.364	0.847098687
GA	1.193	1.417	0.766283525
LQG	1.384	3.645	0.397693378
Pattern Search	1.007	1.327	0.856898029
Simulated Annealing	1.243	1.382	0.761904762
PSO	1.551	1.318	0.697107006
JSOA	0.904	1.194	0.953288847

veers to the opposite direction first before following the prescribed trajectory.

In this study, white box modelling approach was used, where rotational kinematics equations developed by Newton and Euler were used to accurately describe the rotational forces and moments/momentums of the TRMS in flight. A PID controller was then subsequently developed for the decoupled and linearized plant, being a nonlinear, complex, system with dynamic couplings. To obtain the optimum values for the PID controller, JSOA was employed which was able to evolve a global solution readily without having to search through the entire solution search space, and time to process increases exponentially as the size of the search agents or population size. A maximum generation with population sizes of 100 and 30 respectively were used in this study. The fitness score of 0.953288847 or about 96% showed highly fit individuals as the global solution evolved, which is excellent for any meaningful control design performance in terms of reference tracking, trajectory tracking and servo and regulatory control.

This should be 'Controlling the TRMS using conventional means is a huge challenge, particularly tuning of the gains especially when the number of parameters to be tuned is large. For a stiff system, determining the gains by trial and error, may be impractically impossible, hence the need and use of intelligent methods like GA among others. Among the many intelligent techniques, JSOA has proven to be unique, in that it is capable of evolving the global solution with relative ease, including systems and processes with very fast changing dynamics. Ultimately the main idea about using optimization techniques in scientific and engineering studies of this kind is to help in tuning some goals (parameters/variables), so as to achieve the best possible or optimum values for our overall design. This is true in all fields of human endeavours.

Availability of data and material

Not applicable.

Conflicts of interest

The authors declare that there is no conflict of interest regarding the publication of this paper.

Ethical standard

The authors have no relevant financial or non-financial interests to disclose.

LITERATURE CITED

Agrawal, A. K., 2013 Optimal Controller Design for Twin Rotor MIMO System .

Al-Mahturi, A. and H. Wahid, 2017 Optimal Tuning of Linear Quadratic Regulator Controller Using a Particle Swarm Optimization for Two-Rotor Aerodynamical System. World Academy of Science, Engineering and Technology-International Journal of Electronics and Communication Engineering **11**: 196–203.

Basturk, H. I., 2006 Quasi-LPV Modelling and Control of Twin Rotor Multiple-Input Multiple-Output System .

Butt, S. S. and H. Aschemann, 2015 Multi-variable Integral Sliding Mode Control of a Two Degrees of Freedom Helicopter. 8th Vienna International Conference on Mathematical Modelling - MATHMOD 2015 .

Chaudhary, C. and A. Kumar, 2019a Control of Twin Rotor MIMO System using PID and LQR Controller. Journal of Aircraft and Spacecraft Technology **3**: 211–220.

Chaudhary, C. and A. Kumar, 2019b Control of Twin Rotor MIMO System using PID and LQR Controller. Journal of Aircraft and Spacecraft Technology **3**: 211–220.

Choudhary, S. K., 2017 H Optimal Feedback Control of a Twin Rotor MIMO System. International Journal of Modelling and Simulation **37**: 46–53.

Dimassi, H., S. H. Said, A. Loria, and F. M. M'Sahli, 2019 An Adaptive Observer for a Class of Nonlinear Systems with a High-Gain Approach. Application to the Twin-Rotor System. International Journal of Control **3**.

Ezekiel, D. M., S. Ravi, and O. Matsebe, 2020a Modelling of the Twin Rotor MIMO System (TRMS) Using the First Principles Approach. IEEE: 2020 International Conference on Computer, Communication, and Informatics (ICCCI) pp. 726–732.

Ezekiel, D. M., S. Ravi, and O. Matsebe, 2020b Pitch and Yaw Angular Motions (Rotations) Control of the 1-DOF and 2-DOF TRMS: A Survey. Archives of Computational Methods in Engineering .

Ghellab, M. Z., S. Zeghlache, and A. Bouguerra, 2018 Real-Time Implementation of Fuzzy Gain-Scheduled PID Controller for Twin Rotor MIMO System (TRMS). Advances in Modelling Analysis **73**: 137–149.

Instruments, F., 2000 Twin Rotor MIMO System Advanced Teaching Manual 33-007-4M5 .

Instruments, F., 2006 Twin Rotor MIMO System Control Experiments Manual: 33949S .

Juang, J.-G., R.-W. Lin, and W.-K. Liu, 2008 Comparison of Classical Control and Intelligent Control for a MIMO System. Applied Mathematics and Computation **205**: 778–791.

Klee, H. and R. Allen, 2018 Simulation of Dynamic Systems with MATLAB and Simulink .

Mondal, S., 2012a Adaptive Second Order Sliding Mode Control Strategies For Uncertain Systems .

Mondal, S., 2012b Adaptive Second Order Sliding Mode Control Strategies For Uncertain Systems .

Mondal, S. and C. Mahanta, 2012 Adaptive Second-Order Sliding-Mode Controller for a Twin Rotor Multi-Input–Multi-Output System. IET Control Theory and Applications **6**: 2157–2167.

Mones, M. and T. Diaa-Eldeen, 2017 Experimental Nonlinear Identification of a Lab-Scale Helicopter System using MLP Neural Network. 13th International Computer Engineering Conference (ICENCO) .

Peraza-Vázquez, H., A. Peña-Delgado, P. Ranjan, C. Barde, A. Choubey, *et al.*, 2022 A Bio-Inspired Method for Mathematical Optimization Inspired by Arachnida Salticidae. Mathematics **10**: 102.

Raghavan, R. and S. Thomas, 2017 Practically Implementable Model Predictive Controller for a Twin Rotor Multi-Input Multi-Output System. Journal of Control, Automation, and Electrical Systems **28**: 358–370.

Sodhi, P. and I. Kar, 2014 Adaptive Backstepping Control for A Twin Rotor MIMO System .

Tao, C. W., J. S. Taur, and Y. C. Chen, 2010 Design of a Parallel Distributed Fuzzy LQR Controller for the Twin Rotor Multi-Input Multi-Output System. Fuzzy Sets and Systems **161**: 2081–2103.

Toha, S. F. and M. O. Tokhi, 2010 Augmented feedforward and feedback control of a twin rotor system using real-coded moga. In *IEEE Congress on Evolutionary Computation*, Barcelona, Spain.

Toha, S. F. and M. O. Tokhi, 2011 PID and Inverse-Model-Based Control of a Twin Rotor System. Robotica **29**: 929–938.

Wen, P. and T.-W. Lu, 2008 Decoupling Control of a Twin Rotor MIMO System using Robust Deadbeat Control Technique. IET Control Theory & Applications **2**: 999–1007.

Yang, X., J. Cui, D. Lao, and J. Chen, 2016 Input Shaping Enhanced Active Disturbance Rejection Control for a Twin Rotor Multi-Input Multi-Output System (TRMS). ISA Transactions **62**: 287–298.

How to cite this article: Ezekiel, D. M., Samikannu, R., and Matsebe, O. Bio-Inspired Jumping Spider Optimization for Controller Tuning/Parameter Estimation of an Uncertain Aerodynamic MIMO System. *Chaos Theory and Applications*, 6(3), 205-217, 2024.

CHAOS
Theory and Applications
in Applied Sciences and Engineering

e-ISSN: 2687-4539
RESEARCH ARTICLE
Vol.6 / No.3 / 2024 / pp.218-227
https://doi.org/10.51537/chaos.1446633

3D Chaotic Nonlinear Dynamic Population-Growing Mathematical System Modeling with Multiple Controllers

Shaymaa H. Salih *,1, **Nadia M. G. Al-Saidi** *,2, **Suzan J. Obaiys** α,3 **and Yeliz Karaca** §,4

*Department of Applied Sciences, University of Technology, Baghdad, 10066, Iraq, αDepartment of Computer Systems and Technology, Faculty of Computer Science and Information Technology, University Malaya, Kuala Lumpur 50603, Malaysia, §University of Massachusetts (*UMass*) Chan Medical School, Worcester, MA 01655, USA.

ABSTRACT Modeling, stabilization, and identification processes are significant stages in the process of developing knowledge about chaotic dynamical systems which entail the effective prediction depending on the degree of uncertainty toleration in the forecast, accuracy of the current state to be measured as well as a time scale resting on the dynamics of the system. Control of under-activated dynamical systems has been considered substantially, and it is for periods and is currently developing in various domains such as biology, data analysis, computing systems, and so forth. Dynamic systems of growing population signifies a model describing the way a population evolves over time during which population goes through major life events, split into discrete time periods. The size of the population at a given time period is determined by the rate of growth as well as other related factors. Most progress has been made in model-based control theory, which has drawbacks when the system under consideration is exceedingly complicated, and no model can be constructed. Accordingly, a 3D-discrete and dynamic human population growth system with many controllers is proposed by examining the stability and symmetry of controller system clarifications. The symmetric stability control results are presented by considering a special parametric dynamic system in its coefficients besides suggesting periodic functional coefficients in terms of sin and cos functions. The controllers have the ability to reduce population growth rate unpredictability or enhance system stability under various external conditions. The unique and very effective strategies in relevant domains could provide a deeper understanding of their impact as well as the theoretical or technological innovations thereof. These controllers are capable of reducing population growth rate unpredictability or improving system stability under various external conditions, and applicable strategies in the relevant domains can provide profound comprehension over the impact along with the theoretical as well as technological advancements.

KEYWORDS
Control system
Dynamic system
Difference system
Stability analysis
Growing human population
Stabilization
Mathematical modeling
3D-discrete chaotic systems
Kendall coefficient
Discrete systems
Difference equation
Multiple controllers
Jacobian matrix model

INTRODUCTION

A difference equation is a type of mathematical equation that describes the relationship between a function and its differences (or "deltas"). The general form of a difference equation is:

$$h(n) = H(h(n-1), h(n-2), ..., h(n-k))$$

where $h(n)$ is the function being studied, H is some function of the previous values of y, and n is the independent variable (often thought of as time). The theory of difference equations involves the study of properties and solutions of equations of this form, including stability, existence and uniqueness of solutions, and methods for finding explicit solutions.
Difference equations are used to model a wide range of phenomena in fields such as mathematics, physics, engineering, economics and many others. There are different methods to solve difference equations such as Z-transform, Laplace transform, generating function, and more.

A discrete and dynamic system of growing population refers to a model that describes how a population changes over time. In

Manuscript received: 2 April 2024,
Revised: 17 May 2024,
Accepted: 6 June 2024.

[1]Shaymaa.h.salih@uotechnology.edu.iq
[2]nadia.m.ghanim@uotechnology.edu.iq
[3]suzan@um.edu.my
[4]yeliz.karaca@ieee.org(**Corresponding author**)

this type of system, the population going through major life events is divided into discrete time periods, and the size of the population at each time period is determined by the rate of growth and other factors. The population may change due to various factors such as births, deaths, migration, and changes in reproductive rates (Keyfitz 2005; Schoen 2013). One common model used to describe the growth of a population over time is the logistic growth model. This model takes into account the carrying capacity of the environment, which is the maximum number of individuals that can be supported by the available resources. The logistic growth model predicts that the population will grow at a faster rate until it reaches the carrying capacity, at which point the growth rate will start to decrease (Iannelli and Milner 2005; Salih and Al-Saidi 2022).

There are many different factors that can affect the growth of a population, including environmental conditions, resource availability, and interactions with other species. Understanding how these factors influence population growth can help us better predict and manage the population of a given species (N. M. Al-Saidi 2023; Shaw and Neubert 2018).

If a growing population has several controllers, it means that there are multiple factors or mechanisms that can influence the rate of population growth (Li and Ma 2022; Rending L. and P. 2022; Dhinakaran V. and H. 2021; Yellin and Samuelson 1974). Some common controllers of population growth going through major life events include:

- Birth rate: The number of births in a population over a given period of time can influence population growth. It can be represented by:
  $P_{birth} = \beta * P$,
  where P_{birth} refers to the increase in population based on births, β is the birth rate, and P is the initial population.
- Death rate: The number of deaths in a population over a given period of time can also influence population growth. It can be represented by:
  $P_{death} = \lambda * P$,
  where P_{death} refers to the decrease in population based on death, λ is the death rate.
- Migration: The movement of individuals into or out of a population can affect its size, such that, $P_M = M$,
  This represents the change in population based on migration.
- Reproductive rates: The number of offspring produced by individuals in a population can impact the population growth. It can be represented by:
  $P_R = R * P$,
  where P_R refers to the change in population based on reproductive, and R is the rate of reproductive.
- Environmental conditions: The availability of resources, such as food and water, as well as the presence of predators or other environmental factors, can affect population growth. It can be represented by:
  $P_E = f(E, P)$,
  where P_E refers to the change in population based on environmental conditions, and f is the impact rate of the environmental impact on the population.
- Human activity: Human actions, such as habitat destruction or the introduction of invasive species, can also influence population growth.
  $P_H = f(H, P)$,
  where P_H refers to the change in population based on human activity, and f is the impact of the human activity on the population.

Therefore, the total population dynamics after considering all the influence factors can be represented by:
$P_{total} = P + P_{birth}\text{-}P_{death} + P_M + P_R + P_E + P_H$

Understanding the various controllers of population growth can help us better predict and manage the size of a population over time.

For a long time, control of under-activated dynamical systems has been considered. The majority of development has been made in model-based control theory, which has limitations when the system under examination is extremely complex and no model can be built. This needs data-driven control approaches like machine learning, which has now spread to many disciplines, including control theory.

Control of under-activated growth systems refers to the process of regulating the growth of a system, such as a cell or organism, when it is not growing at its optimal rate. This can be achieved through a variety of methods; such as manipulating the levels of hormones or other signaling molecules, changing the environment that system is growing in, or applying genetic modifications. Hormones play a crucial role in controlling growth and development, and a balance of hormones is essential for normal growth. For example, the hormone insulin promotes cell growth and division, while the growth hormone stimulates the growth of bones and muscles. Manipulating the levels of these hormones can help to regulate growth in under-activated systems.

Environmental factors such as temperature, light, and nutrient availability can also affect growth. By controlling these factors, it is possible to regulate the growth of under-activated systems. Genetic modifications can also be used to control growth. For example, knocking out or over-expressing certain genes can affect the rate of growth, and can be used to regulate growth in under-activated systems. It is also important to note that in some cases under activation could be a symptom of a disease or malfunction of some internal process, in that case a medical or biological approach should be taken.

In this paper, a 3D-discrete and dynamic human population growth system with many controllers is proposed by examining the stability and symmetry of controller system clarifications. The symmetric stability control results are presented by considering a special parametric dynamic system in its coefficients besides suggesting periodic functional coefficients in terms of *sin* and *cos* functions. The controller laws for one, two and three dimensions are addressed, while numerical simulations are provided for supporting the preliminary findings of the study.

THE GROWING HUMAN POPULATION SYSTEMS

In this part, some of the 3D-dynamic and discrete systems of the growing human population (SGHP) P_1, P_2, P_3 is formulated. In Shaw and Neubert (2018), Joeland Samuelson presented the 3D-SGHP, as follows:

$$\begin{aligned} \frac{dP_1}{d\tau} &= -\lambda_1 P_1 + \beta_1 P_3 \\ \frac{dP_2}{d\tau} &= -\lambda_2 P_2 + \beta_2 P_3 \\ \frac{dP_3}{d\tau} &= -\lambda_3 P_3, \end{aligned} \tag{1}$$

where λ_i, $i = 1, 2, 3$ are the population rate and β_j, $j = 1, 2$ are the connections of the population, which are admitted positive

values. System (1) was extended into the following structure by Waldstatter (Waldstatter 1989)

$$\begin{aligned}\frac{dP_1}{d\tau} &= -\lambda_1 P_1 + \beta_1 P_3\\ \frac{dP_2}{d\tau} &= -\lambda_2 P_2 + \beta_2 P_3\\ \frac{dP_3}{d\tau} &= -\lambda_3 P_3 + \beta_3,\end{aligned} \tag{2}$$

where β_3 is a realistic constant. Pollard (1997) generated System (2) as follows

$$\begin{aligned}\frac{dP_1}{d\tau} &= -\lambda_1 P_1 + \beta_1 P_3\\ \frac{dP_2}{d\tau} &= -\lambda_2 P_2 + \beta_2 P_3\\ \frac{dP_3}{d\tau} &= -(\lambda_3 + \beta_3) P_3.\end{aligned} \tag{3}$$

Later, the author considered the Kendall observation to the system to get non-linearity system. Kendall discovered that the differential equations could describe a population of single males, single females, and couples, with the following system

$$\begin{aligned}\frac{dP_1}{d\tau} &= -\lambda_1 P_1 + \beta_1 P_3 - K_1\\ \frac{dP_2}{d\tau} &= -\lambda_2 P_2 + \beta_2 P_3 - K_2\\ \frac{dP_3}{d\tau} &= -(\lambda_3 + \beta_3) P_3 + K_3.\end{aligned} \tag{4}$$

The Kendall coefficient of concordance is a measure of the strength and direction of association between two variables in a population. It can be used to determine whether there is a statistically significant relationship between the variables, and if so, whether the relationship is positive or negative. The Kendall coefficient is often used in studies of population growth, as it can help researchers understand the factors that influence population size and change over time. It is calculated by comparing the ranks of the values of the two variables in a sample, and it can range from -1 (perfect negative association) to +1 (perfect positive association). A value of 0 indicates no association between the variables (Kendall 1997). Hadeler (2012) suggested an extension of System (4) arithmetically by adding the separation rate of pairs σ as follows:

$$\begin{aligned}\frac{dP_1}{d\tau} &= -\lambda_1 P_1 + (\beta_1 + \sigma) P_3 - K_1\\ \frac{dP_2}{d\tau} &= -\lambda_2 P_2 + (\beta_2 + \sigma) P_3 - K_2\\ \frac{dP_3}{d\tau} &= -(\lambda_3 + \beta_3 + \sigma) P_3 + K_3.\end{aligned} \tag{5}$$

In this effort, we consider the system of the structure

$$\begin{aligned}\frac{dP_1}{d\tau} &= -\lambda_1 P_1 + \sigma_1 P_3 - K_1\\ \frac{dP_2}{d\tau} &= -\lambda_2 P_2 + \sigma_2 P_3 - K_2\\ \frac{dP_3}{d\tau} &= -(\lambda_3 + \sigma_3) P_3 + K_3,\end{aligned} \tag{6}$$

where $\sigma_i = \beta_i + \sigma$, $i = 1, 2, 3$.
A 3D dynamic system of rising population could refer to a mathematical model that mimics the three-dimensional growth of a population through time. This could be used to investigate issues such as food availability, sickness, and social and environmental situations that influence population growth. Typically, the model would include variables that reflect these components as well as equations that describe how they interact and change over time. It could also incorporate three-dimensional population growth visualizations or simulations.
System (6) can be viewed as 3D discrete system of growing population, using the information

$$\Delta^n P_i = P_i^{n+1} - P_i^n, \quad i = 1, 2, 3$$

thus, we have 3D-SGHP

$$\begin{aligned}P_1^{n+1} &= (1 - \lambda_1) P_1^n + \sigma_1 P_3^n - K_1\\ P_2^{n+1} &= (1 - \lambda_2) P_2^n + \sigma_2 P_3^n - K_2\\ P_3^{n+1} &= -(\lambda_3 + \sigma_3 - 1) P_3^n + K_3.\end{aligned} \tag{7}$$

In terms of a matrix formula, System (7) can be viewed as follows:

$$P(n+1) = \Lambda(n) P(n) \Xi(n) + \Sigma(n), \tag{8}$$

where Λ, Ξ and Σ are square matrices of the same order. The solution of System (8) can be established by using the concept of the technique of variation of parameters.

Proposition 1.

Let $M_1(n)$ and $M_2(n)$ be fundamental matrix solution of the systems (Murty and Prasannam 1997)

$$P(n+1) = \Lambda(n) P(n) \Xi(n)$$

and

$$P(n+1) = \Xi^*(n) P(n) \Xi(n),$$

respectively. Then the solution of the of the homogeneous matrix difference system

$$P(n+1) = \Lambda(n) P(n) \Xi(n). \tag{9}$$

is given by the formula

$$P(n) = M_1(n) \Pi M_2^*(n)$$

where Π is an arbitrary constant square matrix of the same order. Moreover, any the solution of System (8) is formulated by

$$P(n) = M_1(n) \Pi M_2^*(n) + \bar{P}(n),$$

where $\bar{P}(n)$ is a particular solution of System (8).

A 3D discrete system of growing population refers to a mathematical model that represents the growth of a population in three dimensions over discrete intervals of time, rather than continuously (H. Natiq 2022). This means that the population size and other variables in the model are updated at specific points in time, rather than constantly changing. A 3D discrete system could be used to study the same types of factors that affect population growth as a continuous model, but the equations and approach may be different. Discrete models can be useful for understanding how a system changes over time in a more granular way, as the model is updated at specific points rather than continuously.

Example 1.

Let $K_i = 0$ in System (7), then the general solution becomes

$$P_1^n = \frac{(\sigma_1 c_3((\lambda_1-1)^n - (-\lambda_3-\sigma_3+1)^n))}{(\lambda_1+\lambda_3+\sigma_3-2)} + c_1(\lambda_1-1)^n$$
$$P_2^n = \frac{(c_3\sigma_2((\lambda_2-1)^n - (-(\lambda_3+\sigma_3)+1)^n))}{(\lambda_2+\lambda_3+\sigma_3-2)} + c_2(\lambda_2-1)^n$$
$$P_3^n = c_3(-(\lambda_3+\sigma_3)+1)^n, \quad (c_1,c_2,c_3) \in \mathbb{Z}^3$$

In general, when $K_i \neq 0$, we have

$$P_1^n = \frac{(\sigma_1 c_3((\lambda_1-1)^n - (-\lambda_3-\sigma_3+1)^n))}{(\lambda_1+\lambda_3+\sigma_3-2)} + c_1(\lambda_1-1)^n - \\ - \frac{\sigma_1 K_3 + K_1(\lambda_3+\sigma_3)}{(\lambda_1-2)(\lambda_3+\sigma_3)}$$
$$P_2^n = \frac{(c_3\sigma_2((\lambda_2-1)^n - (-(\lambda_3+\sigma_3)+1)^n))}{(\lambda_2+\lambda_3+\sigma_3-2)} + c_2(\lambda_2-1)^n - \\ - \frac{\sigma_2 K_3 + K_2(\lambda_3+\sigma_3)}{(\lambda_2-2)(\lambda_3+\sigma_3)}$$
$$P_3^n = c_3(-(\lambda_3+\sigma_3)+1)^n + \frac{K_3}{\lambda_3+\sigma_3}, \quad (c_1,c_2,c_3) \in \mathbb{Z}^3,$$

where $\lambda_3+\sigma_3 \neq 0$, $\lambda_1 \neq 2$ and $\lambda_2 \neq 2$.

Example 2.
Suppose the following data:

- $\lambda_1 = \lambda_2 = \sigma_1 = \sigma_2 = 0.5$ and $\lambda_3+\sigma_3 = 0.5$ then we obtain the following numerical solution of System (7) (see Fig.1-A)

$$(P_1^n, P_2^n, P_3^n) = ((-1/2)^n(-2c+(-1)^n-1), \\ (-1/2)^n(-2c+(-1)^n-1), 2^{1-n}\Big)$$

  where c is a constant.
- $\lambda_1 = \lambda_2 = 0.5, \sigma_1 = 0.6, \sigma_2 = 0.9$ and $\lambda_3+\sigma_3 = 0.75$ then we get the following numerical solution of System (7) (see Fig.1-B)

$$(P_1^n, P_2^n, P_3^n) = \Big(\frac{1}{5}(-1)^{n+1}2^{1-2n}((5c_1+8)2^n - 8(-1)^n), \\ \frac{1}{5}(-1)^n 2^{1-2n}(12(-1)^n - (5c_2+12)2^n), 4^{1-n}\Big)$$

Negative values of growing population

The suggested system may have negative values for the growing population. There are several potential negative consequences associated with a growing population, including:

- Strain on Resources: As the population grows, there is an increased demand for natural resources such as food, water, and energy. This can lead to depletion of resources and increased pollution, which can have negative impacts on the environment and public health.
- Overcrowding: A growing population can lead to overcrowding in cities and other areas, which can contribute to a range of problems such as increased crime, congestion, and a lack of affordable housing.
- Unequal Distribution: Even though the population may be growing overall, the distribution of people is not always equal. This can lead to disparities in access to resources and opportunities, which can contribute to social and economic inequalities.
- Strain on Social Services: As the population grows, there can be increased demand for social services such as healthcare, education, and welfare programs. This can strain government budgets and resources and can contribute to political and social unrest.
- Environmental Impact: A growing population can have significant impacts on the environment, including deforestation, loss of biodiversity, and climate change. These negative impacts can have long-term consequences for future generations.

STABILITY ANALYSIS

In this part, we analyze the suggested 3D-SGHP in (6) and its discrete form (7). The Jacobian matrix of Model (6) is given by

$$\mathbf{J} = \begin{pmatrix} -\lambda_1 & 0 & \sigma_1 \\ 0 & -\lambda_2 & \sigma_2 \\ 0 & 0 & -\lambda_3-\sigma_3 \end{pmatrix}$$

where $|\mathbf{J}| = -\lambda_1\lambda_2(\lambda_3+\sigma_3)$. Therefore, the set of eigenvalues of $\mathbf{J}$ is

$$\rho_1 = -\lambda_1, \quad \rho_2 = -\lambda_2, \quad \rho_3 = -(\lambda_3+\sigma_3).$$

System (6) is asymptotically stable whenever $\lambda_1 > 0$, $\lambda_2 > 0$ and $\lambda_3+\sigma_3 > 0$. The corresponding eigenvectors are

$$v_1 = (1,0,0),\ v_2 = (0,1,0),\ v_3 = \left(\frac{\sigma_1}{\lambda_1-\lambda_3-\sigma_3}, \frac{\sigma_2}{\lambda_2-\lambda_3-\sigma_3}, 1\right),$$

where $\lambda_1 \neq \lambda_3+\sigma_3$ and $\lambda_2 \neq \lambda_3+\sigma_3$.

Model (6) has the following set of non-vanishing fixed points for all axis

$$S = \Big\{(P_1,P_2,P_3) : \Big(\frac{(\sigma_1K_3 - K_1(\sigma_3+\lambda_3+1))}{((\lambda_1+1)(\sigma_3+\lambda_3+1))}, \\ \frac{(\sigma_2K_3 - K_2(\sigma_3+\lambda_3+1))}{((\lambda_2+1)(\sigma_3+\lambda_3+1))}, \quad \frac{K_3}{(\sigma_3+\lambda_3+1)}\Big) \\ \Big(-\frac{K_1}{\lambda_1+1}, \quad \frac{(\sigma_2K_3 - K_2(\sigma_3+\lambda_3+1))}{((\lambda_2+1)(\sigma_3+\lambda_3+1))}, \quad \frac{K_3}{(\sigma_3+\lambda_3+1)}\Big) \\ \Big(-\frac{K_1}{\lambda_1+1}, \quad \frac{-K_2}{\lambda_2+1}, \quad \frac{K_3}{(\sigma_3+\lambda_3+1)}\Big)\Big\}$$

whenever $\lambda_1 \neq -1, \lambda_2 \neq -1$ and $\lambda_3+\sigma_3 \neq -1$, and $K_i \in [-1,1]$, $i = 1,2,3$.
The set of the non-vanishing equilibrium points corresponding to System (6) is

$$E = \Big\{(P_1,P_2,P_3) : \Big(\frac{(\sigma_1K_3 - K_1(\sigma_3+\lambda_3))}{(\lambda_1(\sigma_3+\lambda_3))}, \quad \frac{(\sigma_2K_3 - K_2(\sigma_3+\lambda_3))}{(\lambda_2(\sigma_3+\lambda_3))}, \\ \frac{K_3}{(\sigma_3+\lambda_3)}\Big) \\ \Big(-\frac{K_1}{\lambda_1}, \quad \frac{(\sigma_2K_3 - K_2(\sigma_3+\lambda_3))}{(\lambda_2(\sigma_3+\lambda_3))}, \quad \frac{K_3}{(\sigma_3+\lambda_3)}\Big) \\ \Big(-\frac{K_1}{\lambda_1}, \quad -\frac{K_2}{\lambda_2}, \quad \frac{K_3}{(\sigma_3+\lambda_3)}\Big)\Big\},$$

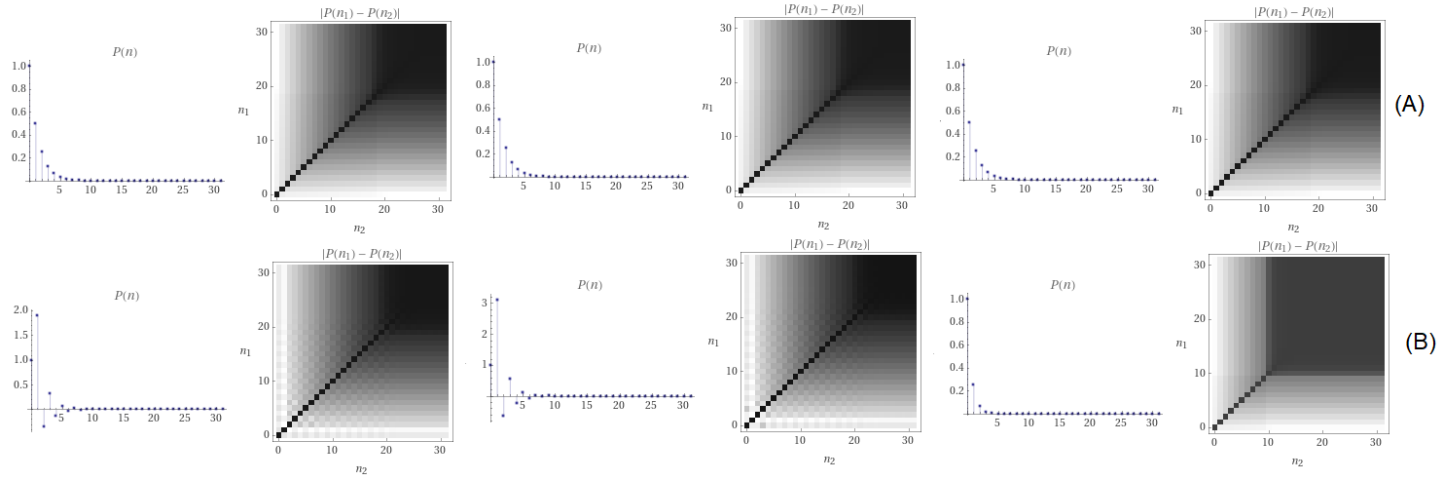

Figure 1 The plot of solutions (P_1, P_2, P_3) of System (7) in Example, respectively.

whenever $\lambda_1 \neq 0, \lambda_2 \neq 0$ and $\lambda_3 + \sigma_3 \neq 0$, and $K_i \in [-1, 1]$, $i = 1, 2, 3$. Note that when $K_i = 0$, $i = 1, 2, 3$, then the origin is the only equilibrium point and fixed point of System (6). Hence, $(0, 0, 0)$ is the unique solution for the system.

Special case: $\lambda_1 = \lambda_2$

In this case System (6) reduces into 2D-system, as follows:

$$\begin{aligned} \frac{dP_4}{d\tau} &= -\lambda P_4 + (\sigma_1 - \sigma_2)P_3 - (K_1 - K_2) \\ \frac{dP_3}{d\tau} &= -(\lambda_3 + \sigma_3)P_3 + K_3, \end{aligned} \tag{10}$$

where $P_4 = P_1 - P_2$, and $\lambda_1 = \lambda_2 = \lambda$.

$$\mathbf{J} = \begin{pmatrix} -\lambda & \sigma_1 - \sigma_2 \\ 0 & -\lambda_3 - \sigma_3 \end{pmatrix}$$

where $|\mathbf{J}| = \lambda(\lambda_3 + \sigma_3)$. Therefore, the set of eigenvalues of $\mathbf{J}$ is

$$\varrho_1 = -\lambda, \quad \varrho_2 = -(\lambda_3 + \sigma_3).$$

System (10) is asymptotically stable whenever $\lambda > 0$ and $\lambda_3 + \sigma_3 > 0$. The corresponding eigenvectors are

$$v_1 = (1, 0), \quad v_2 = \left(-\frac{-\sigma_1 + \sigma_2}{\lambda - \lambda_3 - \sigma_3}, 1\right),$$

where $\lambda \neq -(\lambda_3 + \sigma_3)$.

Yields the following general solution;

$$\begin{aligned} P_4(\tau) &= \frac{-(\sigma_1\alpha_1 e^{\tau(-(\lambda_3+\sigma_3))})}{\lambda_3 + \sigma_3 - \lambda} + \frac{\sigma_2\alpha_1 e^{\tau(-(\lambda_3+\sigma_3))}}{\lambda_3 + \sigma_3 - \lambda} + \frac{\sigma_1 K_3}{\lambda(\lambda_3 + \sigma_3)} - \\ &- \frac{\sigma_2 K_3}{\lambda(\lambda_3 + \sigma_3)} - \frac{\sigma_3 K_1}{\lambda(\lambda_3 + \sigma_3)} - \frac{\lambda_3 K_1}{\lambda(\lambda_3 + \sigma_3)} + \frac{\sigma_3 K_2}{\lambda(\lambda_3 + \sigma_3)} + \\ &+ \frac{\lambda_3 K_2}{\lambda(\lambda_3 + \sigma_3)} + \alpha_2 e^{\lambda\tau} \\ P_3(\tau) &= \alpha_1 e^{-\lambda_3\tau - \sigma_3\tau} + \frac{K_3}{(\lambda_3 + \sigma_3)}, \end{aligned}$$

where α_1 and α_2 are fixed constants.

Example 3.

For a constant a, we suggest the parametric connections system corresponding to (10), as follows

$$\begin{aligned} \frac{dP_4}{d\tau} &= -\cos(a)P_4 + (\sigma_1 - \sigma_2)P_3 - (K_1 - K_2) \\ \frac{dP_3}{d\tau} &= -\sin(a)P_3 + K_3. \end{aligned} \tag{11}$$

Then the solution becomes

$$\begin{aligned} P_4(\tau) &= e^{-1/2\tau\sin(2a)\csc(a)} \int_1^\tau \Big(-1/2 e^{1/2\xi\csc(a)\sin(2a) - \xi\sin(a)} * \\ &\csc(a)(-2e^{\xi\sin(a)}\sigma_1 - 2\sin(a)\sigma_1 + 2e^{\xi\sin(a)}\sigma_2 + 2\sin(a)\sigma_2 + \\ &+ 2e^{\xi\sin(a)}\sin(a)K_1 - 2e^{\xi\sin(a)}\sin(a)K_2\Big) d\xi + \alpha_1 e^{-1/2\tau\sin(2a)K_3\csc(a)} \\ P_3(\tau) &= \alpha_2 e^{-\tau\sin(a)} + K_3\csc(a), \end{aligned}$$

where α_1 and α_2 are constants. Fig. 2 shows the symmetric behavior of the solution when $\sigma_1 = \sigma_2$ and $K_3 = \pm 1$. In this case, we obtain the solution

$$\begin{aligned} P_4(\tau) &= \alpha_1 e^{-\tau\cos(a)} - K_1\sec(a) + K_2\sec(a) \\ P_3(\tau) &= \alpha_2 e^{-\tau\sin(a)} \pm \csc(a). \end{aligned}$$

A parametric dynamic system is a mathematical model that describes the behavior of a system over time. It is defined by a set of differential equations, which are functions that describe how the system changes with respect to time. The parameters of the system are variables that can be adjusted to change the behavior of the system. These equations can be used to predict the future behavior of the system, given the current state and the parameters. These systems are widely used in fields such as physics, engineering, and economics to model and analyze real-world systems.

A parametric dynamic system with periodic coefficients is a type of mathematical model that describes the behavior of a sys- tem over time, where the parameters of the system are functions that vary periodically with time. These systems are often used to model physical systems that exhibit periodic behavior, such as oscillations or waves. The mathematical equations that define the system

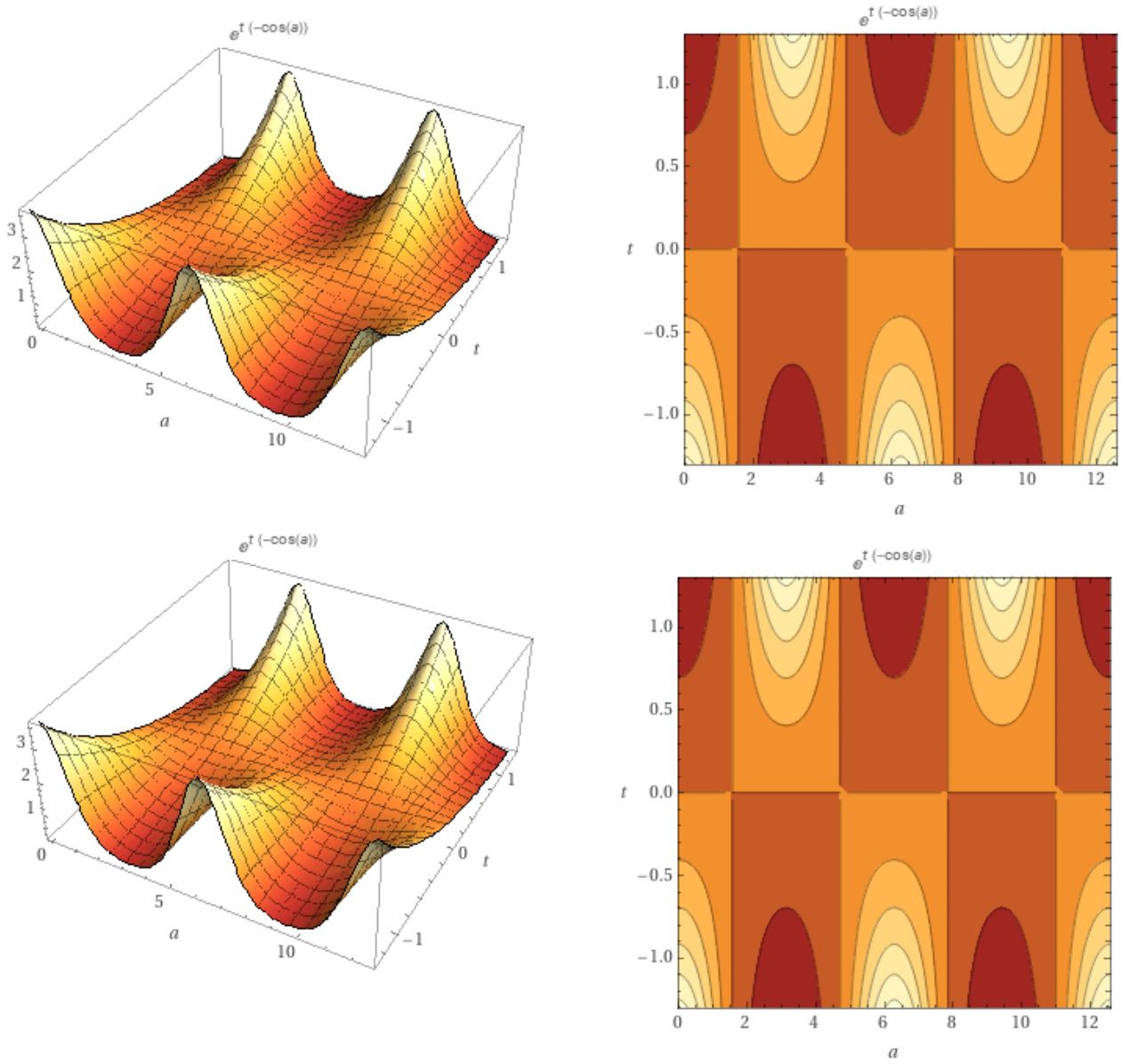

Figure 2 The plot of solutions (P_4, P_3) of System (11) in Example, when $\sigma_1 = \sigma_2$ and $K_3 = \pm 1$, respectively.

include terms that represent the periodic variations of the parameters, and the solution of these equations will also exhibit periodic behavior. These types of systems can be analyzed using techniques from the field of dynamic systems, including frequency analysis and bifurcation theory, to understand the behavior of the system and how it responds to changes in the parameters.

TYPES OF STABILIZATION OF NONLINEAR DYNAMIC SYSTEMS

Stabilization of a dynamic system refers to the process of making a system's behavior more predictable and consistent over time. This can be achieved by various means, such as adjusting the system's parameters, adding control inputs, or implementing a feedback control loop. The specific methods used will depend on the system's characteristics and the desired behavior.

In control theory, the stability of a dynamic system refers to the ability of the system to return to its equilibrium state after being subjected to some disturbance. A system is considered stable if, after a disturbance, the system returns to its equilibrium state or settles into a new equilibrium state that is acceptable. There are several ways to stabilize a dynamic system, including feedback control and feedforward control.

Feedback control involves using the output of the system as input to a controller, which then adjusts the input to the system to bring the output back to the desired equilibrium state. This can be done using a variety of control algorithms, such as PID (proportional-integral-derivative) control or state-space control. Therefore, the controller is a device or algorithm that regulates the behavior of a dynamic system. It compares the system's output (also called the process variable) with the desired output (also called the set-point) and calculates an error signal. The controller then uses this error

signal to adjust the system's inputs (also called the manipulated variables) in order to bring the output closer to the set-point. There are many different types of controllers, such as PID controllers, state-space controllers, and model predictive controllers, each with their own strengths and weaknesses (Hadeler 2012).
Feedforward control involves predicting the effect of a disturbance on the system and applying a counteracting input to the system to prevent the disturbance from affecting the equilibrium state. This can be done using techniques such as model predictive control or adaptive control. In general, the choice of control strategy will depend on the specific characteristics of the system and the requirements of the application.
In mathematics and physics, a chaotic system is a system that exhibits the property of chaos, which is defined as a periodic long-term behavior that is highly sensitive to initial conditions. This means that small differences in initial conditions can lead to drastically different outcomes over time. In other words, the behavior of a chaotic system is seemingly random and unpredictable. Examples of chaotic systems include the weather, the stock market, and some mechanical systems such as the double pendulum.

(1,2,3) D Controllers of System

By adding some control parameters, the chaotic system corresponding to (6) can be reformulated as follows:

$$\begin{aligned}\Delta P_1(\tau) &= -\lambda_1 P_1(\tau-1) + \sigma_1 P_3(\tau-1) - K_1\\ \Delta P_2(\tau) &= -\lambda_2 P_2(\tau-1) + \sigma_2 P_3(\tau-1) - K_2\\ \Delta P_3(\tau) &= -(\lambda_3+\sigma_3) P_3(\tau-1) + K_3.\end{aligned} \tag{12}$$

This proposition details the natural dynamics of the proposed system with its solution. Based on these results, the manipulation of the system toward desired outcomes using control strategies is given in Proposition 2.
Proposition 2

System (12) can be controlled by 1D-controller

$$U_1(\tau) = -\sigma_1 P_3(\tau),$$

whenever $\lambda_1 > 0, \lambda_2 > 0$ and $\lambda_3 + \sigma_3 > 0$.

Proof.
Consider the system (12). Then under the suggested controller, we have the following system

$$\begin{aligned}\Delta P_1(\tau) &= -\lambda_1 P_1(\tau-1) + \sigma_1 P_3(\tau-1) - K_1 + U_1(\tau-1)\\ \Delta P_2(\tau) &= -\lambda_2 P_2(\tau-1) + \sigma_2 P_3(\tau-1) - K_2\\ \Delta P_3(\tau) &= -(\lambda_3+\sigma_3) P_3(\tau-1) + K_3.\end{aligned} \tag{13}$$

Consequently, we obtain the difference system

$$\begin{aligned}\Delta P_1(\tau) &= -\lambda_1 P_1(\tau-1) + \sigma_1 P_3(\tau-1) - K_1 - \sigma_1 P_3(\tau-1)\\ \Delta P_2(\tau) &= -\lambda_2 P_2(\tau-1) + \sigma_2 P_3(\tau-1) - K_2\\ \Delta P_3(\tau) &= -(\lambda_3+\sigma_3) P_3(\tau-1) + K_3,\end{aligned} \tag{14}$$

which is equivalent to

$$\begin{aligned}\Delta P_1(\tau) &= -\lambda_1 P_1(\tau-1) - K_1\\ \Delta P_2(\tau) &= -\lambda_2 P_2(\tau-1) + \sigma_2 P_3(\tau-1) - K_2\\ \Delta P_3(\tau) &= -(\lambda_3+\sigma_3) P_3(\tau-1) + K_3.\end{aligned} \tag{15}$$

So,

$$\mathbf{J} = \begin{pmatrix} -\lambda_1 & 0 & 0\\ 0 & -\lambda_2 & \sigma_2\\ 0 & 0 & -\lambda_3-\sigma_3\end{pmatrix}$$

where $|\mathbf{J}| = -\lambda_1\lambda_2(\lambda_3+\sigma_3)$.
Therefore, the set of eigenvalues of $\mathbf{J}$ is

$$v_1 = -\lambda_1, \quad v_2 = -\lambda_2, \quad v_3 = -(\lambda_3+\sigma_3).$$

System (15) is asymptotically stable whenever $\lambda_1 > 0$, $\lambda_2 > 0$ and $\lambda_3 + \sigma_3 > 0$. The corresponding eigenvectors are

$$v_1 = (1,0,0), \quad v_2 = (0,1,0), \quad v_3 = \left(0, \frac{\sigma_2}{\lambda_2-\lambda_3-\sigma_3}, 1\right),$$

where $\lambda_1 \neq \lambda_3 + \sigma_3$ and $\lambda_2 \neq \lambda_3 + \sigma_3$.
In view of the conditions, System (15) is asymptotically stable.
Note that the solution of System (15) is given by the formula

$$\begin{aligned}P_1(n) &= c_1(-\lambda_1)^{n-1} - \frac{(K_1(1-(-\lambda_1)^n))}{(\lambda_1+1)},\\ P_2(n) &= c_2(-\lambda_2)^n - \frac{c_3\sigma_2((-\lambda_2)^n - (-\lambda_3-\sigma_3)^n)}{\lambda_2-\lambda_3-\sigma_3} - \\ &\qquad \frac{\lambda_3 K_2 + K_2}{(1+\lambda_2)(1+\lambda_3+\sigma_3)},\\ P_3(n) &= c_3(-\lambda_3-\sigma_3)^n + \frac{K_3}{\lambda_3+\sigma_3+1},\end{aligned}$$

where $(c_1, c_2, c_3) \in \mathbb{Z}^3$.

Proposition 3 builds on the simpler controller pertaining to Proposition 2 by the incorporation of more extensive or reliable control mechanisms. This progression not only shows how to improve upon simpler models to achieve greater effectiveness, but it also improves comprehension and applicability of controlling complex dynamical systems in real-world situations.
Proposition 3
System (12) can be controlled by 2D-controller

$$U_1(\tau) = -\sigma_1 P_3(\tau), \quad U_2(\tau) = -\sigma_2 P_3(\tau)$$

whenever $\lambda_1 > 0, \lambda_2 > 0$ and $\lambda_3 + \sigma_3 > 0$.
Proof.

Consider the system (12). Then under the recommended controllers, we have the following system

$$\begin{aligned}\Delta P_1(\tau) &= -\lambda_1 P_1(\tau-1) + \sigma_1 P_3(\tau-1) - K_1 + U_1(\tau-1)\\ \Delta P_2(\tau) &= -\lambda_2 P_2(\tau-1) + \sigma_2 P_3(\tau-1) - K_2 + U_2(\tau-1)\\ \Delta P_3(\tau) &= -(\lambda_3+\sigma_3) P_3(\tau-1) + K_3.\end{aligned} \tag{16}$$

Consequently, we obtain the difference system

$$\begin{aligned}\Delta P_1(\tau) &= -\lambda_1 P_1(\tau-1) + \sigma_1 P_3(\tau-1) - K_1 - \sigma_1 P_3(\tau-1)\\ \Delta P_2(\tau) &= -\lambda_2 P_2(\tau-1) + \sigma_2 P_3(\tau-1) - K_2 - \sigma_2 P_3(\tau-1)\\ \Delta P_3(\tau) &= -(\lambda_3+\sigma_3) P_3(\tau-1) + K_3,\end{aligned} \tag{17}$$

which is equivalent to

$$\begin{aligned}\Delta P_1(\tau) &= -\lambda_1 P_1(\tau-1) - K_1\\ \Delta P_2(\tau) &= -\lambda_2 P_2(\tau-1) - K_2\\ \Delta P_3(\tau) &= -(\lambda_3+\sigma_3) P_3(\tau-1) + K_3.\end{aligned} \tag{18}$$

Hence,

$$\mathbf{J} = \begin{pmatrix} -\lambda_1 & 0 & 0 \\ 0 & -\lambda_2 & 0 \\ 0 & 0 & -\lambda_3 - \sigma_3 \end{pmatrix}$$

where $|\mathbf{J}| = -\lambda_1\lambda_2(\lambda_3 + \sigma_3)$. Therefore, the set of eigenvalues of $\mathbf{J}$ is

$$\varepsilon_1 = -\lambda_1, \quad \varepsilon_2 = -\lambda_2, \quad \varepsilon_3 = -(\lambda_3 + \sigma_3).$$

System (18) is asymptotically stable whenever $\lambda_1 > 0$, $\lambda_2 > 0$ and $\lambda_3 + \sigma_3 > 0$. The corresponding eigenvectors are

$$v_1 = (1,0,0), \quad v_2 = (0,1,0), \quad v_3 = (0,0,1),$$

where $\lambda_1 \neq \lambda_3$ and $\lambda_2 \neq \lambda_3$. In view of the conditions, System (18) is asymptotically stable.

Note that the solution of System (18) is given by the formula

$$\begin{aligned} P_1(n) &= c_1(-\lambda_1)^{n-1} - \frac{(K_1(1-(-\lambda_1)^n))}{(\lambda_1+1)}, \\ P_2(n) &= c_2(-\lambda_2)^{n-1} - \frac{(K_2(1-(-\lambda_2)^n))}{(\lambda_2+1)}, \\ P_3(n) &= c_3(-\lambda_3-\sigma_3)^{n-1} - \frac{(K_3(\lambda_3+\sigma_3)(1-(-\lambda_3-\sigma_3)^n))}{((-\lambda_3-\sigma_3)(\lambda_3+\sigma_3+1))}, \end{aligned}$$

where $(c_1, c_2, c_3) \in \mathbb{Z}^3$.

Proposition 4 is essential to the development of the study control strategy narrative because it demonstrates extensive and reliable control capabilities and broadens our understanding of the dynamics and control mechanisms of the system from a theoretical and practical standpoint.

Proposition 4

System (12) can be controlled by 3D-controller

$$U_1(\tau) = -\sigma_1 P_3(\tau), \quad U_2(\tau) = -\sigma_2 P_3(\tau), \quad U_3(\tau) = \sigma_3 P_3(\tau)$$

whenever $\lambda_i > 0, i = 1,2,3$.

Proof.

Consider the system (12). Then under the recommended controllers, we have the following system

$$\begin{aligned} \Delta P_1(\tau) &= -\lambda_1 P_1(\tau-1) + \sigma_1 P_3(\tau-1) - K_1 + U_1(\tau-1) \\ \Delta P_2(\tau) &= -\lambda_2 P_2(\tau-1) + \sigma_2 P_3(\tau-1) - K_2 + U_2(\tau-1) \\ \Delta P_3(\tau) &= -(\lambda_3+\sigma_3) P_3(\tau-1) + K_3 + U_3(\tau-1). \end{aligned} \tag{19}$$

Consequently, we obtain the difference system

$$\begin{aligned} \Delta P_1(\tau) &= -\lambda_1 P_1(\tau-1) + \sigma_1 P_3(\tau-1) - K_1 - \sigma_1 P_3(\tau-1) \\ \Delta P_2(\tau) &= -\lambda_2 P_2(\tau-1) + \sigma_2 P_3(\tau-1) - K_2 - \sigma_2 P_3(\tau-1) \\ \Delta P_3(\tau) &= -(\lambda_3+\sigma_3) P_3(\tau-1) + K_3 + \sigma_3 P_3(\tau-1), \end{aligned} \tag{20}$$

which is equivalent to

$$\begin{aligned} \Delta P_1(\tau) &= -\lambda_1 P_1(\tau-1) - K_1 \\ \Delta P_2(\tau) &= -\lambda_2 P_2(\tau-1) - K_2 \\ \Delta P_3(\tau) &= -\lambda_3 P_3(\tau-1) + K_3. \end{aligned} \tag{21}$$

Then,

$$\mathbf{J} = \begin{pmatrix} -\lambda_1 & 0 & 0 \\ 0 & -\lambda_2 & 0 \\ 0 & 0 & -\lambda_3 \end{pmatrix}$$

where $|\mathbf{J}| = -\lambda_1\lambda_2\lambda_3$. Therefore, the set of eigenvalues of $\mathbf{J}$ is

$$\vartheta_1 = -\lambda_1, \quad \vartheta_2 = -\lambda_2, \quad \vartheta_3 = -\lambda_3.$$

System (21) is asymptotically stable whenever $\lambda_1 > 0$, $\lambda_2 > 0$ and $\lambda_3 > 0$. The corresponding eigenvectors are

$$v_1 = (1,0,0), \quad v_2 = (0,1,0), \quad v_3 = (0,0,1).$$

In view of the conditions, System (21) is asymptotically stable. Note that the solution of System (21) is given by the formula

$$\begin{aligned} P_1(n) &= c_1(-\lambda_1)^{n-1} - \frac{(K_1(1-(-\lambda_1)^n))}{\lambda_1+1}, \\ P_2(n) &= c_2(-\lambda_2)^{n-1} - \frac{(K_2(1-(-\lambda_2)^n))}{\lambda_2+1}, \\ P_3(n) &= c_3(-\lambda_3)^{n-1} + \frac{K_3(1-(-\lambda_3)^n)}{\lambda_3+1}, \end{aligned}$$

where $(c_1, c_2, c_3) \in \mathbb{Z}^3$.

Stabilization of System (10)

There are several methods for stabilizing a 2D dynamic system, including: feedback control, Lyapunov stability analysis, state-space representation, etc. In our study, the adaptive control is considered; and thus, the related method involves adapting the control input to the system based on the current state, in order to achieve stability. However, to stabilize (10) for the special case, when $\lambda_1 = \lambda_2$, it will perform as follows:

The chaotic system corresponding to (10) can be realized as follows:

$$\begin{aligned} \Delta P_4(\tau) &= -\lambda P_4(\tau-1) + (\sigma_1-\sigma_2) P_3(\tau-1) - (K_1-K_2) \\ \Delta P_3(\tau) &= -(\lambda_3+\sigma_3) P_3(\tau-1) + K_3. \end{aligned} \tag{22}$$

Proposition 5

System (22) can be controlled by 1D-controller

$$V_1(\tau) = -(\sigma_1-\sigma_2) P_3(\tau),$$

whenever $\lambda > 0$ and $\lambda_3 + \sigma_3 > 0$.

Proof.

Consider the system (22). Then under the suggested controller, we have the following system

$$\begin{aligned} \Delta P_4(\tau) &= -\lambda P_4(\tau-1) + (\sigma_1-\sigma_2) P_3(\tau-1) - K_1 + V_1(\tau-1) \\ \Delta P_3(\tau) &= -(\lambda_3+\sigma_3) P_3(\tau-1) + K_3. \end{aligned} \tag{23}$$

Consequently, we obtain the difference system

$$\begin{aligned} \Delta P_4(\tau) &= -\lambda P_4(\tau-1) + (\sigma_1-\sigma_2) P_3(\tau-1) - K_1 - (\sigma_1-\sigma_2) P_3(\tau-1) \\ \Delta P_3(\tau) &= -(\lambda_3+\sigma_3) P_3(\tau-1) + K_3, \end{aligned} \tag{24}$$

which is equivalent to

$$\begin{aligned}\Delta P_4(\tau) &= -\lambda P_4(\tau-1) - K_1\\ \Delta P_3(\tau) &= -(\lambda_3+\sigma_3)P_3(\tau-1) + K_3.\end{aligned} \tag{25}$$

Thus,

$$\mathbf{J} = \begin{pmatrix} -\lambda & 0 \\ 0 & -\lambda_3-\sigma_3 \end{pmatrix}$$

where $|\mathbf{J}| = \lambda(\lambda_3+\sigma_3)$. Therefore, the set of eigenvalues of $\mathbf{J}$ is

$$v_1 = -\lambda, \quad v_2 = -(\lambda_3+\sigma_3).$$

System (25) is asymptotically stable whenever $\lambda > 0$ and $\lambda_3+\sigma_3 > 0$. The corresponding eigenvectors are

$$v_1 = (1,0), \quad v_2 = (0,1).$$

In view of the conditions, System (25) is asymptotically stable. Note that the solution of System (25) is given by the formula

$$\begin{aligned}P_4(n) &= c_1(-\lambda)^{n-1} - \frac{(K_1(1-(-\lambda)^n))}{\lambda+1},\\ P_3(n) &= c_3(-\lambda_3-\sigma_3)^{n-1} + \frac{K_3(\lambda_3+\sigma_3)(1-(-\lambda_3-\sigma_3)^n)}{(-\lambda_3-\sigma_3)(\lambda_3+\sigma_3+1)},\end{aligned}$$

where $(c_1, c_2) \in \mathbb{Z}^2$.

Proposition 6
System (22) can be controlled by 2D-controller

$$V_1(\tau) = -(\sigma_1-\sigma_2)P_3(\tau), \quad V_2(\tau) = \sigma_3 P_3(\tau)$$

whenever $\lambda > 0$ and $\lambda_3 > 0$.

Proof.

Consider the system (22). Then under the suggested controllers, we have the following system

$$\begin{aligned}\Delta P_4(\tau) &= -\lambda P_4(\tau-1) + (\sigma_1-\sigma_2)P_3(\tau-1) - K_1 + V_1(\tau-1)\\ \Delta P_3(\tau) &= -(\lambda_3+\sigma_3)P_3(\tau-1) + K_3 + V_2(\tau-1).\end{aligned} \tag{26}$$

Consequently, we obtain the difference system

$$\begin{aligned}\Delta P_4(\tau) &= -\lambda P_4(\tau-1) + (\sigma_1-\sigma_2)P_3(\tau-1) - K_1 - (\sigma_1-\sigma_2)P_3(\tau-1)\\ \Delta P_3(\tau) &= -(\lambda_3+\sigma_3)P_3(\tau-1) + K_3 + \sigma_3 P_3(\tau-1),\end{aligned} \tag{27}$$

which is equivalent to

$$\begin{aligned}\Delta P_4(\tau) &= -\lambda P_4(\tau-1) - K_1\\ \Delta P_3(\tau) &= -\lambda_3 P_3(\tau-1) + K_3.\end{aligned} \tag{28}$$

But,

$$\mathbf{J} = \begin{pmatrix} -\lambda & 0 \\ 0 & -\lambda_3 \end{pmatrix}$$

where $|\mathbf{J}| = \lambda\lambda_3$; therefore, the set of eigenvalues of $\mathbf{J}$ is

$$v_1 = -\lambda, \quad v_2 = -\lambda_3.$$

System (28) is asymptotically stable whenever $\lambda > 0$ and $\lambda_3 > 0$. The corresponding eigenvectors are

$$v_1 = (1,0), \quad v_2 = (0,1).$$

In view of the conditions, System (28) is asymptotically stable. Note that the solution of System (28) is given by the formula

$$\begin{aligned}P_4(n) &= c_1(-\lambda)^{n-1} - \frac{(K_1(1-(-\lambda)^n))}{\lambda+1},\\ P_3(n) &= c_3(-\lambda_3)^{n-1} + \frac{K_3(1-(-\lambda_3)^n)}{\lambda_3+1},\end{aligned}$$

where $(c_1, c_2) \in \mathbb{Z}^2$.

EXEMPLARY APPLICATIONS

An application of the above examples is when dynamic systems with controllers are assumed to be informative systems. The informative problem for control refers to the challenge of ensuring that an autonomous system has enough information to make appropriate decisions and execute its intended actions. This can be especially difficult in complex or dynamic environments where the system may need to process and interpret a large amount of data in real time. It can also be a concern in situations where the system's decision-making process is opaque or difficult to understand. To address the informative problem, researchers may use techniques such as machine learning, computer vision, and sensor fusion to help the system make more accurate and informed decisions. Additionally, they may also implement methods to increase the transparency of the system's decision-making process, such as explainable AI or interpretative machine learning. Note that the data set is informative for the property P (.) if there is if there exists a controller U such that,

$$\Omega_\Delta \subseteq \Omega_{\{P,U\}},$$

where Ω_Δ indicates the set of all systems that are consistent with the data Δ. The growth of population can present a number of challenges, including strain on resources such as food, water, and housing, as well as increased pressure on infrastructure and public services. Therefore, it can be viewed as an informative problem. Additionally, population growth can contribute to environmental degradation and climate change. It can also exacerbate economic and social inequality. It is a complex issue that requires a multifaceted approach to address, involving strategies such as family planning, education and economic development, and sustainable resource management.

The question is how to control growth of population?
There are several strategies that can be implemented to control population growth and address its associated challenges. Some of these include the following points:

- Family planning: Providing access to birth control and education about reproductive health can help individuals and couples make informed decisions about their fertility and family size.
- Education and economic development: Investing in education and economic opportunities for women and girls can lead to lower fertility rates, as women with more education and economic resources tend to have fewer children.
- Sustainable resource management: Managing resources such as water, food, and energy in a sustainable manner can help to mitigate the strain that population growth places on these resources.

- Migration management: Implementing policies to manage migration can help to prevent overpopulation in certain areas and balance the population in a more sustainable way.
- Climate change mitigation: Mitigating climate change and its effects can help to reduce the negative impact of population growth on the environment.

It is important to note that population growth is a complex issue that is influenced by a variety of variables and factors, and addressing it will require a multifaceted approach that concerns diverse sectors and stakeholders across different fields and areas.

CONCLUSION

Control of under-activated dynamical systems refers to the process of manipulating the inputs of a system in order to achieve a desired behavior or output. This can be achieved through a variety of methods, such as feedback control, adaptive control, or optimal control. The specific approach used will depend on the characteristics of the system and the desired outcome. In under-activated systems, the control inputs may have limited effect on the system's behavior, making control more challenging. In these cases, techniques such as input shaping or hybrid control may be used to improve performance. From above, we considered different 3D- systems for growing population of humans. Furthermore, we suggested a set of special cases of the system, including 2D-system and parametric 2D-system. We further discussed the stability of the proposed systems in view of its analysis. Moreover, we gave a set of controllers of chaotic systems. We showed that the proposed system can be controlled by 1D, 2D and 3D controller laws through reverse-engineering efforts extracted from existing systems to be modeled and developed accordingly. For the future efforts, one can generalize the proposed systems using any types of fractional calculus, fractals (locally fractional calculus) and quantum calculus.

Availability of data and material

Not applicable.

Conflicts of interest

The authors declare that there is no conflict of interest regarding the publication of this paper.

Authors' Contributions

All authors contributed equally and significantly to writing this article. All authors read and agreed to the published version of the manuscript.

Funding

This study did not receive any funding in any form.

Acknowledgements

The authors would like to thank the University of Technology, Iraq, and the Faculty of Computer Science and Information Technology, University Malaya, Malaysia.

LITERATURE CITED

Dhinakaran V., N. M. A.-S. K. R. S. J., Hayder N. and I. H., 2021 A new megastable chaotic oscillator with blinking oscillation terms. Complexity **2021**: 1–12.

H. Natiq, S. J. O. M. N. M. . A. K. F., N. M. Al-Saidi, 2022 Image encryption based on local fractional derivative complex logistic map. Symmetry **14**: 1874, 2022.

Hadeler, K. P., 2012 Pair formation. Journal of mathematical biology **64**: 613–645.

Iannelli, M. M., Mimmo and F. A. Milner, 2005 *Gender-structured population modeling: mathematical methods, numerics, and simulations*. Society for Industrial and Applied Mathematics.

Kendall, D. G., 1997 Stochastic processes and population growth. Journal of the Royal Statistical Society **11**: 230–282.

Keyfitz, H. C., N., 2005 *Applied Mathematical Demography*. Springer New York, NY.

Li, H. L.-Y. M. W. M. M. G. M., Ye Xuan and J. Y. Ma, 2022 Population dynamic study of prey-predator interactions with weak allee effect, fear effect, and delay. Journal of Mathematics **2022**: 1–15.

Murty, P. A., K. and V. Prasannam, 1997 First order difference system-existence and uniqueness. Proceedings of the American Mathematical Society **125**: 3533–3539.

N. M. Al-Saidi, D. B. R. W. I., H. Natiq, 2023 The dynamic and discrete systems of variable fractional order in the sense of the lozi structure map. AIMS Mathematics **8**: 1–20.

Pollard, J. H., 1997 Modelling the interaction between the sexes. Mathematical and Computer Modelling **26**: 11–24.

Rending L., M. W. F. A. K. F. N. M. A.-S., Balamurali R. and V.-T. P., 2022 Synchronization and different patterns in a network of diffusively coupled elegant wang–zhang–bao circuits. The European Physical Journal Special Topics **231**: 3987–3997.

Salih, S. H. and N. Al-Saidi, 2022 3d-chaotic discrete system of vector borne disease using environment factor with deep analysis. AIMS Mathematics **7**: 3972–3987.

Schoen, R., 2013 *Modeling multigroup populations*. Springer New York, NY.

Shaw, H. K., Allison K. and M. G. Neubert, 2018 Sex difference and allee effects shape the dynamics of sex-structured invasions. Journal of Animal Ecology **87**: 36–46.

Waldstatter, R., 1989 Pair formation in sexually-transmitted diseases. Mathematical and statistical approaches to AIDS epidemiology pp. 260–274.

Yellin, J. and P. A. Samuelson, 1974 A dynamical model for human population. Proceedings of the National Academy of Sciences **71**: 2813–2817.

How to cite this article: Salih, S. H., Al-Saidi, N. M. G., Obaiys, S. J. and Karaca, Y. 3D Chaotic Nonlinear Dynamic Population-Growing Mathematical System Modeling with Multiple Controllers. *Chaos Theory and Applications*, 6(3), 218-227, 2024.